

Geometric and Radiometric Analysis of a CCD-Camera Based Photogrammetric Close-Range System

Dr. sc. techn. Horst A. Beyer

Zurich, May 1992

This publication is an edited version of (content of title page):

DISSERTATION ETH Nr. 9701

Geometric and Radiometric Analysis of a CCD-Camera Based Photogrammetric Close-Range System

ABHANDLUNG

zur Erlangung des Titels

DOKTOR DER TECHNISCHEN
WISSENSCHAFTEN

der

EIDGENÖSSISCHEN TECHNISCHEN HOCHSCHULE
ZÜRICH

vorgelegt von

Horst A. Beyer

Dipl. Verm. Ing. ETH, Zürich

Master of Science, Ohio State University, Columbus, USA

geboren am 11. Januar 1958

von Österreich

Angenommen auf Antrag von:

Prof. Dr. A. Grün, Referent

Prof. Dr. H. Tiziani, Korreferent

Zürich, Mai 1992

First draft: July 1991
Second draft: November 1991
Oral exam: February 19, 1992

Geometric and Radiometric Analysis of a CCD-Camera
Based Photogrammetric Close-Range System

Horst A. Beyer

Copyright © 1992, Dr. Horst A. Beyer
All rights reserved

Published by: Institut für Geodäsie und Photogrammetrie
ETH-Hönggerberg
CH-8093 Zürich

ISBN 3-906513-24-6

VORWORT

Digitale Systeme für den Nahbereich spielen heute eine überragende Rolle in der photogrammetrischen Forschung und Entwicklung. Durch die On-line- und Echtzeitfähigkeit eröffnen sich dieser optischen, berührungslosen Messtechnik eine Fülle neuer Applikationen, wie zum Beispiel in der industriellen Messtechnik, der Medizin und der Robotik.

Mitentscheidend für den zukünftigen Erfolg dieser Systeme wird neben ihrem Grad an Automatisierung und ihrer Auswertegeschwindigkeit vor allem ihre Genauigkeitsleistung sein. Daher muss dem Studium des Genauigkeitsverhaltens solcher Systeme ein Höchstmass an Aufmerksamkeit zukommen.

Wesentliche Komponenten digitalphotogrammetrischer Systeme für den Nahbereich sind optoelektronische Kamera, Datentransfereinheit und Datenkonvertierung von analoger in digitale Form zur weiteren Verarbeitung im Computer. Diese Komponenten definieren die Qualität der Ausgangsdaten und sind somit bestimmend für die Qualität der Ergebnisse des Gesamtsystems.

Unter der Vielzahl optoelektronischer Sensoren wird heute der CCD-Chip mit Abstand am häufigsten eingesetzt, die wichtigsten Datentransfermodi sind Composite Video mit PLL-Liniensynchronisation, pixelsynchron ("Pixelclock") und digital. Die Analog-Digital-Wandlung erfolgt bei analoger Übertragung auf handelsüblichen "Framegrabberboards". Von der Generierung des Bildsignals auf dem Chip bis zu seiner Digitalisierung und Weiterverarbeitung im Computer ist dieses einer Vielzahl von Fehlereinflüssen ausgesetzt (ca. zwei Dutzend Fehlerursachen). Diese Fehler können geometrische und/oder radiometrische Auswirkungen haben. Das Ziel der vorliegenden Arbeit ist nun, die Ursachen der wichtigsten Fehlereinflüsse zu analysieren und ihre Auswirkungen zu quantifizieren. Dabei werden einzelne Fehlerkomponenten separat analysiert und abschliessend ein Systemtest unter Benutzung eines dreidimensionalen Testfelds durchgeführt, welcher den heutigen Stand der geometrischen Leistungsfähigkeit derartiger Systeme festschreibt.

Diese Arbeit ist ein bedeutender Beitrag zum besseren Verständnis des geometrischen und radiometrischen Verhaltens der Komponenten CCD-Kamera, Signalübertragung und A/D-Wandlung eines digitalphotogrammetrischen Nahbereichssystems. Dem Autor ist es gelungen, Methodik und Kenntnisse der Hardwareanalyse, die ausserhalb des engeren Fachgebietes angesiedelt sind, erfolgreich zu integrieren.

Die Arbeit schliesst mit einem umfassenden Systemtest. Dieser weist nach, dass heute eine Relativgenauigkeit von 1:70 000 (oder ca. 1/100 Pixel) mit preiswerten, leicht zugänglichen Hardwarekomponenten erreicht werden kann. Dies hebt die digitale Nahbereichsphotogrammetrie auf ein bisher nicht realisiertes Genauigkeitsniveau und eröffnet neue Applikationsperspektiven für die Zukunft.

Die vorliegende Arbeit zeugt nach Inhalt und Umfang vom grossen Fleiss, enormen Engagement und fachübergreifender Kompetenz des Autors. Sie kann als wesentlicher Baustein in der Entwicklung einer Untersuchungsmethodik von digitalphotogrammetrischen CCD-Kamerasystemen für den Nahbereich gelten. Es ist daher zu erwarten, dass ihr für die kommenden Jahre Referenzcharakter zukommt.

Dem Autor sei für seinen grossen Einsatz herzlich gedankt!

Zürich, Juni 1992

Prof. Dr. Armin Grün
(Professur Photogrammetrie)

WORKS

The first of the works mentioned above is the "Tragedy of Hamlet, Prince of Denmark," which is the most famous of Shakespeare's plays. It is a tragedy that deals with the theme of revenge. The play is set in Denmark, and it tells the story of a man who kills his father and then is haunted by his ghost.

The second of the works mentioned above is the "Tragedy of Othello, the Moor of Venice," which is another tragedy. It deals with the theme of jealousy. The play is set in Venice, and it tells the story of a man who kills his wife because he is jealous of her.

The third of the works mentioned above is the "Tragedy of King Lear," which is a tragedy that deals with the theme of power. The play is set in Britain, and it tells the story of a king who divides his kingdom among his three daughters, only to find out that they have all betrayed him.

The fourth of the works mentioned above is the "Tragedy of Macbeth," which is a tragedy that deals with the theme of ambition. The play is set in Scotland, and it tells the story of a man who kills his king because he wants to become king himself.

The fifth of the works mentioned above is the "Tragedy of Antony and Cleopatra," which is a tragedy that deals with the theme of love. The play is set in Egypt, and it tells the story of a man who kills himself because of his love for a woman.

The sixth of the works mentioned above is the "Tragedy of Julius Caesar," which is a tragedy that deals with the theme of power. The play is set in Rome, and it tells the story of a man who is killed because he is too powerful.

The seventh of the works mentioned above is the "Tragedy of Titus Andronicus," which is a tragedy that deals with the theme of revenge. The play is set in Rome, and it tells the story of a man who kills his enemies because they have killed his family.

The eighth of the works mentioned above is the "Tragedy of Troilus and Cressida," which is a tragedy that deals with the theme of love. The play is set in Troy, and it tells the story of a man who kills himself because of his love for a woman.

The ninth of the works mentioned above is the "Tragedy of Coriolanus," which is a tragedy that deals with the theme of power. The play is set in Rome, and it tells the story of a man who is killed because he is too powerful.

The tenth of the works mentioned above is the "Tragedy of Timon of Athens," which is a tragedy that deals with the theme of power. The play is set in Athens, and it tells the story of a man who is killed because he is too powerful.

ABSTRACT

The advent of filmless imaging systems, especially of Charge-Coupled Devices (CCD), has created manifold opportunities and new applications which have led to significant changes in Photogrammetry. The exacting demands of Photogrammetry on the radiometric and geometric characteristics of the imaging sensor and all other elements involved in the acquisition of imagery with solid-state sensors, require a detailed analysis of the factors affecting the performance.

This analysis can build on extensive knowledge acquired over the last twenty years for the calibration of film based cameras. For example the modelling of systematic errors introduced by lenses is identical for both systems. Calibration and analysis techniques, such as the bundle adjustment with self-calibration, are important tools. Another source of a great deal of information are applications of solid-state sensors in astronomy. Exacting radiometric requirements have led to the development of specialized sensors, cameras, image acquisition systems, and calibration techniques. These techniques are currently only partially applicable to photogrammetric tasks though. They are tuned to be used with extremely specialized hardware (cameras, image acquisition systems, testing arrangements) which is typically not available for photogrammetric applications. One task of this dissertation was thus to investigate the effects of cameras, signal transmission techniques, and frame grabbers as they are widely available on the market as off-the-shelf equipment. The individual components were investigated first, then the combined radiometric and geometric performance of the system was analyzed, and finally the performance of a system for three-dimensional measurements was verified. This in turn required the installation of an image acquisition system with advanced capabilities to perform various comparative investigations, to set up a three-dimensional testfield, and to write a large amount of software for analysis and calibration.

The geometric regularity and the excellent radiometric characteristics of solid-state sensors make them ideal measurement devices. A number of investigations have shown that the regularity of the sensor element spacing is in the order of $1/100^{\text{th}}$ of the spacing. The uniformity of response from sensor element to sensor element is 1% and better for many off-the-shelf cameras. The geometric regularity of the sensor would thus allow to measure positions of targets imaged on such a sensor with a precision of $1/100^{\text{th}}$ of the spacing and better. This is actually achieved and surpassed with special sensors in star tracking applications. The mechanical design and the electronics of CCD-cameras are usually not designed for photogrammetric purposes. The mechanical design is often not sufficiently stable, i.e. the assembly of lens, housing and sensor is not rigid. The camera electronics are designed for visual purposes (e.g. surveillance), thus potentially introducing significant degradations due to a number of factors such as low-pass-filters, gamma correction, addition of video signals, to name but a few.

The largest drawback with respect to the radiometric and geometric performance, but an advantage with respect to economy, is the use of standard analog video signals for the transmission of the imagery acquired by solid-state sensors. These standards were developed in the 1950's for broadcasting and are not at all tuned for the requirements of precise measurements. The radiometric and geometric properties of these signals were analyzed, potential drawbacks discussed, as well as methods for determination and compensation and/or elimination of deficiencies investigated and performed.

Frame grabbers are another critical component of the image acquisition system. They must convert the analog transmitted imagery into matrices of numbers, the digital image.

The radiometric and geometric performance of a number of electronic components and of different synchronization techniques of the frame grabber were analyzed. These tests revealed a number of critical issues such as proper DC-restoration, degrading effects of low-pass-filters, deviations from linearity, low level patterns, and the performance of pixel-synchronous sampling as compared to PLL line-synchronization. This allows to separate influences of the frame grabber from those of the camera. The assessment of the effects of the two synchronization techniques, pixel-synchronous sampling and PLL line-synchronization, lead to the detection of a geometric deformation (which can be introduced when composite video signals are used in connection with PLL line-synchronization) and the confirmation of the degrading effects of line-jitter. It was furthermore shown that pixel-synchronous sampling provides a transmission without loss for photogrammetric purposes. The investigation of several radiometric characteristics of the complete system demonstrated some of the insufficiencies of typical off-the-shelf hardware. Potential trouble spots, such as degradations of the radiometric uniformity at the borders of the imagery, were detected. The difficulty of radiometric calibration of the system was addressed.

A test strategy for the assessment of the geometric stability of the system was developed. The effects of the synchronization on the radiometric performance was used to develop test methods to rapidly pinpoint imprecisions of the frame grabber synchronization. The analysis of the repeatability proved that pixel-synchronous frame grabbing provides identical geometric characteristics as digital transmission. The short time repeatability for both digital image transmission as well as pixel-synchronous sampling was shown to be in the order of 0.004 pixel. The analysis of PLL line-synchronization using pixel-synchronous frame grabbing as reference confirmed that line jitter reduces the internal precision in row direction by a factor of six. Disturbances of the PLL line-synchronization, introduced by composite video signals, were shown to lead to geometric deformations reaching 0.3 pixel. The study of warm-up-effects allowed to determine the minimal time required by the system (camera and frame grabber) to reach a steady state. When using pixel-synchronous sampling the major contributing factor to warm-up effects are thermally-induced deformations of the camera body, i.e. the assembly of lens and sensor. The geometric stability of the image acquisition system was verified with a test of over one week duration. It could be shown that for durations of several days a repeatability of well below $1/100^{\text{th}}$ of a pixel can be achieved. Finally the effects of local variations of the illumination and/or of shadows on the position determination with Least-Squares-Matching were analyzed. It was empirically demonstrated that gradients of a few per cent can lead to errors in the estimated position of several hundred's of a pixel.

The geometric precision and accuracy of the system was verified with a three-dimensional testfield. The part of the testfield used in the tests spans a volume of 2600 x 2000 x 1100 mm with 162 targets of 20 mm diameter. The position of the targets was determined with a precision of 0.02 to 0.03 mm by theodolite measurements. Two sets of 48 frames were acquired, one with pixel-synchronous sampling and the other with PLL line-synchronization. The relative accuracy attained with the pixel-synchronously grabbed imagery reaches 1 part in 50 000 in object space and is $1/85^{\text{th}}$ of the pixel spacing in the image when using 30 control points were used. This is reduced to 1 part in 46 000 and $1/50^{\text{th}}$ of the pixel spacing with a minimally constrained network. The accuracy attained with the imagery acquired with PLL line-synchronization is only slightly lower. It was thus shown that very high accuracies can be attained with PLL line-synchronization when appropriate modelling of the geometric deformation and a large number of images are used. A comparison of the object coordinates computed with the two

data sets indicated a relative accuracy of 1 part in 70 000 and 60 000 for the X and Y axes respectively. The accuracy in image space of the comparison is $1/100^{\text{th}}$ of the pixel spacing. Finally some factors which limit the accuracy and approaches for their elimination are discussed.

ZUSAMMENFASSUNG

Das Aufkommen von filmlosen Bildaufnahmesystemen, insbesondere von CCD-Bildsensoren (Charge-Coupled Device) öffnet der Photogrammetrie neue Möglichkeiten und zahlreiche Anwendungsgebiete. Dies führt zu grossen Änderungen in der Photogrammetrie. Die hohen Anforderungen der Photogrammetrie an die radiometrische und geometrische Qualität der Bilder und somit an alle in den Bildaufnahmeprozess involvierten Elemente erfordern eine detaillierte Analyse leistungsbeeinflussender Faktoren.

Bei der Analyse radiometrischer und geometrischer Eigenschaften kann dabei auf das umfangreiche Wissen über Kalibrierungsverfahren von film-basierenden Kameras zurückgegriffen werden. Die Modellierung systematischer Kamera-Fehler von Objektiven ist identisch. Die Grundlage für hochentwickelte Kalibrierungsverfahren und Analysen bildet die Bündelblockausgleichung mit Selbstkalibrierung. Dabei können auch Erfahrungen über den Einsatz von CCD-Bildsensoren in der Astronomie genutzt werden. Hohe Anforderungen an die radiometrische Qualität führten dort zur Entwicklung von speziellen Sensoren, Kameras, Bildaufnahmesystemen und Kalibrierungsmethoden. Wegen der spezialisierten Ausrüstung sind diese Kameras, Aufnahmesysteme und Kalibrierverfahren nur bedingt für photogrammetrische Problemstellungen einsetzbar.

Die Aufgabe dieser Arbeit bestand darin, die Eigenschaften handelsüblicher und weit verbreiteter CCD-Kameras sowie Methoden der Signalübertragung und des Frame Grabblings zu untersuchen. Hierbei wurden zunächst die einzelnen Komponenten untersucht, danach wurde die radiometrische und geometrische Leistung des Systems getestet, und zuletzt wurde die Genauigkeit von drei-dimensionalen Messungen mit einem Testfeld überprüft. Dies erforderte die Installation eines flexiblen Bildaufnahmesystems, der Aufbau eines drei-dimensionalen Testfeldes und die Entwicklung von spezieller Software für Analyse und Kalibrierung.

Die geometrische Regelmässigkeit und die ausgezeichneten radiometrischen Charakteristika von Halbleiter-Bildsensoren sind für Messaufgaben gut geeignet. Eine Reihe von in der Literatur dokumentierten Untersuchungen zeigen, dass die Regelmässigkeit der Abstände der Sensorelemente im Bereich von $1/100^{\text{tel}}$ des Abstandes der Elemente liegt. Die Abweichungen der Sensorelement-Empfindlichkeit beträgt ebenfalls etwa ein Prozent. Es sollte damit möglich sein, die Position von Punkten mit einer Genauigkeit von $1/100^{\text{tel}}$ Pixel bestimmen zu können. Derart hohe Genauigkeiten werden mit speziellen Sensoren in astronomischen Orientierungssystemen erreicht.

Standard CCD-Kameras sind üblicherweise nicht für photogrammetrische Anwendungen ausgelegt, weil die mechanische Konstruktion meist nicht ausreichend stabil und die Elektronik auf visuelle Kriterien abgestimmt ist. Problematisch sind bei diesen CCD-Kameras auch der Tiefpassfilter, die Gammakorrektur und die Anbringung der Synchronisationssignale.

Die grössten Probleme entstehen bei der Verwendung des Standard Video Signals. Diese Signale wurden in den fünfziger Jahren entwickelt und sind nicht auf die Anforderungen

für hochgenaue Messungen abgestimmt. Schwachstellen der Signale und deren Kompensation werden diskutiert.

Frame Grabber bilden eine weitere kritische Komponente bei der Bildaufnahme. Sie haben die Aufgabe, aus den analogen Signalen eine Matrix von Zahlen, das digitale Bild, zu generieren. Die radiometrischen und geometrischen Eigenschaften einiger elektronischer Komponenten und verschiedener Synchronisationsverfahren wurden untersucht und ein Frame Grabber wurde getestet. Diese Tests deckten kritische Faktoren wie DC-Restaurierung, Tiefpassfilter, Linearität und weitere unbekannte Einflüsse auf. Die Leistungsfähigkeit von pixelsynchroner Bildaufnahme und PLL-Zeilensynchronisation konnte untersucht werden. Eine geometrische Deformation, die durch die Verwendung von kompositen Videosignalen mit PLL-Zeilensynchronisation entstehen, wurde nachgewiesen. Ebenfalls konnte die Degradation der Stabilität durch "Line-jitter" festgestellt werden. Die Annahme, dass pixelsynchrone Bildaufnahme zu einer Ausschaltung dieser Synchronisationsfehler führt, konnte bestätigt werden. Einige Unzulänglichkeiten von typischer "off-the-shelf" Ausrüstung konnten anhand von radiometrischen Untersuchungen am System gezeigt werden. Dabei wurden potentielle Fehlerquellen und Probleme der radiometrischen Kalibrierung untersucht.

Zusätzlich wurden Tests zur Analyse der geometrischen Stabilität des Systems und anderer wichtiger Einfluss-Faktoren entwickelt. Sehr empfindliche radiometrische Verfahren zur schnellen Evaluation der Synchronisation wurden entwickelt. Es konnte gezeigt werden, dass die pixelsynchrone Bildaufnahme eine geometrische Qualität liefert, welche einer digitalen Bildübertragung vergleichbar ist. Eine Wiederholbarkeit von 0.004 Pixel konnte mit beiden Verfahren erreicht werden. Die PLL-Zeilensynchronisation führt durch den Einfluss von "line-jitter" zu einer Verschlechterung der Wiederholbarkeit in Zeilenrichtung um einen Faktor sechs. Ein Vergleich der Geometrie bei Verwendung der pixelsynchronen Bildaufnahme als Referenz zeigte, dass geometrische Deformationen von bis zu 0.3 Pixel auftreten können. Die minimale Aufwärmzeit des Systems wurde bestimmt. Bei der Verwendung von pixelsynchroner Bildaufnahme werden die Deformationen grösstenteils durch thermische Veränderungen an der Kamera hervorgerufen. Die geometrische Stabilität des Systems wurde mit einem über eine Woche dauernden Test überprüft. Dabei konnte eine Wiederholbarkeit von besser als 0.01 Pixel über einen Zeitraum von einem Tag erreicht werden. Ausserdem wurde der Einfluss von lokalen Helligkeitsgradienten auf die Positionsbestimmung mit Kleinsten Quadrate Korrelation bestimmt.

Die Genauigkeit des Systems wurde zuletzt mit einem drei-dimensionalen Testfeld überprüft. Das Testfeld umfasst ein Volumen von 2600 x 2000 x 1100 mm mit 162 Zielmarken mit einem Durchmesser von 20 mm. Die Koordinaten der Zielmarken wurden mit Theodoliten auf eine Genauigkeit von 0.02 bis 0.03 mm bestimmt. Datensätze mit 48 Bildern, welche je mit PLL-Zeilensynchronisation als auch mit pixelsynchroner Bildaufnahme aufgenommen wurden, konnten untersucht werden. Die aus einem Vergleich mit den Referenzkoordinaten bestimmte relative Messgenauigkeit erreicht mit den pixelsynchron aufgenommenen Bildern und 30 Passpunkten 1 : 85000 im Objektraum und $1/85^{\text{tel}}$ des Pixelabstandes im Bildraum. Bei einer minimalen Lagerung des Netzes wurde 1 : 46000 oder $1/50^{\text{tel}}$ des Pixelabstandes nachgewiesen. Die drei-dimensionale Messgenauigkeit mit PLL-Zeilensynchronisation ist um nur einige Prozent schlechter. Ein Vergleich der zwei Datensätze ergab eine Relativgenauigkeit von 1 : 70000 und 60000 in der X und Y Achse. Die so erhaltene Genauigkeit im Bildraum entspricht $1/100^{\text{tel}}$ des Pixelabstandes. Abschliessend werden Faktoren besprochen, welche die Genauigkeit limitieren, und Möglichkeiten zu ihrer Ausschaltung diskutiert.

TABLE OF CONTENTS

1	INTRODUCTION.....	1
1.1	Statement of the Problem and Research Objectives.....	1
1.2	Approach and Organisation.....	2
2	SYSTEM OVERVIEW	4
2.1	Digital Photogrammetric Station (DIPS).....	4
2.2	Real-Time Photogrammetric System	4
2.2.1	Illumination	6
2.3	Cameras	7
2.4	Testfields	8
2.4.1	Reference Coordinates.....	10
2.5	Software.....	15
2.5.1	Image Acquisition with DEDIP.....	16
3	IMAGE ACQUISITION WITH SOLID-STATE SENSORS.....	18
3.1	Signal Transmission and Frame Grabbing	18
3.2	The Solid-State Camera.....	19
3.3	The Solid-State Sensor	20
3.4	Television Standards	21
3.4.1	Conventional Video Standards	21
3.4.2	High-Definition Television	24
3.5	Camera Electronics.....	25
3.5.1	Analog Cameras	25
3.5.2	Digital Camera.....	28
3.6	Frame Grabbing.....	29
3.6.1	Analog Front End	30
3.6.2	Synchronization	33
	Synchronization with a Phase-Locked-Loop	33
	Synchronization with a Fixed Master Clock	36
	Synchronization with Pixel-clock	36
3.7	Analog versus Digital Transmission	38
3.8	Data Buffering	39
3.9	Analog-to-Digital Conversion	39
4	EVALUATION OF THE FRAME GRABBER PERFORMANCE	43
4.1	Test Setup	43
4.2	Offset and Gain Adjustment.....	44
4.3	DC-Restoration.....	44
4.4	Noise.....	46
	Method 1.....	46
	Method 2.....	47
	Method 3.....	48
	Systematic Patterns.....	48
	Noise and Signal Level.....	49
4.5	Linearity	50
4.6	MTF of Frame Grabber	51
4.6.1	Impulse Response	51
4.6.2	Determination and Analysis of the MTF.....	52

4.7	Synchronization	55
4.7.1	Synchronization with PLL.....	56
4.7.2	Pixel-synchronous Sampling	57
4.8	Conclusions of Chapter	61
5	RADIOMETRIC EVALUATION OF CAMERA/FRAME GRABBER AS A SYSTEM	62
5.1	Installation Testing	62
5.1.1	Basic Installation and Border Effects	62
5.1.2	Analog Offset and Gain.....	65
5.1.3	DC-Restoration.....	65
5.2	Basic Radiometric Properties	67
5.2.1	Dark Signal Non-Uniformity (Fixed-Pattern Offset Non-Uniformity).....	67
5.2.2	Camera Power Supply and Patterns	69
5.3	Photo Response Non-Uniformity and Radiometric Correction.....	70
	Test with Nikon Lens	71
	Test with CCTV-lens.....	73
5.3.1	Uniformity of Geometry from PRNU	75
5.4	Noise.....	75
5.4.1	Photon Transfer Function (Photon Transfer Curve).....	77
	Signal-to-Noise Ratio and Dynamic Range	78
5.4.2	Averaging	78
5.5	Graylevel Shift and Transfer Function	79
5.6	Conclusions of Chapter	80
6	REPEATABILITY OF IMAGE TARGET LOCATIONS	82
6.1	Least Squares Matching	82
6.1.1	Oscillations of Least Squares Matching	83
	Comparison between Templates	88
	Dependence of LSM on Approximations.....	90
6.2	Averaging	90
6.3	Synchronization.....	91
6.3.1	PLL Line-Synchronization versus Pixel-synchronous Sampling.....	91
	Analysis by Image Subtraction.....	93
	Analysis with Temporal Noise from Averaging	94
	Analysis using the Relation of Temporal Noise to Grayvalues	95
	Positional Repeatability and Geometric Deformations	96
	Line-Displacement	99
6.3.2	Analog versus Digital Transmission	99
6.4	Target Size.....	103
6.5	Test Configurations for Warm-Up-Effects and Repeatability.....	104
6.6	Warm-Up-Effects	105
6.7	Repeatability.....	108
6.8	Local Illumination Gradients.....	112
6.8.1	Empirical Verification	113
6.8.2	Assessment with Simulated Data	118
6.9	Conclusions of Chapter	120
7	THREE-DIMENSIONAL PERFORMANCE ANALYSIS WITH A TEST-FIELD	121
7.1	Mathematical Model.....	121

7.2	Test Arrangement and Network	126
7.3	Measurement of Image Coordinates	129
7.3.1	Approximations	131
7.3.2	Automatic Measurement	134
7.3.3	Measurement Speed.....	135
7.4	Performance with Pixel-synchronous Frame Grabbing	136
7.4.1	Modelling of Systematic Errors.....	136
7.4.2	Potential Limiting Factors	141
7.4.3	Influence of Local Illumination Gradients	149
7.4.4	Degradations from Obliqueness and Small Image Scale	156
	Further Additional Parameters	157
7.5	Performance with PLL Line-Synchronisation.....	165
7.6	Comparison of Results from the Two Synchronization Modes	173
7.7	Conclusions of the Three-Dimensional Performance Analysis.....	175
8	CONCLUSIONS	176
9	REFERENCES.....	178
10	ABBREVIATIONS AND GLOSSARY	184
10.1	Abbreviations	184
10.2	Synchronization Modes for SONY-XC77CE Camera	184
10.3	Abbreviations used in Tables of Chapter 7	185
10.4	Bundle Versions of Chapter 7	185
11	ACKNOWLEDGMENTS	186
12	CURRICULUM VITAE.....	187

1		
111		
112		
113		
114		
115		
116		
117		
118		
119		
120		
121		
122		
123		
124		
125		
126		
127		
128		
129		
130		
131		
132		
133		
134		
135		
136		
137		
138		
139		
140		
141		
142		
143		
144		
145		
146		
147		
148		
149		
150		
151		
152		
153		
154		
155		
156		
157		
158		
159		
160		
161		
162		
163		
164		
165		
166		
167		
168		
169		
170		
171		
172		
173		
174		
175		
176		
177		
178		
179		
180		
181		
182		
183		
184		
185		
186		
187		
188		
189		
190		
191		
192		
193		
194		
195		
196		
197		
198		
199		
200		

LIST OF FIGURES

Figure 1.1	Real-Time Photogrammetry: Tasks and Hardware.....	3
Figure 2.1	Components of the Digital Photogrammetric Station.....	4
Figure 2.2	Hardware architecture of Image Acquisition Workstation.....	5
Figure 2.3	Picture of the image acquisition workstation.....	6
Figure 2.4	Fibre-optic illumination system and testfield with theodolite, camera, and illumination.....	7
Figure 2.5	SONY-XC77CE camera with a FUJINON 9 mm lens.....	8
Figure 2.6	Camera and connection to system.....	8
Figure 2.7	Small testfield consisting of a moving plate on a stage.....	9
Figure 2.8	Testfield and targets.....	9
Figure 2.9	Floor plan of testfield.....	10
Figure 2.10	Plots of the comparison of the two sets of measurements of tf91 versus tf90.....	13
Figure 2.11	Plots of comparison of tf90 with tf89 and of tf91 with tf90.....	14
Figure 2.12	Modules of DEDIP relevant to the RTPS.....	15
Figure 2.13	Panel for the generation of the camera and image acquisition configuration.....	16
Figure 2.14	Screen during acquisition of images with panels for image acqui- sition and image processing.....	17
Figure 3.1	Signal transmission and frame grabbing with analog versus dig- ital cameras.....	18
Figure 3.2	Functional elements of a solid-state camera.....	19
Figure 3.3	Frame and fields in interlaced video.....	22
Figure 3.4	The CCIR video signal.....	23
Figure 3.5	A line and the horizontal synchronisation pulse of the CCIR vid- eo signal.....	24
Figure 3.6	Block diagram of a typical CCD camera.....	26
Figure 3.7	Images taken with automatic AGC of a grayscale on black and white background.....	27
Figure 3.8	Images of grayscale taken with and without gamma correction by the camera.....	28
Figure 3.9	Effect of aperture correction on MTF (data from <i>HCS, 1990</i>).....	28
Figure 3.10	Basic elements of a digital camera.....	29
Figure 3.11	Typical image acquisition components of a frame grabber.....	30
Figure 3.12	Analog front end.....	30
Figure 3.13	Image with signal reflections from improper termination.....	31
Figure 3.14	Simple DC restoration circuit and clamping error.....	31
Figure 3.15	Two DC-restoration circuits with sample and hold.....	32
Figure 3.16	Signals and their flow in frame grabbing with PLL synchronisa- tion.....	33
Figure 3.17	Components and signals of a PLL.....	34
Figure 3.18	VCO control voltage during capture and locking.....	34
Figure 3.19	Line-jitter shown for an image grabbed from a video recorder.....	35
Figure 3.20	Some effects of frame grabber synchronisation with a PLL.....	35
Figure 3.21	Phase pattern from cross-talk of pixel-clock when sampling with a frequency different to the sensor element clock frequency.....	36
Figure 3.22	Signals and their flow in pixel-synchronous frame grabbing.....	37

Figure 3.23	HSYNC detection by edge detector.....	37
Figure 3.24	Image showing line-displacement for some lines.....	37
Figure 3.25	Characteristics of pixel-synchronous frame grabbing.....	38
Figure 3.26	Frame Grabber: Data Synchronisation and Buffering.....	39
Figure 3.27	Schematic diagram of a 3-bit flash analog-to-digital converter.....	40
Figure 3.28	Timing adjustment of sampling clock.....	41
Figure 3.29	Dependence of SNR on input frequency of the analog signal of an 8-bit 50 MHz ADC.....	42
Figure 4.1	Test configurations for testing of frame grabber.....	43
Figure 4.2	Cross-section through first 200 lines of an image showing typical errors with wrong DC-restoration.....	45
Figure 4.3	Image showing increase of average image intensity within x due to instability of sample-and-hold of DC-restoration circuit.....	45
Figure 4.4	Expected and observed standard deviation of average for a consecutively increasing number of frames.....	46
Figure 4.5	Single and average frame and image containing the temporal noise showing typical patterns.....	49
Figure 4.6	Plot of temporal noise versus grayvalue and residuals as determined from linear ramp images.....	49
Figure 4.7	Residuals of line fit to ramp data and histograms for one line of an individual frame (top) and an average of five frames (bottom).....	50
Figure 4.8	Residuals of a histogram taken over 512 lines from one frame to show the inexistence of missing codes.....	51
Figure 4.9	Impulse response without a) and with b) a LPF in the input. The asymmetric response and the ringing are visible from the images and profiles for the version with LPF.....	52
Figure 4.10	Parts of imagery and profiles of line sweep images without (top) and with (bottom) the LPF in the input.....	53
Figure 4.11	MTF determination of frame grabber.....	54
Figure 4.12	MTFs of MAX-SCAN frame grabber. Left from multiburst images, right from line sweep signals.....	55
Figure 4.13	Line position and residuals of line fit for three different frame grabber configurations without averaging.....	59
Figure 4.14	Line position and residuals of line fit for three different frame grabber configurations with averaging over five frames.....	60
Figure 5.1	Signals at the sensor read-out a) and the video signal for one row.....	63
Figure 5.2	Image showing a complete frame and surrounding areas.....	64
Figure 5.3	Profiles through upper left and right as well as top and bottom edges of image from above figure.....	64
Figure 5.4	DC-restoration on sync level during broadcast pulses (settings of Oscilloscope: clamping pulse 5V/50µsec; composite video 1V/50µsec).....	65
Figure 5.5	DC-restoration on sync level during broadcast pulses.....	66
Figure 5.6	Images taken with different clamping pulse timing (thresholded to visualize the small grayvalue differences!).....	66
Figure 5.7	DC-restoration from hardware pulse generated from rising edges and detail of pulse with video signal.....	67

Figure 5.8	Average and standard deviations of frames.	68
Figure 5.9	Averaged frames showing the large difference in the low level patterns between different boards.	69
Figure 5.10	Offset and gain variations (the images are stretched for visualisation).	72
Figure 5.11	Radiometric correction with CCTV-type lens. Shown are offset and gain images for two methods.	73
Figure 5.12	Image before (left) and after (right) radiometric correction.	74
Figure 5.13	Noise from uniform field images and from a series of images from the testfield.	76
Figure 5.14	Photon transfer function and determination of system gain factor.	77
Figure 5.15	Signal-to-noise ratio as a function of grayvalue	78
Figure 5.16	Testing for transfer function	79
Figure 5.17	Gray step card on dark background with profile through gray scale.	79
Figure 5.18	Linearity: grayvalue versus intensity and residuals of fit versus intensity.	80
Figure 5.19	Profiles of background and gray step card.	81
Figure 6.1	Image used for repeatability testing with vectors showing residuals with respect to the average of the point locations for twenty images.	83
Figure 6.2	Oscillatory behaviour of shift and scale in x (top) and y (bottom) during 50 iterations for point 4035. The units for shifts are pixel.	84
Figure 6.3	Change in last iterations of template matching when oscillations occur.	84
Figure 6.4	Templates of the different versions and a typical point of an image.	86
Figure 6.5	Changes of shifts in x and y with detection of oscillations.	86
Figure 6.6	Residuals of version 2.	87
Figure 6.7	Changes of the shift in x during template matching with a template adapted in size and radiometry to the targets of the image. Typical long-periodic oscillatory patterns are shown.	87
Figure 6.8	Part of image with two of the points at which errors occurred (left) and plot of repeatability analysis before re-measurement of the wrongly measured points (right).	88
Figure 6.9	Plots of residuals of versions 3 (left) and 4 (right) compared to version 2. The targets which were re-measured in version 4 with a different template are circled.	89
Figure 6.10	Part of an image with profile showing local illumination gradients.	90
Figure 6.11	Plot of residuals of version 5.	90
Figure 6.12	Parts of the imagery acquired with the three configurations and histogram of image acquired with the xc77_cvp configuration.	92
Figure 6.13	Subtraction of consecutive images.	93
Figure 6.14	Temporal noise for different synchronization methods.	94
Figure 6.15	Plots of temporal noise versus grayvalue, gradient in x and gradient in y for three configurations.	95

Figure 6.16	Analysis of geometry.	97
Figure 6.17	Position of plumbline for xc77_cv and xc77_cvp configurations.	98
Figure 6.18	Residuals from line fit and differences of position from row to row for a line acquired with PLL line-synchronization and with pixel-synchronous frame grabbing.	98
Figure 6.19	Image showing typical line-displacement.	99
Figure 6.20	Image (size is 1280 x 1024) and histogram.	100
Figure 6.21	Results of subtraction of two analog transmitted images with averages differing by 3 DN.	100
Figure 6.22	Temporal noise with analog and digital transmission.	101
Figure 6.22	Plots of temporal noise versus grayvalue, gradient in x and gradient in y for three configurations. Note that the values for the noise were multiplied by 10.	102
Figure 6.23	Analysis of repeatability as a function of target size and template size.	104
Figure 6.24	Test arrangement for warm-up and repeatability evaluation.	105
Figure 6.25	Warm-up-effects of XC77 with pixel-synchronous frame grabbing.	106
Figure 6.26	Repeatability of first day.	107
Figure 6.27	Repeatability analysis for a period of 9 days.	109
Figure 6.28	Repeatability when correcting for trend (b) and repeatability for the duration of days 2 to 5 and days 8 to 9 (c).	110
Figure 6.29	Repeatability for all days without removal of average image displacement (left, version 53) and with removal thereof (right, version 54).	111
Figure 6.30	Repeatability for days 2 to 5 (left, version 55) and days 8 and 9 (right, version 56).	111
Figure 6.31	Plane view of testfield, curtains, and camera stations.	112
Figure 6.32	Imagery with profiles. a) with lights on the side on. b) with the lights off.	113
Figure 6.33	Patches and templates for 5 x 5 and 7 x 7 template sizes for a point of left column.	114
Figure 6.34	Repeatability analysis for the 7 x 7 template of version 111.	116
Figure 6.35	Repeatability analysis for the 7 x 7 template of version 112 showing the positional variations induced by the change in illumination.	117
Figure 6.36	Displacements for 7 x 7 template (a and b) and 5 x 5 template (c and d) for left and right columns of targets.	118
Figure 6.37	Local illumination gradient.	119
Figure 7.1	The pixel and image coordinate systems.	121
Figure 7.2	Image showing the lights, curtain, camera and testfield.	126
Figure 7.3	Schematic plane and perspective views of the test arrangement.	127
Figure 7.4	An image of the testfield taken at station 12 and zoomed portions thereof showing the large range in size of target images.	129
Figure 7.5	Operator input, processes and data of the three-dimensional performance analysis.	130
Figure 7.6	Semiautomatic measurement of pixel coordinates for the initial orientation and calibration.	133

Figure 7.7	Interactive verification of errors from template matching, image coordinate residuals, and comparison to checkpoints.	135
Figure 7.8	Distortion profile for radial symmetric distortion (K_1, K_2, K_3).	139
Figure 7.9	Effects of additional parameters of version cvp223 on a 6 by 4 mm grid (image format is 8 by 6 mm).	140
Figure 7.10	Geometry for assessing the difference between the location of the centre of the object circle in the image and the centre of its elliptical image.	142
Figure 7.11	Residuals of version cvp223 for 6 images grabbed at stations 12xx.	144
Figure 7.12	Check point differences for version cvp223 for 6 images of stations 15xx (top) and an image at station 1330 (bottom).	145
Figure 7.13	Differences to check points in object space for version cvp223.	146
Figure 7.14	Residuals (top) and checkpoint differences (bottom) for images taken at stations 15xx of version cvp221.	147
Figure 7.15	Differences to check points in object space for version cvp221.	148
Figure 7.16	Shadows and light intensity variations. The profiles refer to the line with grayvalue 0.	149
Figure 7.17	Residuals (top) and checkpoint differences (bottom) for images taken at station 15xx of version cvp243.	151
Figure 7.18	Differences to control and check points in object space for version cvp243.	152
Figure 7.19	Differences to control and check points in object space for version cvp323.	154
Figure 7.20	Differences to control and check points in object space for version cvp343.	155
Figure 7.21	Image of target on front structure under oblique view.	156
Figure 7.22	Residuals (top) and checkpoint differences (bottom) for images taken at station 15xx. of version cvp601.	160
Figure 7.23	Differences to control and check points in object space for version cvp601.	161
Figure 7.24	Residuals (top) and checkpoint differences (bottom) for images taken at station 15xx of version cvp611.	162
Figure 7.25	Differences to control and check points in object space for version cvp611.	163
Figure 7.26	a) Areas of the 42 images of target 3023 (target at left bottom of wall).	164
Figure 7.27	Comparison of image coordinates of imagery acquired pixel-synchronously and with PLL line-synchronisation images. They are the plots of stations 15xx (in a) and 25xx (in b).	166
Figure 7.28	Results of comparison of image coordinates between pixel-synchronous and PLL line-synchronisation.	167
Figure 7.29	Residuals from line fit to plumbline for pixel-synchronous (top) and PLL line-synchronisation (bottom).	168
Figure 7.30	Residuals (top) and checkpoint differences for images taken at station 15xx of version cv611.	171
Figure 7.31	Differences to check points in object space for version cv611.	172
Figure 7.32	Differences of object point coordinates of version cvp611 and cv611.	174

1	Introduction	1
2	1. The Problem	2
3	2. The Method	3
4	3. The Results	4
5	4. The Discussion	5
6	5. The Conclusion	6
7	6. The Acknowledgments	7
8	7. The References	8
9	8. The Appendix	9
10	9. The Bibliography	10
11	10. The Index	11
12	11. The Glossary	12
13	12. The List of Figures	13
14	13. The List of Tables	14
15	14. The List of Equations	15
16	15. The List of Symbols	16
17	16. The List of Abbreviations	17
18	17. The List of Acronyms	18
19	18. The List of Initials	19
20	19. The List of Roman Numerals	20
21	20. The List of Greek Letters	21
22	21. The List of Latin Letters	22
23	22. The List of Numbers	23
24	23. The List of Units	24
25	24. The List of Symbols	25
26	25. The List of Abbreviations	26
27	26. The List of Acronyms	27
28	27. The List of Initials	28
29	28. The List of Roman Numerals	29
30	29. The List of Greek Letters	30
31	30. The List of Latin Letters	31
32	31. The List of Numbers	32
33	32. The List of Units	33
34	33. The List of Symbols	34
35	34. The List of Abbreviations	35
36	35. The List of Acronyms	36
37	36. The List of Initials	37
38	37. The List of Roman Numerals	38
39	38. The List of Greek Letters	39
40	39. The List of Latin Letters	40
41	40. The List of Numbers	41
42	41. The List of Units	42
43	42. The List of Symbols	43
44	43. The List of Abbreviations	44
45	44. The List of Acronyms	45
46	45. The List of Initials	46
47	46. The List of Roman Numerals	47
48	47. The List of Greek Letters	48
49	48. The List of Latin Letters	49
50	49. The List of Numbers	50
51	50. The List of Units	51
52	51. The List of Symbols	52
53	52. The List of Abbreviations	53
54	53. The List of Acronyms	54
55	54. The List of Initials	55
56	55. The List of Roman Numerals	56
57	56. The List of Greek Letters	57
58	57. The List of Latin Letters	58
59	58. The List of Numbers	59
60	59. The List of Units	60
61	60. The List of Symbols	61
62	61. The List of Abbreviations	62
63	62. The List of Acronyms	63
64	63. The List of Initials	64
65	64. The List of Roman Numerals	65
66	65. The List of Greek Letters	66
67	66. The List of Latin Letters	67
68	67. The List of Numbers	68
69	68. The List of Units	69
70	69. The List of Symbols	70
71	70. The List of Abbreviations	71
72	71. The List of Acronyms	72
73	72. The List of Initials	73
74	73. The List of Roman Numerals	74
75	74. The List of Greek Letters	75
76	75. The List of Latin Letters	76
77	76. The List of Numbers	77
78	77. The List of Units	78
79	78. The List of Symbols	79
80	79. The List of Abbreviations	80
81	80. The List of Acronyms	81
82	81. The List of Initials	82
83	82. The List of Roman Numerals	83
84	83. The List of Greek Letters	84
85	84. The List of Latin Letters	85
86	85. The List of Numbers	86
87	86. The List of Units	87
88	87. The List of Symbols	88
89	88. The List of Abbreviations	89
90	89. The List of Acronyms	90
91	90. The List of Initials	91
92	91. The List of Roman Numerals	92
93	92. The List of Greek Letters	93
94	93. The List of Latin Letters	94
95	94. The List of Numbers	95
96	95. The List of Units	96
97	96. The List of Symbols	97
98	97. The List of Abbreviations	98
99	98. The List of Acronyms	99
100	99. The List of Initials	100
101	100. The List of Roman Numerals	101
102	101. The List of Greek Letters	102
103	102. The List of Latin Letters	103
104	103. The List of Numbers	104
105	104. The List of Units	105
106	105. The List of Symbols	106
107	106. The List of Abbreviations	107
108	107. The List of Acronyms	108
109	108. The List of Initials	109
110	109. The List of Roman Numerals	110
111	110. The List of Greek Letters	111
112	111. The List of Latin Letters	112
113	112. The List of Numbers	113
114	113. The List of Units	114
115	114. The List of Symbols	115
116	115. The List of Abbreviations	116
117	116. The List of Acronyms	117
118	117. The List of Initials	118
119	118. The List of Roman Numerals	119
120	119. The List of Greek Letters	120
121	120. The List of Latin Letters	121
122	121. The List of Numbers	122
123	122. The List of Units	123
124	123. The List of Symbols	124
125	124. The List of Abbreviations	125
126	125. The List of Acronyms	126
127	126. The List of Initials	127
128	127. The List of Roman Numerals	128
129	128. The List of Greek Letters	129
130	129. The List of Latin Letters	130
131	130. The List of Numbers	131
132	131. The List of Units	132
133	132. The List of Symbols	133
134	133. The List of Abbreviations	134
135	134. The List of Acronyms	135
136	135. The List of Initials	136
137	136. The List of Roman Numerals	137
138	137. The List of Greek Letters	138
139	138. The List of Latin Letters	139
140	139. The List of Numbers	140
141	140. The List of Units	141
142	141. The List of Symbols	142
143	142. The List of Abbreviations	143
144	143. The List of Acronyms	144
145	144. The List of Initials	145
146	145. The List of Roman Numerals	146
147	146. The List of Greek Letters	147
148	147. The List of Latin Letters	148
149	148. The List of Numbers	149
150	149. The List of Units	150
151	150. The List of Symbols	151
152	151. The List of Abbreviations	152
153	152. The List of Acronyms	153
154	153. The List of Initials	154
155	154. The List of Roman Numerals	155
156	155. The List of Greek Letters	156
157	156. The List of Latin Letters	157
158	157. The List of Numbers	158
159	158. The List of Units	159
160	159. The List of Symbols	160
161	160. The List of Abbreviations	161
162	161. The List of Acronyms	162
163	162. The List of Initials	163
164	163. The List of Roman Numerals	164
165	164. The List of Greek Letters	165
166	165. The List of Latin Letters	166
167	166. The List of Numbers	167
168	167. The List of Units	168
169	168. The List of Symbols	169
170	169. The List of Abbreviations	170
171	170. The List of Acronyms	171
172	171. The List of Initials	172
173	172. The List of Roman Numerals	173
174	173. The List of Greek Letters	174
175	174. The List of Latin Letters	175
176	175. The List of Numbers	176
177	176. The List of Units	177
178	177. The List of Symbols	178
179	178. The List of Abbreviations	179
180	179. The List of Acronyms	180
181	180. The List of Initials	181
182	181. The List of Roman Numerals	182
183	182. The List of Greek Letters	183
184	183. The List of Latin Letters	184
185	184. The List of Numbers	185
186	185. The List of Units	186
187	186. The List of Symbols	187
188	187. The List of Abbreviations	188
189	188. The List of Acronyms	189
190	189. The List of Initials	190
191	190. The List of Roman Numerals	191
192	191. The List of Greek Letters	192
193	192. The List of Latin Letters	193
194	193. The List of Numbers	194
195	194. The List of Units	195
196	195. The List of Symbols	196
197	196. The List of Abbreviations	197
198	197. The List of Acronyms	198
199	198. The List of Initials	199
200	199. The List of Roman Numerals	200

LIST OF TABLES

Table 2.1	Data on SONY-XC77CE and Aqua-TV HR-480 cameras.	7
Table 2.2	Results of bundle adjustments.....	12
Table 2.3	Results of comparisons after transformations	12
Table 3.1	Basic data of the RS-170 and CCIR video standards.....	23
Table 3.2	Comparison of signal transmission methods	38
Table 3.3	SNR and resolution of ADCs.....	41
Table 4.1	Frame grabber configurations used for the testing.....	44
Table 4.2	Statistics of frames from two series.	47
Table 4.3	RMS values for the temporal noise for different sampling speeds, synchronization methods and input signal levels.....	47
Table 4.4	Results of analysis of linearity for one line of an individual frame and from the average of five frames in brackets	50
Table 4.5	MTF determination of MAX-SCAN with multiburst images.....	54
Table 4.6	Results of line-jitter analysis.....	57
Table 4.7	Statistics of template matching for the pixel-synchronous sam- pled images.	57
Table 5.1	Statistics of frame and fields with different derivation of the clamping pulse for DC-restoration.....	66
Table 5.2	Results of DSNU analysis.....	68
Table 5.3	Statistics of images grabbed with different power supplies of camera.	70
Table 5.4	Gain variation or PRNU.....	72
Table 5.5	Average and standard deviation before and after radiometric cor- rection.....	73
Table 5.6	Radiometric correction using a CCTV type lens	74
Table 6.1	Statistics on the performance evaluation of LSM without and with detection of oscillations and for different templates.....	85
Table 6.2	Results of comparison to version 2.	89
Table 6.3	Repeatability values for different averaging methods.	91
Table 6.4	Configurations for the evaluation of synchronization.....	92
Table 6.5	Statistics of subtraction using absolute value of grayvalue differ- ences.	94
Table 6.6	RMS values from repeatability analysis for different synchroni- zations.	96
Table 6.7	Maximum residuals from repeatability analysis for different syn- chronizations.	96
Table 6.8	RMS values from repeatability analysis for pixel-synchronous and digital transmission.	103
Table 6.9	Repeatability as a function of target size.	103
Table 6.10	Influence of warm-up-effects.....	107
Table 6.11	Repeatability	108
Table 6.12	Analysis of shadows.....	115
Table 6.13	Error due to shadows determined with simulations.	119
Table 7.1	Computational performance of some hardware configurations for LSM.....	136
Table 7.2	Results of bundle adjustment with and without additional param- eters.	137

Table 7.3	Initial and adjusted values of pixel spacing and interior orientation elements with the standard deviation from version cvp223.	137
Table 7.4	Correlation among additional parameters for version cvp223.	138
Table 7.5	Additional parameters and test values for version cvp223 (see <i>Gruen, 1978</i> for testing procedure).	138
Table 7.6	Influence of additional parameters at an image point $x = 3$, $y = 2$ mm.	139
Table 7.7	Results of bundle adjustment with 30 control points and a minimum constraint configuration.	143
Table 7.8	Testing of difference of empirical precision estimates with the test criterion $t(0.95, 139) = 1.66$	143
Table 7.9	Results for template size of 7×7 (cvp223) and 5×5 (cvp243) in the presence of shadows.	150
Table 7.10	Testing of difference of empirical precision estimates with the test criterion $t(0.95, 112) = 1.66$	150
Table 7.11	Results for template size of 7×7 and 5×5 in the presence of shadows after elimination of points in columns 12 and 17 as well as points on the wall close to the ceiling.	153
Table 7.12	Eliminations due to effects of sides of structure on images of targets (numbers in brackets refer to the ones in the figures).	157
Table 7.13	Results of bundle adjustments with different additional parameter sets.	157
Table 7.14	Description of versions	158
Table 7.15	Results of bundle adjustments with different additional parameter sets.	158
Table 7.16	Correlations between object coordinates, exterior orientation elements and additional parameters for three versions with increasing number of additional parameters.	158
Table 7.17	Testing of additional parameter groups.	159
Table 7.18	Squared mean of standard deviation of image coordinates from LSM for PLL line-synchronization and pixel-synchronous sampling.	169
Table 7.19	Results for pixel-synchronous (cvp601, cvp611) and PLL line-synchronization (cv601, cv611).	169
Table 7.20	Squared mean of image coordinate residuals.	170
Table 7.21	Additional parameters for PLL line-synchronization and pixel-synchronous grabbing.	170
Table 7.22	Initial and adjusted values of pixel spacing and interior orientation elements with the standard deviation from version cvp223.	170
Table 7.23	Statistics of comparison of object coordinates from cvp611 and cv611 for 140 object points (after a similarity transformation).	173

1 INTRODUCTION

1.1 Statement of the Problem and Research Objectives

Photogrammetry has undergone significant changes in recent years. They have been initiated in part by the advent of film-less imaging systems, such as imaging tubes and solid-state sensors. The charge-coupled device, invented only twenty years ago (*Sangster, 1970; Boyle and Smith, 1970*), was proven to be an excellent image sensor. The excellent geometric uniformity and stability make it ideally suited for Digital Photogrammetry. Another important development is the introduction of fast analog-to-digital converters, with the first commercial flash analog-to-digital converter introduced in 1977. Frame grabbers integrating them with high-speed memory and processing elements have become a standard commodity. The ongoing rapid increase of the performance of computers and other processing systems have enabled photogrammetrists to employ ever more demanding algorithms. The latter are of fundamental importance. Highly accurate methods for target location, such as Least Squares Matching (*Grün, 1985*), are a prerequisite for attaining high precisions for three-dimensional measurements. Existing methods and algorithms such as self-calibration and the bundle adjustment provide important tools for data processing. System software, such as window systems and graphical user interfaces, have enabled the development of powerful and user-friendly tools for data processing and analysis with semi-automated and fully-automated methods.

These developments made "Real-Time Photogrammetry" (*Grün, 1988*) possible, although the concept of Real-Time Photogrammetry dates back to the 1950's (*Rosenberg, 1955*). Imaging tubes and solid-state imaging sensors allow imagery to be directly acquired into a frame buffer or computer memory where it can be used to extract and derive results. The delay from image acquisition to delivery of results can reach from less than 20 msec in high speed robotics (*Beyer et al., 1989*) to several seconds (*Haggrén, 1991*) to minutes in complex industrial inspection tasks. Real-Time Photogrammetry does not only lead to a higher degree of automation of existing tasks, but completely new application areas are opened up. For example tasks in industrial quality control require immediate feedback to the production process which does not allow the time for film processing. Some application areas are robotics, machine vision, quality control, industrial metrology, biology, bio-mechanics, and medicine. Many photogrammetric tasks currently performed with small to medium format film cameras can also be performed with solid-state cameras and Real-Time Photogrammetry.

The first applications of Real-Time Photogrammetry employed vidicon-tube cameras and were realised in the 1970's (*Wong, 1969; Pinkney, 1978; Kratky, 1979; Burner et al., 1985*). They were limited in accuracy by the lack of stability of imaging tubes. Other approaches use lateral effect photodetectors (e.g. *Woltring, 1975; Selcom, 1982*). Real-Time Photogrammetric systems employing solid-state sensors were developed in the first half of the eighties (*El-Hakim, 1986; Wong and Ho, 1986; Haggrén, 1984 and 1986; Murai et al. 1986; Grün and Beyer, 1986*). At the same time a number of investigations analysed different aspects of the calibration of solid-state cameras (e.g. *Gülch, 1984 and 1985; Curry et al., 1986; Dähler, 1986*). Accuracies of up to 0.1 of the pixel spacing could be verified with these systems. The increasing interest in characterisation and calibration of imaging systems with of solid-state sensors is evidenced by the large number of publications from diverse scientific communities, e.g. *Abi-Ayad, 1989; Bani-Hashemi, 1991; Burner et al., 1990; Faugeras and Toscani, 1987; Haggrén and Heikkilä, 1989;*

Kamgar-Parsi and Eastman, 1991; Lenz, 1990; Luhmann, 1988; MacLean et al., 1990; Putskorius and Feldkamp, 1988; Tsai, 1987; Wang and Tsai, 1991; Wei and Ma 1991; Wieting, 1990; Wiley and Wong, 1990.

The aim of this work was to develop a high precision Real-Time Photogrammetric System (RTPS) with greater flexibility and higher accuracy. The exacting demands placed on the system in terms of accuracy required an analysis of the radiometric and geometric properties of all elements involved in image acquisition, information extraction, and positioning with solid-state sensor based imaging systems. This analysis can build on the extensive knowledge existing in photogrammetry for the calibration of film-based cameras, and on information from other domains on solid-state sensor technology, as well as on numerous investigations of these sensors for astronomical purposes and space applications. The tasks entailed in this work are thus:

- Develop a Real-Time Photogrammetric System with advanced capabilities;
- Implement an image acquisition system allowing for various investigations;
- Set-up testfields and test facilities for the analysis of the performance;
- Investigate the radiometric and geometric characteristics of all system components in order to get an overview of the numerous problems and to be able to assess the importance of each effect; and
- Demonstrate the accuracy of the system in a 3D test with a testfield.

Automation is not an aim of the project. The level of automation is determined by the processing speed required to perform the required investigations with reasonable effort. High-precision in the context of Real-Time Photogrammetry is understood as the aim to achieve a precision of 0.01 to 0.02 of the pixel spacing in image space. This corresponds to a relative precision of 1 : 50000 to 1 : 100000 in object space. This precision places such a system in direct competition with medium format film cameras and Coordinates Measurement Machines (CMM). Many industrial quality control applications, which could not be solved with photogrammetric systems due to time restrictions, are feasible with such a system.

1.2 Approach and Organisation

The aim of Real-Time Photogrammetry (RTP) is to obtain three-dimensional (geometric) information on objects in a timely manner. The information to be derived can be complex three-dimensional descriptions requiring object recognition, or simply the object space coordinates of points. Figure 1.1 gives a schematic representation of the sub-tasks of Real-Time Photogrammetry according to *Grün and Beyer, 1987*. Details on the processing tasks can be found there. In a first step the allocation of the tasks to appropriate hardware needs to be solved. In an initial approach a turnkey image processing system was used as a basis (*Grün, 1986; Grün and Beyer, 1986*). The shortfalls of such a system for Real-Time Photogrammetry were quickly realised (*Beyer, 1987a; Dähler, 1987; Grün et al., 1987*) and a system based on a modular design approach was developed (*Grün and Beyer, 1990*). The **Digital Photogrammetric Station (DIPS)** and the hardware components of the RTPS are outlined in chapter 2. The testfields and the measurement of reference coordinates for the three-dimensional accuracy verification are also discussed and an outline of the developed software is given.

In chapter 3 the expected radiometric and geometric characteristics of imaging with solid-state sensors are analysed first. A short investigation of the effects of optical elements

and the sensor is given. Thereafter television standards, camera electronics, issues of signal transmission and frame grabbing are addressed. The chapter ends with a discussion of data buffering and the analog-to-digital conversion.

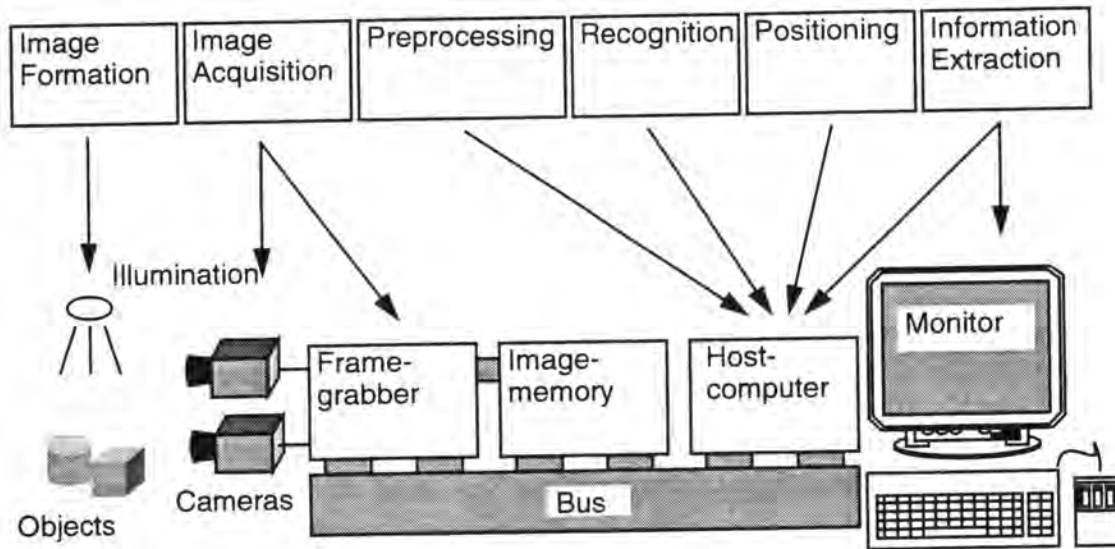


Figure 1.1 Real-Time Photogrammetry: Tasks and Hardware

Several performance characteristics of the frame grabber are analysed in chapter 4. This includes the radiometric properties affected by electronic components such as the analog offset and gain controls, the DC-restoration, etc. The impulse response and the modulation transfer function of the frame grabber with and without low-pass-filtering is determined and the effects discussed. The performance of the synchronisation and its influence on the geometry is investigated.

The radiometric properties and the radiometric calibration of the complete system (lighting, camera, frame grabber) are discussed in chapter 5. Some of the difficulties to be encountered with off-the-shelf hardware are shown. The difficulties to perform radiometric calibrations under practical conditions are outlined.

The repeatability (internal precision) of the image positions of targets is evaluated in chapter 6. A high internal precision of the locations of image features is a prerequisite for accurate three-dimensional measurements. Several radiometric and geometric methods were developed to pinpoint degradations from synchronisation. The influence of the target size, shadows, and local illumination gradients on the precision and accuracy of the image positions of targets are investigated. The study of warm-up-effects and of repeatability is needed to assess the time required by the system to reach a stable temperature condition and the level of internal precision to be expected over time frames of hours and days.

Chapter 7 gives the assessment of the three-dimensional performance with a testfield. The mathematical model is reviewed, the measurement methods are discussed, the accuracy with pixel-synchronous frame grabbing, the differences to PLL line-synchronisation, and a number of degrading and limiting factors are demonstrated and discussed.

The conclusions in chapter 8 provide an overview of the factors which degrade and/or limit the radiometric and geometric performance of solid-state imaging systems and thus the three-dimensional accuracy. An outlook is given via issues and problems to be investigated in the future.

2 SYSTEM OVERVIEW

2.1 Digital Photogrammetric Station (DIPS)

The **Real-Time Photogrammetric System (RTPS)** forms part of the **Digital Photogrammetric Station (DIPS II)** developed at the Institute of Geodesy and Photogrammetry. An initial version was based on a turn-key image processing system with a general purpose host computer. The system is described in *Grün, 1986* and *Grün and Beyer, 1986*. Initial experiments performed are reported in *Beyer, 1987*; *Grün and Baltsavias, 1987*; *Dähler, 1987*; *Novak et al., 1990*. It was soon found that the system was not well suited for Real-Time Photogrammetry.

The second version of the system uses a modular design concept. At the core are servers and workstations, interconnected by a network, which are supplemented by special purpose systems. Some of them are shown in Figure 2.1, such as the CCD-cameras, testfields, image acquisition systems, output devices, etc. The image acquisition workstation represents the hardware architecture of the Real-Time Photogrammetric System.

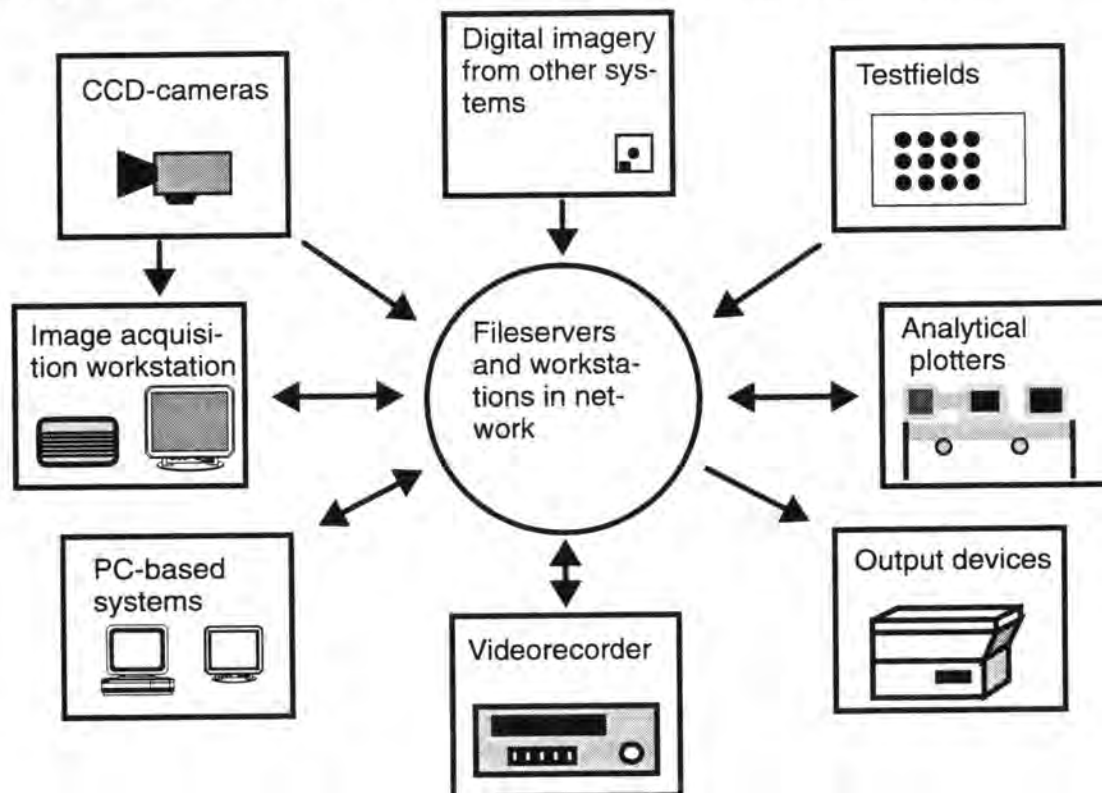


Figure 2.1 Components of the Digital Photogrammetric Station.

2.2 Real-Time Photogrammetric System

The Real-Time Photogrammetric System is structured similar to that shown in Figure 1.1 with frame grabber, image memory, and computer. Figure 2.2 shows the hardware architecture and Figure 2.3 an image of the RTPS. A Sun-3E workstation, serving as a host, is housed in a 20 slot VME-bus chassis with frame grabbers and image memory boards from Datacube.

The MAX-SCAN frame grabber provides a great deal of flexibility (*Datacube, 1988*). The numerous jumpers, programmable switches and controls make the board ideal for investigations and comparisons, but at the same time difficult to handle for a novice user without extensive knowledge of electronics. Some of the capabilities of this frame grabber are:

- inputs for video, VSYNC, HSYNC and pixel-clock signals and digital data
- 8-bit analog-to-digital converter with a sampling frequency of up to 20 MHz
- several synchronization methods to derive the sampling-clock, including PLL line-synchronization and pixel-synchronous sampling
- programmable image size and active image region up to 8k by 8k.
- use of a FIFO (First In First Out) for data buffering

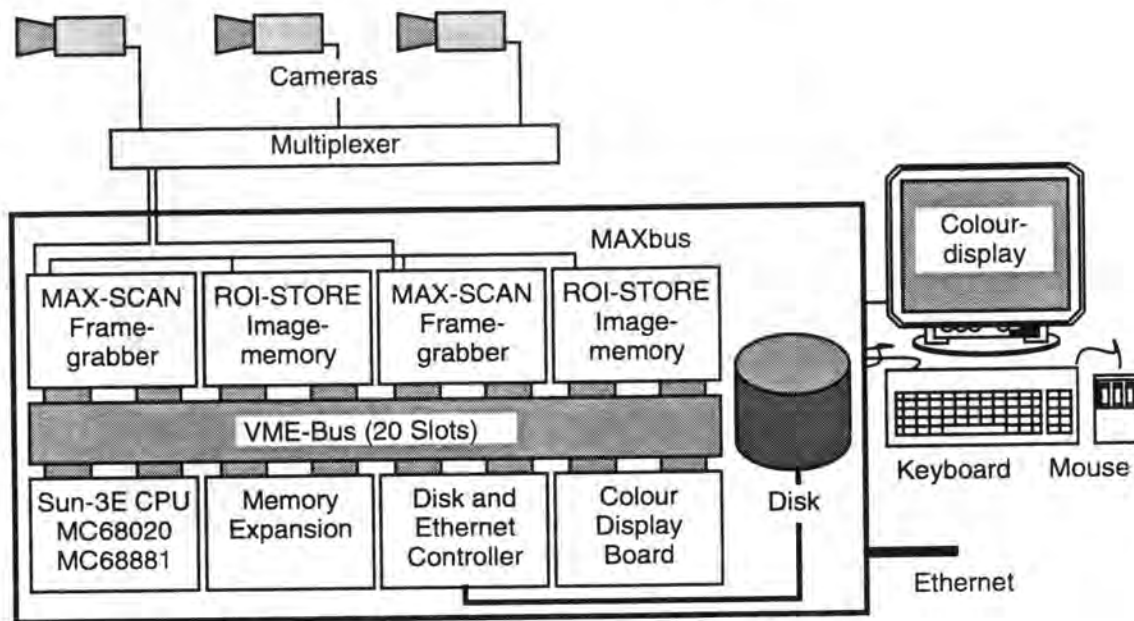


Figure 2.2 Hardware architecture of Image Acquisition Workstation.

The image data of the MAX-SCAN is passed via a MAX-BUS connection to a ROI-STORE image memory. This data path is capable to transfer data with a frequency of up to 10 MHz, providing for a 20 MByte/sec link over two MAX-BUS connections. The 2 MBytes of image memory of each ROI-STORE are sufficient for standard CCD-cameras. When "high resolution" cameras, i.e. cameras with over 1k by 1k sensor elements, are used, more than one board is useful if several images should be acquired in a series. The hardware configuration is suited to acquire and store series of 5 and 8 frames consecutively (i.e. within 0.32 and 0.2 sec) for an image format of 728 x 568 and 512 x 512 pixel respectively.

The Sun-3E workstation is used to control the imaging hardware and to process the data. A major advantage of the system is the on-line display of approximately five images with a size of 512 x 512 pixel per second on the high-resolution workstation monitor and the availability of powerful software which can directly access the images stored in the image memory of the ROI-STORE through double buffering. The on-line display speed proved sufficient for focusing and was extremely helpful when adjusting the settings of the camera and/or frame grabber. The system is compact and transportable. In view of the rapidly increasing performance of workstations, the Sun-3E has become a relatively

slow computer since its installation in autumn 1989. The workstation is therefore solely used to perform basic processing and analysis functions required for image acquisition. All other processing is performed on much more powerful SPARCStations, hence the title “image acquisition workstation”.

Today a standard workstation without a VME-bus would be more advantageous. It could be connected via a bus-translator (e.g. S-bus to VME-bus convertor in case of a SPARC-Station) to a VME-bus chassis. Such a solution could take advantage of the much lower cost of such workstations as compared to VME-bus based machines and the much higher performance than the computer currently used. Frame grabbers integratable into low-cost workstations provide an even more economical possibility for a RTPS with capabilities comparable to the one developed.

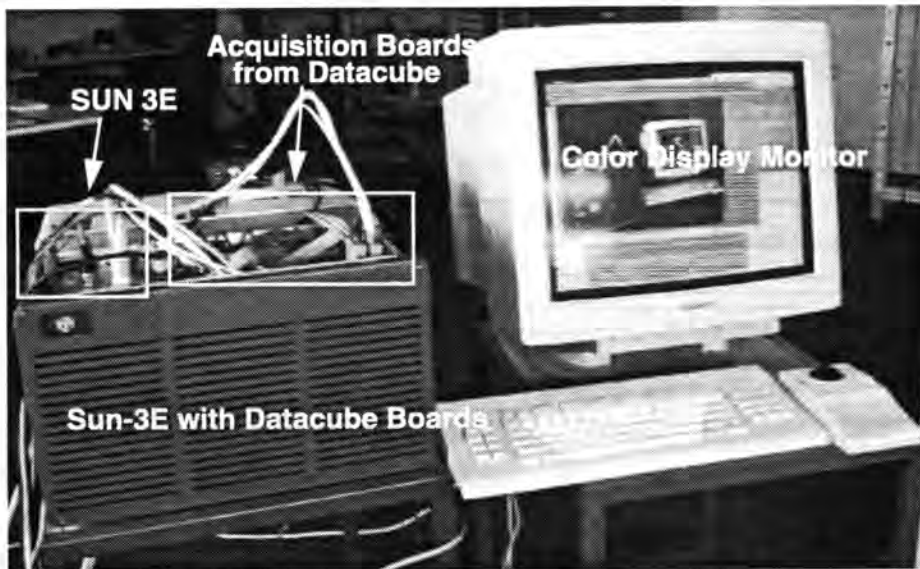


Figure 2.3 Picture of the image acquisition workstation.

2.2.1 Illumination

The illumination is a critical component of any RTP system as will be shown in chapter 7. Two types of illumination systems were employed. A ring-light system consisting either of a fibre-optic illumination with a special assembly, or fluorescent ring-lights were used together with retro-reflective targets as discussed in *Beyer, 1991b*. Both systems dependent on the 50 Hz frequency of the power supply and change their intensity accordingly. Normal targets were initially illuminated with halogen filament lights, but it was found that they emit too much heat for a room with limited air conditioning. Electronically controlled fluorescent lights were chosen instead. These are triggered at a 35 kHz rate eliminating any possibility of interference between the lighting and the camera acquisition frequency. The light is furthermore very stable over longer periods of time. A light color emitting most of the light in the spectral region between 450 and 650 nm was chosen. A uniform and diffuse illumination was created by combining the fluorescent lights with curtains for diffusion as shown in Figure 2.4.

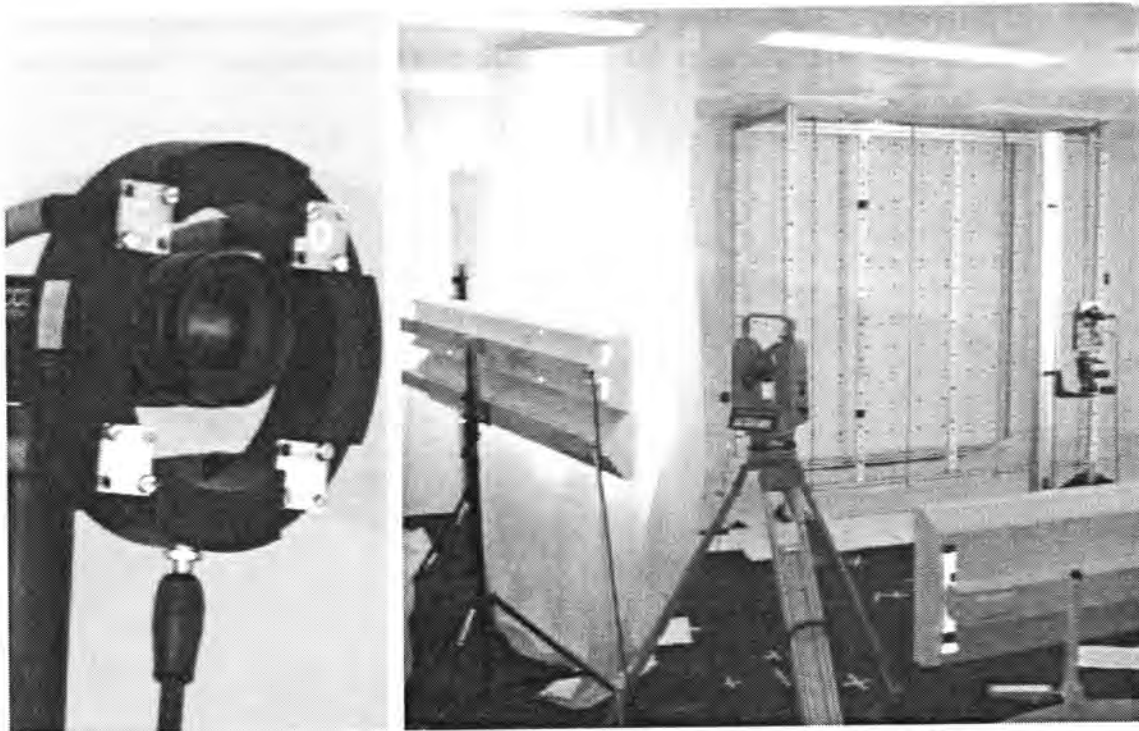


Figure 2.4 Fibre-optic illumination system and testfield with theodolite, camera, and illumination

2.3 Cameras

Most of the investigations were performed with several **SONY-XC77CE** cameras. Initial tests were done with an Aqua-TV HR-480 camera. These cameras will later only be referred to as the HR480 and **XC77**, respectively. They are typical of low-cost off-the-shelf solid-state cameras with an image format of approximately 700 by 550 pixels. Table 2.1 summaries basic characteristics of both cameras.

	XC77	HR480
Sensor type	IT	FT
Number of sensor elements	756 x 581	604 x 576
Sensor element spacing	11 x 11 μm	10 x 7.8 μm
Sensor clock frequency	14.1875 MHz	11.25 MHz
SNR	50 dB	-
Optical black	60 elements/line	-

Table 2.1 Data on SONY-XC77CE and Aqua-TV HR-480 cameras.

Figure 2.5 shows the **XC77** with a 9 mm (FUJINON) lens. The camera is light and small (105 mm long) compared to the smallest film based cameras used in photogrammetric applications. Data was transmitted between the **XC77** camera and the MAX-SCAN frame grabber with two 75 Ohm coaxial cables. One was used for the composite video and the other for the pixel-clock signal (see section 3.6). Figure 2.6 shows a typical configuration for the SONY **XC77CE** camera connected to the MAX-SCAN frame grabber. The cable from camera to the support box was 5 m and the cables from the latter to the

frame grabber were 4 m to 20 m long. The cameras had to be modified to drive the pixel-clock signal for longer distances than one meter (*Raynor, 1989*). Up to twenty meter cables were used in tests after changing the impedance of the frame grabber's pixel-clock input.

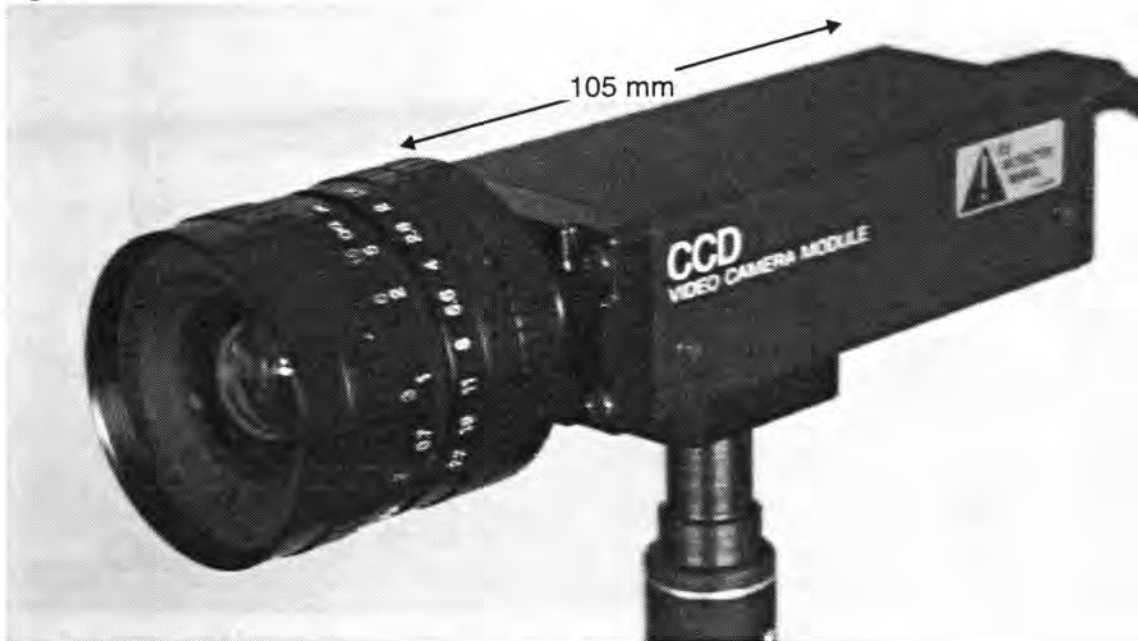


Figure 2.5 SONY-XC77CE camera with a FUJINON 9 mm lens.

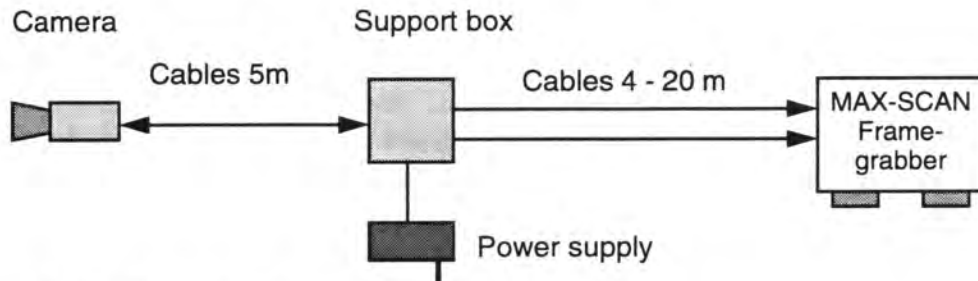


Figure 2.6 Camera and connection to system.

Some tests were also performed with a Megaplus camera. This camera employs a Frame-Transfer sensor with very small sensor elements spaced at $6.8 \times 6.8 \mu\text{m}$. It is of special interest as it provides both analog and digital output. A comparison between the performance of analog and digital data transmission was thus performed with this camera. Details on the camera can be found in the excellent and detailed manuals (*Videk, 1987*)

2.4 Testfields

A **small testfield** consisting of targets on a plate which can be positioned on a stage was used initially (see Figure 2.7). Movement of the stages was used to generate a three-dimensional field of points. Results obtained with that testfield are reported in *Beyer, 1987a*. The construction of the stage and plate proved insufficiently stable. The measurements required to obtain precise reference coordinates for each position of the plate with theodolites proved too time consuming.

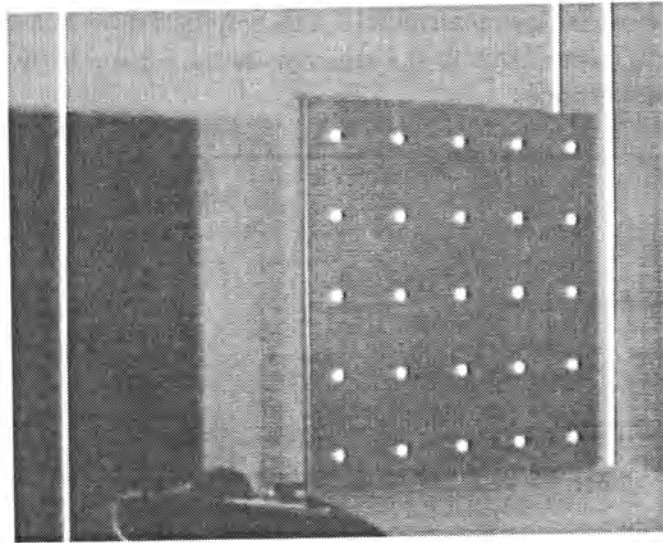


Figure 2.7 Small testfield consisting of a moving plate on a stage.

Therefore a **large testfield** was constructed, consisting of targets placed on a wall and on an aluminium structure in front of the wall. The targets were black circles on a white background with a small white dot in the centre (see Figure 2.8, dot not visible). The small dots were located with an accuracy of $5\ \mu\text{m}$ to $6\ \mu\text{m}$ in the centre of each target. These serve as targets for reference measurements with theodolites. The targets have diameters of 14 and 20 mm, with 136 points on the wall and 50 points on the front structure for each size. The testfield spanned 4.2 m horizontally, 2 m vertically, and the targets on the front rods were 1.1 m from the wall. The X and Y-axis of the coordinate system were located parallel to the wall with the X-axis parallel to the floor. The Z-axis pointed away from the wall towards the room.



Figure 2.8 Testfield and targets.

Figure 2.9 shows the location of the testfield in the room. The space to the sides is limited due to the wall on one side of the testfield. The height of the room is only slightly larger than the testfield. This restricts the space available for positioning cameras, i.e. constrains the network design.

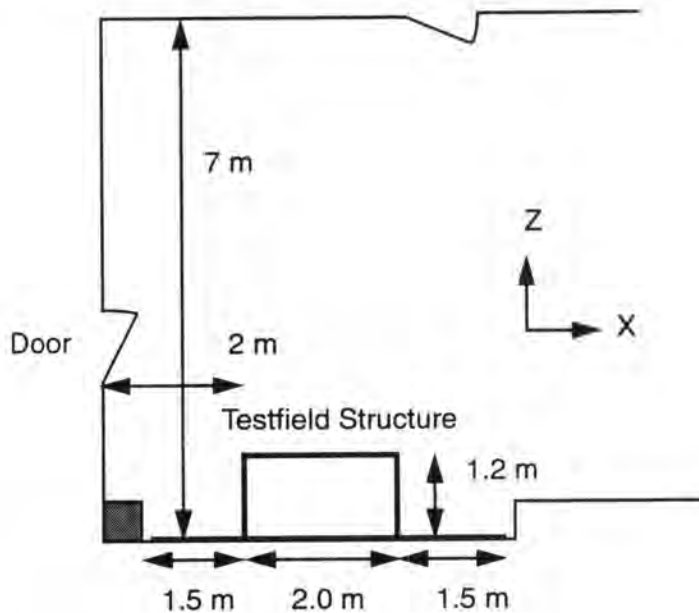


Figure 2.9 Floor plan of testfield

2.4.1 Reference Coordinates

The stability of the testfield and the precision of the reference coordinates were assessed with the results of three measurement campaigns. The first measurements (performed in October 1989 and referred to as tf89) were performed with theodolites (Kern E2, WILD T2000). All targets were measured within one week. The theodolites were aligned and only one set of angles was measured, allowing for no thorough checking on blunders. The second measurements (performed in September 1990 and referred to as tf90) were performed with a CRC-2 camera. The illumination conditions were very poor and the space of the room restricted the network. The third test (performed in June 1991 and referred to as tf91) was again measured with theodolites. Two sets of measurements were made, separated by three days during which imagery with CCD-cameras was acquired. The theodolite observations were converted to pseudo image coordinates and adjusted with a bundle adjustment. The results of the bundle adjustments are given in Table 2.2 and results of comparisons are given in Table 2.3.

The two sets of the third measurement campaign (tf91) are used to analyze the **short time stability** of the testfield. The results of the first and second period are transformed onto each other, using the points on the wall only, with a three-dimensional similarity transformation. The inner precision of both bundle adjustments (B1w, B1f, B2w and B2f) is better than 0.03 mm in X and Y and approximately 0.05 mm in Z. The comparison between them shows a good correspondence of the RMS values, but the largest differences are very large, reaching 0.2 mm in the Z-axis. No measurement errors could be located in the theodolite observations. Therefore the results of each set were compared to the results from tf90 (see Figure 2.10 and Table 2.3). The second set of measurements

appears to be more precise. The points exhibiting the large differences between the first and second set show discrepancies with an opposite direction with respect to tf90, as visible in plots of the comparisons given in Figure 2.10. The final results of the tf91 measurement were computed in a combined bundle adjustment of the two sets.

The **long term stability and accuracy** was analyzed by comparing the results of the three measurement campaigns onto each other. The results of the second testfield measurements (tf90) were transformed onto the ones of the first period (tf89) and the results compared. This can only be performed for the points located on the wall as the front structure was displaced between the two measurement campaigns. Figure 2.11 gives the plots of the discrepancies for the points on the wall. The results of the analysis are collected in Table 2.2. There are a few large discrepancies between the two measurements, one of them reaching 0.8 mm (see Figure 2.11). The RMS-values for the X-axis indicate that a relative accuracy of 1 : 100 000 was attained. The results for the accuracy in depth are degraded due to the larger residuals for some points. The coordinates of the tf91 set were then transformed onto the coordinates from each of the tf89 and tf90 measurements using the points located on the wall and the residuals from the transformation analyzed. The analysis shows that the stability of the points on the wall is quite good and an accuracy of approximately 0.04 mm in X and Y was attained. The Z coordinates are slightly worse. The plots show that the front structure is less stable. It had been repositioned one to two weeks prior to the second set of measurements (tf90) and some of the movement is evident from the plots. Nevertheless it is astonishing that such an aluminium structure, which is simply resting on the floor, remains stable to within a few tenth of millimeters for long periods of time.

The testfield is therefore **suitable as a reference for precisions of up to 0.04 to 0.05 mm**, which can be maintained for longer periods of time. The testfield proved to have several **limitations**, some of which are:

- the space for the camera positions is constrained
- the targets are too small to show the limiting precision as found in the repeatability testing and the analysis of the influence of target size on repeatability
- the reference measurements with theodolites are time consuming and not sufficiently precise to prove a relative accuracy at the required level
- image acquisition requires the displacement of the camera and fine positioning thereof to limit covering of targets on the wall by the vertical rods of the front structure
- the stability of the front structure is insufficient to serve as high precision reference
- it is difficult to illuminate the testfield without creating shadows on or too close to targets on the wall

Version	No.Pts.	$\max_{\sigma X}$ [mm]	$\max_{\sigma Y}$ [mm]	$\max_{\sigma Z}$ [mm]	σ_X [mm]	σ_Y [mm]	σ_Z [mm]
B1w	57	0.028	0.027	0.067	0.023	0.023	0.052
B2w	56	0.023	0.022	0.058	0.019	0.018	0.042
B1f	20	0.032	0.037	0.054	0.029	0.035	0.045
B2f	38	0.025	0.028	0.046	0.022	0.027	0.035
Bw	57	0.022	0.021	0.053	0.017	0.017	0.038
Bf	38	0.026	0.028	0.046	0.022	0.026	0.034

Table 2.2 Results of bundle adjustments

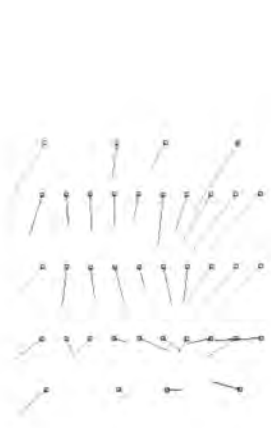
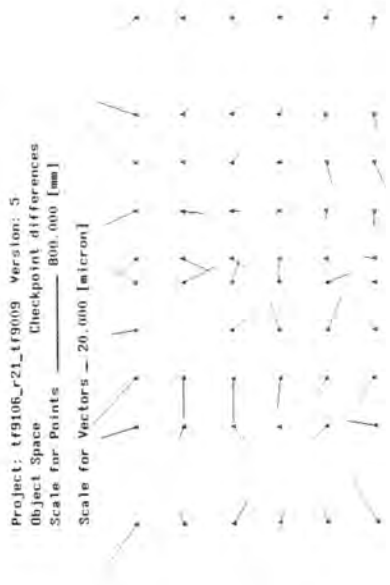
B1w Bundle results for tf91, first set, targets on wall
 B2w bundle results for tf91, second set, targets on wall
 B1f bundle results for tf91, first set, targets on front
 B2f bundle results for tf91, second set, targets on front
 Bw bundle results for tf91, targets on wall
 Bf bundle results for tf91, targets on front

Version	No.	MAXX [mm]	MAXY [mm]	MAXZ [mm]	RMSX [mm]	RMSY [mm]	RMSZ [mm]
C1/2w	59	0.072	0.050	0.249	0.022	0.018	0.069
C1w	60	0.148	0.121	0.159	0.047	0.044	0.064
C2w	59	0.124	0.104	0.107	0.044	0.039	0.054
C1/2f	20	0.074	0.020	0.112	0.029	0.011	0.035
C 90/89	136	0.192	0.126	0.876	0.040	0.036	0.107
C91/89	60	0.074	0.057	0.233	0.033	0.021	0.073
C91/90	60	0.130	0.095	0.146	0.044	0.038	0.049

Table 2.3 Results of comparisons after transformations

C1/2w comparison of first and second set of tf91, targets on wall (B1w and B2w)
 C1w comparison of first set (B1w) to tf90
 C2w comparison of second set (B2w) to tf90
 C1/2f comparison of first and second set of tf91, targets in front (B1f and B2f)
 C90/89 comparison of tf90 to tf89 for targets on wall
 C91/89 comparison of tf91 to tf89 for targets on wall
 C91/90 comparison of tf91 to tf90 for targets on wall

Tf91 second set versus tf90



Tf91 first set versus tf90

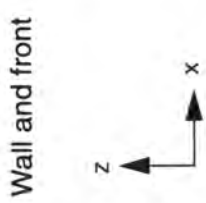
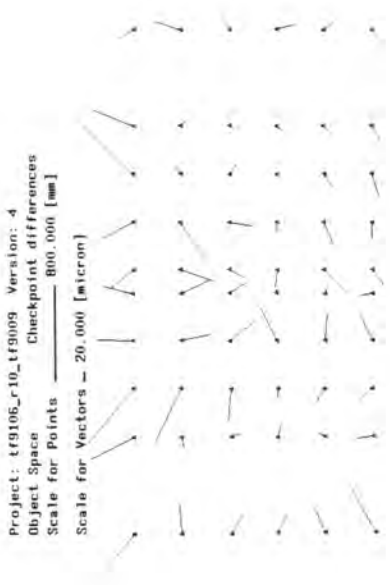
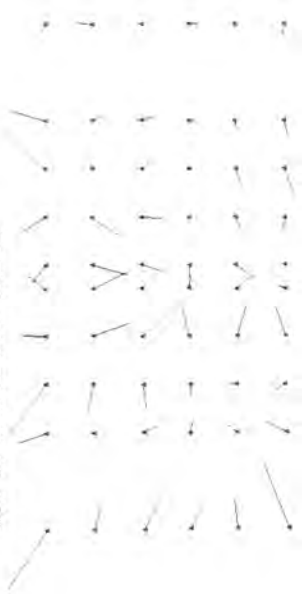


Figure 2.10 Plots of the comparison of the two sets of measurements of tf91 versus tf90.

tf91 versus tf90

Project: tf9106_tf9009 Version: 6
Object Space Checkpoint differences
Scale for Points 800,000 [mm]
Scale for Vectors 20,000 [micron]



Front and wall

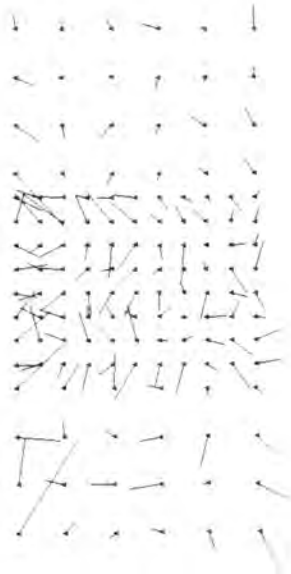


Front and wall



tf90 versus tf89

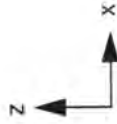
Project: tf9009_vs_tf89 Version: 1
Object Space Checkpoint differences
Scale for Points 800,000 [mm]
Scale for Vectors 20,000 [micron]



Wall



Wall



Wall



Figure 2.11 Plots of comparison of tf90 with tf89 and of tf91 with tf90.

2.5 Software

Research and development have numerous, partially conflicting, requirements on software for Real-Time Photogrammetry. Research requires extensive functions for analysis and visualization, while the timing requirements of Real-Time Photogrammetry can require the complete elimination of such "overhead". The characterization of solid-state imaging systems and their components require image processing functions (e.g. averaging, statistics, filtering), target location algorithms, and a connection between the digital imagery to geometric descriptions thereof. A number of image processing packages have a vast number of functions, but usually lack extensions for target location, drivers for image acquisition boards, bundle adjustments and other photogrammetric functions. The lack of appropriate software for high performance workstations made the development of the software package **DEDIP (Development Environment for Digital Photogrammetry)** a prerequisite to carry on this research (Beyer, 1987b).

It was built on some existing programs for bundle adjustment developed on a Macintosh and a UNIX-computer (GAP, General Analytical Positioning) and an image display and processing program on the SUN (IMDIS, Image Display). DEDIP uses the **SunView window environment** and is **coded in C**. SunView was chosen as it was easy to program and provided the required performance when the development was started in autumn of 1987. The software of DEDIP developed within this work consists of over 100000 lines of C source code. Only a short overview of DEDIP is given here.

The basis of the program is formed by core modules for input/output of imagery, display functions, utility functions for accessing files and images through SunView, help functions, and other generally required tools. Based on these modules, applications for specific tasks are constructed. The modules relevant to this work are image acquisition, image processing, interactive target location, the positioning module GAP (General Analytical Positioning), and a matrix library. Several other modules were developed within other projects (e.g.: Lü, 1988a and b; Lü and Zhang, 1988; Novak et al. 1990; Wilkins, 1990; Gruen and Beyer, 1990). The functionality of some modules will be shown in the chapters on performance analysis. The module Image Acquisition is given as an example of the software.

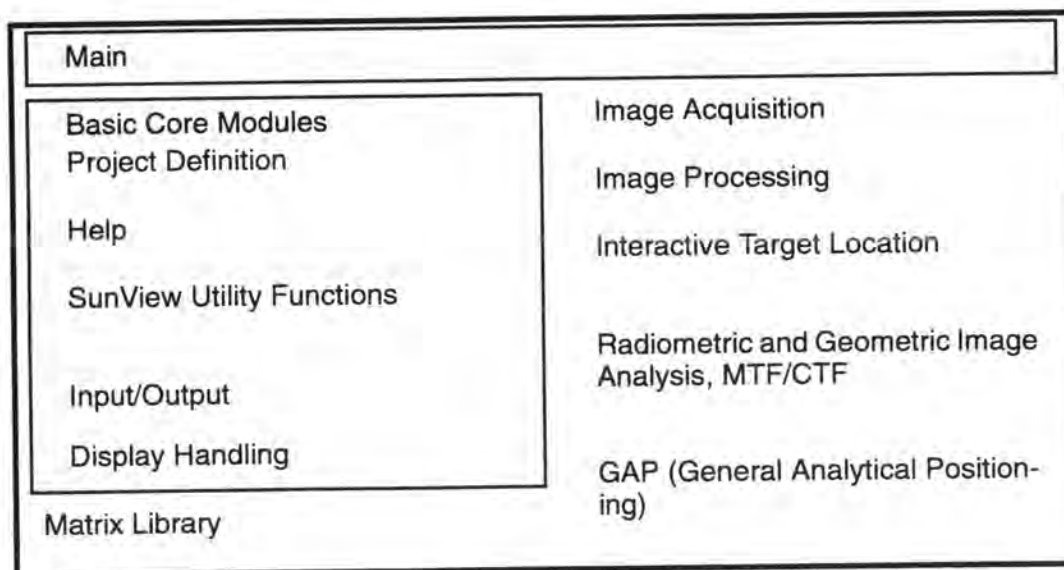


Figure 2.12 Modules of DEDIP relevant to the RTPS

2.5.1 Image Acquisition with DEDIP

The software for image acquisition was written device independent employing definitions for frame grabbers, frame memories, and display devices. The program can simultaneously support different frame grabbers, image memory boards and display devices. Two phases are differentiated, the initialization phase and the acquisition phase.

During **initialization** definitions of existing frame grabbers, image memories, display devices, and cameras are accessed. The existence of the hardware components, except the cameras, is verified at that stage and components found are initialized. Thereafter the user can generate a particular acquisition configuration. This step is shown in the figure below. The user can select, as shown, a particular camera with a particular synchroniza-

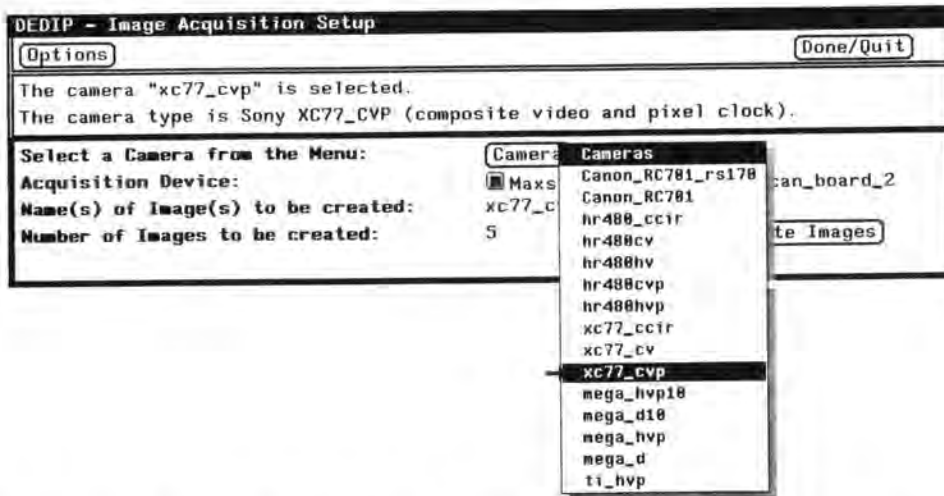


Figure 2.13 Panel for the generation of the camera and image acquisition configuration.

tion method from a menu. Thereafter a frame grabber can be selected (here the MAX-SCAN's are given). The system determines the image memory where the acquired data is to be stored, verifies the availability of the memory on the device and notifies the user by indicating the number of images which can be allocated (the space can only be used by one image, although theoretically one could create overlapping images). The user can change that number to a smaller one, for example if several different cameras need to be used with the same frame grabber. By pressing on the button "Create Images" (bottom right of panel) the user initiates the creation of a number of data structures from which all devices, locations of images, etc. can be found.

The **acquisition** is performed with another panel shown in Figure 2.14. Here the user selects individual images or groups of images to be acquired. The system verifies if they can be acquired, i.e. if they are on a device (camera, disk) from which images can be grabbed and/or loaded into memory. When acquiring an image, or a group of images, the system performs the required initialization, grabs the imagery, and displays the image acquired or the last image if several images were selected for acquisition. The "Display On-line" is used for adjusting the camera position and orientation and for focusing. The frame grabber is switched to continuously acquire images (25 frames/sec for the CCIR-video norm on the MAX-SCAN/ROI-STORE combination) and the workstation displays the imagery continuously from the image memory of the ROI-STORE on the workstation screen. The Sun-3E is capable of displaying approximately five images of 512 x 512 pixels per second. The selected images can also be reviewed and saved automatically.

There are additional panels to interactively control the analog offset and gain through sliders or keyboard inputs and to change settings of particular boards. The latter is used to fine tune the frame grabber to some cameras.

The image store of the ROI-STORE frame buffer is memory mapped into the workstation address space. All algorithms can therefore be performed equally well on images residing in the image memory of that board. The image processing panel shown to the right of Figure 2.14 is used to visually verify the image quality through look-up-tables, profile measurements, etc., and with statistical analysis routines. This allows the user to check the image quality quasi on-line, such that settings of the camera(s) and/or frame grabber(s) can be adjusted.

The development of this tool proved indispensable for the cumbersome work of adjusting the frame grabber to the peculiarities of the different cameras. Software for the acquisition with the RS-170 and CCIR norms was written, functions for pixel-synchronous acquisition from several cameras were implemented, and acquisition of the Megaplex with the analog (using video, VSYNC, HSYNC and pixel-clock) and digital interface were installed.

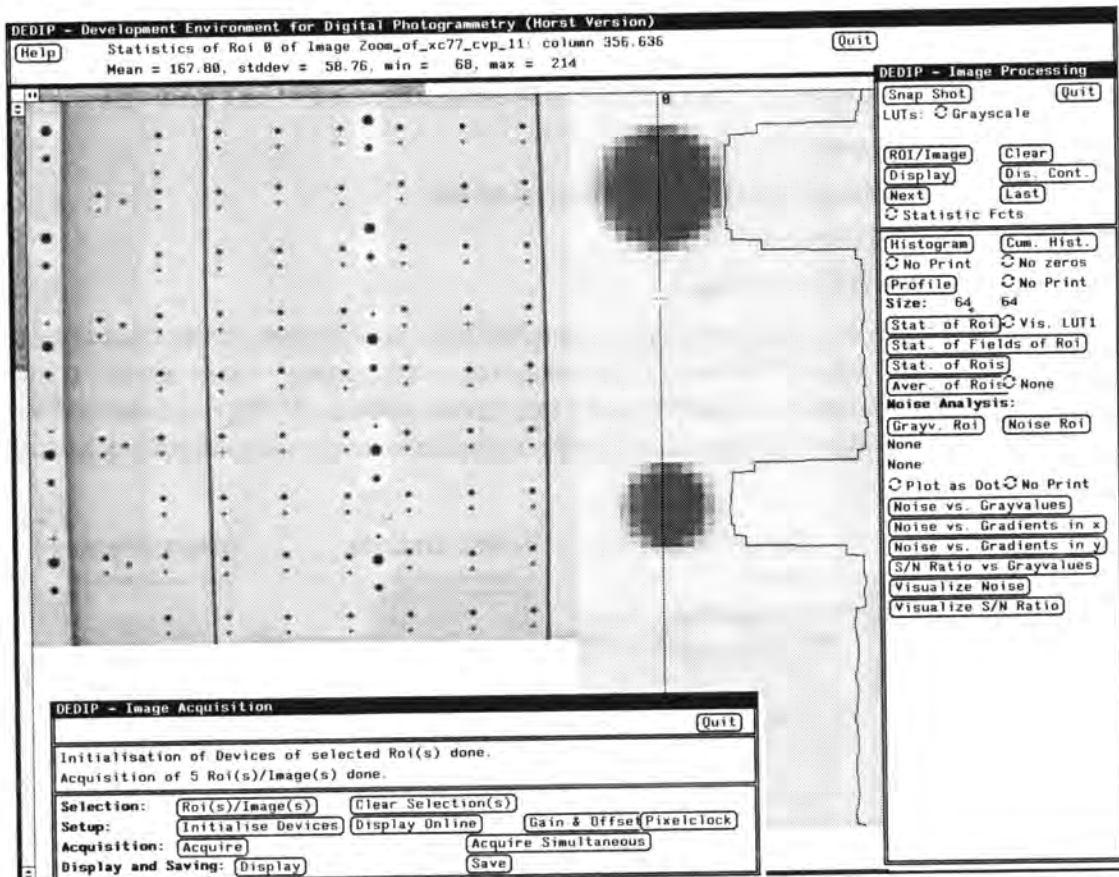


Figure 2.14 Screen during acquisition of images with panels for image acquisition and image processing.

3 IMAGE ACQUISITION WITH SOLID-STATE SENSORS

The (system) calibration of film-based cameras has attained an extremely high level of performance. Relative accuracies of 1 part in 100 000 are considered routine and relative accuracies of 1 part in a million have been attained (*Fraser, 1992*). Solid-state imaging sensors are a comparatively new medium for image acquisition with quite different characteristics. They have some distinct advantages over film, such as no time-dependent distortions due to an extreme stability as compared to film, a wide spectral sensitivity and a stable interior orientation. Disadvantages of solid-state imaging sensors include their small dynamic range (except for some special devices), their small size with comparatively few sensor elements (a sensor would have to deliver approximately 20000 x 20000 pixels to match the information content of an aerial image and 6000 x 6000 pixels to match that of an typical medium format close-range camera), and the fact that the imagery is sampled via a discrete grid. This chapter gives an overview of imaging with solid-state sensors. Optical elements, the sensor, electronics, and signal transmission are discussed.

3.1 Signal Transmission and Frame Grabbing

The technology and methods of transferring the image data from the sensor output to a digital memory are discussed in this chapter. The basic functions to be performed are:

- analog signal processing in the camera
- transmission of data from camera to frame grabber
- analog-to-digital conversion
- data buffering and data storage

Figure 3.1 shows two different methods to perform the transmission of the image information. An "analog camera" transmits the image data with analog video signals and the analog-to-digital conversion is performed in the frame grabber. A "digital camera" performs the analog-to-digital conversion already in the camera and uses digital signals for the transmission.

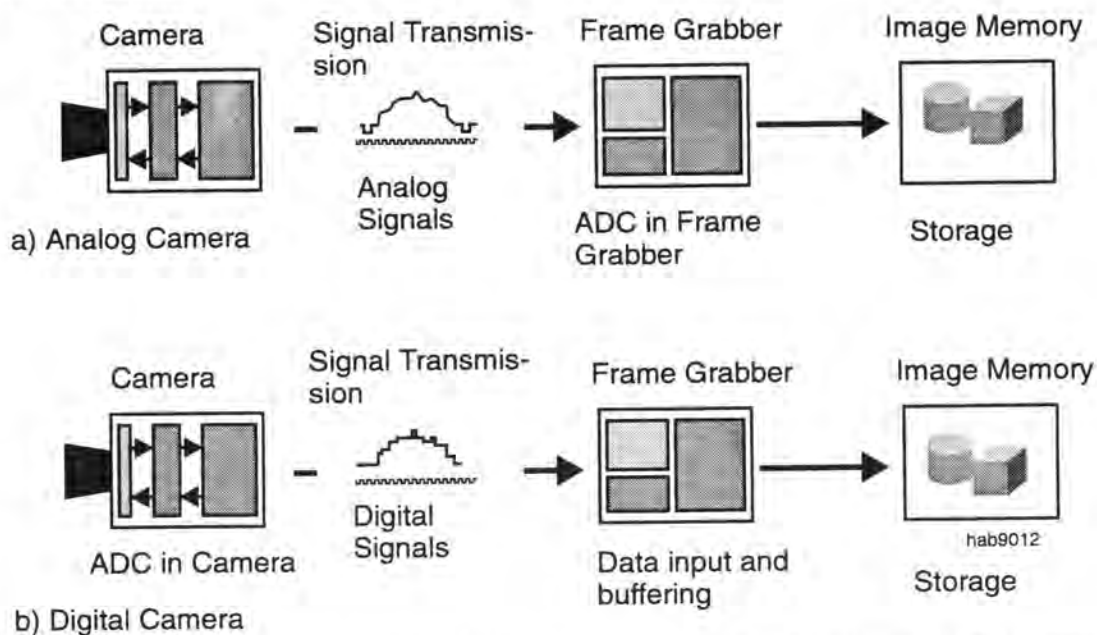


Figure 3.1 Signal transmission and frame grabbing with analog versus digital cameras.

Signals as defined by television standards, cameras with their processing elements, frame grabbing and analog-to-digital conversion will be discussed. The fundamentals to assess the radiometric and geometric performance of the signal transmission will be provided.

3.2 The Solid-State Camera

Imaging with solid-state sensor based cameras differs from film-based cameras in the type of lens, the replacement of the film with the solid-state sensor, and the transfer of the "image" from the sensor to the computer memory. Cameras with solid-state imaging devices are usually erroneously called CCD-cameras, with CCD standing for charge-coupled device. This is incorrect as there are also other devices than CCDs employed in such cameras. This term shall nevertheless be used here in the sense that it encompasses also other solid-state imaging sensors.

Figure 3.2 illustrates a cross-section through the lens and body of a solid-state camera

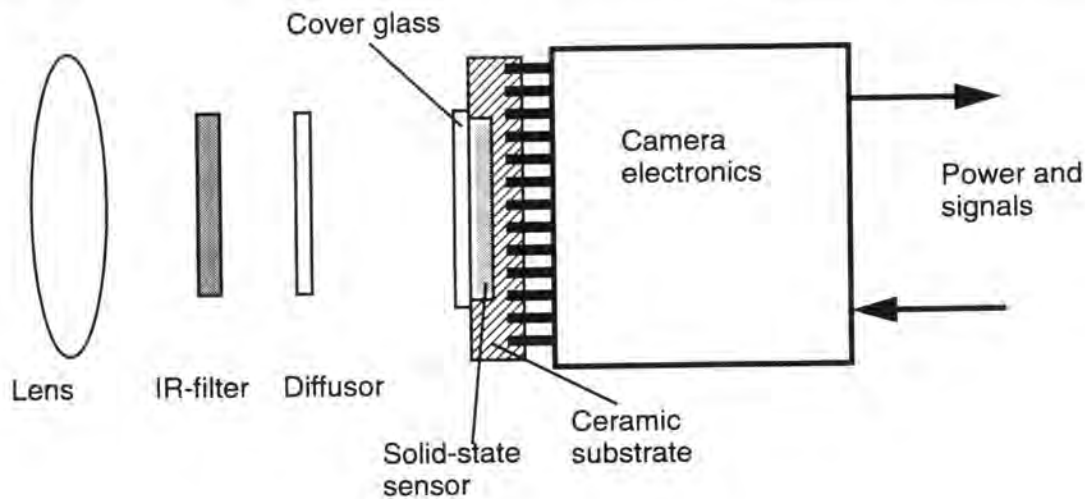


Figure 3.2 Functional elements of a solid-state camera.

with the major functional elements. The lens is usually a CCTV-lens (Close Circuit Television) with a C-mount or a CS-mount. Some cameras, like the Megaplus have an F-mount. The distance from mount to imaging plane is 17.526 mm and 12.5 mm for C- and CS-mount lenses respectively. They are not always designed for cameras with IR-filters and it has been found that some have optical elements which physically conflict with the IR-filter. Cameras with F-mounts have the disadvantage that it is difficult to obtain lenses with a focal length adapted to the size of the sensor to obtain a reasonable field of view. Typical sensor sizes are the 1/2 and 2/3 inch with a format of 4.8 x 6.4 and 6.6 x 8.8 mm respectively. Some sensors have different formats, especially the so called "scientific sensors" with over 1024 x 1024 sensor elements.

In addition to the optical elements shown, some cameras have an LCD- or mechanical shutter (electronic shuttering is achieved by read-out techniques). The IR-filter is used to cut-off light with wavelengths above 700 nm to eliminate optical scattering at longer wavelength. Often a BG38 filter is used, which results together with the spectral sensitivity of the solid-state sensor in a spectral sensitivity close to the human eye. The diffuser, often a birefringent quartz plate, is found in most cameras using interline-transfer sensors. It serves as an optical low-pass filter to suppress aliasing. If birefringent quartz

plates are used, care must be taken with polarization filters. Changes in the polarization lead to displacements of the imagery (*Baltsavias et al., 1990* and *Beyer, 1991g*). The sensor is located on a ceramic substrate and usually protected by a glass plate. The IR-filter, diffuser, and cover glass are typically not accounted for in the lens design. This decreases the imaging performance of the system. Some newer designs integrate the IR-filter and the protection glass directly on the sensor surface. This eliminates some of the extra refractive surfaces.

The camera electronics serve many different purposes. Their function can be simplified to the point where the only task is to assure that an image with maximum quality is obtained at the camera output. Details of the camera electronics and their functions are given in section 3.5.

The assembly of sensor and lens is often not very stable. In some cameras it was found that there is no direct connection between the sensor and the lens mount. The sensor is kept in place by the pins on the electronics, which are rather loosely attached to the camera housing. Few manufacturers use constructions where the sensor is fixed to the front part of the camera housing and to the lens mount. The sensor is usually aligned to the optical axis as far as it is defined by the lens mount. The issue of the location of the principle point has not been addressed by any manufacturer so far. It is therefore to be expected that the interior orientation of the camera needs to be determined. Well-constructed solid-state cameras should provide for sufficient stability. As none of these components are built with photogrammetric applications in mind they are potential sources of systematic errors.

3.3 The Solid-State Sensor

The solid-state sensor and its electro-optical and geometrical characteristics are of major interest for high-precision geometric measurements. A wealth of literature exists on solid-state imaging devices. Most publications, however, do not investigate the geometric properties, but are only concerned with their radiometric properties. Scientific publications in the last years are usually only concerned with sensors for astronomical and other applications requiring exceptional electro-optical performance. Such sensors are usually cooled and read-out at slow rates. The properties of these sensors are naturally of great interest, but the long image acquisition time and the high price makes them ill suited for most applications in Real-Time Photogrammetry. They will be of interest where accuracies surpassing those achieved with standard solid-state cameras are required. A short introduction on the fundamentals of the sensors and their read-out architectures is given in *Baltsavias et al., 1990* and *Beyer, 1991g*. An extensive review of solid-state sensor technology, read-out architectures, electro-optical performance measures is given in *Beyer, 1992* and the references given therein.

The **geometric performance** which can be expected from such sensors is of major interest. The uniformity of the sensor element spacing and/or apertures as well as the flatness of the sensor surface can be used to assess the geometric accuracy which can be achieved. Manufacturers do not provide specifications on the regularity of the spacing or the surface flatness. One way to estimate the precision of the sensor geometry is via the precision of fabrication devices. The estimates for waver-steppers indicate that local systematic errors for a system applicable to 0.5 μm design rules are smaller than 0.15 μm and that RMS errors are 0.1 μm (*Allan, 1984; Pol et al., 1987; Pool et al., 1990*). Assum-

ing a 10 μm sensor element spacing this would correspond to a regularity of $1/100^{\text{th}}$ of the spacing.

The spacing of the sensor elements was verified by measurements. *Curry et al., 1986*, measured the sensor element spacing and found that it was within 0.2 μm of the manufacturer specification for a 45.54 μm spacing. No values for the regularity are given. *Hantke et al., 1985* investigated linear arrays with a knife edge method. The maximum spacing errors were found to be smaller than 0.2 μm and the regularity of the spacing was reported to be, in qualitative terms, "excellent". The sensor element spacing of the investigated linear array was given to be 13 μm . The regularity of that sensor was thus at least $1/65^{\text{th}}$ of the spacing. *Lenz, 1988*, uses a Moiré technique to check the regularity of an interline-transfer sensor. He states that "with an estimated phase-measurement accuracy of approximately $2\pi/100$, corresponding to $1/100$ sel, no significant deviation of an ideal sensor element raster could be found" (sel ... sensor element).

Another method to assess the regularity of the sensor element aperture size is the uniformity of response (see section 5.3). This figure is degraded by additional errors such as material non-uniformities and noise, but can be easily determined (if a uniform illumination can be generated). A uniformity of response better than 5% is aimed at for general TV-applications. This would require that a sensor with 10 μm square sensor elements has a uniformity in the order of 0.2 μm . For many sensors uniformities of 1% and even of 0.1% in astronomical applications have been indicated by many authors, e.g. *Blouke et al., 1987*. *Lake, 1990*, even states that the positional tolerances of an 12 x 12 μm sensor element is about 0.05 μm . This corresponds to $1/240^{\text{th}}$ of the sensor element size.

Accuracies of that level have actually been achieved in star tracking applications where RMS residuals of $1/200$ pixel have been reported (*Stanton et al., 1987*). This corresponds to a relative accuracy of 1 : 50 000 with respect to the comparatively small field of view. A backside-illuminated Frame-transfer CCD-sensor with a 30 μm sensor element size was used.

All these investigations indicate that the regularity of the sensor elements is better than $1/50^{\text{th}}$ to $1/100^{\text{th}}$ of the spacing. Nevertheless it cannot be directly expected that this accuracy can be attained in photogrammetric applications. All measures given above have been obtained with an illumination incident almost vertically onto the sensor element surface and/or without passing through the gates on the sensor surface. The surface topography of sensors is extremely uneven. Gates and other surface elements create a surface topography reaching several micron variations. A global bow of large area sensors reaching 50 μm have been reported by *Blouke et al., 1987*. It will therefore be left to further investigations to assess to what degree the surface topography plays an actual limiting factor for the mensuration precision which can be attained with solid-state sensors.

3.4 Television Standards

3.4.1 Conventional Video Standards

Video standards play a fundamental role in the transmission of image data. The first standard for black-and-white television was adopted by the Federal Communications Commission (FCC) of the U.S.A. on July 1, 1941. This standard, called RS-170, was defined by the National Television Systems Committee (NTSC) and the Electronics Industries Association (EIA). The Comité Consultatif International des Radiocommunications (CCIR) defined the CCIR video norms for black-and-white television in the 1950s. There

are now thirteen norms called CCIR-A to CCIR-M used in various countries. The NTSC standard for color television is an enhancement of the RS-170 video standard accepted in 1953. The PAL (phase alternate line) and SECAM (sequential color and memory) color standards were also defined in the 1950's. The NTSC standard is used in 32 countries throughout North America, parts of South America, Japan, and the Philippines. PAL and SECAM are used in Europe, Asia, Australasia, and parts of South America and Africa; PAL in 63 countries and SECAM in 42 countries (*Jurgen, 1988*). The requirement that color standards be compatible with the existing black-and-white standards resulted in several shortcomings. One of the problems is that high frequency luminance signals are treated by decoders as color information. Problems of the NTSC standard, which are similar to the ones of PAL and SECAM, are discussed in *Jurgen, 1988* and *Hopkins, 1988*. Frame grabbing of color video signals is covered in *Siegel, 1988*. The following discussion is limited to the CCIR black-and-white video standard. The RS-170 standard differs only with respect to the timing characteristics. The analysis with respect to the radiometric and geometric performance is identical.

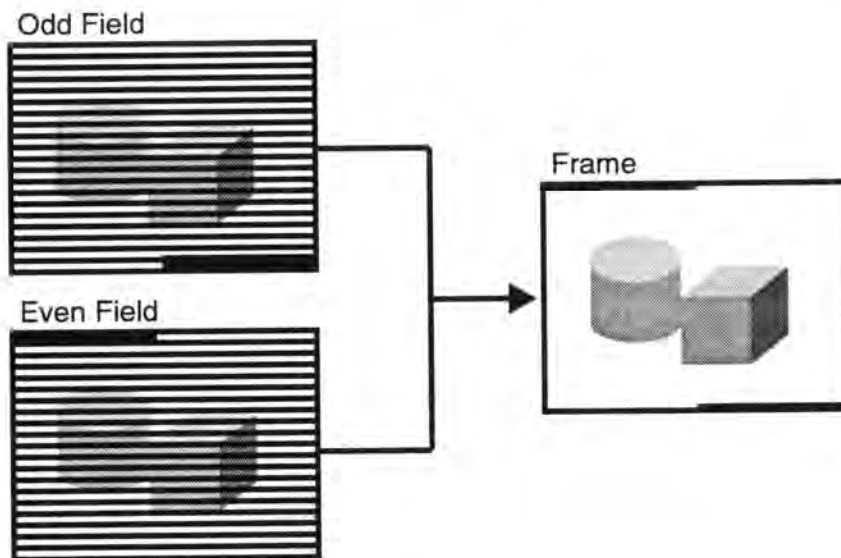


Figure 3.3 Frame and fields in interlaced video

The **CCIR video standard** uses the principle of interlacing. **Interlaced scanning** means that the centre-to-centre spacing of adjacent lines in the time domain is two or more times the spacing of adjacent lines in the spatial domain. The principle of 2:1 interlacing is depicted in the figure above. It shows that a **frame** (image) consists of two fields. The even field contains all lines with even line numbers and the odd field those with odd line numbers. A **field** is one of two (in 2:1 interlacing) or more parts of a frame when interlacing is used.

Figure 3.4 shows details of several signals during the **vertical retrace period**. This period is used by the electron beam in display monitors to return from the bottom of the screen to the top. The start of each field is indicated with the **vertical synchronization pulse (VSYNC)**. The image data of the **odd field** starts with a complete line and ends with a half-line. The situation for the **even field** is reversed. The period between the last line of one field and the first of the next field contains several blank lines, some pulses used by monitors to perform the vertical retrace, and again some blank lines. **Composite**

video contains all image and synchronization information. Other signals shown in the figure are the **composite sync** (containing the synchronization information of composite video only), **vertical sync** (indicating the start of a field), and **horizontal sync** (containing pulses for the start of each line). The timing characteristics of the CCIR and RS-170 video standards are given in Table 3.1.

Composite video at start of odd field

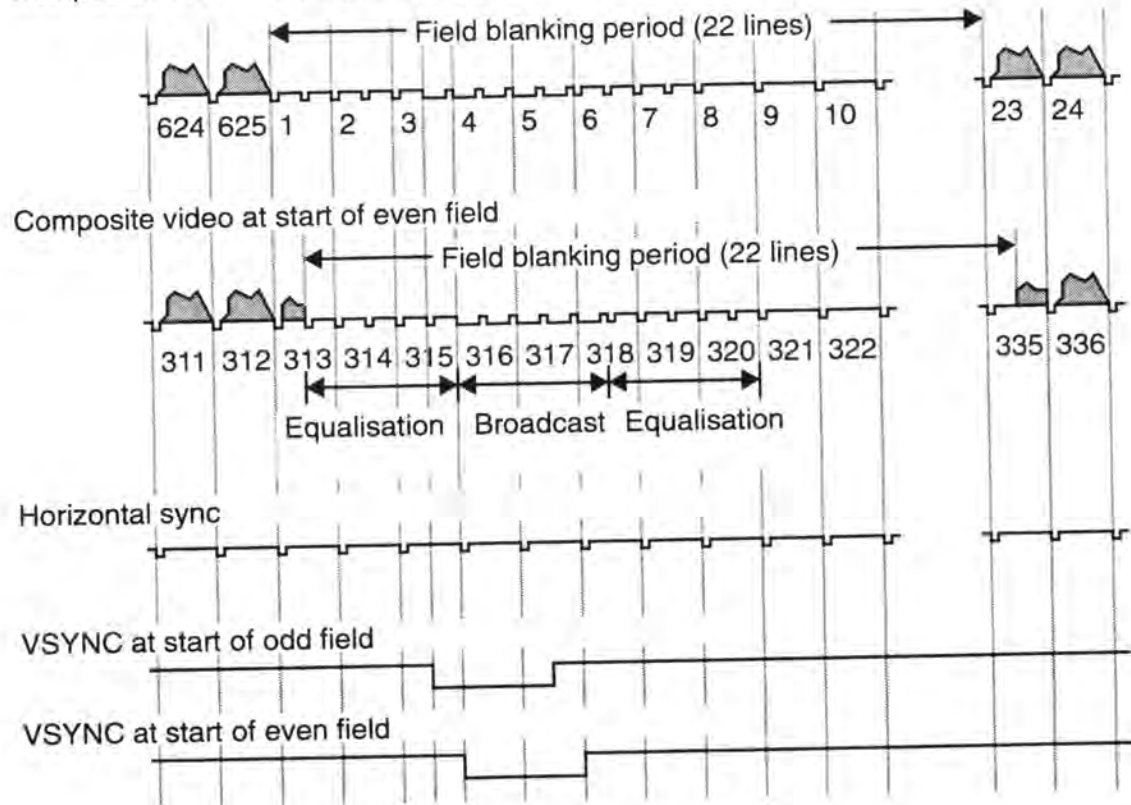


Figure 3.4 The CCIR video signal

	RS 170	CCIR
Frame Rate / Field Rate	30 / 60 Hz	25 / 50 Hz
Interlacing	2:1	2:1
Number of lines	525	625
Number of active lines	480	576
Field time	16 2/3 ms	20 ms
Time per line	63.49 μ s	64 μ s
Line frequency	15750 Hz	15625 Hz
Active line period	~52.5 μ s	52 μ s
Nominal video bandwidth	4.5 MHz	5.5 MHz
Resolution (Nyquist)	472	572
Aspect Ratio	4 : 3	4 : 3

Table 3.1 Basic data of the RS-170 and CCIR video standards.

Figure 3.5 shows the composite video signal for one line with image data and the horizontal synchronization pulse. Each line consists of the horizontal blanking period with front porch, line sync pulse, and back porch and the active image period. The falling edge of the line sync pulse indicates the start of a new line with the **horizontal synchronization signal (HSYNC)**. The voltage level corresponding to "black" is indicated by the **blanking level**. The geometric and radiometric properties, advantages and disadvantages of the video signals are discussed in *Beyer, 1987a, 1988, 1991c and e; Dähler, 1987, and Simmons, 1987*.

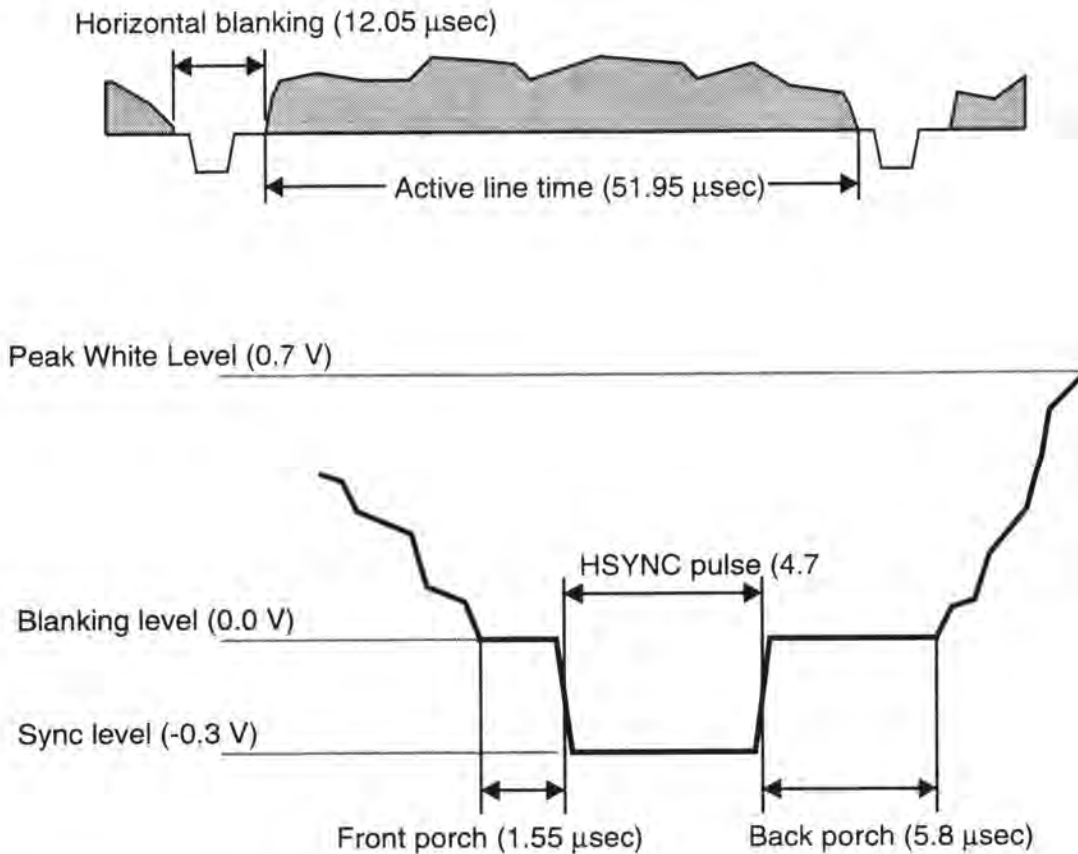


Figure 3.5 A line and the horizontal synchronisation pulse of the CCIR video signal.

A signal not defined in any of the standards mentioned above is the **pixel-clock**. It is a periodic signal with a frequency identical to the sensor element clock. It can have a phase shift with respect to the transmitted data. This must be accommodated by the frame grabber as discussed later. The pixel-clock provides for a transmission of the scale within each line. The advantages resulting from its use are discussed in section 3.6.2.

3.4.2 High-Definition Television

The standard TV signal is not well adapted to the human visual system in terms of dynamic range, spatial and angular resolution. The human visual system could use a dynamic range of 1 to 10 000, a temporal resolution of up to 80 Hz, and an angular resolution of thirty cycles per degree (*Kunt, 1988*). Several efforts are under way to improve the existing standards and/or to introduce a new standard (or standards) which provides for significantly improved performance, generally referred to as **HDTV (High-Definition Television)**.

The development of HDTV was pioneered by NHK (Nippon Hoso Kyodai, Japan Broadcasting Corporation). The demonstration of the **MUSE** system (multiple sub-Nyquist encoding), called **Hi-Vision**, dates back to 1982. In the meantime several proposals for standards have been put forward and many research and development initiatives are under way in Japan, the United States of America, and Europe. Hi-Vision uses 1125 lines per frame, 2:1 interlacing, a field rate of 60 Hz, and a 16:9 aspect ratio. The **Advanced Television Systems Committee (ATSC)** proposed a sampling frequency of 74.25 MHz resulting in 1920 pixels during the active line time. The system developed within the European project Eureka 95 called D2-MAC (multiplexed analog components) uses 1152 lines and a 50-Hz field frequency instead. There are proposals to use a new line synchronization signal which allows the derivation of the timing from zero crossings between the negative and positive pulses. The MUSE system uses another synchronization scheme and performs synchronization with a PLL employing a digital phase comparison (Ninomya *et al.*, 1988). All synchronization schemes are tuned towards visual observation and not to perform measurements with the transmitted imagery.

The major drawback of this development with respect to digital photogrammetry is that the requirements are to a large extent determined by considerations of the broadcasting industry. Compatibility of the signals for existing television sets is a very high priority. Aspects of image quality for subpixel measurement could not be found in any publication. A digital standard, as wished by the computer industry, would be very useful for latter applications. Although the signals might not lead to a major improvement for photogrammetric applications the tremendous financial interest in broadcasting applications is leading to sensors with a larger number of sensor elements which will be significantly cheaper than comparable current sensors (Beyer, 1992).

3.5 Camera Electronics

The output of a sensor contains noise from several sources and often short-duration spikes from clocks. The camera must perform appropriate signal processing to reduce noise, remove any high frequency cross-talk and keep a constant black level reference. This signal can either be sampled by an analog-to-digital converter in the camera (digital camera) or transmitted to a frame grabber as analog signal (analog camera). Both require the transmission of synchronization signals, but only the latter depend on highly accurate timing to achieve a geometric and radiometric correct transmission. This section will first cover the elements and characteristics of typical analog cameras and then those of digital cameras.

3.5.1 Analog Cameras

Figure 3.6 shows a block diagram with typical functions of a standard CCD camera. The camera requires power supply and should be able to synchronize to external synchronization signals. The DC-to-DC converter generates the internal DC voltages required by the various electronic components. The external sync detection circuitry performs two tasks. Firstly it detects the existence of an external sync source and sets the camera to use the internal clock or the external sync source to derive the master clock with a voltage controlled oscillator. Secondly it converts the incoming signals (composite video, composite sync, VSYNC, HSYNC, pixel-clock) to internal signals (typically VSYNC and HSYNC). The video timing generator creates all the video synchronization signals, blanking signals, and signals for the sensor clock generator. The sensor clock generator accepts HSYNC, VSYNC, master clock, and in some cameras signals for field/frame in-

tegration in Interline-Transfer (IT) sensors or field/frame mode in Frame-Transfer (FT) sensors or reset pulses, and generates all signals to drive the sensor. These are usually the clocks to drive the phases of the vertical and horizontal CCDs and the transfer from integration sites to vertical CCD registers in IT sensors, signals determining the sampling at the sensor output, and the black reference timing.

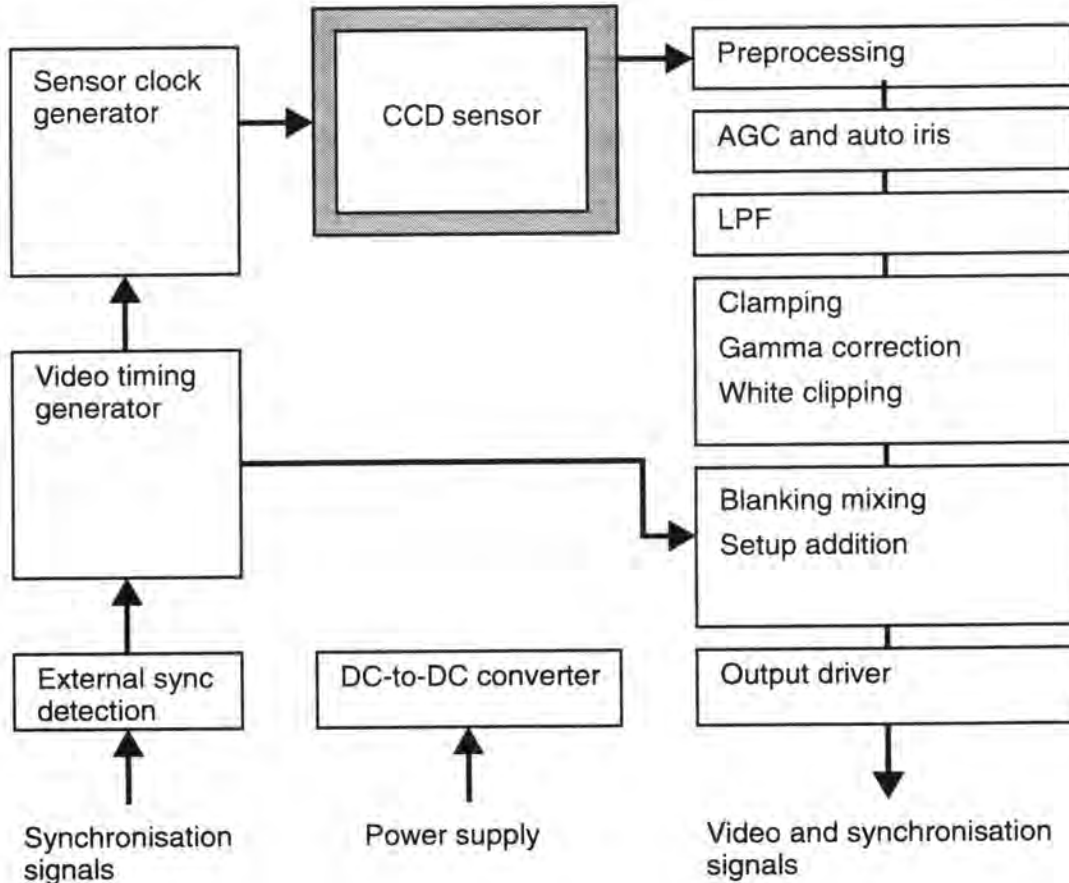


Figure 3.6 Block diagram of a typical CCD camera.

The output of the sensor is first preprocessed. This can be a simple sample-and-hold or an advanced preprocessing scheme such as correlated-double-sampling (CDS). The aim of this stage is to reduce sensor noise.

Auto iris and automatic gain control (AGC) are functions to adjust the average image brightness. This function must be switchable as it is most undesirable in many applications. Figure 3.7 shows the large influence of automatic gain control on a grayscale taken with a bright and dark background. As the AGC tries to adjust the average picture level (APL) the grayscale is imaged too bright in the image with the black paper as background and too dark in the image with the white paper as background.

A low-pass filter (LPF) is used to remove any clocking transients and other high frequency artifacts. The possible negative side effects, such as a feature shift and ringing are discussed in *Dähler, 1987; Baltasvias et al., 1990* and *Lenz, 1988*. Clamping removes any signal components which would result in a negative signal with respect to the blanking level. Gamma correction is used to compensate for the non-linear behavior of typical TV monitors. Latter have a gamma of around 2, requiring a transfer function with a gamma of around 0.5 to obtain an overall linear response. This results in an attenuation of dark

image areas versus bright areas. An example of the effects of gamma correction are shown in Figure 3.8. Two images of a grayscale chart (logarithmic changing intensity) were grabbed with and without gamma correction. The density of the grayscale chart increases by 0.1 from step to step. The intensity (and therefore also the grayvalues) should vary by \log_{10} from step to step. This characteristic is destroyed when gamma correction is used.

White clipping removes any signal higher than the video norm (typically 0.7V above black reference level). Aperture correction (not shown in 3.6) serves the purpose of improving the MTF characteristics of the sensor. Ideally one would like to have an MTF of one (1.0) up to the Nyquist frequency and zero (0.0) above it. The electrical low-pass decreases the amplitude of signals at higher frequencies. The combination of the low-pass filter and aperture correction can result in MTF characteristics approaching the ideal curve. One must consider though that all aliasing components from sampling by the sensor are also enhanced with this technique.

Some cameras also include a contour correction mechanism which is essentially a high pass filter to enhance contrast at contours. It is undesirable as it introduces an asymmetric response and ringing artifacts.

The next step is the adding of the blanking and synchronization information. This is only required when a composite video signal is to be transmitted. Otherwise only a blanking level is required. All camera timing should be derived from a stable crystal based clock oscillator with counters. Otherwise the HSYNC to HSYNC time will not be an integer multiple resulting in increased jitter and other unpredictable effects. The complete signal is sent via the output driver to the camera output connectors. Other signals which can also be delivered by the camera are composite sync, VSYNC, and pixel-clock.

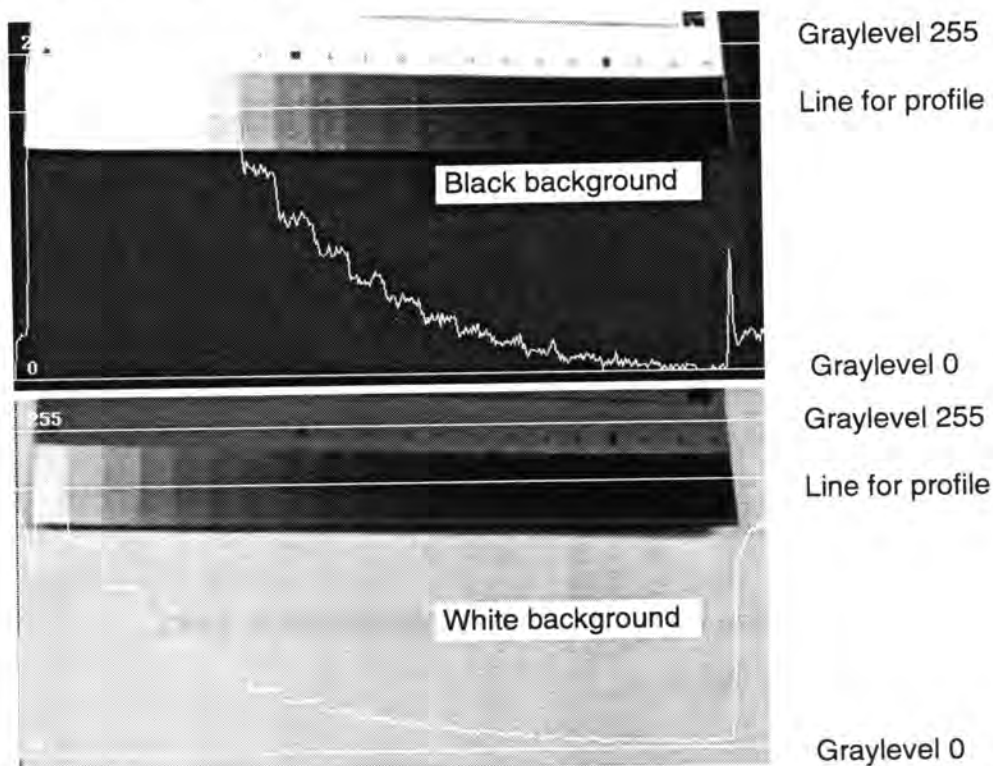


Figure 3.7 Images taken with automatic AGC of a grayscale on black and white background. The profile through the grayscale show the change due to AGC.

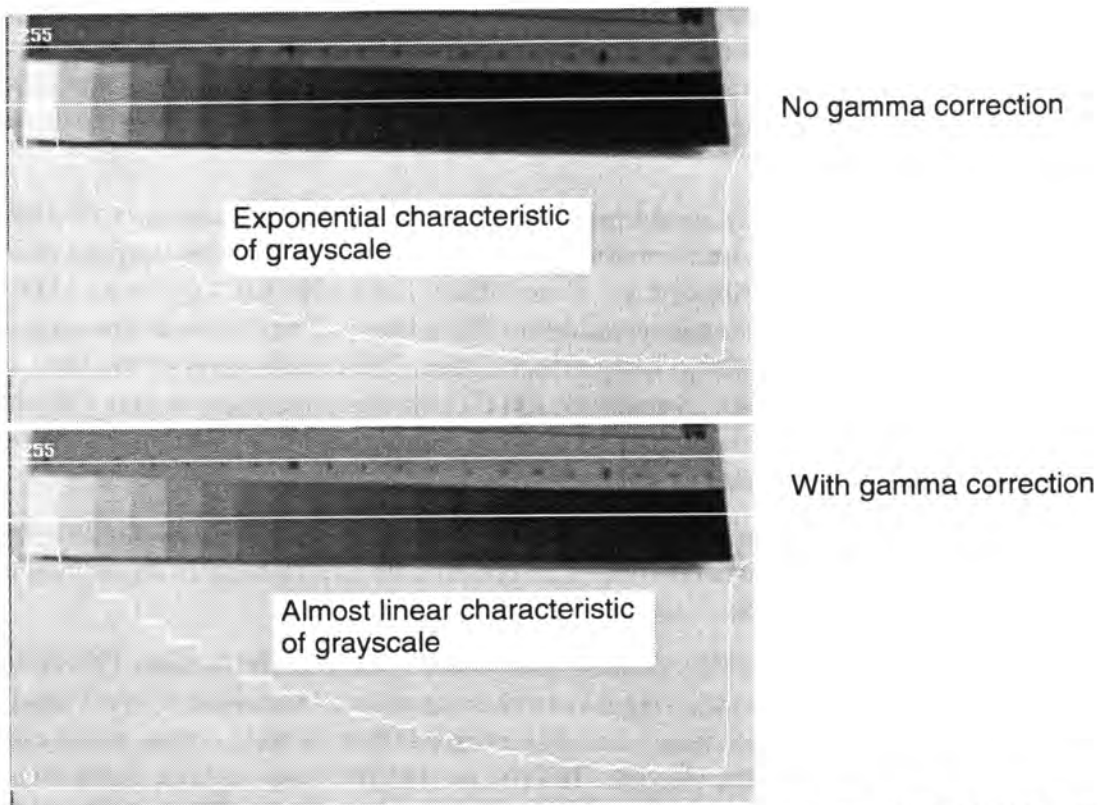


Figure 3.8 Images of grayscale taken with and without gamma correction by the camera.

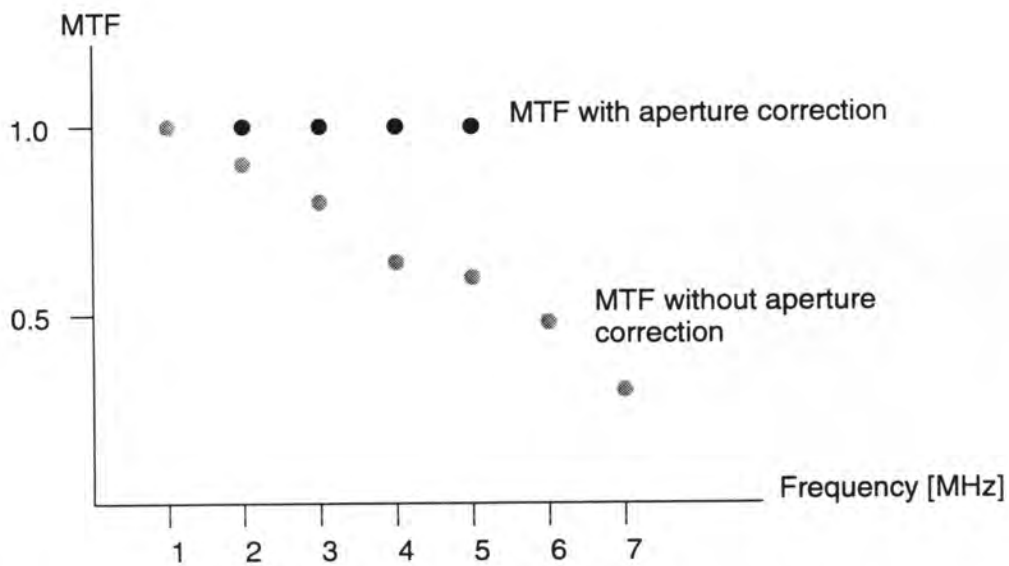


Figure 3.9 Effect of aperture correction on MTF (data from *HCS, 1990*)

3.5.2 Digital Camera

Figure 3.10 shows the layout of a typical digital camera. The signal is preprocessed just like in any analog camera and possibly low-pass filtered. Some cameras perform a black level adjustment. The signal is then passed on to an analog-to-digital converter which

samples the video signal with the sensor element clock frequency. The data from the ADC is passed to output drivers to be transmitted. Besides the digital data pixel-clock, HSYNC and VSYNC are required to convert the data stream back into a two-dimensional matrix of grayvalues. A digital camera can also perform additional tasks as discussed in Büchli et al., 1985; Babey et al., 1985; and Dunbar, 1986.

The **black reference** of cameras is quite often not very well laid out. Some FT sensors use a line on top of the sensor. This is the last line to be read-out. It accumulates smear signals while passing through the imaging area and can be influenced by blooming. This line will contain the maximum amount of dark signal, such that a too high value will be subtracted. Another technique is to use some lines from the field storage area. These are immune to smearing, but could still be influenced from blooming. An alternative method is to use several shielded columns at the start of each line. Care must be taken that the dark level reference from these can be determined with sufficient precision. Otherwise systematic graylevel differences from line to line can be introduced. This requires the use of several (up to several tens) sensor elements per row for black reference. One advantage of this technique is that the level of dark current would be closer to the one of the line to which it is applied than an average over the complete frame.

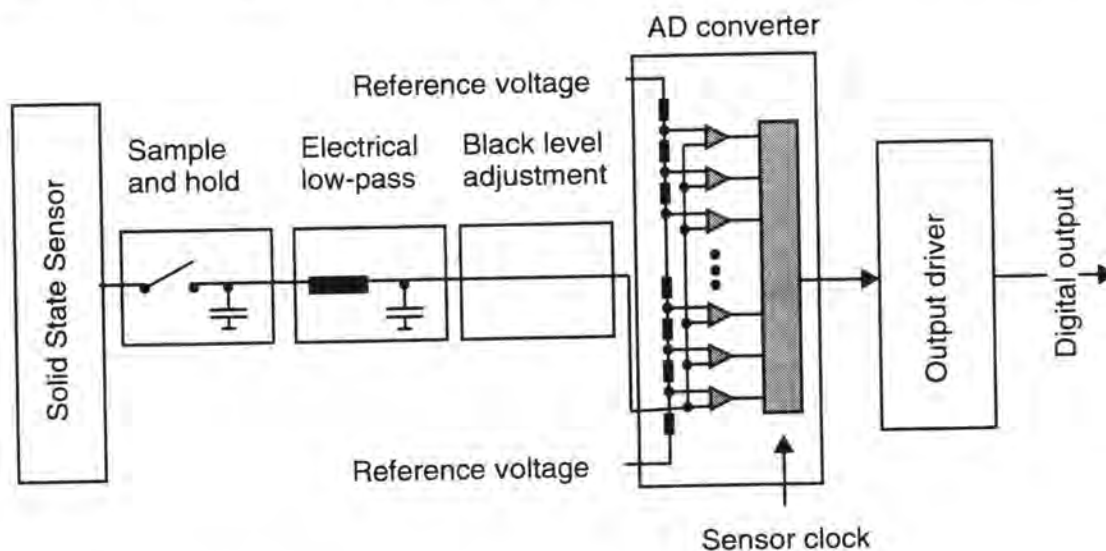


Figure 3.10 Basic elements of a digital camera.

3.6 Frame Grabbing

Frame grabbers exist with a multitude of capabilities which are very hard to generalize. They are either special purpose devices for image acquisition, but can also include storage, processing elements, and display units. The processing capabilities can vary significantly between frame grabbers, e.g. from microprocessors to special hardware for Hough transforms. The coverage of frame grabbers in this chapter is restricted to image acquisition with analog signals for black-and-white images.

Figure 3.11 shows the basic components of a frame grabber. The **analog front end** consists of the input and impedance matching unit and the DC-restoration and analog pre-processing section. The analog front end provides a raw video signal to the sync separator and the preprocessed video signal to the analog-to-digital converter. The **syn-**

chronization section comprises the sync separator, synchronization detection, internal sync/address generation, and the generation of synchronization signals for the output to external devices such as cameras, light strobes, etc. The **analog-to-digital converter (ADC)** receives the preprocessed video signal, the sampling clock, and reference voltages. It performs the ADC and passes the data on to a data buffer, typically via a latch. The **sync output section** contains the output drivers to send signals to external devices to be synchronized. The **buffer** can be a memory which is synchronized with the sensor clock or a FIFO (first in first out).

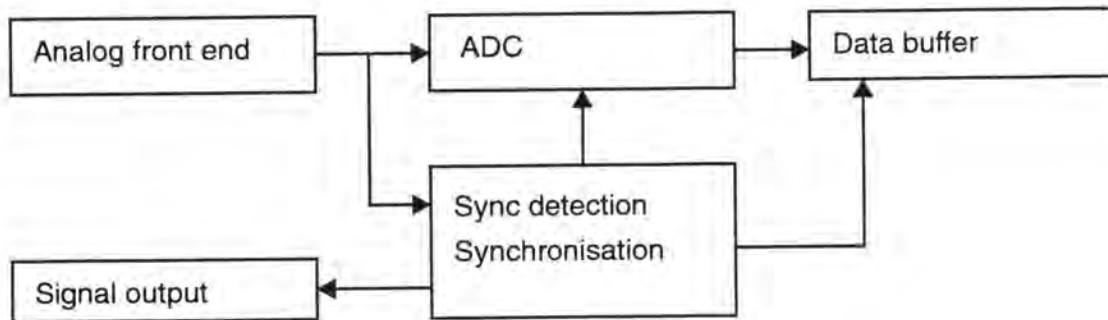


Figure 3.11 Typical image acquisition components of a frame grabber.

3.6.1 Analog Front End

Figure 3.12 gives an overview of the elements of the analog front end. The input section

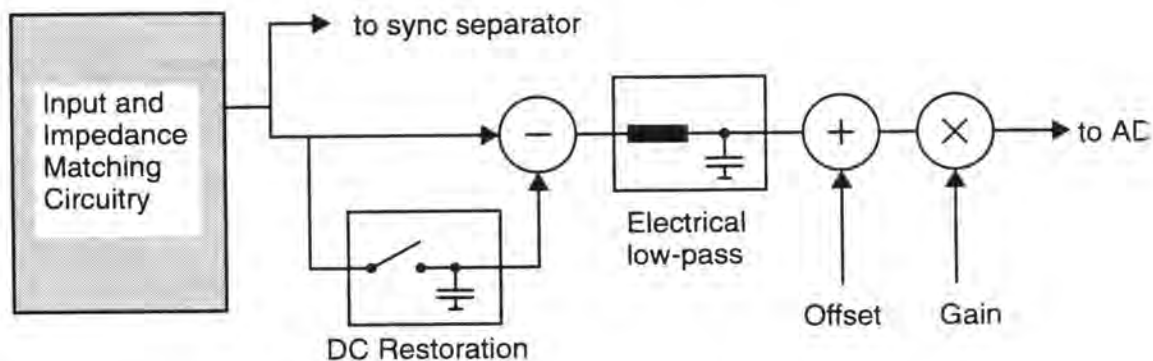


Figure 3.12 Analog front end.

of the analog front end must be sufficiently flexible to connect signals with different impedance and input voltage levels. Advanced frame grabbers accept composite video, VSYNC, HSYNC, and pixel-clock signals. Video is typically terminated at 75 Ohm and AC-coupled. The synchronization signals require considerable flexibility to adjust the input impedance and threshold level for signal detection. This has been generally found to be a problem for the pixel-clock. Some cameras can drive a 300 Ohm termination with TTL levels, but some deliver only a 1 Vpp (Volt peak-to-peak) signal at the camera output. The input must be well designed to eliminate any imprecision in signal detection at

this stage (*Raynor and Seitz, 1990*). Improper termination can lead to adverse effects as shown in Figure 3.13 where a signal reflection occurs in a long cable. This results in low-pass filter effects and ringing through signal reflections.

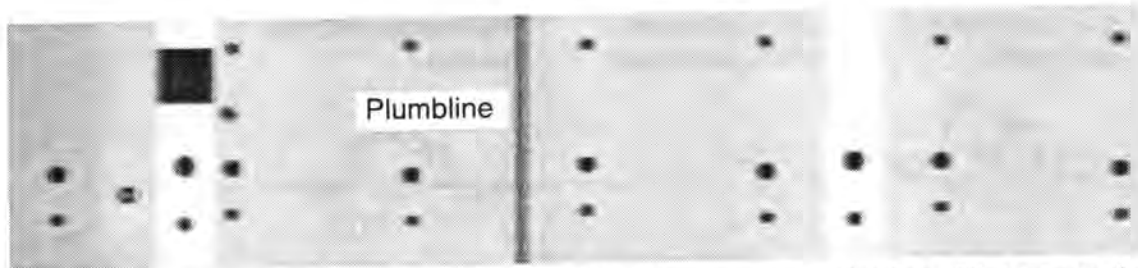


Figure 3.13 Image with signal reflections from improper termination. Ringing to the right of the plumbline and target are discernible.

The video signal is split after the impedance matching circuitry and one part of the video signal is directed to the synchronisation section and the other to the analog preprocessing elements.

A very important part of preprocessing is **DC restoration** (or **black level clamping**). The DC restoration must change the voltage level of the signal such that the back porch is at zero volt, or an internally set reference level. The DC restoration must be fast enough to react to changes in the level induced by the capacitor of the AC coupling input due to changes in the average picture level. It must also provide for a stable output for potentially long line periods of slow scanned large area sensors or linear arrays. Figure 3.14 shows a simple DC restoration circuit using a switch to discharge the capacitor of the AC coupling input during the back porch. Such a DC restoration circuit will result in a clamp error when the average picture level changes significantly as shown in Figure 3.14 (*Raynor and Seitz, 1990*). Figure 3.15 shows a DC restoration circuit with a sample

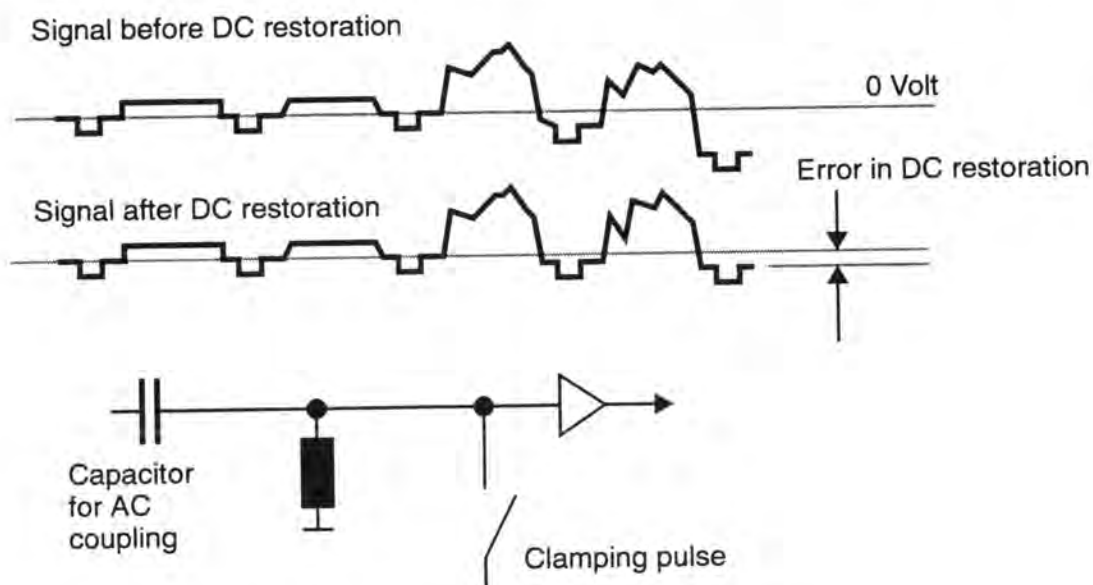


Figure 3.14 Simple DC restoration circuit and clamping error.

and hold and one using an additional feedback loop as reported by *Raynor and Seitz, 1990*. The first one samples the video signal at the back porch during a time determined

by the clamping pulse. The second uses the video signal after the video amplifier and the black level reference of the ADC to derive a precise and stable DC restoration via its feedback loop as shown in the figure.

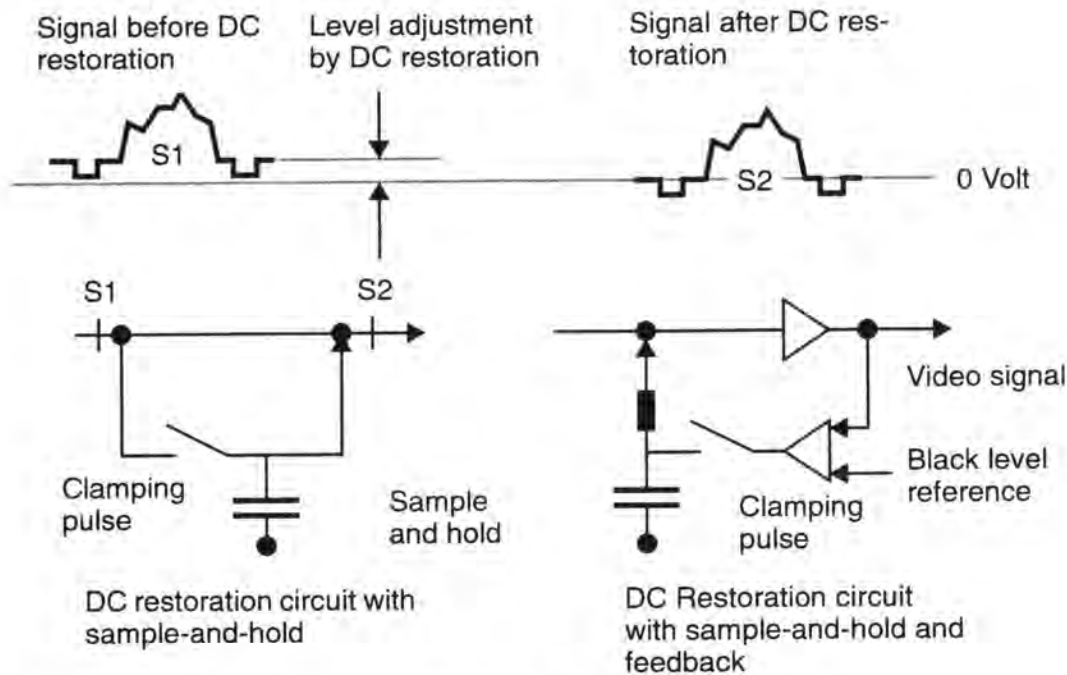


Figure 3.15 Two DC-restoration circuits with sample and hold.

The location and duration of the clamping pulse is also of importance. As shown in section 4.3 the DC restoration with composite video requires special attention due to the nature of the blanking level during the vertical retrace period. The duration of the clamping pulse should be as long as possible to provide for a precise DC restoration. Any variation in the level results in a systematic grayvalue shift for that line. The accuracy of DC-restoration for the method given in Figure 3.15 on the left is about 1% for a sampling time of 1 μsec (~ 10 pixel times at 10 MHz sampling rate). It will therefore be more accurate than the typical sampling time is longer than 1 μsec . Nevertheless it would be more precise if a feedback loop using the ADC is employed, as done in some digital cameras (which is only possible if the signal fits already within the input range of the ADC).

Further processing elements of the analog front end are a low-pass filter, analog offset, and gain. The low-pass filter (LPF) suppresses any high frequency disturbances introduced during the signal transmission or in the frame grabber. The non-symmetrical behavior and other negative effects as already discussed in above make the use of the LPF in many applications questionable. The effects of a LPF in the analog input are shown in section 4.6 and Figure 4.9.

Analog offset and analog gain can be used to adjust the average scene brightness or the amplification before AD conversion. The analog offset and gain should not be changed during an application as they change the radiometric characteristics of the imagery. The preprocessed video signal is thereafter passed to the ADC. It is typically shifted and sometimes inverted to fit into the input range of the ADC. *Raynor and Seitz, 1990*, provides an excellent discussion on the problems associated with the analog front end.

3.6.2 Synchronization

When using composite video without separate VSYNC and HSYNC signals, the frame grabber must derive them. The image information of the composite video signal is removed with the **sync separator** (sync stripper). After removal of equalization and broadcast pulses by **sync conditioning** the HSYNC can either be used as input to a PLL or to an edge detection circuitry when a pixel-clock signal or a fixed sampling clock is used. The signal from the sync separator is also directed to a circuitry to detect the VSYNC, typically with a LPF and edge detectors. When using VSYNC and HSYNC from the camera, all the cleaning of the synchronization signals can be bypassed.

The synchronization methods have paramount influence on the geometric precision of the signal transmission. The following will give a brief introduction to the synchronization methods and the resulting effects. Quantitative results from measurements will be given on several occasions in later chapters.

Synchronization with a Phase-Locked-Loop

When no pixel-clock is available from the camera, the frame grabber can derive the sampling clock from the horizontal synchronization via a phase-locked-loop (PLL). The basic analysis of this technique is identical whether composite video or an HSYNC signal is available from the camera. Figure 3.16 shows the signals when using CSYNC (composite sync) as input. The horizontal sync is derived from the composite video as outlined above and introduced to the PLL together with a feedback of the frame grabber HSYNC. The PLL in turn creates a sampling clock (always referred to as the internal clock of the frame grabber used for AD conversion) which is used to derive the frame grabber HSYNC via a counter. The latter defines the number of sampling clock periods from HSYNC to HSYNC signal and thus in turn the sampling clock frequency.

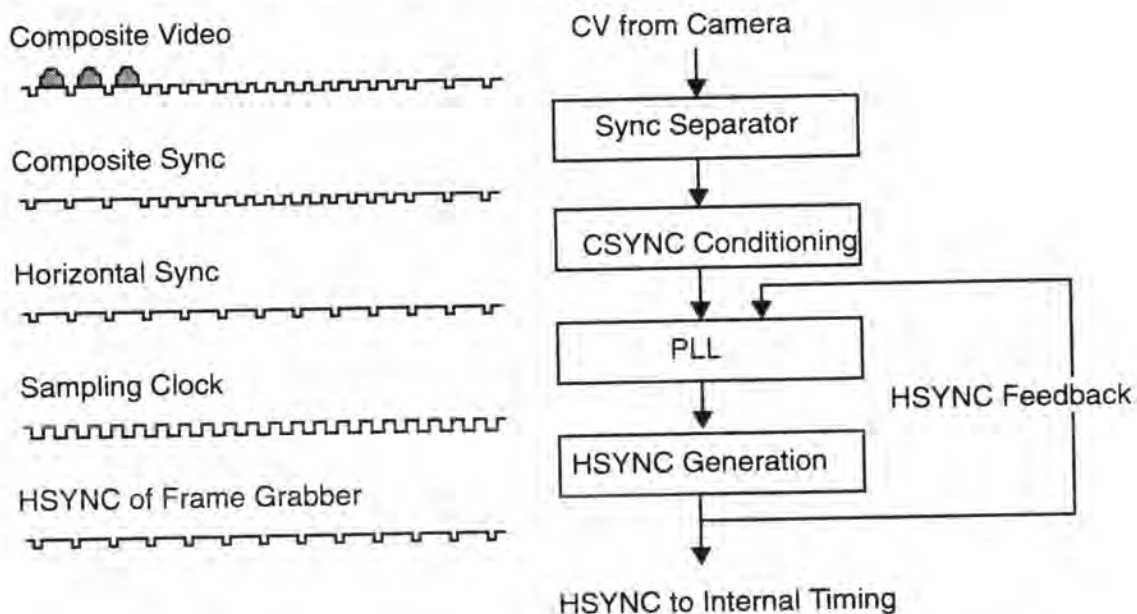


Figure 3.16 Signals and their flow in frame grabbing with PLL synchronisation.

Figure 3.17 shows the **phase-locked-loop (PLL)** in detail. It consists of a phase comparator, low-pass filter, and voltage controlled oscillator (VCO). The phase comparator receives the camera and frame grabber HSYNCs (horizontal synchronization signals).

Depending on the relative phase position of the two signals, a control signal is output. This is passed through the low-pass filter to the VCO.

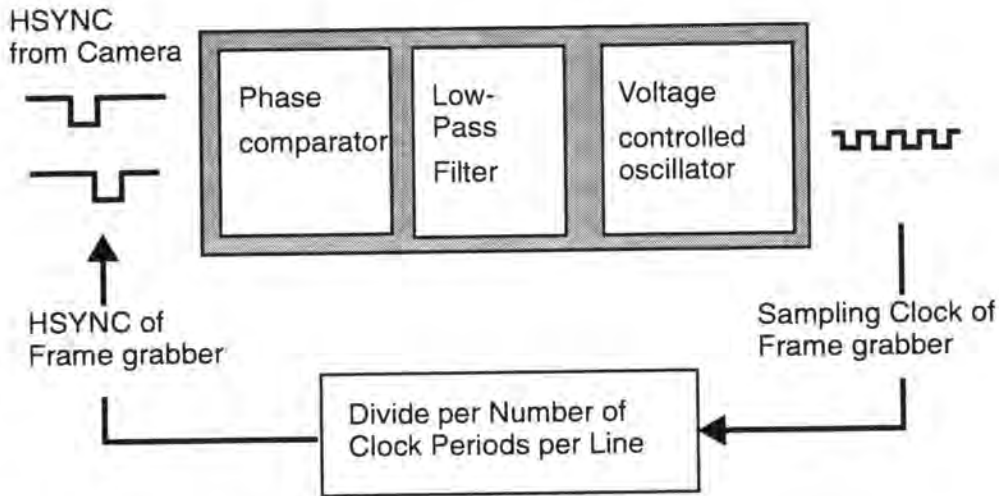


Figure 3.17 Components and signals of a PLL

Figure 3.18 shows the typical characteristics of the control voltage from the phase comparator after the low-pass filter (Horowitz and Hill, 1982). The control voltage to the VCO oscillates for some time after capture and then becomes more or less stable once the system has locked onto the camera HSYNC. Any imprecision in the phase comparison and the PLL control loop will result in a displacement of the sampling position, the result of which is called **line-jitter** (Gruen and Beyer, 1987; Beyer, 1987, 1988, 1991c and e; Dähler, 1987; Luhmann and Wester-Ebbinghaus, 1987; Lenz, 1988; Heikkilä, 1988). Line-jitter is influenced by several components. First the HSYNC is defined as a

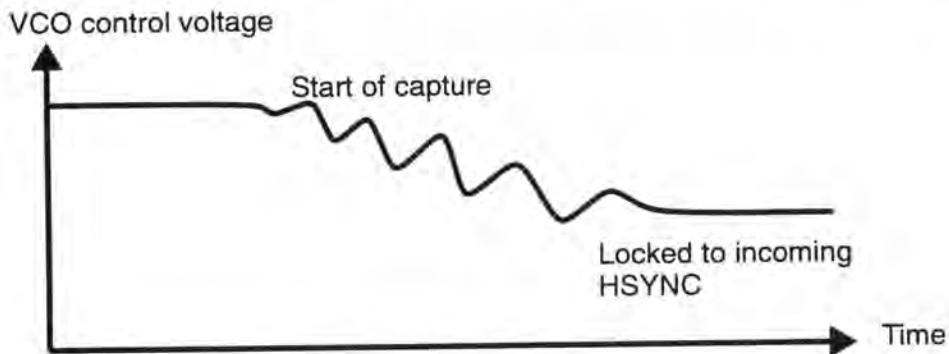


Figure 3.18 VCO control voltage during capture and locking (after Horowitz and Hill, 1982).

specific level on the HSYNC pulse. Assuming that a timing precision of 0.1 of a pixel is required (10 nsec for the typical 10 MHz sampling frequency) and a transition time of 100 nsec for the HSYNC pulse results in a threshold range of less than 30 mV. Typically the transition time is much larger (~250 nsec). Any noise components, DC drifts, and clock cross-talk will therefore result in line-jitter (see Dähler, 1987). Secondly the PLL can be disturbed during the VSYNC period if the signal quality is not good during this time. This typically occurs with video recorders, leading to large line-jitter as shown in the figure below. The sync stripper and sync conditioning must be well designed to re-

duce synchronization imprecisions induced by them (*Heinrich et al., 1986*). Direct VSYNC and HSYNC can provide for better synchronization stability than composite video or composite sync. The use of HSYNC instead of CSYNC will eliminate errors due to disturbances in the vertical retrace periods (see section 6.3). The typical precision of the line-to-line synchronization is in the order of 10 to 20 nsec (*Simmons, 1987*). The

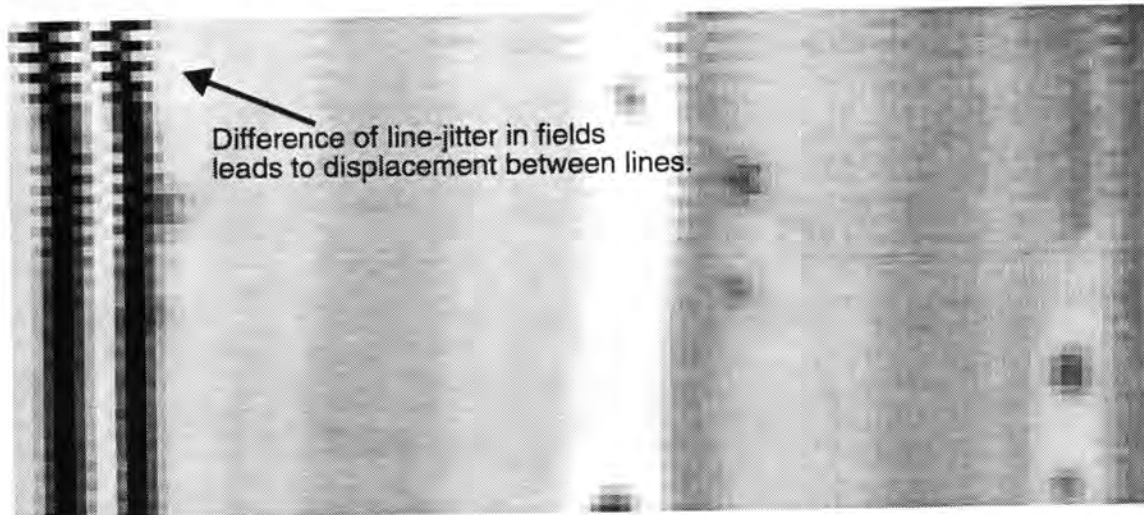


Figure 3.19 Line-jitter shown for an image grabbed from a video recorder.

jitter from field to field is usually considerably larger, and is the decisive factor when interlaced imagery is acquired. Figure 3.20 depicts some of the effects resulting from synchronization with a PLL. They are:

- shear of imagery due to disturbance of PLL in vertical retrace (only with CSYNC)
- line-jitter of typically larger than 0.1 pixel
- changing scale within each line
- resampling of the video signal different from the sensor clock resulting in a scaling in the x direction and aliasing effects (*Dähler, 1987*)
- phase patterns if cross-talk from pixel-clock if sensor element clock spikes exists

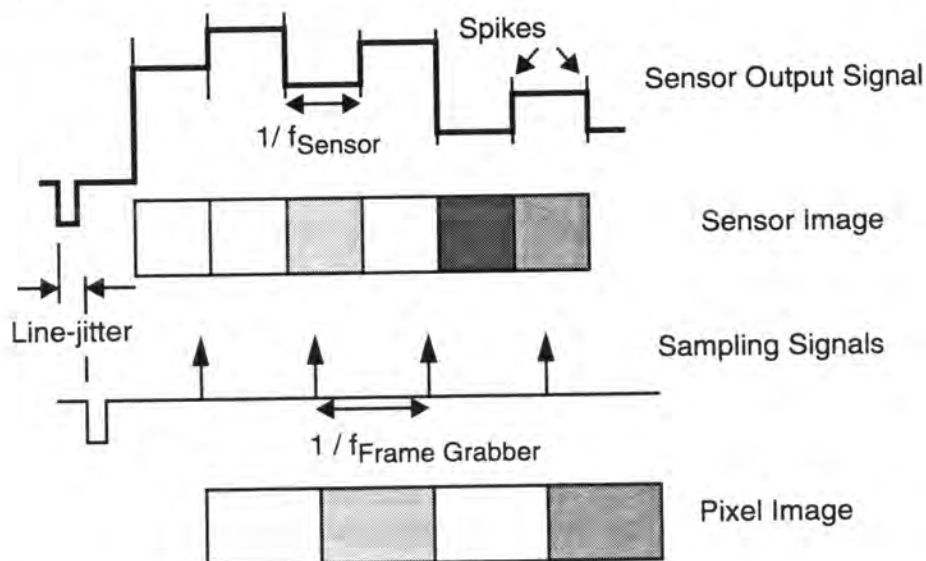


Figure 3.20 Some effects of frame grabber synchronisation with a PLL.

The effect of the pixel-clock cross-talk (influence of the pixel-clock signal on the video signal) is shown in Figure 3.21. This effect can be used to determine line-jitter (*Lenz and Tsai, 1988*). The pixel-clock of the sensor runs at a frequency of 11.25 MHz and sampling was performed with 10.4 MHz. The number of phases per line can be used to determine the number of clock period differences per line of the two clocks.

Line-jitter has been studied by, amongst others, *Beyer, 1987; Dähler, 1987; Lenz, 1987; Luhmann and Wester-Ebbinghaus, 1987; Heikkilä, 1988*.

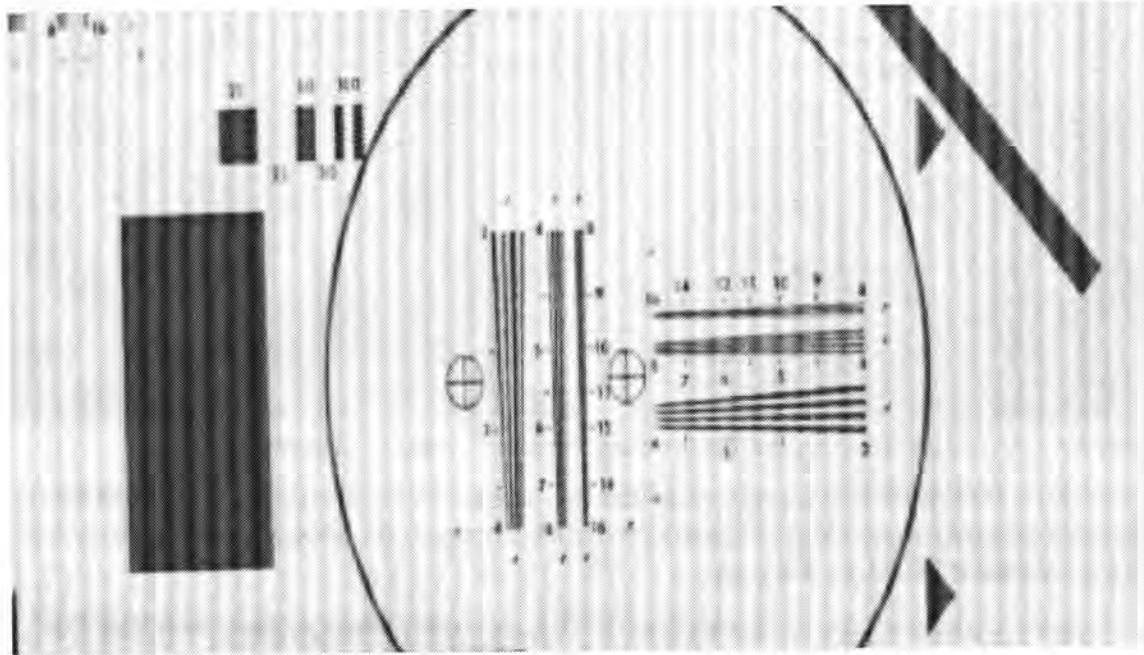


Figure 3.21 Phase pattern from cross-talk of pixel-clock when sampling with a frequency different to the sensor element clock frequency.

Synchronization with a Fixed Master Clock

Instead of using a PLL to derive the sampling clock, a master clock can be used and the sampling clock can be derived from it with a divider. The divider can be reset whenever a HSYNC pulse is detected. The line-jitter of such a frame grabber is determined by the frequency of the master clock with respect to the sensor element clock of the camera. It is typically larger than 0.1 pixel. An example of such a frame grabber is the WIPIX, which uses a 80 MHz master clock resulting in jitter of less than 1/8th of a pixel, assuming a 10 MHz sampling rate (*B+K Elektronik, 1990*). Details of this synchronization and resulting errors are discussed in *Beyer, 1988 and 1991c and f*.

Synchronization with Pixel-clock

The typical signals for horizontal synchronization with a pixel-clock are shown in the figure below. The HSYNC and pixel-clock from the camera are used in an edge detection circuit. The internal HSYNC is controlled from this edge detection circuit and the pixel-clock is used as sampling clock. As shown in Figure 3.23 any subpixel jitter is eliminated by the edge detection. The only status to be determined is whether or not the HSYNC signal has traversed a certain threshold level within the last pixel period.

When HSYNC is derived from the composite video, **line-displacement** can occur. As shown in the next figure this results in the displacement of a complete line of one pixel.

With appropriate selection of the pixel-clock phase to be used in the edge detection circuitry, line-displacement can be eliminated.

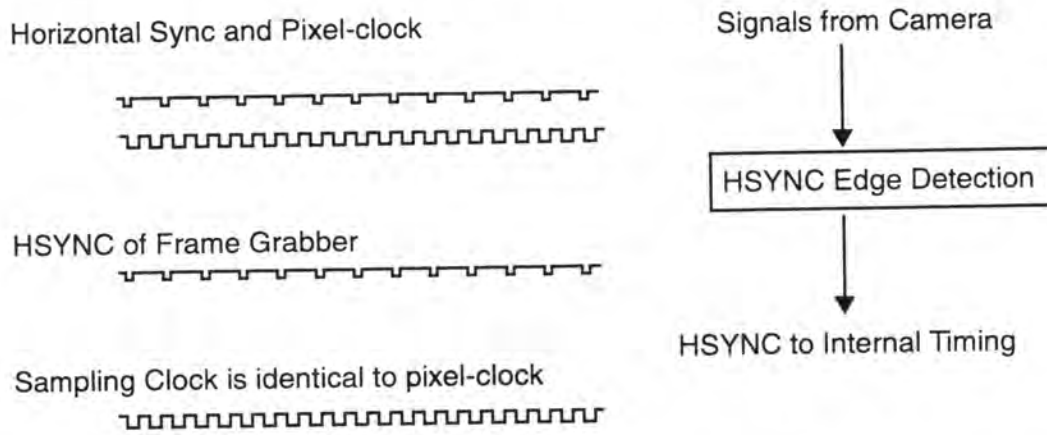


Figure 3.22 Signals and their flow in pixel-synchronous frame grabbing.

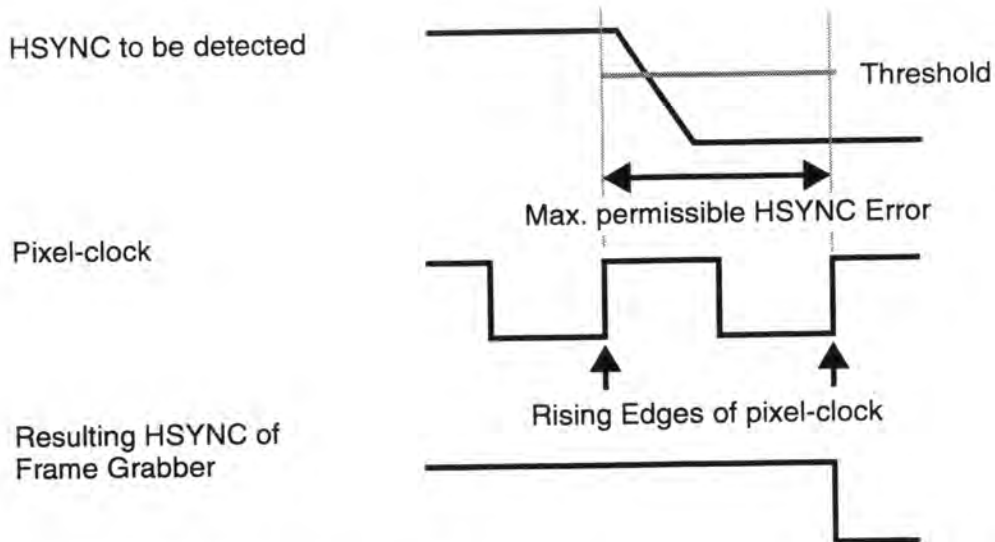


Figure 3.23 HSYNC detection by edge detector.

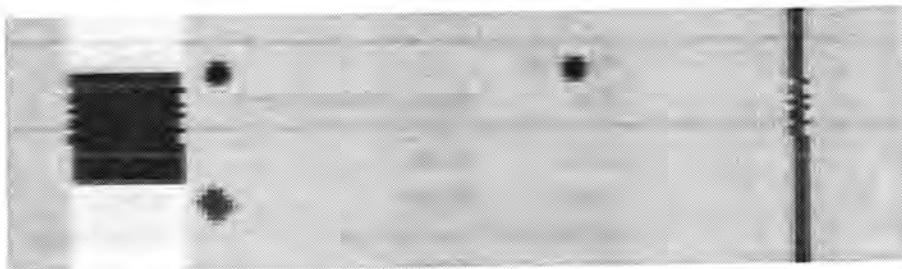


Figure 3.24 Image showing line-displacement for some lines.

The use of a pixel-clock for synchronization and ADC results in a stable geometry, elimination of line-jitter and a one-to-one mapping of sensor elements to pixels (pixels refer to the data stored in the memory). Figure 3.25 depicts the characteristics of pixel-synchronous frame grabbing:

- no (subpixel) line-jitter
- the sampling clock is identical to the sensor clock
- the sensor is mapped one-to-one to the image memory

The sampling precision is now completely determined by the quality of the pixel-clock signal and the ADC timing characteristics.

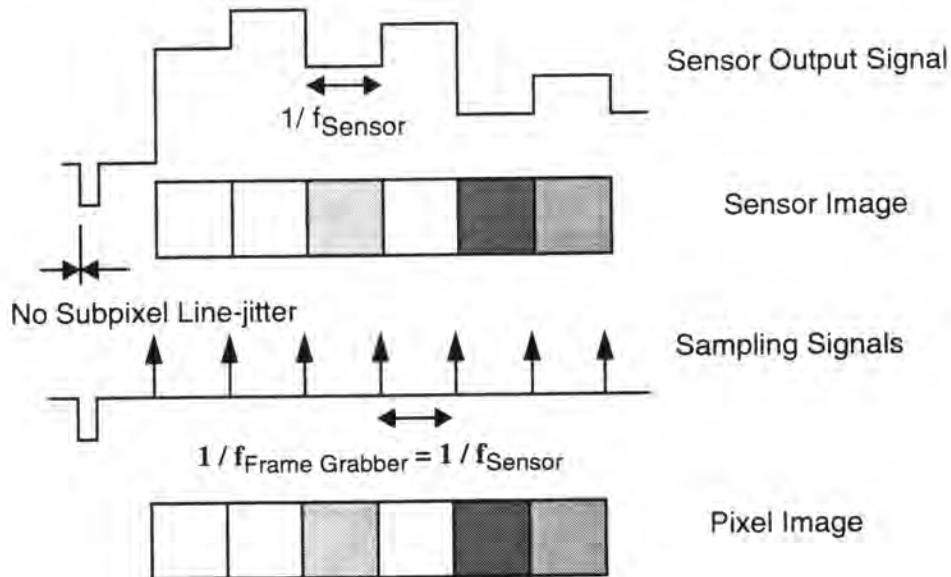


Figure 3.25 Characteristics of pixel-synchronous frame grabbing.

3.7 Analog versus Digital Transmission

Table 3.2 compares the various signal transmission and synchronization methods. It shows that a large difference exists between analog transmission without a pixel-clock and the other two techniques, PLL line-synchronization and digital transmission. The major difference between pixel-synchronous sampling in the camera with digital transmission versus pixel-synchronous sampling in the frame grabber is the elimination of noise during transmission. The separation of the digital camera makes it easier to eliminate influences of other devices such as the computer and its power supply. The current higher cost of digital cameras will soon be outweighed by their additional performance and the onset of using ADC in consumer electronics cameras.

Effect	Analog		Digital
	PLL	pixel-synchronous	
Line-jitter	> 0.1	none	none
Noise	larger	lower	lowest
Mapping	undefined	one-to-one	one-to-one
Cost	low	low	higher
Standard	yes	plus pixel-clock	partial
Transmission	simple	simple	difficult over long distances for high frequencies

Table 3.2 Comparison of signal transmission methods

3.8 Data Buffering

The task of data buffering is to provide a means to input the data from the ADC with one frequency and to read it out with another. Devices using a fixed master clock for the ADC can eliminate the data buffering as the sampling clock and the read-out clock can be identical. Frame grabbers allowing for a different sampling clock speed than data read-out use one of the following three methods for data buffering:

- dual ported memory
- memory double buffering
- first-in, first-out

A **dual ported memory** provides simultaneous read and write access capability. Dual ported memory must provide for arbitration between external read access and writing into it from the ADC, with latter requiring priority (Heinrich et al., 1986). **Double buffering** has the advantage that no bus contention and arbitration problems can occur (Raynor et al., 1990). This technique works in an identical fashion to double buffering in computer graphic workstations. One part of the memory is used to write to while the other can be read. The drawback of double buffering is the reduction in memory available for one of the two tasks if both read and write must be performed concurrently. The use of a **first-in first-out (FIFO)** is a very simple and efficient means. The data is written into the FIFO at the sampling clock frequency and read-out at a speed as required by the system. FIFOs are typically used in frame grabbers without image memory.

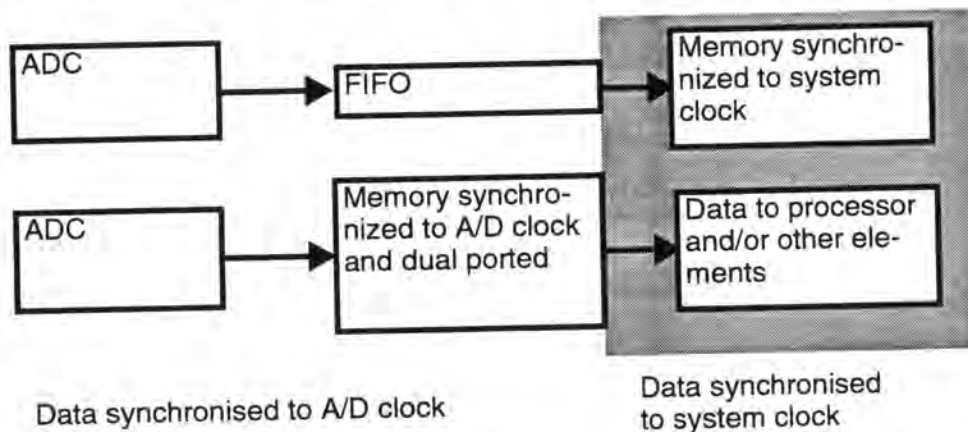


Figure 3.26 Frame Grabber: Data Synchronisation and Buffering

3.9 Analog-to-Digital Conversion

The analog-to-digital conversion by the **analog-to-digital converter (ADC)** must be evaluated with respect to the precision of timing and adding of noise due to several non-ideal characteristics.

There are several methods for the analog-to-digital conversion (Horowitz and Hill, 1982). The high conversion rate required in video applications makes the **parallel or flash analog-to-digital** conversion the most widely used principle. The first commercial flash ADC was introduced by TRW in 1977 (the TRW TDC 1007). Today the conversion rate of ADCs reaches up to 400 MHz for 8 bit ADCs (Akazawa et al., 1987; Yoshi et al., 1987). Frame grabbers use typically 8-bit ADCs with frequencies up to 20-30 MHz (e.g.

Datacube, 1988). Special frame grabbers achieve up to 40 MHz for 8-bit ADCs and 20 MHz for 10 bit ADCs (*Raynor and Seitz, 1990*).

The flash ADC consists of an array of $2n - 1$ comparator stages to produce an n -bit result. Figure 3.27 shows a schematic representation of a typical flash ADC. Inputs to the converter are reference voltages, the video signal to be sampled, and a sampling clock. Reference voltages, at least a lower and an upper, are used to determine the upper and lower limit of the input range. They are used to create the reference voltages for all comparators by appropriate subdivision techniques. Each comparator has an input for the reference voltage and the signal to be sampled. When the sampling clock indicates the time of conversion the result of the comparison is read-out. This indicates whether or not the signal was higher than the reference voltage at this comparator. The result is represented in a so called "thermometer" or "gray" code. The advantage of the gray code is that with continuously increasing voltage there is always only one value changing at each step. The conversion from gray code to binary code is performed by one or more encoding stages.

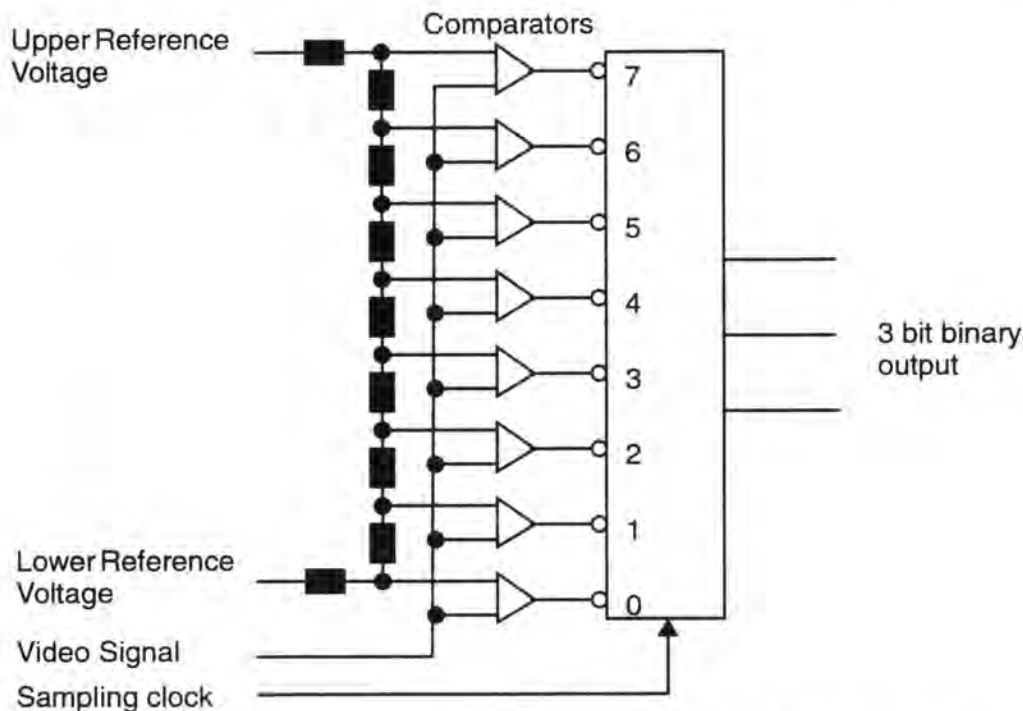


Figure 3.27 Schematic diagram of a 3-bit flash analog-to-digital converter.

The timing relation between the video signal and the sampling clock must be variable if there is a specific period when the video signal should be sampled. With the existence of high frequency cross-talk from the sensor clock or other source the sampling should be performed at time periods not influenced by these. The signal can possibly also vary periodically for each pixel period. These effects require the possibility to adjust the phase relation between the sampling clock and the sampling point on the analog signal. This only makes sense, of course, when pixel-synchronous frame grabbing is used. The next figure shows a diagram of a frame grabber with adjustment possibilities of the sampling clock timing. The inversion of the sampling clock provides for a displacement of half the sampling clock period and the delay element for finer delays.

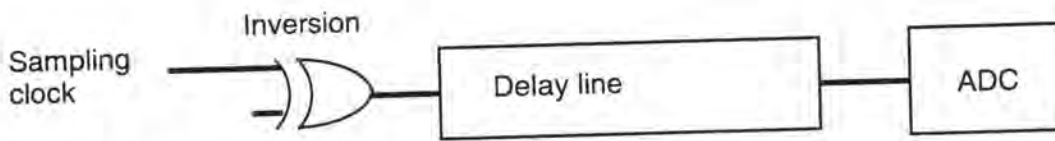


Figure 3.28 Timing adjustment of sampling clock.

The timing within the ADC is another problem. High speed ADCs require that the same signal is available at all comparators with nanosecond precision. The difficulty in delivering the signals at the same time and the timing imprecision of the comparators produces comparator jitter. The result is a displacement of the sampling point and/or an increase in noise, depending on the perspective of the analysis.

There exist a multitude of parameters that can be used to describe the performance of an ADC. Only a few definitions shall be given, further details can for example be found in *Burr-Brown, 1989*.

The **resolution** (n) of an ADC is the number of bits of the output signal resulting in 2^n digital values to represent the analog input signal. The **quantization noise** of an ADC can be assumed to be identical to rounding effects. This gives a quantization noise power of $1/12^{\text{th}}$ of the quantization step. The **signal-to-noise ratio** of an ADC from quantization noise only is given by:

$$\text{SNR} = 20 \log \frac{2^n}{\sqrt{1/12}} \approx 20 \log 2^n + 11 \text{ [dB]} \tag{7.1}$$

with:

n number of bits of ADC

Burr, Brown, 1989, defines the signal-to-noise ratio as:

$$\text{SNR}_{\text{BB}} = 10 \log \frac{\text{sinewave signal power}}{\text{output noise power}} \tag{7.2}$$

which results for an ideal ADC in:

$$\text{SNR}_{\text{BB}} = 6.02 \times n + 1.76 \tag{7.3}$$

Table 3.3 gives the number of values and the SNR for some resolutions of ADCs.

Resolution [bit]	Number of values	SNR [dB]	SNR _{BB} [dB]
6	64	47	38
8	256	59	50
10	1024	71	62
12	4096	83	74

Table 3.3 SNR and resolution of ADCs.

The SNR is usually given as peak signal over RMS noise or RMS signal over RMS noise, resulting in completely different ratios. The SNR depends on the frequency of the input signal. The figure below gives a plot of SNR versus speed for a high speed ADC. It shows the strong decrease of the effective SNR for higher frequencies.

The **linearity error (integral linearity error)** is measured as the deviation of the analog input values from a line fit and is expressed as a percentage of the full scale range. The **differential linearity error** is the deviation of an ADC step width from the ideal step width of 1 LSB (least significant bit). A differential linearity error of larger than 1 LSB results in a **missing code**, which means that one of the 2^n values will not occur.

The **number of effective bits** is the number of bits corresponding to the measured SNR of the ADC by solving equation (7.1) for the number of bits:

$$n = \frac{(\text{SNR}) / 20 + \log \sqrt{1/12}}{\log 2} \quad (7.4)$$

Problems of power supply, grounding, timing imprecisions, and other degrading influences are addressed in *Raynor and Seitz, 1990; Burr-Brown, 1989*.

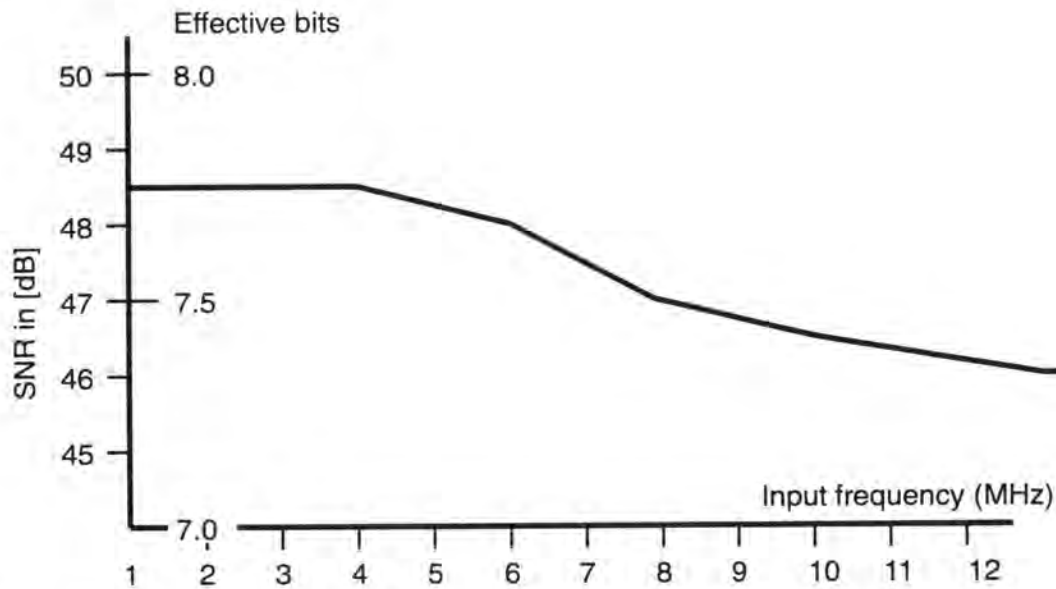


Figure 3.29 Dependence of SNR on input frequency of the analog signal of an 8-bit MHz ADC (after *van de Grift and van de Veen, 1987*).

4 EVALUATION OF THE FRAME GRABBER PERFORMANCE

The performance of the frame grabber is very important when using analog signals for signal transmission. Most of the performance parameters indicated by manufacturers are either insufficient or not representative for the signals and frequencies used. A number of tests were performed to investigate the characteristics of components and performance parameters of frame grabbers. The tests were performed in an order as not to change parameters of tests performed in an earlier step. The following tests were performed:

- Adjustment of frame grabber offset and gain
- Testing of the DC-restoration
- Analysis of noise
- Linearity
- Impulse response and MTF
- Synchronization

4.1 Test Setup

A Tektronix TSG-271 video waveform generator with a 12 bit DA converter was used for the performance evaluation of the frame grabbers. Two types of configurations were employed (see also Figure 4.1):

- In the first configuration the frame grabber is directly connected to the waveform generator. This is the standard configuration used for all frame grabber setups not requiring a pixel-clock.
- In the second configuration the frame grabber receives a pixel-clock signal directly from a camera, whereas the composite video is passed from the camera to the waveform generator, which synchronizes to it. The synchronisation quality is determined by the synchronisation precision of the frame grabber. The jitter for the monochrome signal of the TSG-271 is specified to be smaller than 2 nsec (a digital PLL is used).

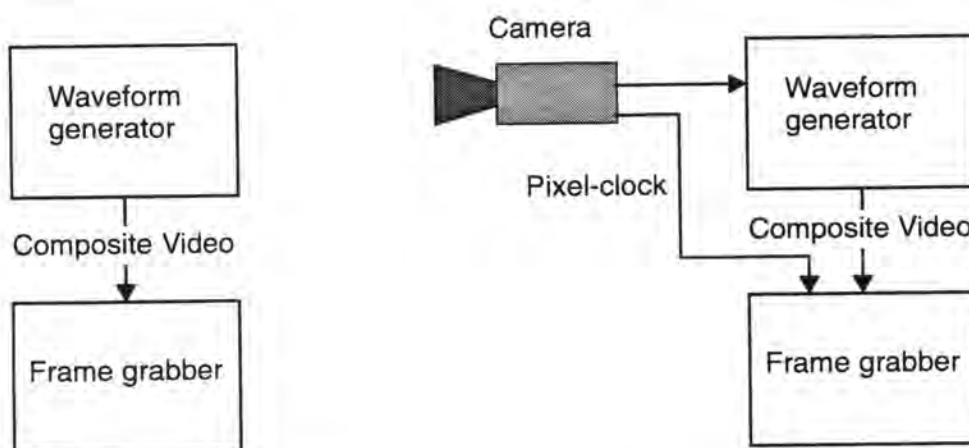


Figure 4.1 Test configurations for testing of frame grabber. On the left side for grabbing with PLL linesynchronisation using composite video from the waveform generator only. On the right the camera is generating the timing and the waveform generator syncs up to the camera signals.

The AD conversion of the second configuration is not pixel-synchronous. It will be shown at the end of this chapter that the performance of the digital PLL in the waveform generator is excellent and the synchronization errors can be neglected for most analyses. The tests are nevertheless designed to eliminate effects of synchronization on the results. Table 4.1 gives the different configurations used for the evaluation. Three different sampling frequencies are used for the performance evaluation.

Configuration	Sampling Speed [MHz]	Synchronization
xc77_ccir	10.4	PLL line-synchr.
hr480_cv	11.25	PLL line-synchr.
xc77_cv	~14.1875	PLL line-synchr.
xc77_cvp	14.1875	Pixel-synchronous

Table 4.1 Frame grabber configurations used for the testing.

4.2 Offset and Gain Adjustment

The video signal is defined to be between 0 and 700 mV, 0 representing black and 700 mV white. It is necessary to adjust the offset and gain such that the 700 mV range is well within the 256 grayvalues generated by the ADC in order to assure that no clipping occurs, e.g. for the determination of temporal noise at 0 and 700 mV. The MAX-SCANs were set such that the range of grayvalues was approximately 20 to 240, with one grayvalue corresponding to a voltage difference of 3.2 mV.

4.3 DC-Restoration

Several issues connected to the analog front end of the frame grabber are collected under this title. The analog front end of the MAX-SCAN frame grabber provides for several adjustments which influence the DC-restoration. They are:

- Impedance of the input (to be set with a jumper)
- AC-coupling or DC-coupling (to be set with jumpers)
- Use of clamping pulse from hardware or via the horizontal look up tables (software switch)
- Hardware clamping pulse derived from the negative or positive going edge (to be selected with a jumper)

The input impedance for the video signal is set to 75 Ohm as specified for the signal. Two techniques are used to determine the best settings for the other elements:

- The derivation of the clamping pulse on “wrong” positions resulting in uneven brightness over the image in the vertical direction is most easily verified with a linear ramp and a look-up-table showing certain transitions, such as the LSB. If the brightness varies from line to line, the vertical stripes of the LSB transitions bend at the top of the image. This is a qualitative quick check useful for adjustment of the frame grabber.
- The second technique uses flat input images and checks the uniformity within the frame and from field to field.

Both AC-coupling and DC-coupling with all other combinations and several length of the software derived clamping pulses are tested. The figure below shows the typical er-



Figure 4.2 Cross-section through first 200 lines of an image showing typical errors with wrong DC-restoration.

rors which occur with imperfect DC-restoration. It shows a vertical profile through an image. The lines at the top of the image are approximately 4 grayvalues brighter than the average, which is 154.4 DN (Digital Number). It takes approximately 100 lines before the normal level is attained. There is also a significant difference between the average grayvalue of the first and second field. The error comes from the use of an improper DC-restoration level during the broadcast pulses and is explained in more detail in section 5.1.3. It must be concluded that the DC-restoration circuit is very slow to re-adapt to a different level with sufficient precision and great care must be taken to use proper derivation of the clamping pulse for the DC-restoration.

The MAX-SCAN uses the DC-restoration mechanism shown in Figure 3.15 with a sample-and-hold. The stability of the DC-restoration (the "holding" of the sample-and-hold) is verified with a uniform image of medium intensity (350mV). A profile through a line of such an image is shown in Figure 4.3. It is evident that the average grayvalue increases from the left to the right within the line. This can be interpreted as a decrease of the DC-restoration signal which is subtracted from the video signal. The difference between left and right is in the order of 0.5 DN, corresponding to ~ 1.6 mV. This decrease occurs within approximately 52 msec. Cameras with longer line times than the standard video signal will incur an even larger decrease of the restoration signal. This effect can also be seen in the averaged frames shown in Figure 4.5, where the brightness of the dark band in the middle increases from left to right.

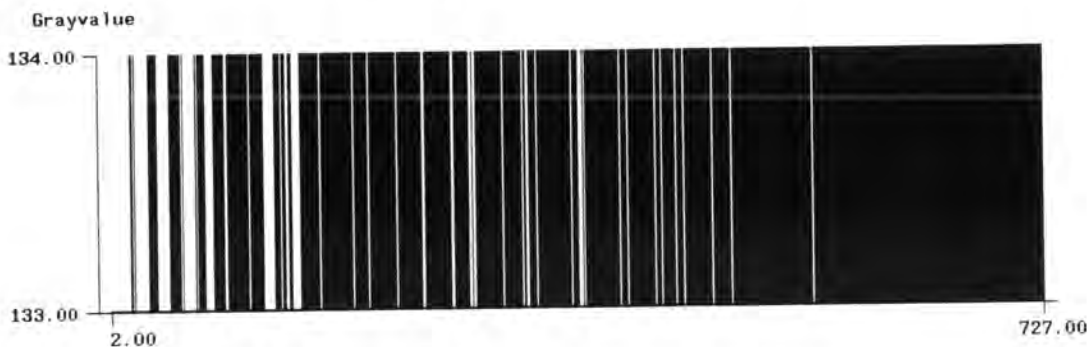


Figure 4.3 Image showing increase of average image intensity within x due to instability of sample-and-hold of DC-restoration circuit.

4.4 Noise

The noise performance of the frame grabber is analysed using images of uniform intensity. The TSG-271 provides for images of 0, 350, and 700 mV. The noise performance was evaluated with all sampling speeds and synchronization methods mentioned above.

Three methods are used in the subsequent analysis:

- Method 1: The standard deviation is determined from the grayvalues of the pixels of a frame or a subarea thereof.
- Method 2: The standard deviation of individual pixels is determined from several frames in a first step. The RMS of these standard deviations over a region or the complete frame is used to characterise the temporal noise.
- Method 3: The standard deviation is computed from the grayvalues of the pixels in several frames.

Each of these methods and the insights into their performance are discussed below. Errors of synchronization can only have a minor influence as the signal to be sampled is flat. In order to eliminate border effects all statistics were computed using 512 by 512 subareas in the centre of the frame.

Method 1

Table 4.2 gives the statistics obtained from individual images of two series, each consisting of five frames which were taken consecutively. The time between the first and second series is approximately 1 minute. The averages within each of the two series vary only by 0.02 grayvalues, whereas the two series have a shift of 0.1 grayvalue. The average of the grayvalues of series vary by up to 3 grayvalues for a given input level over several days. This is not necessarily attributable to the frame grabber as the accuracy of the luminance amplitude is specified to be within 1% (probably of the range), corresponding to over two grayvalues. The variation of the standard deviations from series to series has been observed in many tests, i.e. the values for the second series is larger than for the first.

Assuming that the noise is random, it should decrease when averaging frames with the square root of the number of frames averaged (such statistics do not include a degradation which usually results as the average is stored in an eight bit image anyway). This is almost achieved for the first five images of the first series, but when including the images of the second series this cannot be achieved, already due to the shift between the averages of these frames as given in the table.

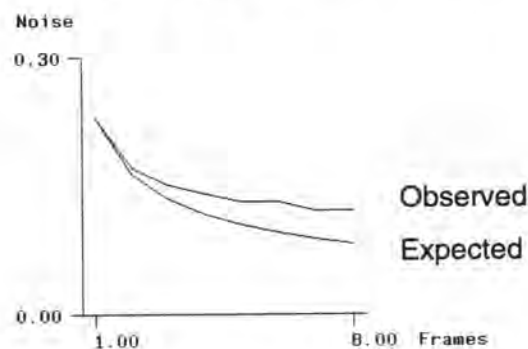


Figure 4.4 Expected and observed standard deviation of average for a consecutively increasing number of frames.

To eliminate long-term drifts the same procedure was performed with 8 images acquired consecutively, i.e. within 320 msec. The following figure shows a plot of the expected and actual standard deviation. It shows that even here a lower limit of approximately 0.1 grayvalue is achieved, and no further reduction by averaging can be obtained. Averaging of the frames in this test (the situation for imagery taken with cameras is different and is analyzed later) typically results in an improvement, but not according to the statistical expectations. This can be attributed to disturbances from other sources.

Frame	Series	A [DN]	σ [DN]	No	A ₂ [DN]	σ_2 [DN]	$\sigma_{2exp.}$ [DN]
1	1	134.05	0.22	1	134.05	0.22	-
2	1	134.04	0.22	2	134.04	0.17	0.16
3	1	134.03	0.20	3	134.04	0.14	0.13
4	1	134.02	0.17	4	134.04	0.11	0.11
5	1	134.03	0.18	5	134.03	0.10	0.10
6	2	133.91	0.29	6	134.01	0.10	0.09
7	2	133.90	0.30	7	134.00	0.10	0.08
8	2	133.91	0.29	8	133.99	0.10	0.08
9	2	133.90	0.31	9	133.98	0.11	0.07
10	2	133.90	0.31	10	133.97	0.11	0.07

Table 4.2 Statistics of frames from two series.

- A average of frame
 s standard deviation of frame
 No number of frames averaged
 A₂ average of averaged frame
 σ_2 standard deviation of averaged frame (when no rounding is used!)
 $\sigma_{2exp.}$ expected standard deviation

Method 2

The second analysis method uses the information gained by analyzing the statistics of individual pixels over time. These are to some degree immune to the patterns observed above, but as one can see from the noise image in Figure 4.5 the noise level is related to the changes in brightness in the averaged image. The RMS values of the temporal noise components of several tests determined with the various synchronization methods and sampling speeds are compiled in Table 4.3.

Setup and sampling speed	0 mV [DN]	350 mV [DN]	700 mV input signal level [DN]
xc77_ccir, 10.4 MHz	0.17	0.22	0.40
hr480_cv, 11.25 MHz	0.31	0.31	0.33
xc77_cv, 14.1875 MHz	0.17	0.28	0.29
xc77_cvp, 14.1875 MHz	0.33	0.29	0.37

Table 4.3 RMS values for the temporal noise for different sampling speeds, synchronization methods and input signal levels.

The root mean square error is computed from the standard deviations of each pixel, which was in turn determined by frame averaging. Comparing the results to the theoretical performance limit of an ADC, which would correspond to a standard deviation of 0.29 grayvalues, shows that the results for several tests are better than the theoretical limit. The worst case represents a peak signal-to-noise ratio of 56dB, with a theoretical limit of 58.9dB. The largest maximum temporal noise is 1.2 grayvalues. If larger temporal noise components occur, there is usually some malfunction of the board or its setup.

Interestingly there is no clear dependence of the noise level on the sampling speed. This is attributable to the fact that the imagery is flat. The decrease in SNR of ADCs is a function of the input signal frequency and not the sampling frequency (at least not for the range of sampling frequencies used here).

Method 3

As the input signal is flat, one can also compute the standard deviation for a pixels grayvalue over all pixels in a series of frames. This includes the temporal characteristics and uniformity over the frames. The worst values of all tests corresponds to a peak SNR of 54.4 dB.

Systematic Patterns

The images and the averaged images exhibit patterns which are very similar for all images taken with one particular frame grabber. Figure 4.5 shows some typical imagery taken with the setup using the pixel-clock from the XC77 camera. The top image is one of the frames thresholded to visualize the patterns. The horizontal running large bands which vary in brightness are evident. These bands are several hundred pixels wide and stationary in time. On the lower portion of the image "phase patterns" running at approximately an 45 degree angle are visible. The next image is the average of five frames, thresholded at the average image intensity. Again the bands are visible. It is also evident that the dark bands tend to get brighter to the right side of the image, which is in accordance with the conclusions drawn for the effects of DC-restoration. The bottom image depicts the temporal noise determined during the averaging of the five frames. Bright areas mean that the temporal noise in this region is higher. Interesting is the relation between the noise level and the darker and brighter regions in the averaged image. The phase patterns are still visible in the averaged image and the noise image. This is not always the case though, depending on the synchronization method. The bands could be humming between the 50 Hz power supply and the imagery. The phase patterns have a period of 25 pixel when digitizing at 14.2 MHz. The origin of the "phase patterns" is analyzed in more detail in connection with the XC77 camera in section 5.1. Both effects - the bands and the "phase pattern" - are very small as the peak-to-peak differences in the imagery are less than 4 grayvalues, corresponding to 13 mV or 1.8% of the effective range.

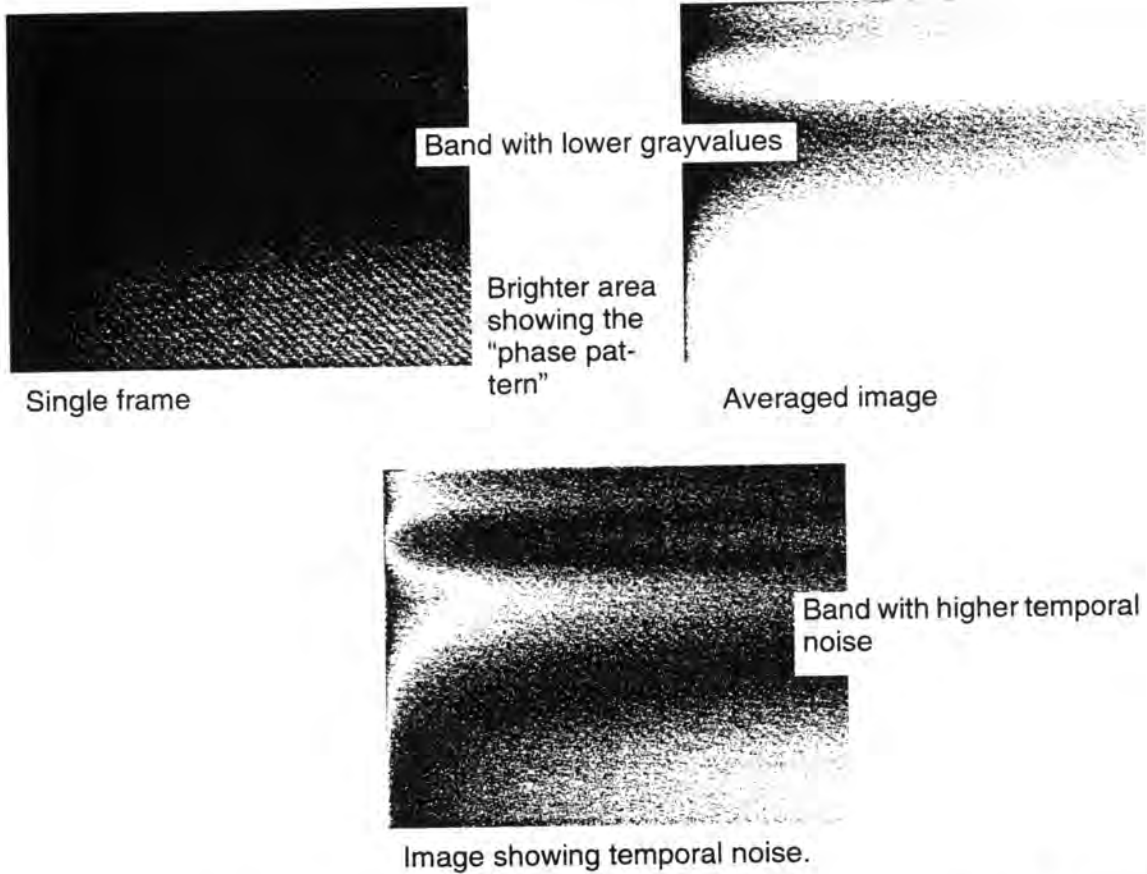


Figure 4.5 Single and average frame and image containing the temporal noise showing typical patterns.

Noise and Signal Level

The temporal noise of the frame grabber, i.e. of the analog-to-digital converter, should be independent of signal level. The statistics of Table 4.3 do indicate an increase of temporal noise with signal level. An eventual dependence of the temporal noise on the input signal level was verified using five linear ramp images with the xc77_cvp configuration (see section 4.5 for an example image). These were averaged and the temporal noise multiplied by 10 for each pixel was stored in another frame. Figure 4.6 shows the histogram of such a frame with a fitted line and the residuals. The increase of temporal noise

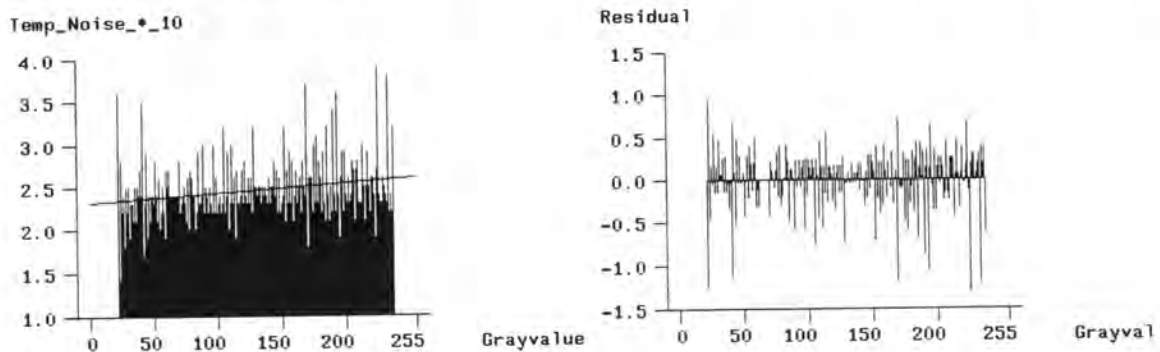


Figure 4.6 Plot of temporal noise versus grayvalue and residuals as determined from linear ramp images.

from grayvalue 20 to 240 would be 0.03 DN. The increase for the corresponding synchronization method in Table 4.3 is 0.04 DN. This increase is not noteworthy with respect to the level of other influences such as the systematic patterns. The origin of the large increase for the other synchronization methods evident from Table 4.3 cannot be explained.

4.5 Linearity

Linearity and related parameters of the ADC and frame grabber are determined using a linear ramp going from 0 mV to 700 mV. The results given here are for the "xc77_cvp" configuration and one frame grabber only. They are representative for all setups and both frame grabbers tested.

The first test is to fit a line to the ramp for one line of the image. The results of the fit are compiled in Table 4.4 and a plot of the residuals of the fit is shown in Figure 4.7. It shows a strong deviation from linearity. The maximum integral non-linearity reaches 3.6 DN corresponding to 11.5 mV or 1.6% of full range. This large integral non-linearity can stem from both amplifiers and the ADC.

Specification	Value in [DN]	dB of range
Standard deviation of fit	1.18 (1.18)	47
Maximum integral nonlinearity	3.8 (3.7)	37
Maximum differential nonlinearity	1.5 (0.53)	

Table 4.4 Results of analysis of linearity for one line of an individual frame and from the average of five frames in brackets (actual range is 212 and 207).

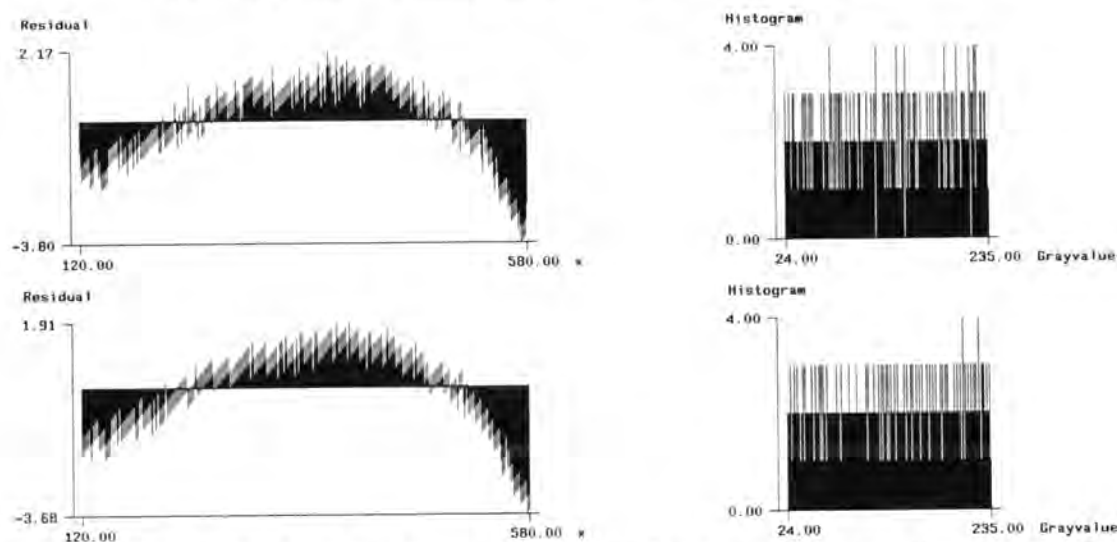


Figure 4.7 Residuals of line fit to ramp data and histograms for one line of an individual frame (top) and an average of five frames (bottom).

The large maximum integral non-linearity is also evident from the results of the noise analysis. The average grayvalue for the image with 350mV input signal deviates by approximately 4 grayvalues from the average of the 0 and 700mV results. This is in accordance with the results obtained here. The deviation of the midpoint corresponds to approximately 12.8 mV. The linearity of the waveform generator is indicated to be small-

er than 1%. Such a large integral non-linearity is typical for many frame grabbers (Raynor, 1989).

The maximum differential non-linearity of 1.5 DN for the individual line would indicate missing codes. This is also evident from the histogram for this line shown in Figure 4.7 on the top right side. Actually there are 3 grayvalues missing. To verify whether or not this is an actual malfunction or a statistical effect a histogram over 512 lines was taken. It is shown in the following figure and no missing codes could be detected.

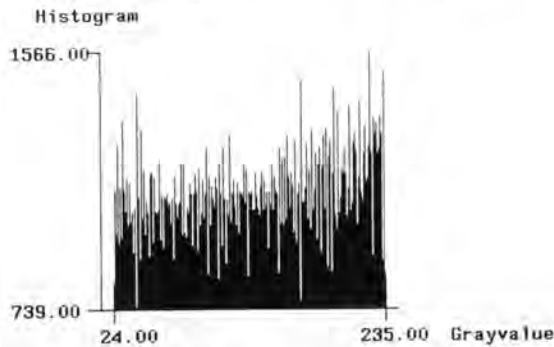


Figure 4.8 Residuals of a histogram taken over 512 lines from one frame to show the inexistence of missing codes.

In a further test five frames are averaged and again one line is used to determine linearity. The results of the analysis are given in Table 4.4 in brackets. There is almost no improvement for the integral linearity. The differential non-linearity is nevertheless reduced to 0.53, indicating that there are no missing codes as is also evident from the histogram of this line shown in Figure 4.7 on the bottom right.

4.6 MTF of Frame Grabber

The MTF of the frame grabber can be determined with and without the low-pass filter (LPF) in the analog input section and with different sampling speeds. The influence of the following parameters is tested:

- influence of the LPF in the analog section on the impulse response and the MTF
- influence of the sampling speed on the MTF.

The impulse response and MTF are analysed with three different images:

- The impulse response is verified using the image shown in Figure 4.9 a. It contains a vertical line with a rise and fall time of 200 nsec. The peak is at 700 mV with the background at 0 mV. The bright area is at a level of 700 mV.
- The MTF is determined using a "line sweep" image shown in Figure 4.10 which contains sine waves of increasing frequency and marks indicating some frequencies.
- The "multiburst" image also shown in Figure 4.11 contains dark and bright vertical bars indicating the peaks for the areas of sine waves with different frequencies.

4.6.1 Impulse Response

The analog front end of the MAX-SCAN provides the possibility to select a 4 MHz low-pass filter. Figure 4.9 shows on the left imagery and profiles. On the left (a) for images grabbed without the LPF using the xc77_cvp configuration and on the right (b) with the

LPF using the xc77_cv configuration. The dark background is 0 mV and the bright line

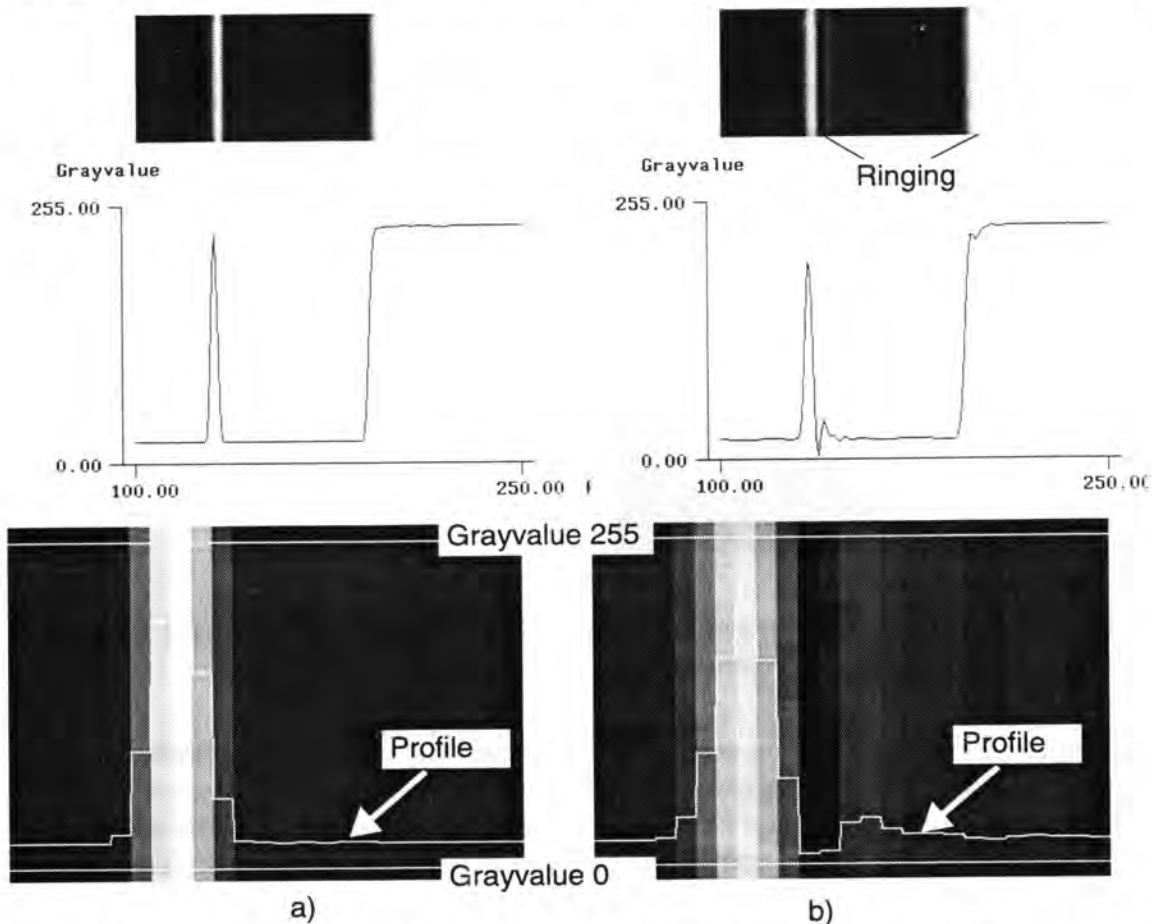


Figure 4.9 Impulse response without a) and with b) a LPF in the input. The asymmetric response and the ringing are visible from the images and profiles for the version with LPF.

as well as the area are at 700 mV. The signal rise and fall time is in the order of 200 nsec.

The middle figures show a cross-section corresponding to the top images, and on the bottom a zoom of the vertical line with profiles are shown. All pictures show that without the LPF the impulse response is very symmetric and no ringing can be detected. The imagery and profiles representing the situation with the LPF indicate the strong asymmetric response and ringing effects. The LPF is designed for typical video applications with a sampling rate of approximately 10 MHz and is thus not tuned to be used with a sampling rate of above 14 MHz. These effects lead to a significant degradation and the LPF is therefore not to be used.

4.6.2 Determination and Analysis of the MTF

The Modulation Transfer Function (MTF), actually only a “working” MTF as not all prerequisites are met, of the frame grabber was nevertheless analyzed both with and without the LPF. Figure 4.10 shows parts of images and cross-sections through frames taken with and without LPF of the line sweep imagery. The enclosing curves of the plots of the residuals of a line fit through the profiles correspond to the MTF. They show that the decrease without the LPF is very small as compared to the reduction with the LPF. In this latter case, the MTF starts to be sharply reduced at 3 MHz and is reduced to 22% at

4 MHz. There is also a strange decrease apparent in the region between one and two MHz which cannot be attributed to a phase shift between signal and sampling locations. This decrease is also apparent in the plots of the MTF in Figure 4.12.

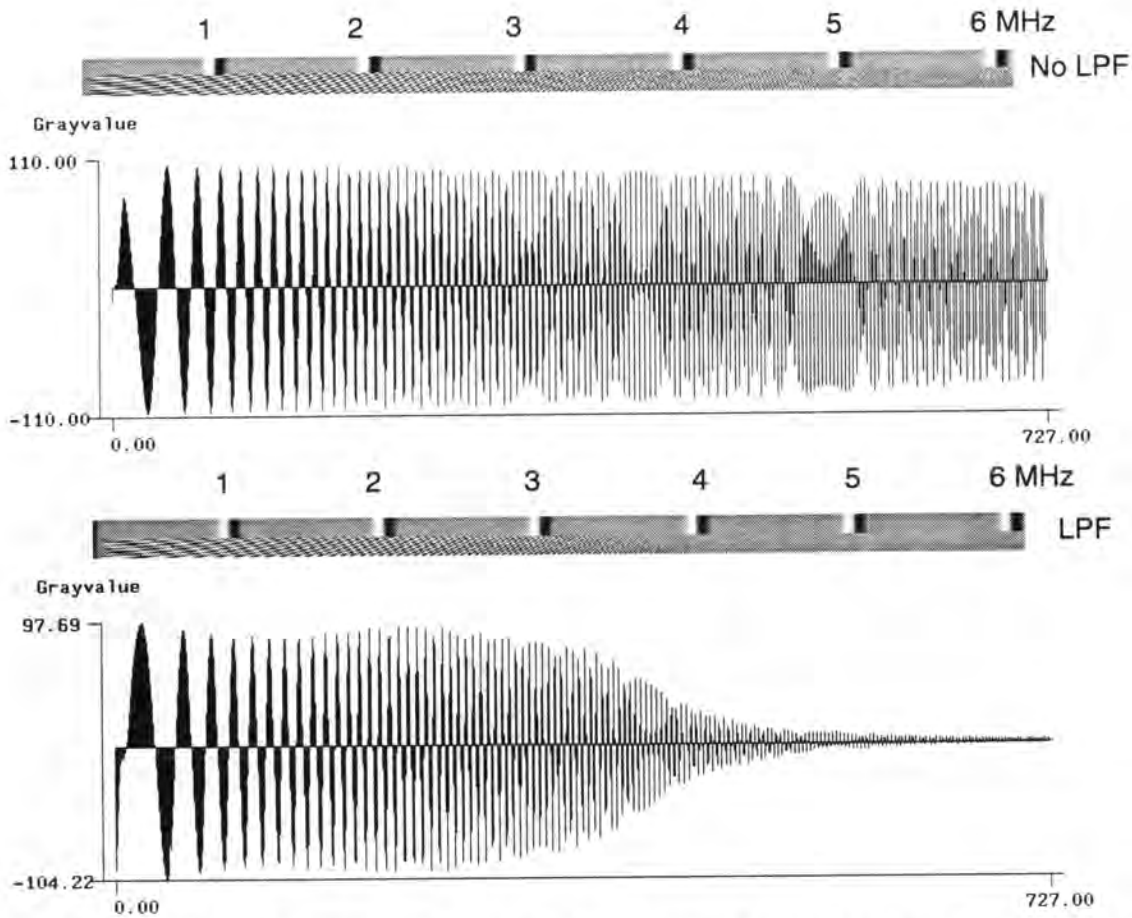


Figure 4.10 Parts of imagery and profiles of line sweep images without (top) and with (bottom) the LPF in the input.

The MTF of the frame grabber was furthermore determined using the multiband imagery containing a sine wave input signal with different frequencies as shown in Figure 4.11 a. One could also use the imagery shown in Figure 4.10, but the line fit using several periods with an identical frequency provide for better accuracy than the ones with varying frequency as those of the line sweep. The image was sampled using the pixel-clock from the camera, which is 14.1875 MHz. The image contains uniform bright and dark vertical bands indicating the peak values of the following sine waves of increasing frequencies (see Figure 4.11).

Figure 4.11 b shows an enlargement of the 0.5 MHz band with the profile and a plot of the sine wave fitted with a least squares adjustment. The results of the fits, which were performed for each band, are compiled in table Table 4.5. It gives the input pattern frequency in MHz, the frequency obtained from the least squares fit in pixels, the sampling frequency as computed from the input signal frequency, the determined pattern frequency in pixels, and the MTF. The results are given for a 10.4 MHz and 14.2 MHz sampling frequency. The sampling frequency is computed with:

$$F_{\text{sampling}} = \frac{F_{\text{input pattern}}}{F_{\text{in pixel}}} \quad (7.5)$$

with:

F_{sampling} sampling frequency

$F_{\text{input pattern}}$ frequency of the input pattern as specified by the waveform generator

$F_{\text{in pixel}}$ frequency from sine fit

The results show that the highest input frequency is already aliased for the 10.4 MHz sampling frequency.

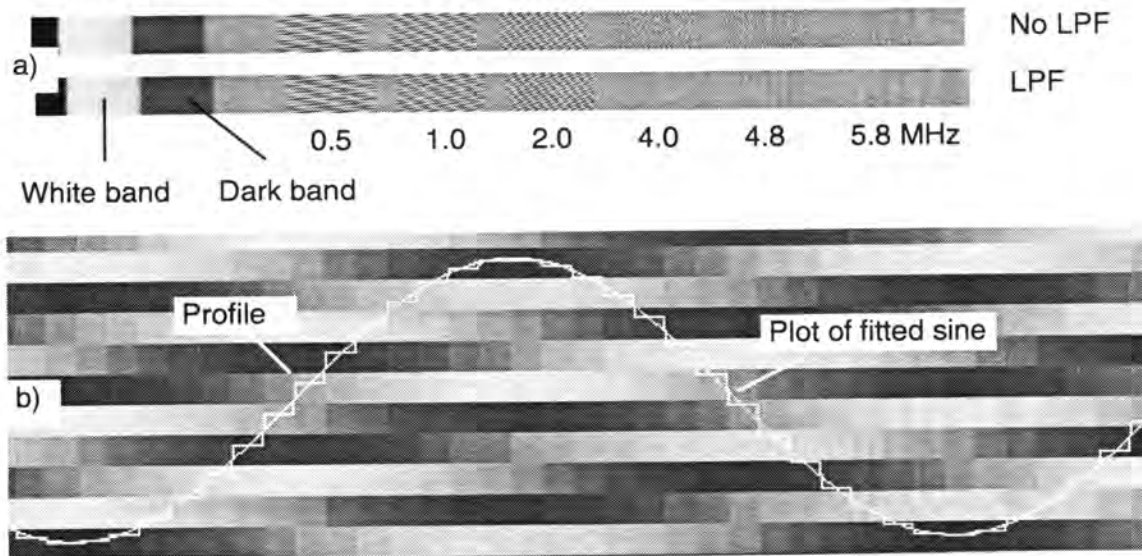


Figure 4.11 MTF determination of frame grabber.

- a) Images used to determine the MTF of the frame grabber. Top without LPF and on bottom with LPF in the input.
 b) Image showing profile and plot of fit for 0.5 MHz sine wave.

Patt. Freq.	10.4 MHz			14.1875 MHz		
	$F_{\text{input pattern}}$	F_{sampling}	MTF	$F_{\text{input pattern}}$	F_{sampling}	MTF
0.0	0.000		1.00	0.000		1.00
0.5	0.048	10.393	1.00	0.035	14.257	1.00
1.0	0.097	10.346	0.99	0.071	14.184	0.99
2.0	0.193	10.349	0.97	0.141	14.184	0.97
4.0	0.387	10.341	0.90	0.282	14.183	0.90
4.8	0.464	10.340	0.86	0.338	14.186	0.87
5.8	0.439	aliased	0.81	0.409	14.184	0.82
Average frequency		10.354 [MHz]			14.197 [MHz]	
σ of frequency		0.022			0.033	

Table 4.5 MTF determination of MAX-SCAN with multiburst images.

The second last row in the table indicates the average sampling speed, as computed by above formula, and the last row the standard deviation. It shows that the frequency of the input pattern can be determined to about 0.2%. The amplitude of the MTF has a standard

deviating of several tenths of a DN resulting in about 1 to 2% for the MTF. This is evident from the good correspondence of the MTF values determined with different sampling frequencies and configurations.

The reduction of the MTF without LPF is quite significant as can be seen in Figure 4.10. The input frequency of 5.8 MHz corresponds to 0.8 of the Nyquist frequency for the xc77_cv and xc77_cvp configurations, or about 36 lp/mm for the XC77 camera. The signal at the Nyquist frequency for the XC77 will therefore be even further degraded.

Figure 4.12 shows the results from the "multiburst" images with and without LPF on the

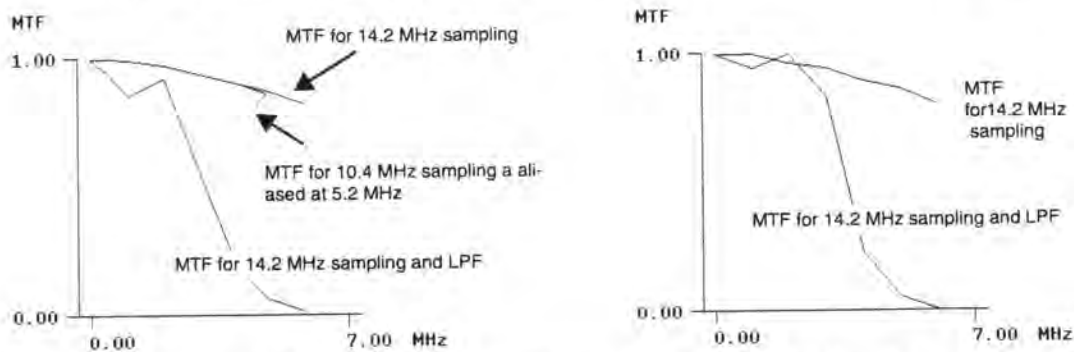


Figure 4.12 MTFs of MAX-SCAN frame grabber. Left from multiburst images, right from line sweep signals.

left. The two curves on top are the MTFs for the 10.4 and 14.2 MHz sampling frequencies. The aliasing occurring at the 10.4 MHz frequency for the input frequency of 5.8 MHz is also shown. The strong reduction of the MTF by the LPF is evident from the lower curve. The MTF for this shows a bizarre behavior at about 1 to 2 MHz signal frequency. On the right hand side the corresponding MTFs as determined from the "line sweep" images are plotted. The results correspond quite well for the case without LPF but differ somehow for the MTF curves with LPF filter.

The specification for the standard temperature range version of this ADC gives a bandwidth of 7 MHz (TRW, 1984). Assuming this specification corresponds to the 3 dB point, the results achieved surpass this specification.

The results show that the MTF is independent of the sampling frequency. The dependence on the input frequency requires compensation when using the frame grabber to determine the MTF of a sensor.

4.7 Synchronization

The performance of the synchronization is the determining factor of the geometric accuracy of the transmission. The following criteria are of interest:

- line-jitter from line to line
- displacement within frame
- stability of synchronization in time
- preservation of scale

The performance of the synchronization with respect to the first three effects is analyzed using the vertical line of the image shown in Figure 4.9. Template matching with a 9 by 1 artificial template is used to determine the position of the line in each row. The position of the line for all rows as well as the residuals from a line fit are plotted. This is per-

formed with the PLL synchronization for the `xc77_ccir` and `xc77_cv` setups, as well as for the pixel-synchronous setup `xc77_cvp`.

4.7.1 Synchronization with PLL

The first pair of graphs at the top of Figure 4.13 shows the plots of the line position and residuals (in pixel) for the “`xc77_ccir`” configuration. There is an apparent change in the position of the line up to about line 200. Thereafter the position becomes more or less stable. The results given in Table 4.6 indicate that this displacement is in the order of 0.2 to 0.4 pixel for the `xc77_ccir` and `xc77_cv` configurations respectively. The standard deviations for the respective setups are 0.06 and 0.08 pixel, whereas the largest residuals reach 0.2 and 0.3 pixel. These numbers might indicate that the synchronization for the `xc77_cv` setup is worse than for the `xc77_ccir`. When converting the respective values into their corresponding timing imprecisions in nanoseconds it can be shown that the opposite is the case for the standard deviations and the maximum residual. The absolute displacement from start to end of the frame is nevertheless larger for the `xc77_cv` setup. The slightly better values for the standard deviation and the largest residual of the `xc77_cv` setup are attributable to the 50% larger extend of the line signal as the sampling speeds differ by a factor of 1.5, when assuming that these errors are influenced by the precision of template matching.

The characteristics of line-jitter correspond very well to the theoretical expectations outlined in *Beyer, 1988 and 1989*, and to the observations made by *Beyer, 1987; Luhmann and Wester-Ebbinghaus, 1987; Heikkilä, 1988; Lenz, 1987; Lenz and Fritsch, 1988*. It is also very typical when comparing the absolute displacement with the schematic of the control current to the VCO shown in Figure 3.18. There is also a pair of bizarre large line-jitter apparent at row 200 for both configurations. They correspond with the region of the dark band in the imagery shown in Figure 4.5. It was nevertheless not possible to prove any connection between the average image brightness and line-jitter. The performance of the PLL is also in accordance to the performance specifications of the frame grabber.

The large displacement of the line from top to bottom can only be detected with this technique, when using a reference image in repeatability analysis (see chapter 6), and with the one using phase shift detection from the pixel-clock interference on the video signal used by *Lenz, 1987*. The magnitude of the displacement corresponds to the ones shown in *Lenz, 1987* as well as *Lenz and Fritsch, 1988*. The displacement must be attributed to a partial loss of the synchronization during the vertical blanking and/or to imprecise signals during that period. No definitive source for the disturbance could be localized as it is not possible to measure the start of the disturbance with the tools available. It is assumed that the equalization and broadcast pulses are the origin of these disturbances as the form of the signal changes during that time.

Whether or not line-jitter can be reduced by averaging was verified by averaging five consecutive frames and performing the same analysis as before. The results are also given in Table 4.6 and plots shown in Figure 4.13. It is apparent that the reduction of the standard deviation and the maximum errors occur, but it is only by a factor of 1.3 to 1.5. The absolute displacement from top to bottom of the frame remains unchanged. The displacement is analogous to the characteristics of a PLL during capture and locking shown in Figure 3.18. It cannot be modelled by a shear only as evident from the residuals shown in the figure on the right.

It can therefore be concluded that with PLL-synchronization line-jitter cannot be eliminated by averaging a small number of frames only. Averaging can suppress the random positional changes of individual lines in time but not systematic deformations such as the shear.

Synchronisation	Standard Deviation		Max. Residual		Displacement	
	[Pixel]	[nsec]	[Pixel]	[nsec]	[Pixel]	[nsec]
xc77_ccir	0.063	6.1	0.20	19.3	0.24	23.2
xc77_ccir, aver.	0.049	4.7	0.13	12.6	0.24	23.2
Improvement	1.3		1.5			
xc77_cv	0.083	5.8	0.26	18.3	0.41	28.9
xc77_cv, aver.	0.064	4.5	0.19	13.4	0.41	28.9
Improvement	1.3		1.4			
xc77_cvp	0.0039	0.35	0.011	0.77	0.001	0.07
xc77_cvp, aver.	0.0031	0.21	0.011	0.77	0.002	0.14
Improvement	1.6		1.00			
Impr. cv -> cvp		17 - 24		17 - 24		> 200

Table 4.6 Results of line-jitter analysis.

The results have not been separated into fields, therefore differences between neighbors are actually attributable to the stability of the PLL from field to field, i.e. over 20 msec. Actually the maximum changes in line position from one to the next line are in the same order as the overall maximum error.

4.7.2 Pixel-synchronous Sampling

The performance of pixel-synchronous sampling is tested with the xc77_cvp configuration. The results are in Table 4.6 and the plots in Figure 4.13 and Figure 4.13 at the bottom. The tremendous improvement is apparent from both. The standard deviation of the line fit and the largest residual are reduced by a factor of more than 17 to 0.003 and 0.011 pixel respectively. The displacement from top to bottom is virtually eliminated. The plots of the position and residuals show the improvement very drastically when taking into account the different scales for the positions and that the scale for the residuals for the xc77_cvp setup as by a factor of 30 larger than these for the others. Interestingly a certain wave pattern can be seen in both the position and residuals, especially for the results from the acquired image.

	Aver. Change [Pixel]	Max. Change [Pixel]	Average σ [Pixel]
One image	0.0025	0.0052	0.012
Average of five	0.0021	0.0051	0.011

Table 4.7 Statistics of template matching for the pixel-synchronous sampled images.

The results do surpass the specifications of the TSG-271 and it was found that the iteration criteria in template matching must be adapted to the situation. Table 4.7 gives the average and maximum change of the position for the least squares template matching (after typically 40 iterations) and the average of the standard deviations for the position

as obtained from the matching. These figures indicate that some limitations result from the template matching either as a function of noise and/or due to rounding errors introduced by the implementation of the matching during resampling and use of 8 bit deep images.

These results show three things:

- The PLL of the TSG-271 is excellent. Its errors must be smaller than those observed here.
- The precision of the template matching for the very small template is approximately 0.01 pixel.
- Pixel-synchronous sampling reduces synchronisation errors to below 0.005 pixel and eliminates any drifts in image position. Actually it is possible that the performance is even better, as the specification of the TSG-271 would already result in a larger displacement as obtained here.

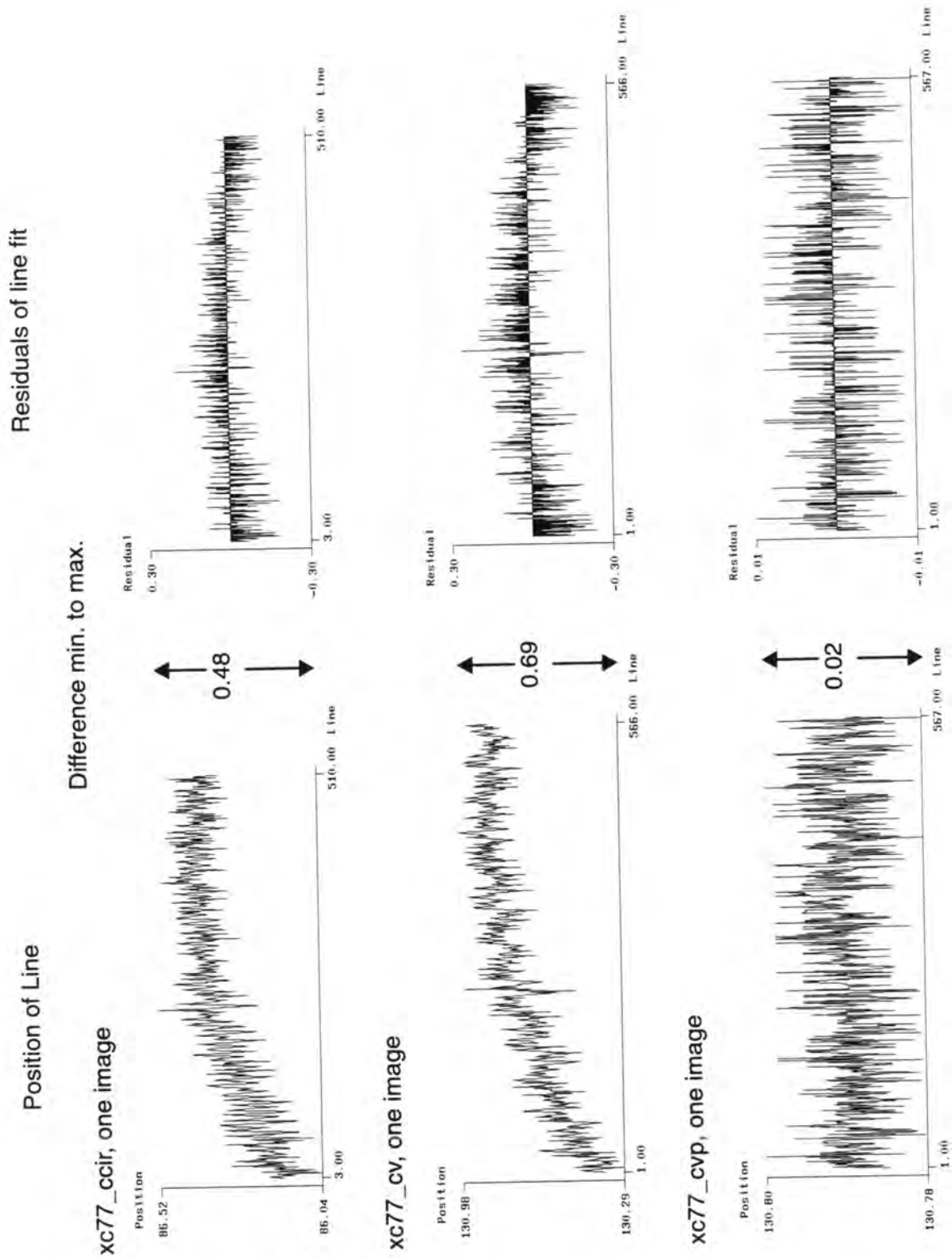


Figure 4.13 Line position and residuals of line fit for three different frame grabber configurations without averaging.

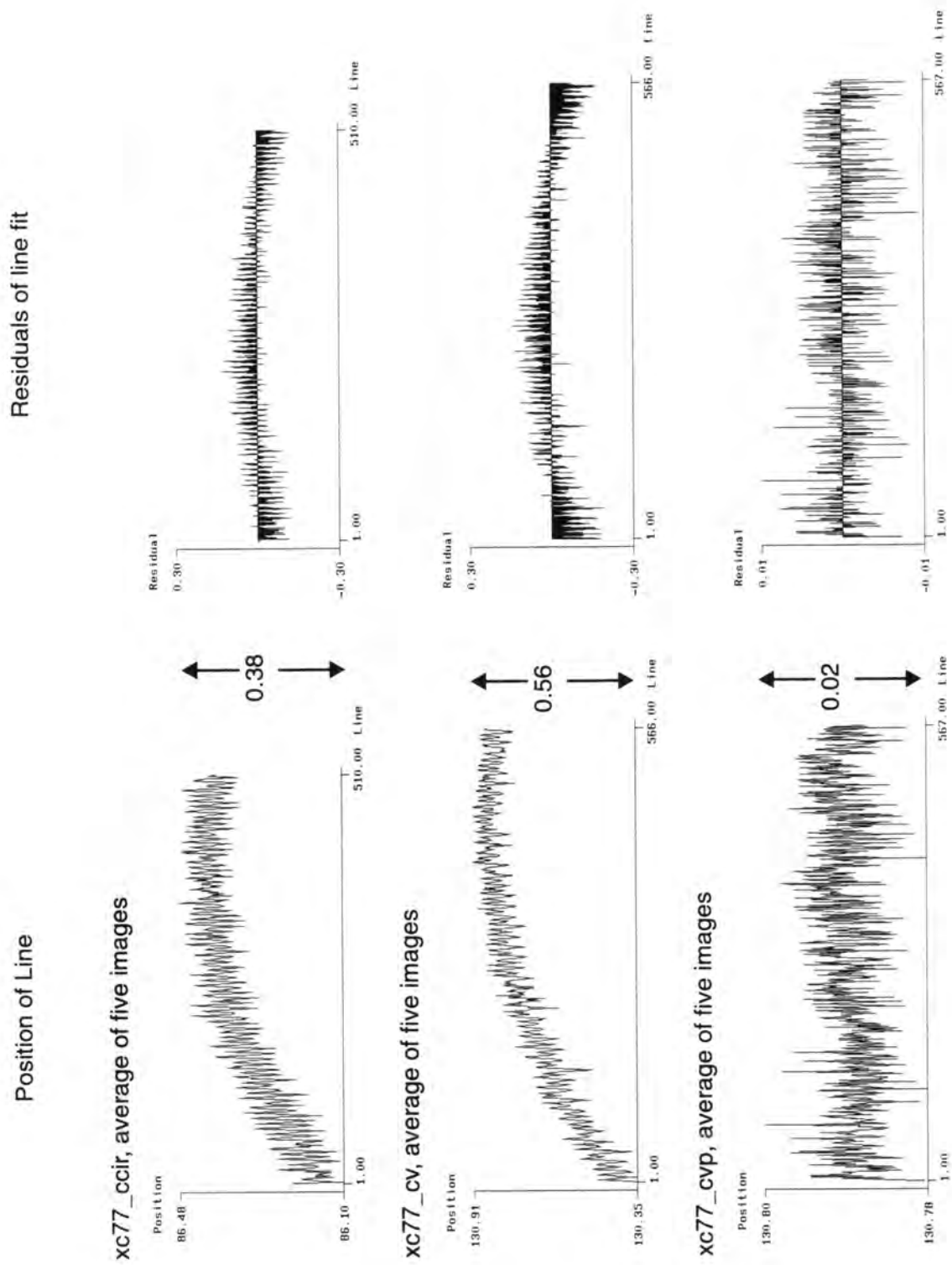


Figure 4.14 Line position and residuals of line fit for three different frame grabber configurations with averaging over five frames.

4.8 Conclusions of Chapter

The tests showed that wrong DC-restoration can lead to background non-uniformities inducing geometric deformations (see section 6.8 for the influence of intensity gradients on the localization of targets). The fall-off of the sample-and-hold mechanism used in many DC-restoration circuits leads to a uniform change of the background which can be disregarded due to several reasons. It is identical for all images, thus leading to identical displacement for all targets and thus in a shift of the principal point. The amount of fall-off across the size of typical targets is also clearly too small to have any noticeable effect.

The temporal noise characteristics of the frame grabber were shown to be close to the theoretical limit of the analog-to-digital converter. More problematic were systematic patterns due to origins which could not be pinpointed. They were assumed to originate from the host computer and other electronic components as they depend on the position of the frame grabber board in the chassis and on the board itself. The observed patterns lead to small displacements as their effect is similar to that of local illumination gradients analyzed in section 6.8. The displacements from the "phase pattern" are expected to be (pseudo) random when assuming that every object point is imaged on many locations which are affected in different direction and magnitude whereas the bands can lead to more systematic effects. The maximum influence reached several hundredths of the pixel spacing as can be judged when comparing the slopes to those of the local illumination gradients in section 6.8.

The integral non-linearity of the frame grabber must be considered when performing radiometric corrections and radiometric operations but are not of importance when considering the position of circular targets only. The impulse response and the modulation transfer function of the frame grabber, especially of the low-pass-filters which might not be adapted to the signal frequencies, have several effects. On one hand the location of features will be displaced due to the asymmetric impulse response of the LPF. Furthermore the internal precision will be degraded as the contrast of (small) targets is reduced due to the reduction of the MTF.

The investigation of the synchronization precision showed that the precision of PLL line-synchronization is decreased due to line-jitter by over an order of magnitude as compared to pixel-synchronous frame grabbing. The random positional changes of line-jitter can be eliminated by averaging whereas the geometric deformation, in a first approximation a shear, which was observed when using CSYNC and PLL line-synchronization, cannot be eliminated through averaging. It can on the other hand be modelled via additional parameters and should thus not significantly degrade the 3D accuracy. It must nevertheless be expected that pixel-synchronous frame grabbing provides for a higher accuracy than PLL line-synchronization, whether or not that can be translated in 3D accuracy has to be shown.

5 RADIOMETRIC EVALUATION OF CAMERA/FRAME GRABBER AS A SYSTEM

In the two preceding chapters the performance characteristics of image acquisition was theoretically discussed and the performance of the frame grabber was analyzed. In this chapter the complete image acquisition system is analyzed. First some problems of typical off-the-shelf hardware, designed for CCTV purposes and not for exacting measurement requirements, are analyzed. Thereafter several radiometric characteristics, such as uniformity, photon transfer function, signal-to-noise ratio, dynamic range of the system, and linearity are analyzed.

5.1 Installation Testing

The MAX-SCAN frame grabber has numerous jumpers and programmable switches, polarity gates, LUTs, etc. to configure the board to the requirements of various cameras. This flexibility proved excellent in enabling the various investigations to be performed, but was one of the most time consuming tasks. Initial releases of the software to control the board were extremely poor. After a newer software release and gaining extensive experience in configuring the board it proved it very good to work with. The procedure to be followed when configuring it for a new camera consists of the following steps:

- Determination of input signals, their voltage levels and impedances.
- Decision of synchronization methods and derivation of the sampling clock frequency (options: internal master clock, PLL, pixel-synchronous)
- Determination of synchronization parameters, i.e. image size and location of active image area with respect to synchronization signals, from the camera data sheet.
- Setting switches and polarity gates.
- Initial installation of hardware and software.
- Debugging and tuning using the testpoints provided on the board (see also *Amorese, 1988*).

A few problems associated with the installation and some peculiarities of the XC77 camera and the frame grabber are discussed in the following.

5.1.1 Basic Installation and Border Effects

Figure 5.1 gives the signals as specified by SONY for the XC77 at the sensor read-out and the resulting video signal. The figure shows the location of the optical black and the loss of image information at the start and end of each line as required by the video norm. The sensor output signal shows the optical black periods of each line. The active image period is reduced by several pixels to meet to the specifications of the CCIR norm. The times can be computed using the sensor clock frequency of 14.1875 MHz or the corresponding clock period of 70.485 nsec. Figure 5.2 shows an image grabbed such that the area around the active picture is shown. One can see the half lines at top and bottom and, on first glance, a uniform image region. An enlargement of the top left and right corners as well as the start and end of half lines at the top and bottom with profiles are shown in Figure 5.3. The enlargements of the left and right edge show a clear drop-off at the border of the imaging area which reduces the uniform image area. A similar drop-off occurs at the top and bottom edges, especially for the bottom. The uniform image area is reduced to about 731 by 568 pixels. The image size was therefore reduced to 728 by 568

pixels (both divisible by eight). The MAX-SCAN includes a mechanism to select the area to be stored with the look-up-tables of the horizontal and vertical counters. This selection occurs with respect to the HSYNC and VSYNC. A large difference in the relative location of these sync signals and the image content from board to board was detected. The adjustment of this selection is performed by acquiring images from the testfield with both boards and measuring the image coordinates of some targets. The difference in pix-

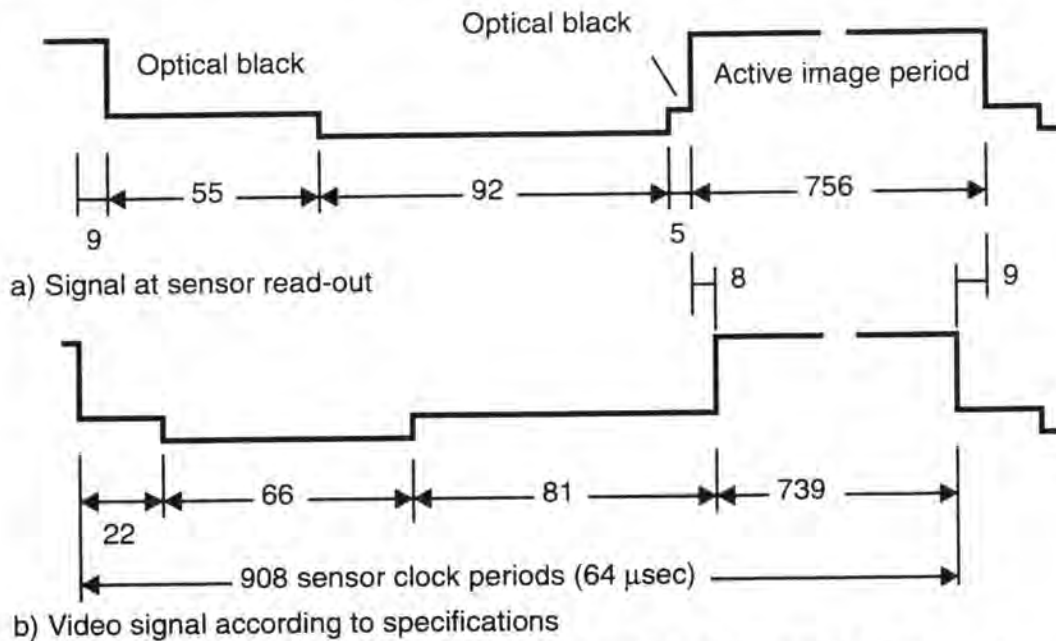


Figure 5.1 Signals at the sensor read-out a) and the video signal for one row.

el coordinates is used to adjust the settings of the LUTs for the boards. The difference between the two boards amounts to 6 pixel in horizontal direction. It was determined to be attributable to the sync stripper and CSYNC conditioning and could also be adjusted by tuning the elements on the board. The displacement was eliminated by adjusting the settings of the LUTs selecting the part of the active image period.

This displacement means that the location of the principal point with respect to the pixel coordinate system is very much dependent on the frame grabber and its setup. This is especially true for systems where only some subpart of the actual image is stored. Typically no specification on the location of this subpart with respect to the sensor is given. This is one of the sources for the large deviations of the principal point from the centre of the digital image.

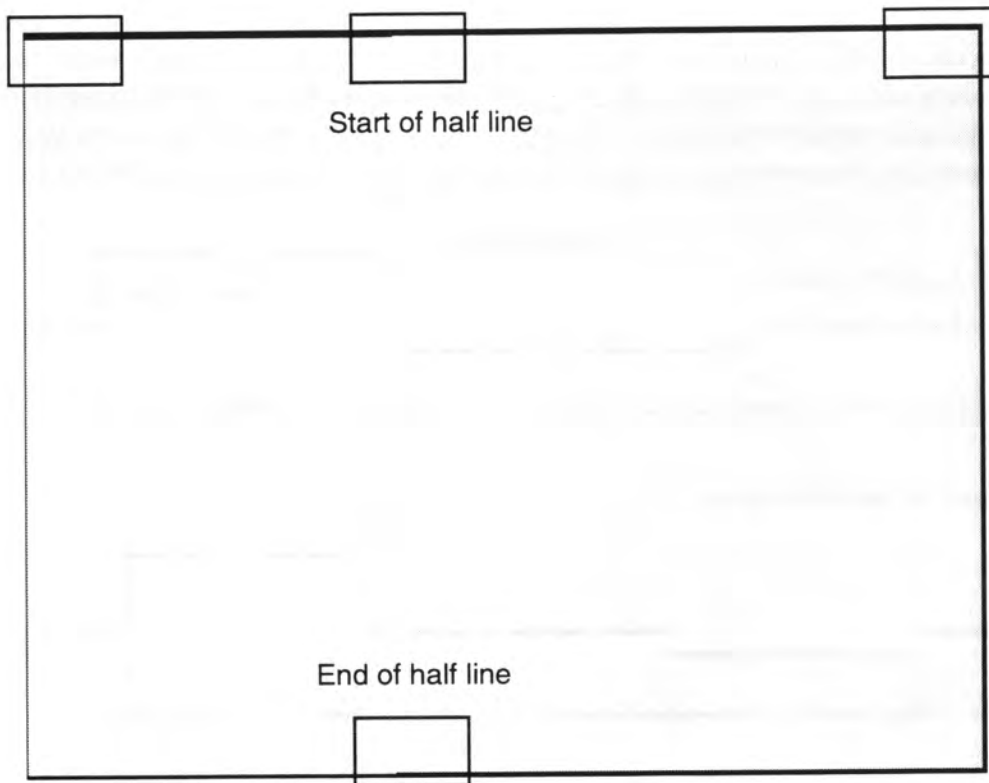


Figure 5.2 Image showing a complete frame and surrounding areas. It was digitised using an image format of 744 by 584 pixel. The rectangular areas are shown in Figure 5.3.

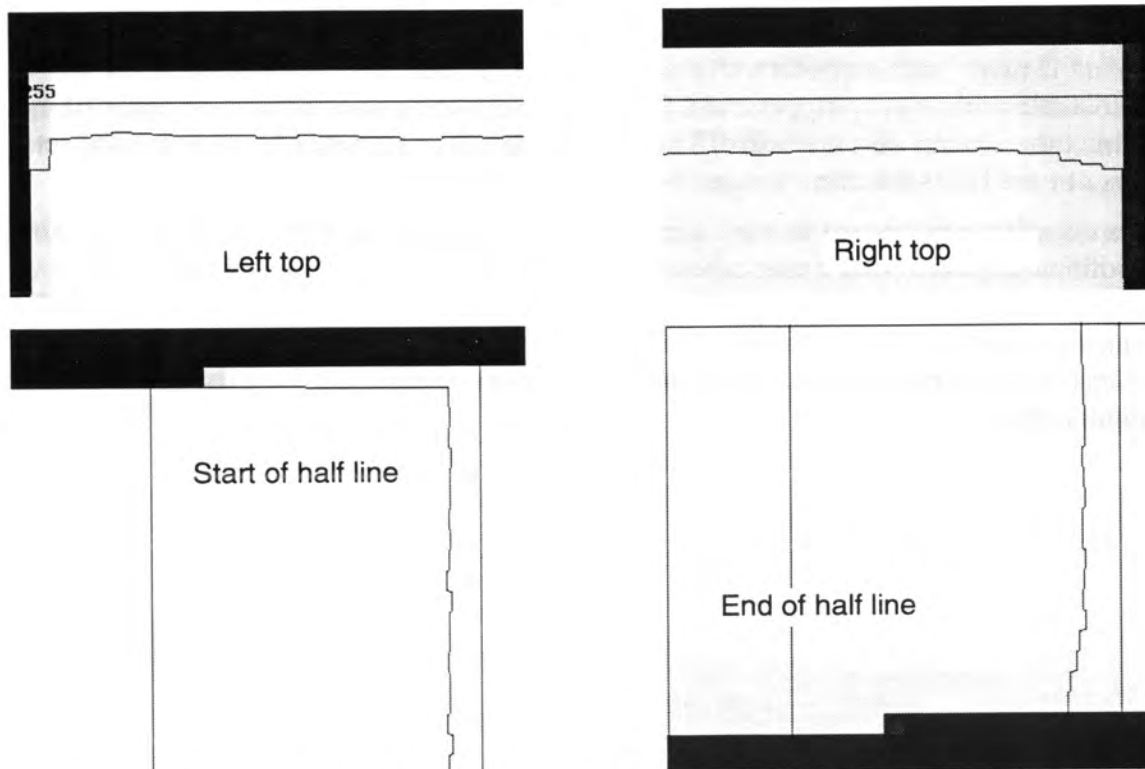


Figure 5.3 Profiles through upper left and right as well as top and bottom edges of image from above figure.

5.1.2 Analog Offset and Gain

If the frame grabber provides for analog offset and gain control, it is useful to adjust it such that no clipping in the dark and bright image regions occurs at the analog-to-digital conversion. Care must be taken as some signals might reach above and below the video specifications due to the ringing effects of filters. The corresponding adjustments were already performed for the testing of the frame grabber but are verified for the camera set-up. The XC77 peak signal reaches above 0.7 mV, but it was decided not to change the settings determined under the frame grabber testing as this is against the specifications of the video norm.

5.1.3 DC-Restoration

Some aspects of the DC-restoration were already tested above. In the following some problems of the derivation of the clamping pulse will be discussed. The discussion assumes that DC restoration must be performed using a composite video signal. The location on the signal where the sampling is to occur is defined to be the back porch as shown in Figure 3.5 (HSYNC pulse). The back porch does not exist during the duration of the broadcast pulses, which can lead to problems as shown hereafter.

Figure 5.4 shows an image from an oscilloscope with the traces of the clamping pulses

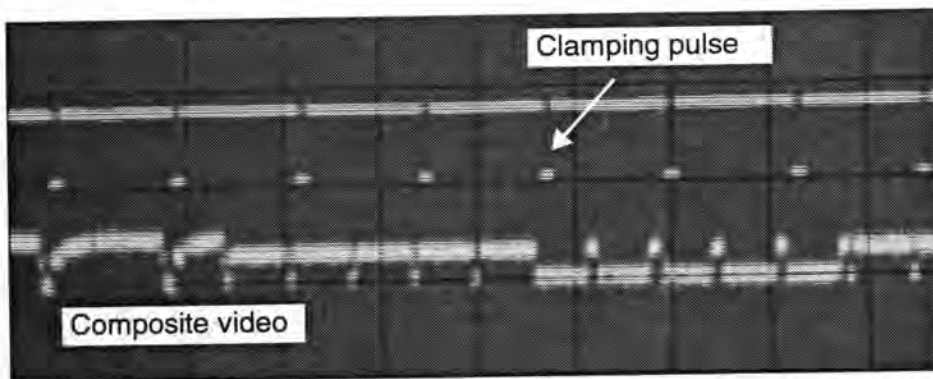


Figure 5.4 DC-restoration on sync level during broadcast pulses (settings of Oscilloscope: clamping pulse 5V/50 μ sec; composite video 1V/50 μ sec).

for the DC restoration circuit on top and the composite video signal below. The clamping pulses are derived from the horizontal sync of the frame grabber which in turn is derived from the negative going edge of the HSYNC from the camera via an edge detector (pixel-synchronous sampling is used here). As can be seen the clamping pulse is on the back porch and thus to the right side of the rising edges of the synchronization signals. During the broadcast pulses the sample and hold would be sampling the sync level, resulting, however, in a wrong DC restoration level. This is shown in Figure 5.5 with the DC-restoration signal shown on top and the composite video on bottom. The DC-restoration signal drops by about 0.3V during the duration of the broadcast pulses. To further check the performance an image without illumination was grabbed and analyzed. Figure 5.6 a) shows such an image. The top of the image is significantly brighter than the rest of the imagery.

A test was performed using the hardware generated DC restoration clamping pulse. Figure 5.7a shows the clamping pulses and composite video signal. It is apparent that the sampling will occur on the blanking level, also during the duration of the broadcast pulses. These clamping pulses are derived from the rising edge of the synchronization sig-

nals. Figure 5.7b shows a close-up of the clamping pulse and the composite video signal. The clamping pulse is approximately 4 μsec long. An image grabbed with this setup is shown in Figure 5.6 b.

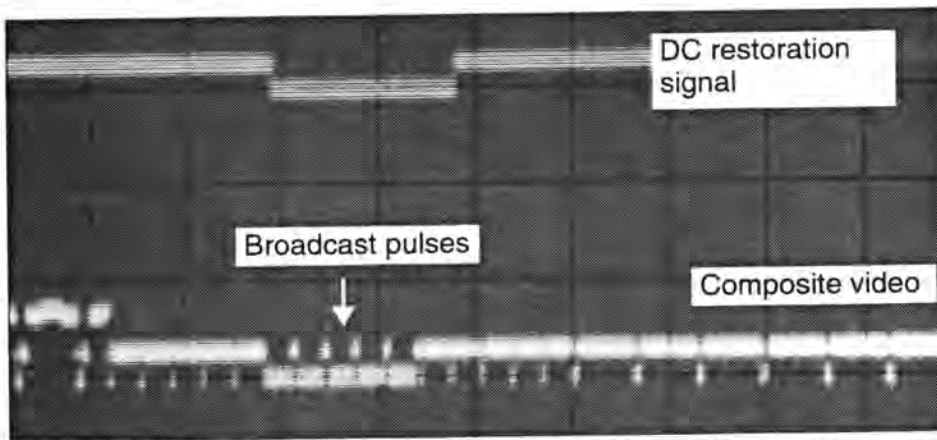


Figure 5.5 DC-restoration on sync level during broadcast pulses (settings of Oscilloscope: signal for DC restoration 1V/100 μsec ; composite video 1V/100 μsec).

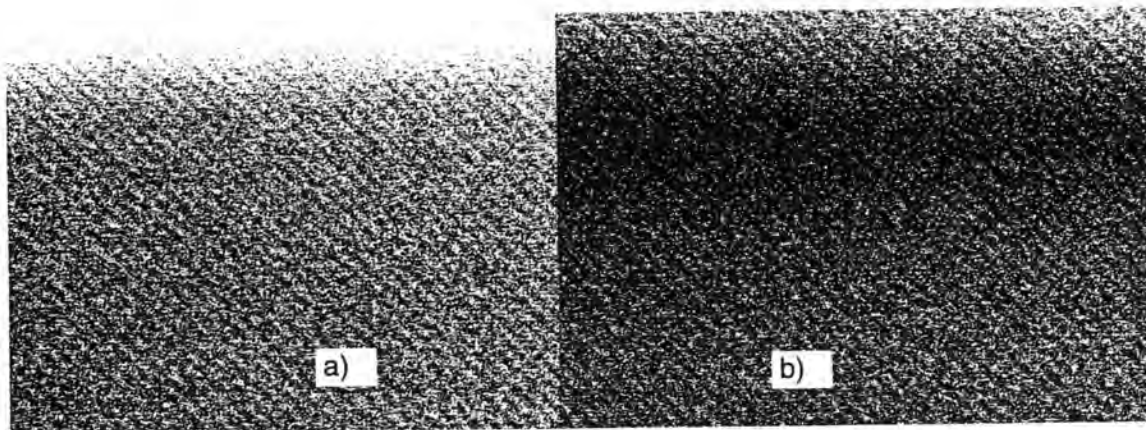


Figure 5.6 Images taken with different clamping pulse timing (thresholded to visualize the small grayvalue differences!).
 a) Clamping pulse derived from negative going edge.
 b) Clamping pulse derived from positive going edge.

The statistics for the images shown in Figure 5.6 are compiled in Table 5.1. The standard deviation of the complete frame shows that the second method is much better. The standard deviation of the two fields indicates that the second method provides for a more uniform performance too.

Clamping from	σ_{Frame}	σ_{Field1}	σ_{Field2}	in [Pixel]
falling edge	1.19	1.12	1.17	
rising edge	0.79	0.79	0.78	

Table 5.1 Statistics of frame and fields with different derivation of the clamping pulse for DC-restoration.

The conclusion of this investigation shows that the DC restoration circuit of this board takes approximately 10 lines to completely adjust to the change of 0.3 V. This is in accordance with the results obtained during the frame grabber testing. The hardware generated DC-restoration is thus used.

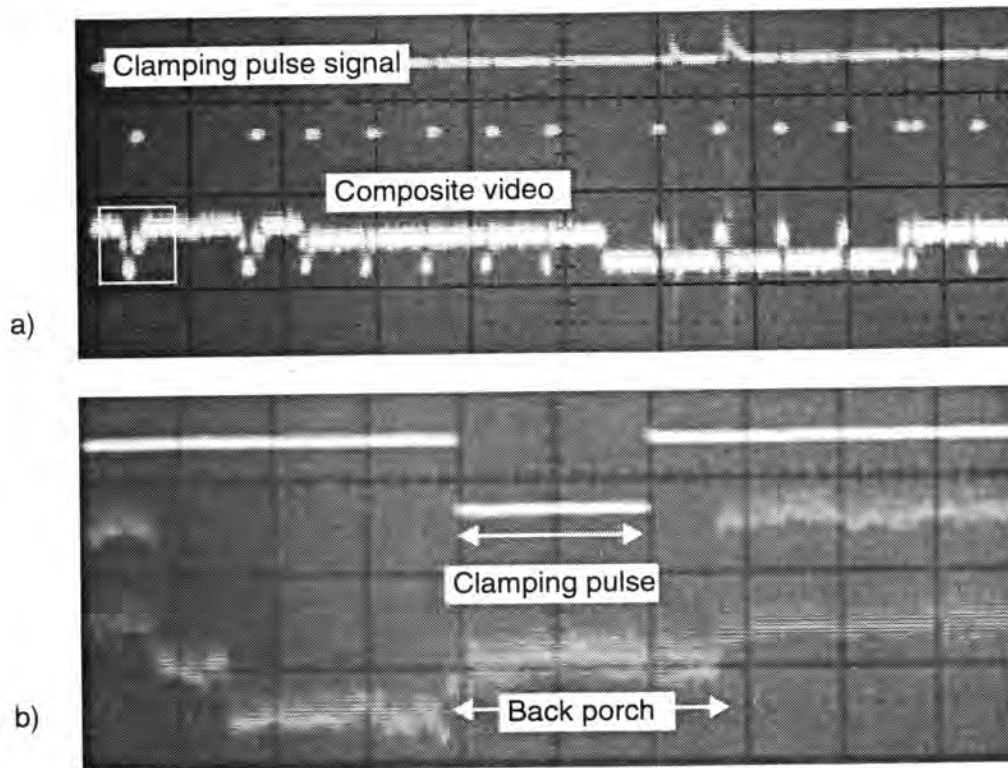


Figure 5.7 DC-restoration from hardware pulse generated from rising edges and detail of pulse with video signal (settings of Oscilloscope: a) clamping pulse 5V/50 μ sec; composite video 1V/50 μ sec b) clamping pulse 5V/2 μ sec; composite video 0.5V/2 μ sec).

5.2 Basic Radiometric Properties

Great care must be taken when analyzing results, not to confuse influences from poor synchronization and actual radiometric changes. Images of flat fields are relatively immune to line-jitter, but any non-uniformity will result in temporal noise due to the variation of sampling position from frame to frame. Strong influences can also come from phase patterns as a result of cross-talk from sensor clock and/or pixel-clock transmission.

5.2.1 Dark Signal Non-Uniformity (Fixed-Pattern Offset Non-Uniformity)

The DSNU of one XC77 camera is determined by averaging fifty frames acquired by one frame grabber board and twenty frames acquired by another board. They were grabbed as sets of five images each in a period of 4 and 2 minutes respectively. Figure 5.8 shows the average and standard deviation versus the frame number for the series containing 50 frames. The average varies for only 0.1 DN peak-to-peak and the standard deviation for 0.02 DN. The average of fifty frames shows no phase pattern, but the dark horizontal band and other vertical patterns are visible (see Figure 5.9). Again it is apparent that the temporal noise is lower in the region of the dark band. The RMS of the temporal noise component is 0.67 DN and the standard deviation of the averaged frame is 0.40 DN. The

identical test is performed using the second frame grabber. The statistics are slightly worse, but the patterns in the imagery are different (see Figure 5.9).

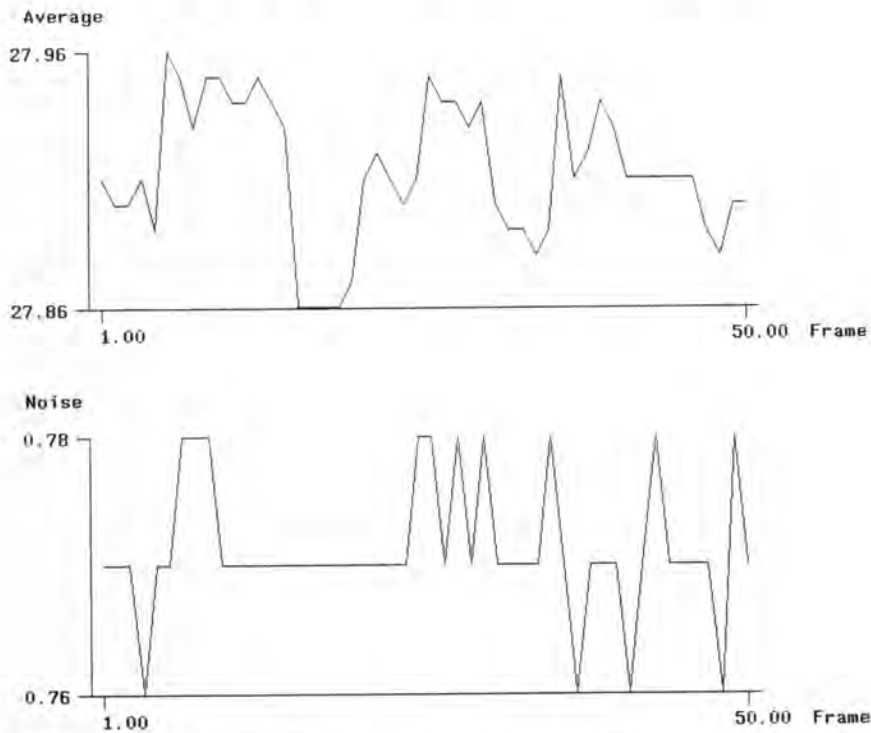


Figure 5.8 Average and standard deviations of frames.

The average of 50 frames contains only 3 pixels which deviate more than 1% of full range from the average, 56 pixel are brighter than the average plus three times the standard deviation and 5 values smaller than the average minus three times the standard deviation. The DSNU of this XC77 is very good and there are no blemishes. Interestingly there is a two pixel wide column on the left side of the image with a grayvalue below the average. This is still a residual influence of the border effects which were observed above. These border effects will only rarely have an influence for measurement purposes, but if targets are very close to the border such effects will have to be eliminated. The pixels which deviate more than 1% of full range from the average are on identical locations for both frame grabbers (after correcting for systematic position differences). As already mentioned during the discussion of the DC-restoration these images are also influenced from other light independent sources such as cross-talk from clock, power supply, etc. The phase patterns which can be observed when only five images are averaged start to disappear when imagery acquired over longer periods are averaged and a vertical stripe pattern is visible. This indicates that the phase pattern is not stationary, which supports the hypothesis that it is some hum.

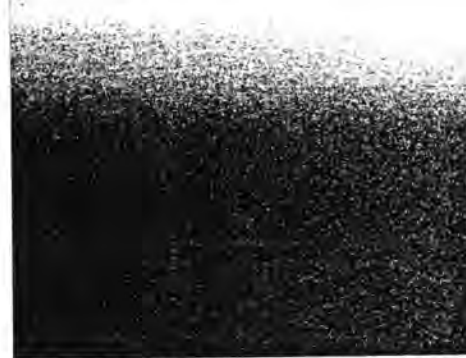
No. of Frames	RMS	Average	σ	in [Pixel]
50	0.67	27.91	0.40	
20	0.87	33.51	0.46	

Table 5.2 Results of DSNU analysis

This test indicates that the DSNU is a factor of both the camera and frame grabber. The latter is clearly the dominating factor in terms of systematic components. The level of temporal noise is significantly higher than the corresponding values from tests using a flat field from a pattern generator. The temporal noise contribution (standard deviation) of the camera amounts to 0.58 DN. This leads to the conclusion that the radiometric correction needs to be determined for every camera / frame grabber combination. The systematic patterns were found to depend even on the location of the frame grabber in the chassis. The radiometric calibration should therefore be determined for each particular configuration.



Average of 50 frames taken with
MAX-SCAN 1



Average of 20 frames taken with
MAX-SCAN 2

Figure 5.9 Averaged frames showing the large difference in the low level patterns between different boards (images are stretched and thresholded to visualise the effects).

5.2.2 Camera Power Supply and Patterns

The imagery of Figure 5.6 shows the same phase patterns as the one of the frame grabber testing. The origin of these phase patterns are investigated in this section.

A possible influence of the camera power supply was tested by using a battery, a laboratory power supply, and by connecting the camera to the supply of the MaxBox which also supplies the VME-bus. A series of five images without illumination on the sensor were taken with each power source. The RMS of the temporal standard deviation of the grayvalue of a pixel in time are determined as well as the average, standard deviation, minimum and maximum of the averaged image for each of these sequences. The results are compiled in Table 5.3. The RMS temporal standard deviation expresses the temporal noise component of individual pixels only, whereas the standard deviation computed from the average expresses the uniformity of the imagery. The statistics show no significant difference between the three power supplies. The power supply of the camera can thus be eliminated as a source for the phase patterns.

The power supply of the VME-bus (+5 V) exhibits patterns with 40 to 50 nsec period and 0.04 Vpp, and patterns with a 10 msec period and 0.08 Vpp. These instabilities depend on the activity of the SUN-3E CPU. Actually one can see whether or not the machine is active from the power supply. High frequency patterns with a frequency of 20 to 25 MHz and 0.04 Vpp as well as patterns of 100 Hz and 0.08 Vpp could be observed. To which degree these instabilities of up to 1.6% of the supply voltage influence the frame grabber could not be verified.

Camera Power Supply	RMS σ [Pixel]	Average [Pixel]	σ [Pixel]	min. [Pixel]	max [Pixel]
Battery	0.72	15.89	0.55	13.6	19.0
Laboratory power supply	0.72	15.73	0.55	13.4	20.0
MaxBox	0.73	16.16	0.54	14.0	20.8

Table 5.3 Statistics of images grabbed with different power supplies of camera.

Strong electromagnetic fields can also be observed inside the chassis containing the boards. Several efforts to shield the frame grabber boards did not lead to any improvement though. The source of these phase patterns could not be located.

5.3 Photo Response Non-Uniformity and Radiometric Correction

The DSNU describes a state which is of no interest to imaging applications - imaging with no incident light. In actual imaging tasks the response of each individual sensor element and/or pixel is of interest. With pixel-synchronous frame grabbing (compare to chapter 6) the response of a pixel consists of the response of a sensor element distorted by influences of the image acquisition system, e.g. non-linearity of amplifiers. The **Photo Response Non-Uniformity (PRNU or fixed-pattern gain variation)** is determined from two images, one taken without light incident on the sensor and one with an amount of light just below saturation. The non-uniformities are modelled by an offset and gain factor for each pixel. This is a simple model and assumes linear gain, which is not correct as shown above. The offset and gain for each pixel can be computed with different methods. Two methods among many possible ones have been tried. The **first method** determines the offset and gain values for each pixel with:

$$\text{gain} = \frac{g_{\text{bright}} - g_{\text{dark}}}{g_{\text{bright}} - g_{\text{dark}}} \quad (5.1)$$

$$\text{offset} = g_{\text{dark}} - \text{gain} \times g_{\text{dark}}$$

and uses the following correction for each pixel:

$$g = \text{offset} + \text{gain} \times g' \quad (5.2)$$

g' original grayvalue
 g corrected grayvalue
 g_{dark} reference value for dark
 g_{bright} reference value for bright
 g'_{dark} grayvalue of pixel in dark image
 g'_{bright} grayvalue of pixel in bright image
 gain gain value for each pixel
 offset offset value for each pixel

The **second method** uses the image without incident illumination to determine the offset values and both images to determine the gain with:

$$\text{gain} = \frac{g_{\text{bright}} - g_{\text{dark}}}{g_{\text{bright}} - g_{\text{dark}}} \quad (5.3)$$

$$\text{offset} = g_{\text{dark}} - g_{\text{dark}} \quad (5.4)$$

The correction of the imagery is performed with:

$$g = g_{\text{dark}} + \text{gain} \times (g' + \text{offset} - g_{\text{dark}}) = g_{\text{dark}} + \text{gain} \times (g' - g_{\text{dark}}) \quad (5.5)$$

The PRNU is the variation in gain determined with above methods. The offset should correspond to the DSNU, which is only the case for the second method. Non-uniformities which are dependent on the light level contribute only to the gain with this method.

A number of factors contribute to PRNU, among them are:

- Uneven brightness of imaged area
- Dirt in optical path and/or on sensor cover glass
- Light fall-off in optics
- Change in material characteristics within the sensor
- Changes in sensor element aperture
- other influences depending on the signal level

The creation of a uniform “flat field” poses considerable practical problems. Several attempts have been undertaken with varying success. In a first attempt the camera was placed without lens directly onto the surface of a lightbox which is covered with sheets of papers, as proposed by *Lenz 1988*. This leads with certain cameras to a strong fall-off of the light intensity towards the corners of the sensor. This originates from the construction of these cameras with the sensor significantly to the back of other optical elements resulting in a variation of the effective aperture across the sensor. This is for example the case for the SONY-XC77CE. Better results are achieved using NIKON 55 and 20 mm lenses. Here only the central part of the format for which the lenses were designed is used and the much larger focal length limits the effects of the light fall-off due to the optics away from the centre. A uniform surface was also created with an Ulbricht sphere, papers on a light box, and papers in a filter holder. The last approach would be the only method to provide for an illumination with light of similar spectral content as used for imaging the objects of interest (assuming that the paper does not alter the spectral characteristics). If radiometric correction is to be used to correct imagery in measurement applications, this will be a must as the PRNU is strongly dependent on wavelength. Using standard CCTV-type lenses leads to significant light fall-off towards the corners, especially when lenses with short focal lengths are used.

Test with Nikon Lens

In this test a 55 mm lens and paper on a light box were used. Five series of five frames each (only 5 frames can be acquired consecutively due to the memory size of the frame store, see section 2.2) were acquired at varying illumination levels, from no light incident onto the sensor to ~95% saturation illumination. The lens was focussed to infinity. The paper on the light box was defocussed as much as possible. The average of the frames with the two extremes are used to compute the offset and gain according to both methods. Figure 5.10 shows a visualization of the results for method 1 (results for method 2 are visually identical in this test). The offset shows characteristics which are similar to the DSNU determined above. Only 3 pixels deviate more than 1% of full range from the average offset. The gain image indicates that the PRNU is very low. Some local changes and horizontal stripes are visible (although only on the computer screen and not in the figure).

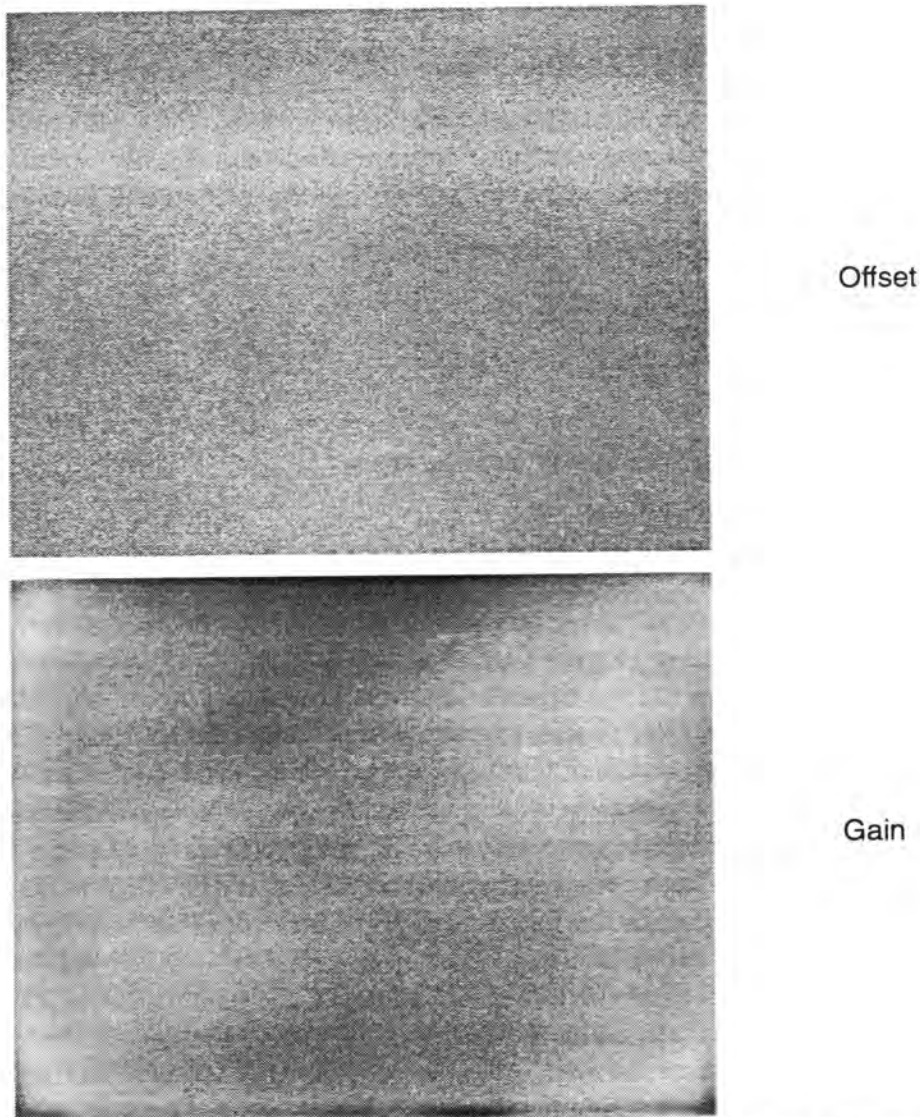


Figure 5.10 Offset and gain variations (the images are stretched for visualisation).

Table 5.4 gives the statistics of the gain with the average gain normalised to 1.0. The largest deviation reaches 5.6% with the standard deviation being 1.1%. Only 1.8% of pixels have a gain variation of more than 3%. The results show that the sensor has no blemishes and an excellent uniformity.

Gain	average	σ	min.	max.	in [DN]
Normalized	1.00	0.011	0.944	1.042	

Table 5.4 Gain variation or PRNU.

After the determination of offset and gain on a pixel by pixel basis the radiometric correction was applied to the averaged frames of each series taken at other illumination levels. The results of the analysis are compiled in Table 5.5. The standard deviation of the frame average must be zero for the two images used to determine the correction. The results indicate that the “uniformity” of images grabbed at other light levels is improved by the radiometric correction.

Level	A_{before}	A_{after}	σ_{before}	σ_{after}	σ_{temporal} in [DN]
1	230.21	230.00	2.48	0.00	1.22
2	136.45	136.45	1.50	1.11	1.08
3	69.58	69.76	1.01	0.77	1.01
4	39.47	38.72	0.76	0.72	0.95
5	20.72	21.00	0.59	0.00	0.79

Table 5.5 Average and standard deviation before and after radiometric correction.

Test with CCTV-lens

This test uses light sheets in a filter holder and a 9 mm lens. The camera is oriented towards the testfield and the light intensity is varied using the aperture and the lens cover. Again five frames of each series were averaged, the radiometric correction was determined using the brightest image and one image grabbed with the lens cover on, and the statistics of the averaged frames before and after the radiometric correction were computed. The results of Table 5.6 show the large effect of the radiometric correction for this imagery (the results after the radiometric correction are identical for both methods). This

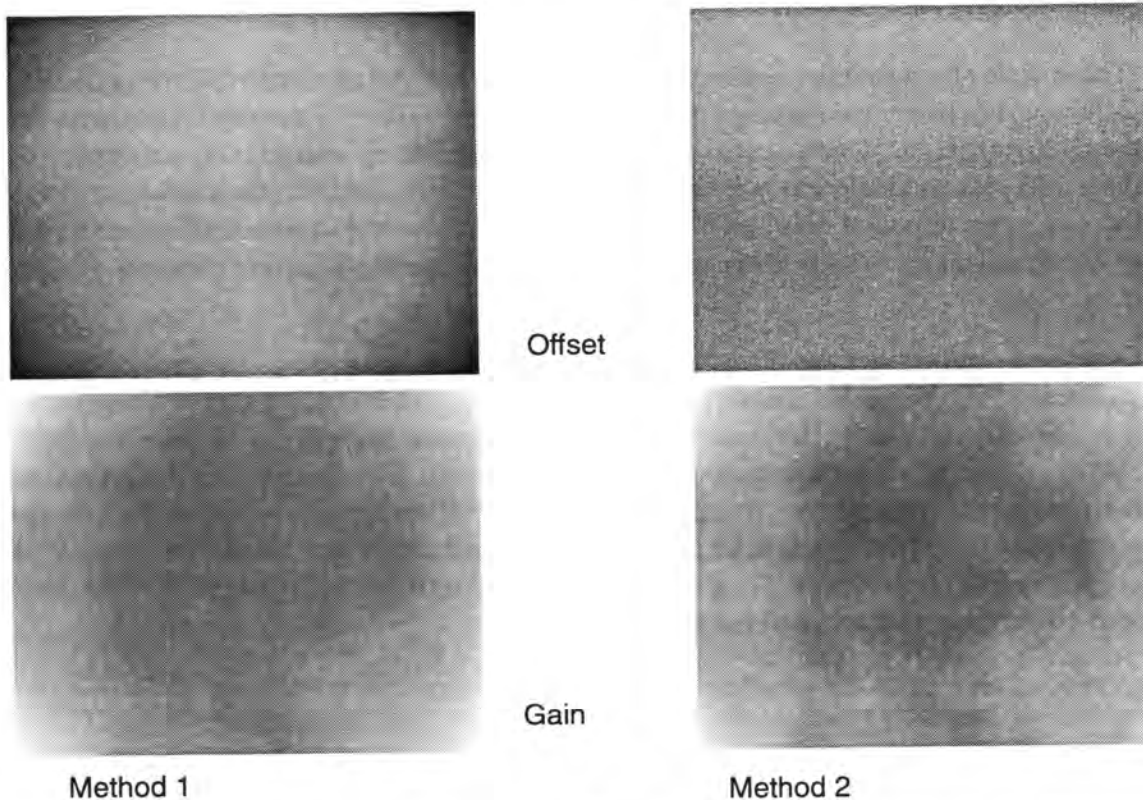


Figure 5.11 Radiometric correction with CCTV-type lens. Shown are offset and gain images for two methods.

is due to the strong changes in intensity due to the lens, which can also be concluded from the standard deviation of the averaged frame before the correction of 15.2 DN. The visualization of both the offset and gain are quite different in this case (see Figure 5.11). The gain obtained with the second method (equations (5.3) and (5.4)) indicates that there might be some residual influence of dirt and/or the paper used to create the “uniform”

field. The results after the radiometric correction are identical for both methods. Figure 5.12 also shows an image grabbed with an aperture of 2.8 before and after radiometric correction.

Aperture	A_{before}	A_{after}	σ_{before}	σ_{after}	σ_{temporal} in [DN]
2.0	226.21	226.00	15.23	0.00	0.98
2.8	148.42	148.66	7.17	3.11	0.98
4.0	95.78	96.11	4.14	2.07	0.89
5.6	64.64	65.00	2.41	1.30	0.82
8.0	46.14	46.55	1.30	0.88	0.73
11.0	35.81	36.23	0.79	0.67	0.69
16.0	31.43	31.94	0.58	0.59	0.62
22.0	29.86	30.31	0.58	0.56	0.67
closed	27.57	28.00	0.51	0.00	0.64

Table 5.6 Radiometric correction using a CCTV type lens

These tests show that the uniformity can be improved by radiometric correction. The differences between the standard deviation of the grayvalues of the corrected frame and the temporal noise indicates in case the former is larger that a residual non-uniformity remains. In case the temporal noise is larger it must be assumed that the read-out noise is increasing the temporal noise level. To prove whether or not the radiometric correction is of any practical use would require an investigation of its effects in three-dimensional accuracy tests.

Other non-uniformities are: Field to field non-uniformity stemming from an uneven adjustment within the fields, possibly also from lighting instabilities and power supply effects. Sensors originally designed for color applications, such as the Valvo NXA 1011, also exhibit an offset difference from column to column. This sensor uses three read-out registers which are intended for red, green and blue. When the sensor is used for BW applications without the color filters, errors in the adjustment of the relative levels result in graylevel offset differences. These differences stem from uneven adjustment of the three read-out paths which are used for the columns.

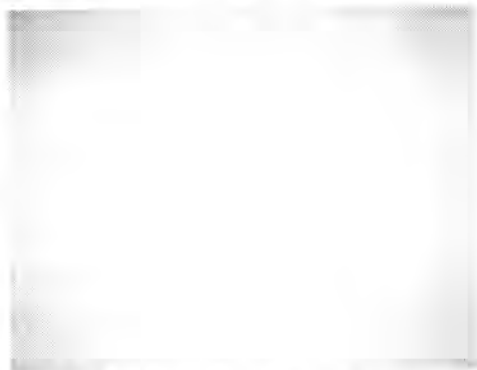


Figure 5.12 Image before (left) and after (right) radiometric correction.

5.3.1 Uniformity of Geometry from PRNU

The PRNU can be used to assess the regularity of the sensor element spacing. The following assumes that all changes in the PRNU are due to changes in the aperture. For the intensity of level 1 in Table 5.5 and the standard deviation of 0.011 for the gain it can be concluded that the standard deviation of the sensor aperture is $0.086 \mu\text{m}$ (assuming an $11 \times 11 \mu\text{m}$ sensor element aperture and spacing). The standard deviation of the aperture corresponds to less than 1% of the sensor element spacing. The SONY-XC77CE would therefore provide a relative precision of 1 : 93000 in horizontal and 1 : 73000 in vertical direction.

5.4 Noise

A number of methods to determine noise are used by various authors, all tuned to the specific possibilities of the processing hardware. The **single pixel method** uses the statistics of a single pixel from a large number of frames. An area around the pixel is used to remove any average intensity variations from illumination or other sources. The **patch method** uses subareas with approximately 20 by 20 pixels. A radiometric correction for DSNU is applied to the patch and the statistics are computed from the patch in one frame. The **frame averaging method** uses a large number of frames with uniform illumination and computes the statistics from all pixels over the frames. The different statistics derivable from averaging have already been discussed during the frame grabber testing.

The noise characteristics of the image acquisition system should be determined for the different noise regimes, i.e. the noise floor, the shot noise domain, and the saturation regime. Two basic methods could be used to determine the temporal noise. First imagery taken from uniform fields can be used together with averaging to obtain temporal noise. This method can be applied with any synchronization method as problems of line-jitter should only have a secondary influence. Images with any scene content can also be used in the event that pixel-synchronous frame grabbing or a digital camera is used (see the following chapter).

Figure 5.14 shows plots of the noise power versus grayvalue determined with the same imagery as for the DSNU analysis using the CCTV-type lens. One additional set of imagery, acquired with an aperture of 1.4 and reaching the saturation limit of the sensor for the most part is also included to evaluate the saturation region (The grayvalue of 255 should basically not be reached, but the XC77 exceeds the upper limit of the video norm).

Figure 5.14 a) shows a plot of a combination of all images. The average of each frame within a series varies for less than 0.02 DN. Thus it can be assumed that the results are not corrupted by changes in illumination intensity. Figure 5.14 c) shows a grayvalue histogram of the data used for Figure 5.14 a). It gives an indication of the quality of the temporal noise values given in Figure 5.14 a). Figure 5.14 b) represents the results obtained from a series of images from the testfield as shown in f) with the corresponding histogram below. Figure 5.14 e) is a combination of the data from both sets to show the correspondence of the results.

No clear read noise level can be found. The shot noise domain reaches up to approximately grayvalues between 200 and 220 DN. The quite early onset of saturation is evidenced by the decrease of temporal noise. Although the results are identical for both methods, it should be stressed that the determination of temporal noise through averag-

ing of imagery with large gradients will only provide correct results when pixel-synchronous sampling or a digital camera is used. Imprecisions in the synchronization lead to large disturbances of this analysis as will be shown later.

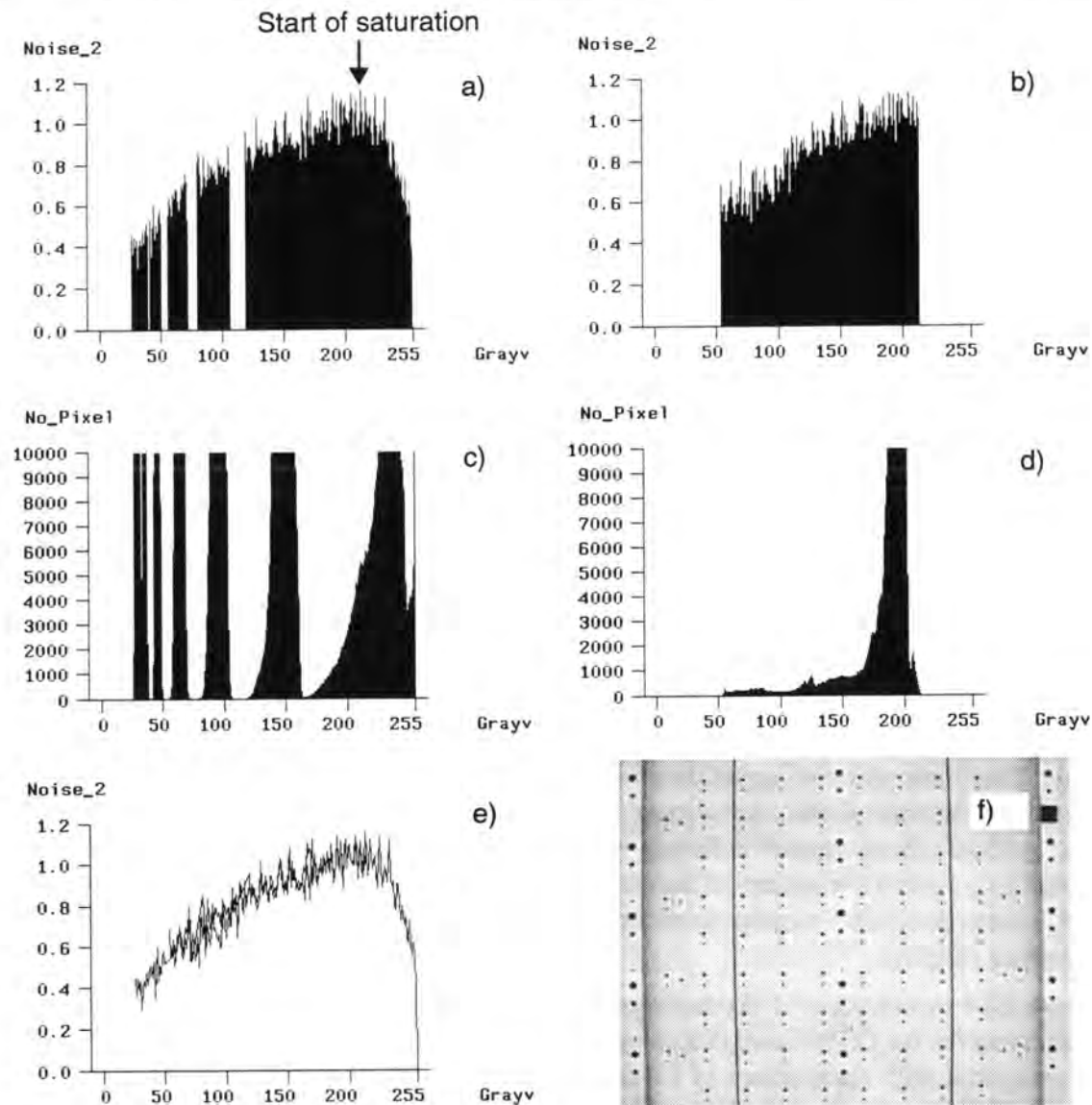


Figure 5.13 Noise from uniform field images and from a series of images from the testfield.

- a) and c) show the temporal noise and the number of pixels for the graylevel for the determination from uniform field images.
- b) and d) show the same when using five frames of the testfield as shown in f)
- e) shows the good coincidence of the two results via combination of plots a) and b).

A functional model for the computation of noise as a function of the grayvalue can be derived and used for example to assess the potential accuracy of target location methods such as Least Squares Matching and to serve as statistical model for matching algorithms in general. It should be pointed out that noise is dependent on the grayvalue and not independent, e.g. as used in some theoretical investigations on the precision of matching algorithms.

5.4.1 Photon Transfer Function (Photon Transfer Curve)

The Photon Transfer Function is used to compute the system gain factor (K) for the conversion of grayvalues in DN to the corresponding number of electrons:

$$S_e = K S_{DN}$$

with:

- S_e number of electrons
- S_{DN} signal in DN
- K system gain factor

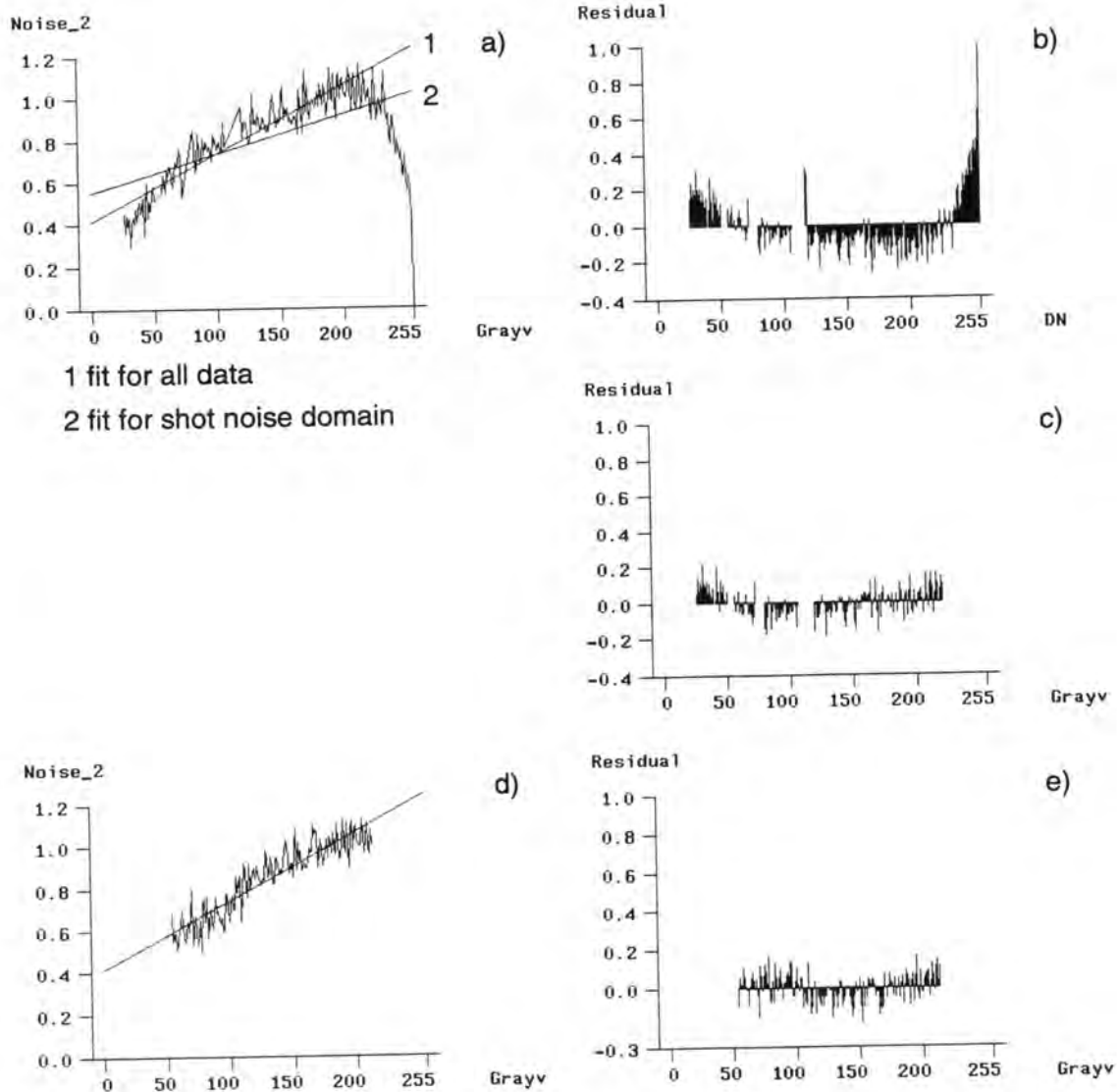


Figure 5.14 Photon transfer function and determination of system gain factor.
 a) Line fit to all data and to temporal noise data up to grayvalue 220.
 b) Residuals of line fit to all data shown in a)
 c) Residuals of line fit to data up to grayvalue 200 of a)
 d) and e) data, line fit and residuals for data from averaging of testfield images.

The system gain factor is the combined gain of sensor read-out, camera gain, signal transmission, frame grabber gain, and ADC gain characteristics. The system gain factor is computed from the temporal noise data by:

$$K = \frac{S_{DN}}{\sigma_{S_{DN}}^2 - \sigma_{R_{DN}}^2} \quad (5.6)$$

with:

$\sigma_{S_{DN}}$ shot noise
 $\sigma_{R_{DN}}$ read-out noise

It can also be computed through a line fit to the shot noise domain. Figure 5.14 a is again the complete set of data from the uniform fields acquired with a CCTV type lens. The lines corresponding to a fit to all data and the data corresponding to grayvalues smaller than 220 DN are indicated. Figure 5.14 b and c show the corresponding residuals of the line fits. The residuals of the fit to all data demonstrate the large deviations due to saturation. Figure 5.14 d and e show the data with the line and the residuals for the testfield imagery. The system gain factor is between 310 and 540. The full well capacity computed with this system gain factor and the grayvalue for 700 mV, which was set to 240 DN, is between 74 400 and 129 600 electrons. Sony specifies a S/N ratio of better than 50 dB. This would require a full well capacity of at least 100 000 if shot noise is considered only. The determination of the system gain factor as performed here is still corrupted by non-linearities of the image acquisition. A more precise method requires to determine the linearity of the system, correct the data and to compute the system gain factor for the corrected data.

Signal-to-Noise Ratio and Dynamic Range

Figure 5.15 gives the signal-to-noise ratio in dB using the data from the uniform fields acquired with a CCTV lens. The highest S/N ratio before the onset of saturation is 47 dB. The dynamic range, computed from the maximum signal of 240 DN and the noise level from DSNU of 0.67 DN, is 51 dB.

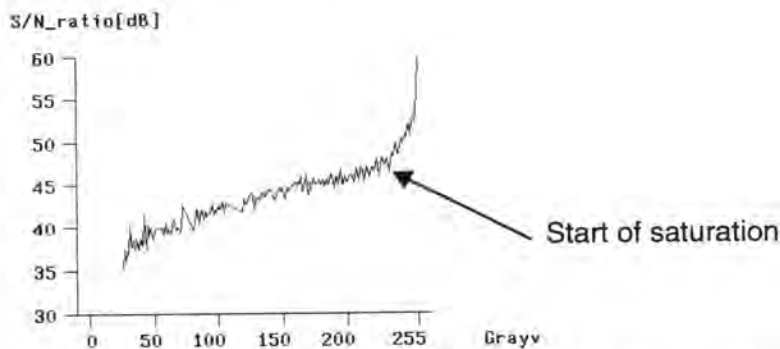


Figure 5.15 Signal-to-noise ratio as a function of grayvalue

5.4.2 Averaging

Systematic components of DSNU and PRNU can be compensated by radiometric correction. Systematic errors which are not stable in time, such as the phase pattern, are more

difficult to eliminate or can not be compensated for at all. Averaging can be performed to decrease the influence of a number of errors and noise sources, such as temporal noise and random effects of line-jitter. The latter will not be compensated but rather smeared. The number of frames which should be averaged to optimize the signal-to-noise ratio must therefore be adapted to the synchronization method and the particular characteristics of the image acquisition. With pixel-synchronous sampling the lower level will be set by systematic errors which are not stable in time. With PLL-line synchronization the effects of line-jitter will have a larger effect and the smearing thereof will only make sense up to a certain number of frames.

5.5 Graylevel Shift and Transfer Function

Several sources can result in shifts of the grayvalues when the average picture level (APL) changes. Two sources, the automatic gain control (AGC) and the DC-restoration, were discussed above. The excellent linearity of solid-state sensors is degraded by the gamma correction in cameras and other non-linearities of the camera and/or frame grabber. The linearity of the latter was already checked.

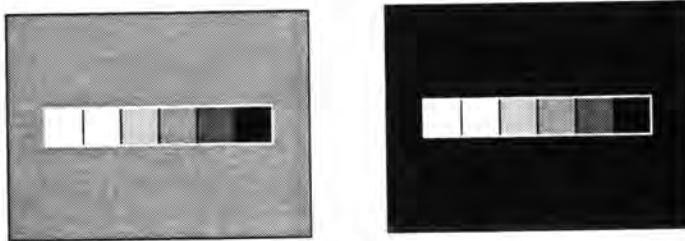


Figure 5.16 Testing for transfer function

The following test configuration is used for a rough check on both. As shown in Figure 5.16 a gray step card is imaged on a bright and dark background. The gray step card covers approximately 15% of the image area. Images are acquired with an XC77 configured without AGC and gamma correction. Figure 5.17 shows a profile with the \log_{10} characteristics of the gray step card for an image with a dark background.

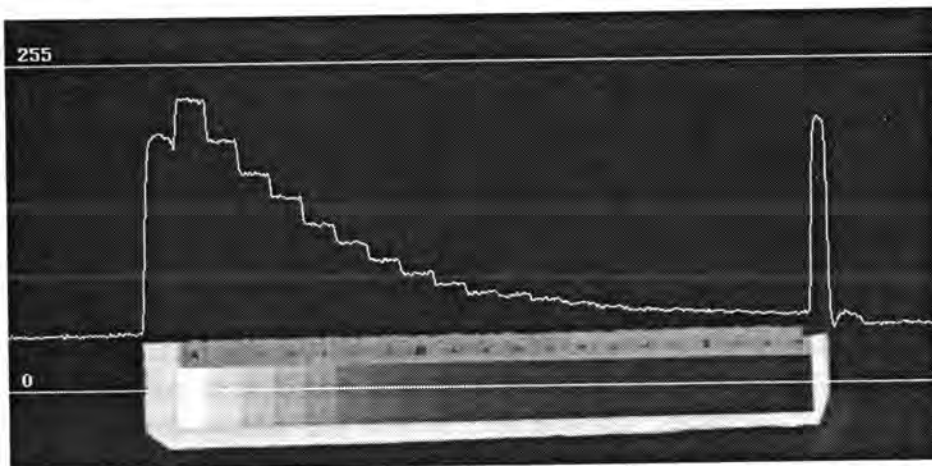


Figure 5.17 Gray step card on dark background with profile through gray scale.

The average grayvalue in an 8 by 8 pixel large region were determined for all graysteps of both images. Figure 5.18 shows a plot of the grayvalues versus the reflectivity of the

graysteps (The density of the card varies from 0.0 to 1.9 in 0.1 increments). The upper curve corresponds to the one with the bright background. The difference in average brightness of the grayscales is 15.1 DN. This is opposite to what would be expected from both AGC and DC restoration. It could be attributable to a change in the average light intensity induced by the change in environmental illumination conditions and a spreading in the optics. The linearity of the two curves is identical though. The residuals of a line fit shown in Figure 5.18 b) are of similar magnitude as those obtained for the frame grabber analysis. It can therefore be concluded that the linearity of the camera is good. This method is not very precise as the gray steps are not very accurate and light intensity variations can lead to distortions.

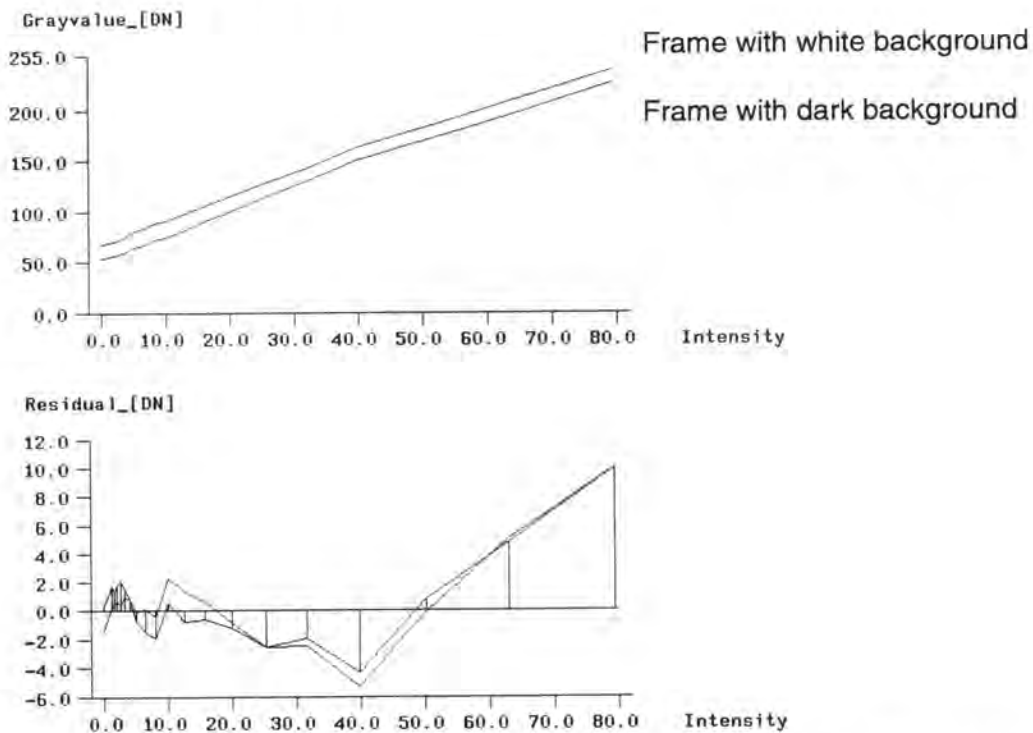


Figure 5.18 Linearity: grayvalue versus intensity and residuals of fit versus intensity.

Figure 5.19 shows on top profiles through the gray scale and the bright background and on bottom the same profile with the line of a fit through it. The change of illumination intensity and the bow of the illumination is apparent. The disturbance of the linearity analysis by this variation in illumination shows that the analysis of linearity is inconclusive as the illumination variations are in the same order of magnitude as the non-linearity.

5.6 Conclusions of Chapter

At first some of the many small problems occurring with off-the-shelf hardware. The degradations found can lead to similar displacements as discussed in the conclusions of chapter 4. The analysis of the DSNU showed once more a dependence thereof on the frame grabber. The PRNU was found to be excellent, although the quality of the uniformity of the illumination used for its determination was judged questionable. The effect of radiometric correction on the 3D accuracy will be difficult to prove due to the many practical difficulties. First of all the effect can be only very small as the PRNU is already in the range of 1%. The dependence of the PRNU on the spectral characteristics and the

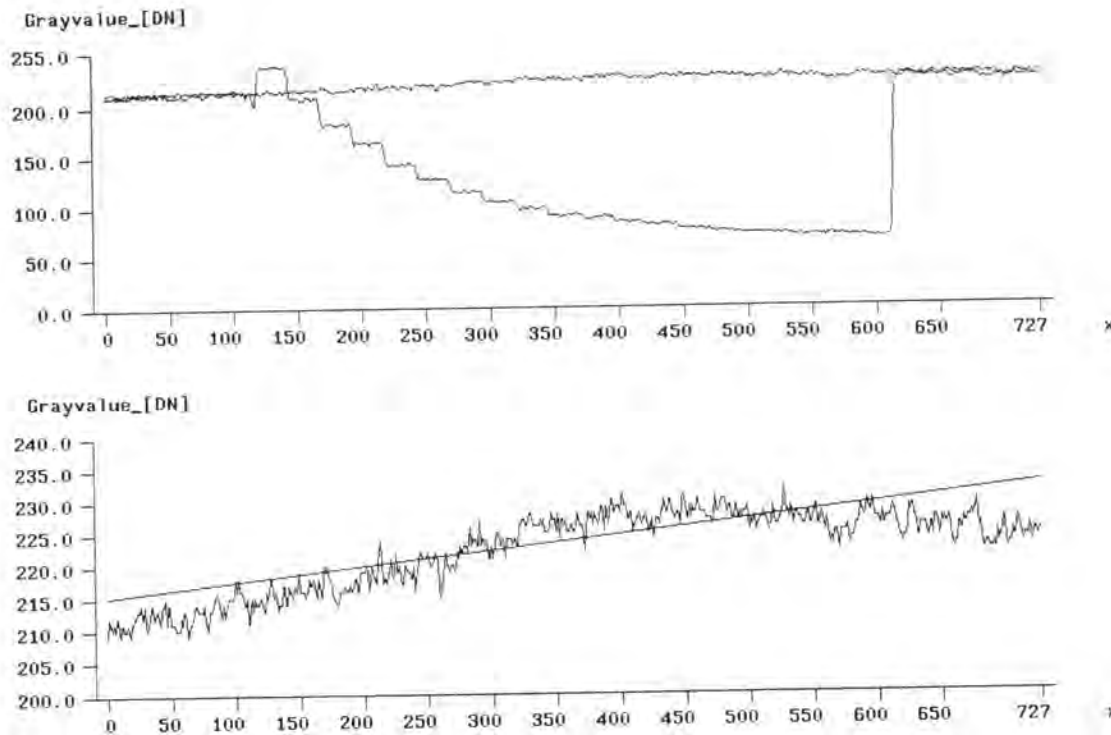


Figure 5.19 Profiles of background and gray step card.

difficulty to generate a uniform illumination which is significantly better than 1% (Ulbricht spheres specify a uniformity of better than 1%) are indicative of the problems to be expected. It must be considered that, assuming Least Squares Matching is used for target location, only local slopes of the DSNU and PRNU across the area of targets will result in displacements of the target location. The total variation of the light fall-off due to the optical system and other influences is thus not relevant. Radial symmetric local intensity variation (e.g. from optics) will furthermore be absorbed via the additional parameters for radial symmetric distortion.

The analysis of temporal noise indicated another deficiency of the camera. The camera reached saturation before the maximum video signal level is attained. The detected gray-level shift and a non-linear transfer function are only of relevance for radiometric analysis of the imagery as they do not affect the 3D measurement accuracy.

Overall one might get the impression that these characteristics are of no major importance. It must therefore be stressed that the good performance of the image acquisition system was only achieved after a large number of (small but time consuming) adjustments. A number of other problems were also detected. Once the boards overheated due to insufficient cooling. This led to a malfunction of the ADC. Some grayvalues appeared as totally different ones. Furthermore apparent differences between the two MAX-SCAN boards were detected. Most obvious were the differences in the selection of the region to be digitized in horizontal direction due to slight variations in the CSYNC conditioning circuitry. Several other smaller differences were also found. The tests provide means for evaluating the performance of cameras and frame grabbers and to pinpoint sources of potential degradations.

6 REPEATABILITY OF IMAGE TARGET LOCATIONS

The repeatability of measurements, or internal precision, in image space is the first geometric criteria for characterizing the performance of an imaging system. Two states of the system have to be differentiated for the analysis of repeatability. The effects occurring just after switching on the image acquisition system (or only the camera) until the system has reached a stable condition are called **warm-up-effects**. The **repeatability**, in radiometry and geometry, describes the performance once a stable temperature condition has been reached. Repeatability can furthermore be considered over short, i.e. a few frame times up to an hour, and long periods, i.e. up to several weeks.

Several radiometric and geometric testing methods were developed for the evaluation of the warm-up-effects and repeatability. Radiometric methods include:

- subtraction of images
- averaging of images
- analysis of temporal noise

The geometric methods include:

- repeatability of point type features
- repeatability of line type features
- geometric deformations of point and line type features

A number of factors influence the repeatability, some of which are:

- Algorithm used for target location
- Averaging
- Synchronization
- Target size
- Shadows and variations of light intensity
- Others: variations of the power supply, target form, target colour, etc.

6.1 Least Squares Matching

Least Squares Matching (LSM) is an appropriate algorithm for measuring the pixel coordinates of features because of its very high accuracy potential (*Gruen, 1985; Baltsavias, 1991*). Its performance must be checked before any other tests can be performed. A simple approach was taken here to verify the performance. A number of images were acquired and the positions of a large number of points were measured in each of the images. The repeatability of the pixel and/or image coordinates is assessed using:

$$\text{RMS}_x = \sqrt{\frac{\sum_i \sum_j (x_j^r - x_{ij})^2}{m \times n}}, \text{RMS}_y = \sqrt{\frac{\sum_i \sum_j (y_j^r - y_{ij})^2}{m \times n}} \quad (6.1)$$

where:

- x_j^r, y_j^r reference values or average of the coordinates of the point for the images used in the analysis
- x_{ij}, y_{ij} pixel or image coordinates of the points
- i index for images
- j index for points
- m number of images
- n number of points

The reference value can be the average of a series or it can be a value which was derived from another measurement when comparisons are to be performed.

6.1.1 Oscillations of Least Squares Matching

Figure 6.1 shows a plot of residuals of the locations for 90 points over twenty frames acquired pixel-synchronously in four series of five frames each. The RMS values are in the order of 0.01 to 0.02 pixel in x and y respectively (see version 1 in Table 6.1). A few of the points have much larger residuals. The origin of these was traced to oscillations of the unknown parameters in LSM. *Baltsavias, 1991* discusses conditions which can lead to such oscillations. The implementation of LSM in DEDIP takes the derivatives from

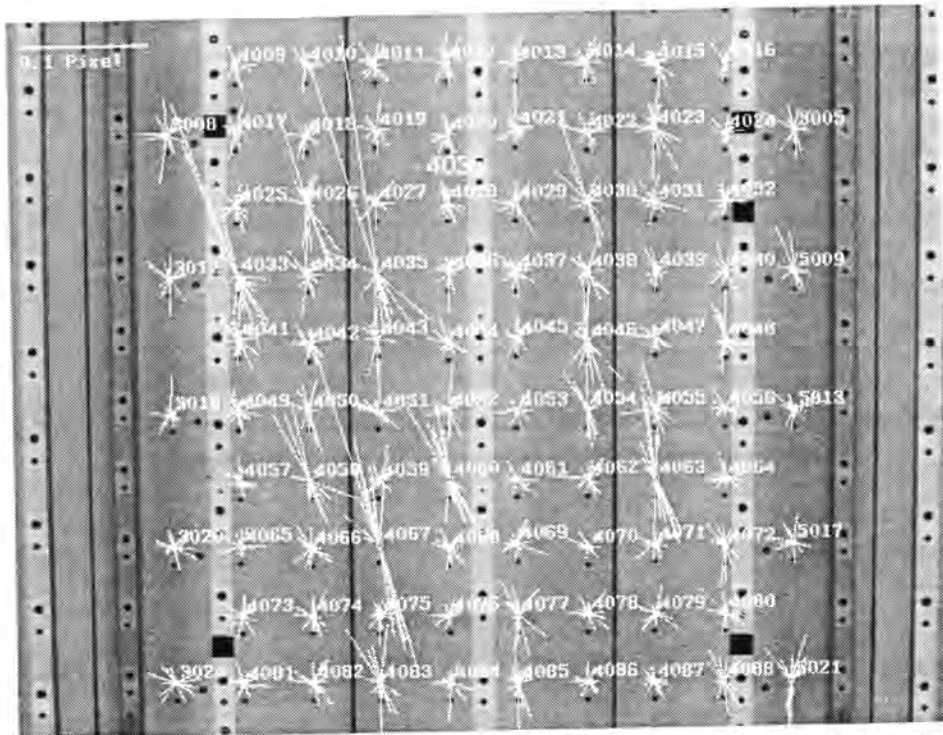


Figure 6.1 Image used for repeatability testing with vectors showing residuals with respect to the average of the point locations for twenty images.

the template only. A radiometric adjustment for the average and standard deviation is applied to the resampled patch in each iteration. The template in this test is approximately 1.5 times larger than the targets to be measured. Figure 6.2 shows plots of the changes for shift and scale parameters in x and y during LSM for a point which exhibits very large residuals in the repeatability analysis and which did not converge during LSM (point 4035, 4th point in the 4th row of Figure 6.1). The plots in Figure 6.2 show that an initial convergence is reached after about 5 iterations. Thereafter oscillations in all unknown parameters occur. The shear in y is eliminated, but the shear in x shows the same characteristics as the shift and scale in x. This can also be predicted when regarding the correlations between these parameters for a radial symmetric target. In this case the oscillations reach a level of 0.4 pixel peak-to-peak.

Figure 6.3 shows the maximum and average change of the shifts in the last iteration of LSM for the same point in 20 frames. The maximum shifts reach 0.11 and 0.28 pixel in x and y-direction respectively. The average shifts reach 0.02 pixel for the y-direction. The size of the maximum shifts is unacceptable and even the average shifts are still larger

than the precision one would like to achieve. It is therefore necessary to detect and eliminate oscillations.

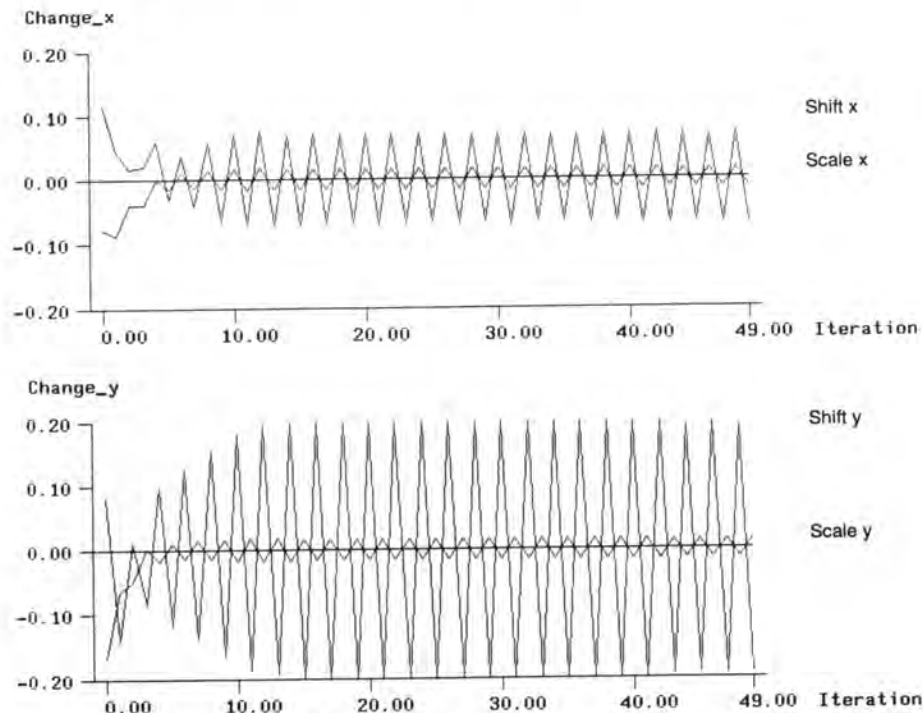


Figure 6.2 Oscillatory behaviour of shift and scale in x (top) and y (bottom) during 50 iterations for point 4035. The units for shifts are pixel.

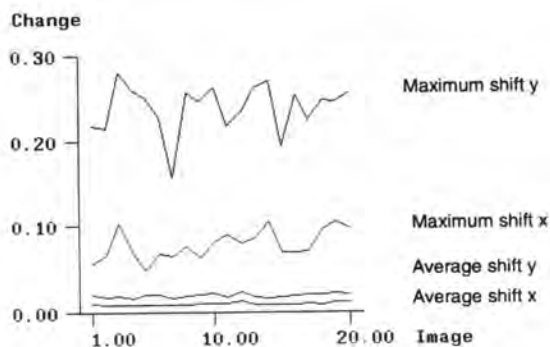


Figure 6.3 Change in last iterations of template matching when oscillations occur.

Two approaches can be pursued:

- Use of better templates
- Extension of the LSM algorithm to detect oscillations and take appropriate counter measures.

The first approach requires determining the characteristics of the template from the imagery such that no oscillations occur. This could possibly be achieved, but it would nevertheless be necessary to check for oscillations. It might also require the use of a large number of templates. It was therefore decided to extend the algorithm such that oscillations of the type seen in Figure 6.2 are detected and appropriate counter measures are taken. Two problems must be solved in order to do this. First a measure to evaluate the

performance of template matching must be set up, and second a strategy for the detection of oscillations and counter measures to be taken needs to be derived.

The RMS values as defined in (6.1) together with the maximum values of the differences are used as **relative performance measures**. The algorithm minimizing these values is deemed the best. Further elements checked are the average and maximum number of iterations, and the maximum changes in the last iteration of LSM. When a large number of iterations is required or the maximum number of iterations has been reached, the characteristics of the changes of unknown parameters during LSM are analysed. The test data consists of a series of 20 images. This imagery was acquired after the complete system (lighting, camera, frame grabber) was running for over one week, thus warm-up-effects can be excluded. The images were grabbed in four series of 5 consecutive frames each. The consecutive frames in a series are each spaced 20 msec, whereas the acquisition of all frames was performed within a few minutes.

The following **strategy for the detection and elimination of oscillations** was developed during a series of tests. The strategy of the eliminations is based on the correlations determined for typical circular targets used in the tests and experience. Oscillations are detected if a shift parameter changes its sign in each of four consecutive iterations and the magnitude of the change is not decreasing. If both shifts show oscillations, the one with the larger magnitude is treated. To counteract oscillations the shear parameter is excluded before the scale parameter of the corresponding axis is excluded. Whenever a parameter is eliminated only half of the change computed in that iteration for the shift for which the oscillation was detected is applied. When the parameters of one shift are already eliminated the parameters of the other shift will be eliminated according to the above sequence.

Version	AV _{It}	MAX _{It}	MAX _{sh} [Pixel]	RMS _x [Pixel]	RMS _y [Pixel]	MAX _x [Pixel]	MAX _y [Pixel]
1	43	50	0.270	0.0091	0.0186	0.053	0.186
2	12	37	< 0.001	0.0070	0.0078	0.029	0.039
3	12	50	0.001	0.0072	0.0081	0.032	0.030
4	14	36	< 0.001	0.0067	0.0079	0.032	0.054
5	12	34	< 0.001	0.0068	0.0076	0.030	0.033

Table 6.1 Statistics on the performance evaluation of LSM without and with detection of oscillations and for different templates.

- AV_{It} Average number of iterations
 MAX_{It} Maximum number of iterations
 MAX_{sh} Maximum change of shift in x and y of last iteration in pixel
 RMS_x Repeatability in x in pixel
 RMS_y Repeatability in y in pixel
 MAX_x Maximum difference from repeatability in x in pixel
 MAX_y Maximum difference from repeatability in y in pixel

The statistics of the LSM of the test data and the relative performance measures are compiled in Table 6.1. It gives the average and maximum number of iterations required by LSM to converge (the maximum number of iterations is 50). Furthermore the maximum shift in the last iteration is given. Version 1 refers to the test without any countermeasures against oscillations, which was already discussed above to present the problem of

oscillations. All other versions use the version of the algorithm including the oscillation detection. **Version 2** uses an identical template as version 1. Versions 3 and 4 use other templates and are discussed later. To eliminate any possibility of a systematic influence of approximations on the performance, the initial positions for the LSM of each point is perturbed with a normally distributed displacement having a standard deviation of 0.5 pixel.

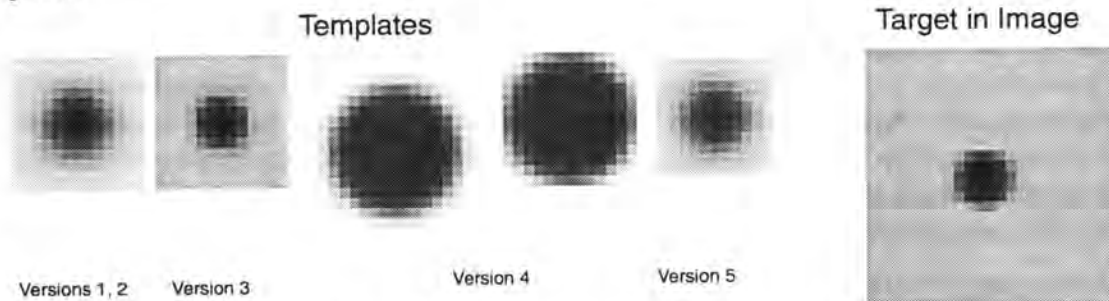


Figure 6.4 Templates of the different versions and a typical point of an image.

The results show that the average number of iterations is drastically reduced when the extended algorithm is used. The maximum change in the last iteration is reduced to below one thousandth of a pixel for all measurements performed in this test (7200 LSM measurements were performed for the results given here). Figure 6.5 shows the changes of the shift in x for the point requiring the largest number of iterations in version 2. Oscil-

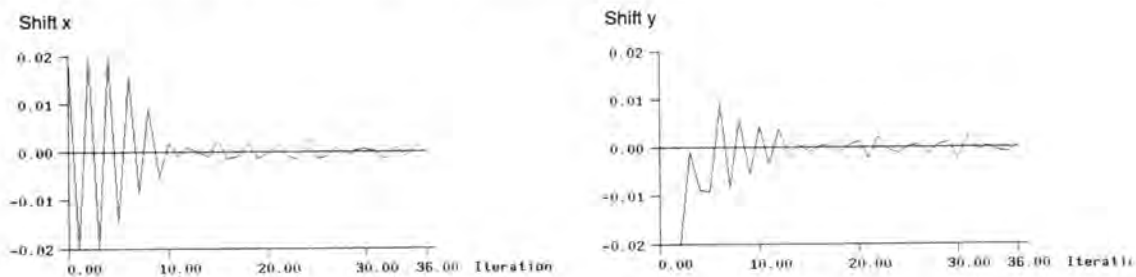


Figure 6.5 Changes of shifts in x and y with detection of oscillations. In iteration 13 an oscillation of the y -shift is detected and the scale in y is eliminated (The y _shift plotted is only 1/2 of the original computed in that iteration!).

lations in y were detected by the algorithm in iterations 13, 23, 32, and 34. The scale in y was eliminated in iteration 13 upon the detection of the oscillation. An oscillation in the x shift was detected in iteration 35 and the shear in x was eliminated. The figure shows that in this case no significant further convergence occurs after 10 to 15 iterations, where the changes of the shifts have decreased to 0.001 to 0.002 pixel. The relative performance measures of Table 6.1 show a significant decrease of both the RMS and maximum values of the residuals in both coordinate axes in version 2 (a factor of 1.3 to 4.7). Figure 6.6 shows a plot of the residuals for version 2. The scale for the vectors is identical to that of the plot for version 1 in Figure 6.1 above. The residuals appear randomly distributed for each of the points and of similar size for all points. No large residuals as in version 1 can be found. It can therefore be assumed that large oscillations, i.e. > 0.01 pixel, are eliminated



Figure 6.6 Residuals of version 2.

Versions 3 and 4 were performed to verify the influence of the template. The template for version 3 (see Figure 6.4) is taken from the imagery. The grayvalues along the x and y axes are used to generate a table of grayvalues as a function of the radius. A centered and symmetric template is then created using these values. As shown in Table 6.1 the average number of iterations remains unchanged, but the maximum number of iterations reaches 50, which means the iteration criterion was not reached (0.0005 pixel for the average of the shifts). Figure 6.7 shows the long periodic oscillation pattern of the changes

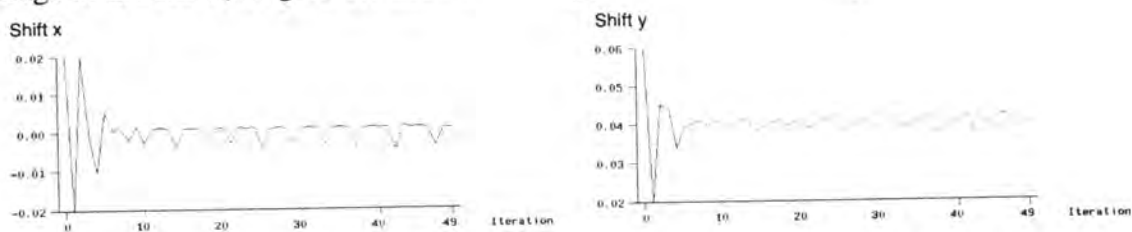


Figure 6.7 Changes of the shift in x during template matching with a template adapted in size and radiometry to the targets of the image. Typical long-periodic oscillatory patterns are shown.

of the shift in x during the iterations. This is even more apparent in the graph on the right of Figure 6.7 indicating the total change as computed in the iterations. This long periodic oscillation is not detected by the algorithm. Although this oscillatory behavior occurs quite often, no further improvements to the algorithm were made as the magnitude of these changes were well below 0.01 pixel.

Version 4 uses a template which is 2.5 times larger than the average point in the image (see Figure 6.4). Even in this case the LSM performs well. The number of iterations and the maximum changes in the last iteration are comparable to version 2. Problems occur at

points which are too close to others. Figure 6.8 shows on the left part of one image where such erroneous measurements occurred. The LSM converges on the large square targets instead on the black targets of the wall to their left (points 4024 and 4032). This effect occurs when a significant part of the large target enters into the patch. The same figure (right) shows the plot of the residuals including the erroneously measured points. The blunders are clearly visible. The points where blunders occurred were re-measured using a smaller template as shown in Figure 6.4. Such blunders could be automatically detected as the change from the initial position becomes very large (more than 5 pixel) and the scale differs from that of the other points. The scale could also be used as a check in practical applications when knowledge on the size of the target and the distance from the camera to the point exists. The results show that a comparable level of performance can be achieved although the template is clearly not adapted to the imagery.

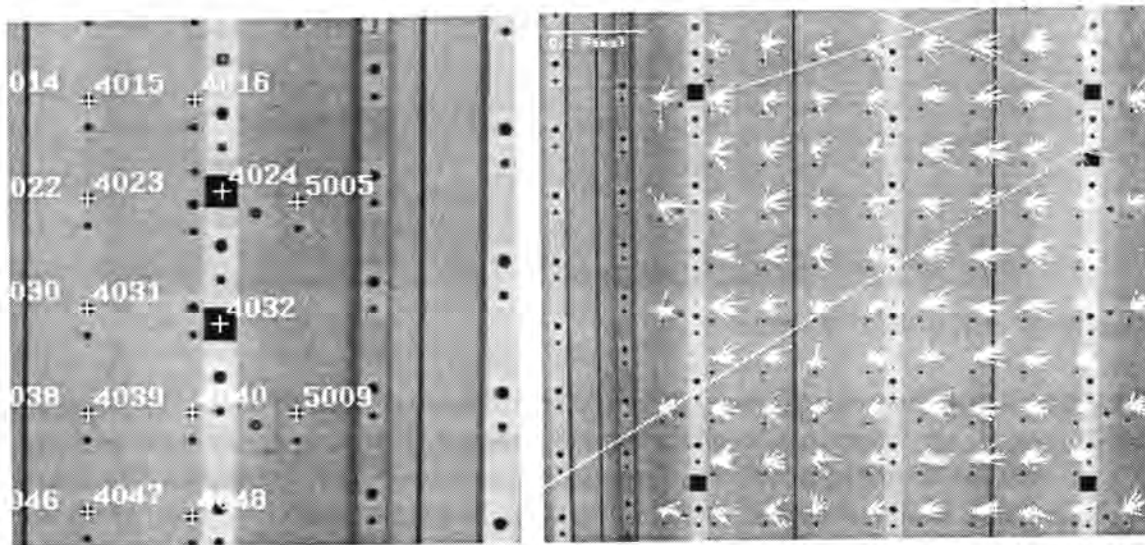


Figure 6.8 Part of image with two of the points at which errors occurred (left) and plot of repeatability analysis before re-measurement of the wrongly measured points (right).

Version 5 was performed using a template which is 1 pixel smaller around the border than that of versions 1 and 2. The performance is even slightly better than that of version 2 as indicated by the performance measures given in Table 6.1. The main purpose of this version is to check the influence of a small change in the size of the template and its effects will be discussed later.

Comparison between Templates

Finally the results of the different versions were compared. The coordinates of the points of version 2 were averaged over the twenty images and used as reference. The results of the performance analysis of versions 1, 3 and 4 with respect to version 2 are shown in Table 6.2.

The performance measures were degraded by a factor of up to 2.6, but the resulting RMS values remained well below 0.02 of a pixel for versions 3 to 5. The Figure 6.9 shows the plots of versions 3 and 4 with respect to version 2. The residuals of both versions exhibit a systematic deviation for each point. In version 3 the residuals of individual points exhibit a systematic characteristic, but the overall distribution is rather random. In version 4 a global tendency in the x-direction for all residuals can be detected, except for those

points which were re-measured with a different template (due to the problem of convergence on a wrong target as discussed above and circled in the figure). The global shift in x between version 4 and 2 is 0.015 pixel. Furthermore the distribution and length appears to be similar for each column of points. The displacements in the columns could be attributable to shadows and a local variation in light intensity (see section 6.8). No definitive explanation of this phenomenon can be given though. Figure 6.10 shows a profile through the imagery with intensity gradients in the x -direction for a number of columns. The influence of shadows is covered later in more detail.

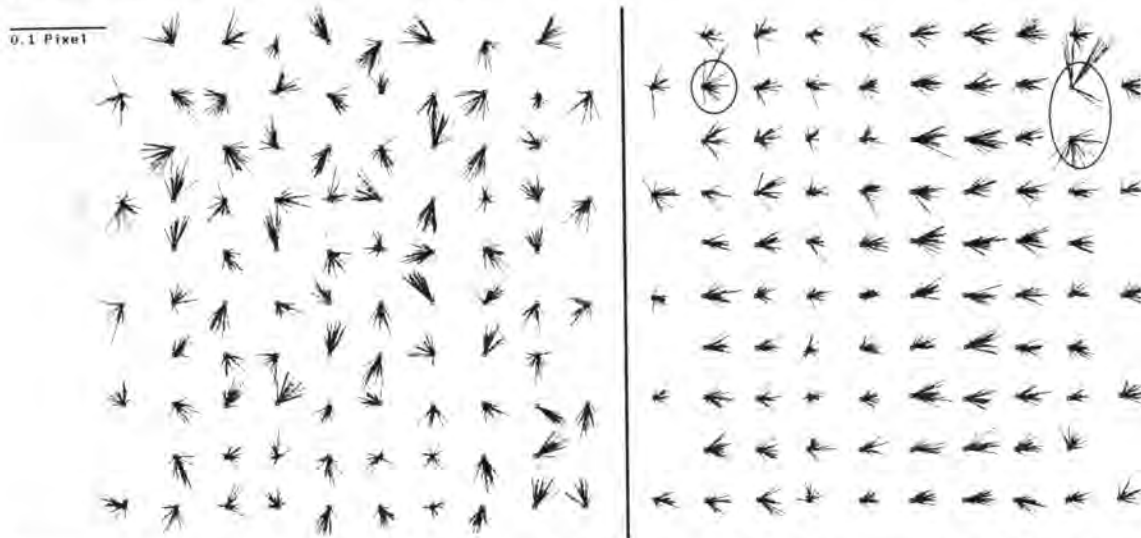


Figure 6.9 Plots of residuals of versions 3 (left) and 4 (right) compared to version 2. The targets which were re-measured in version 4 with a different template are circled.

Version	RMS _x	RMS _y	MAX _x	MAX _y	[Pixel]
1	0.0104	0.0235	0.067	0.148	
3	0.0123	0.0168	0.036	0.049	
4	0.0173	0.0093	0.052	0.073	
5	0.0122	0.0092	0.035	0.032	

Table 6.2 Results of comparison to version 2.

Version 5 gives further insight into the effects of the template size on LSM. As only the size of the template was changed, only minor changes in the results are expected. Figure 6.11 shows on the left side a plot of the residuals of version 5 using the average position as reference, whereas on the right version 2 is used as reference. It is apparent that the average position between these two versions is different. This is exhibited by the systematic distribution of the residuals for many points. Again the points in some columns show similar characteristics. These systematic differences cannot be attributed to oscillations as the largest changes in the last iteration are below 0.001 pixel, but the differences are in the order of 0.01 pixel. It demonstrates that the high level of repeatability of below 0.01 pixel can only be achieved for a particular template and cannot be equated to the target measurement accuracy. To what extent this is influenced by shadows cannot be determined conclusively.

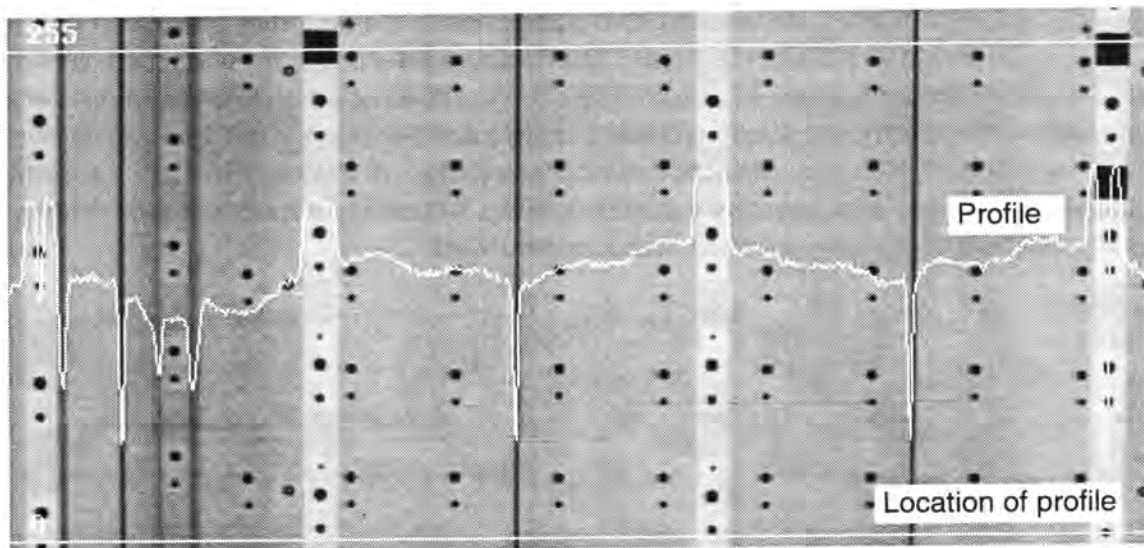


Figure 6.10 Part of an image with profile showing local illumination gradients.

Dependence of LSM on Approximations

As a verification of the influence of LSM alone one image was measured ten times with different approximations. The RMS values with respect to the average of the series are 0.0006 and 0.0005 and the maximum values 0.005 and 0.002 pixel in x and y respectively. This shows that the influence of the approximations have no significant effect and that the convergence criteria is sufficiently small.

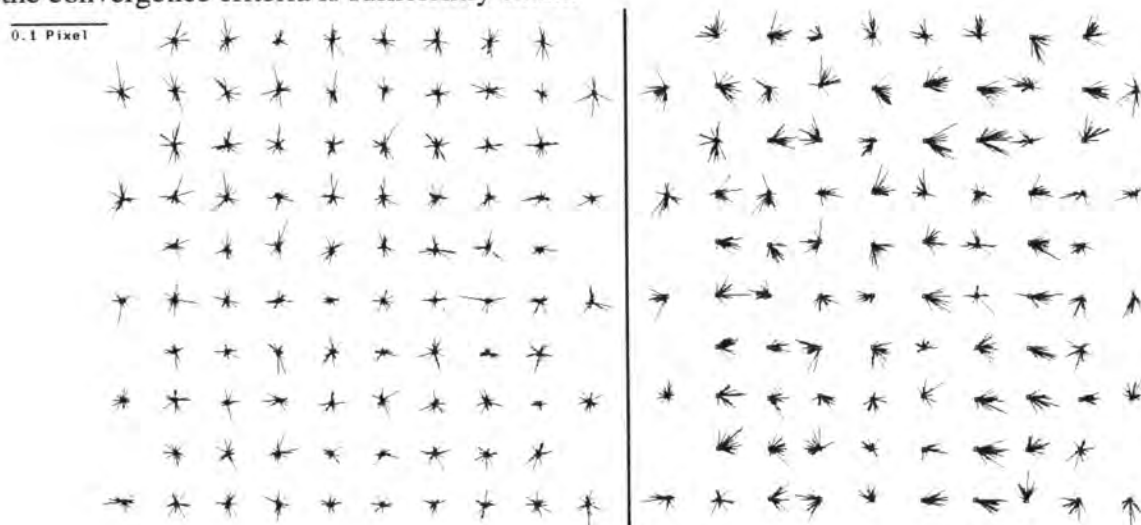


Figure 6.11 Plot of residuals of version 5. On the left the average of version 5 is used as reference. On the right version 2 is used as reference. Note systematic patterns for individual points and within some columns.

6.2 Averaging

Two alternatives for averaging can be employed:

- The images can be averaged and the measurements performed with the averaged image.
- The measurements are performed in the original images and the resulting pixel or image coordinates are averaged.

The first method has the advantage that the averaging can be performed in real-time with special hardware, that the amount of data to be stored is reduced, and that the measurements need only be done in one image. This results in a large savings of computing time in comparison to the second method. The averaging of the image coordinates in the second method can be performed with double precision values, thus eliminating influences from rounding errors. The comparison can provide an estimate of the degree by which the measurement precision is degraded due to the rounding of the averaged imagery to 8-Bit data.

Both techniques were evaluated with the same imagery as used for the tests above. The images which were acquired consecutively are grouped together. Such four groups of images, each with five images were used (Five images were used as only five frames could be acquired consecutively, thus eliminating any long-term degrading effects). Table 6.3 gives the results for both versions of averaging.

Versions 21 and 22 use averaging of the images. Version 21 is the repeatability analysis with respect to the average position of itself. Version 22 uses the results of version 2 of the Least Squares Matching analysis (see section 6.1) as reference. Version 23 uses the results of version 2 and averaging of pixel coordinates. The average position is used as reference. A comparison of versions 21 and 22 with 23 shows that the results are only degraded by a factor of 1.1 when averaging the imagery instead of averaging of the coordinates. For time and storage critical applications it will therefore be advantageous to average the imagery and only store and process the averaged frames. Comparing the results to those of version 2 shows that the improvement is almost according to the statistical expectation even when averaging images. Assuming that the determining factor for the improvement is noise, the maximum number of images to be averaged can be determined from the noise analysis as discussed in chapter 5.

Version	RMS _x	RMS _y	MAX _x	MAX _y	[Pixel]
21	0.0036	0.0041	0.012	0.017	
22	0.0037	0.0045	0.012	0.015	
23	0.0032	0.0042	0.011	0.014	

Table 6.3 Repeatability values for different averaging methods.

6.3 Synchronization

The influence of synchronization on warm-up-effects and repeatability is of major importance. Very large disturbances during warm-up could be found by *Dähler, 1987*, and a large reduction of the repeatability is expected to be incurred by line-jitter (*Beyer, 1988 and 1991c and e*). Two separate studies are shown here. In a first test the effects of synchronization with a PLL at two sampling speeds and pixel-synchronous sampling are compared. In a second pixel-synchronous sampling and digital transmission are analyzed.

6.3.1 PLL Line-Synchronization versus Pixel-synchronous Sampling

The cameras are placed in front of the large testfield and series of five images each are acquired with each of the three setups given in the following table.

Configuration	Synchronization	Sampling Speed
xc77_ccir	PLL	~10.4 MHz
xc77_cv	PLL	~14.1875 MHz
xc7_cvp	pixel-synchronous	14.1875 MHz

Table 6.4 Configurations for the evaluation of synchronization.

The first two configurations use the PLL of the frame grabber to derive the sampling clock. The xc77_cv configuration was adjusted such that the sampling clock had a frequency as close as possible to the pixel-clock frequency of the camera. The last configuration uses the pixel-clock from the camera as sampling clock, the system is pixel-synchronous. Figure 6.12 shows parts of the imagery for the three configurations in the

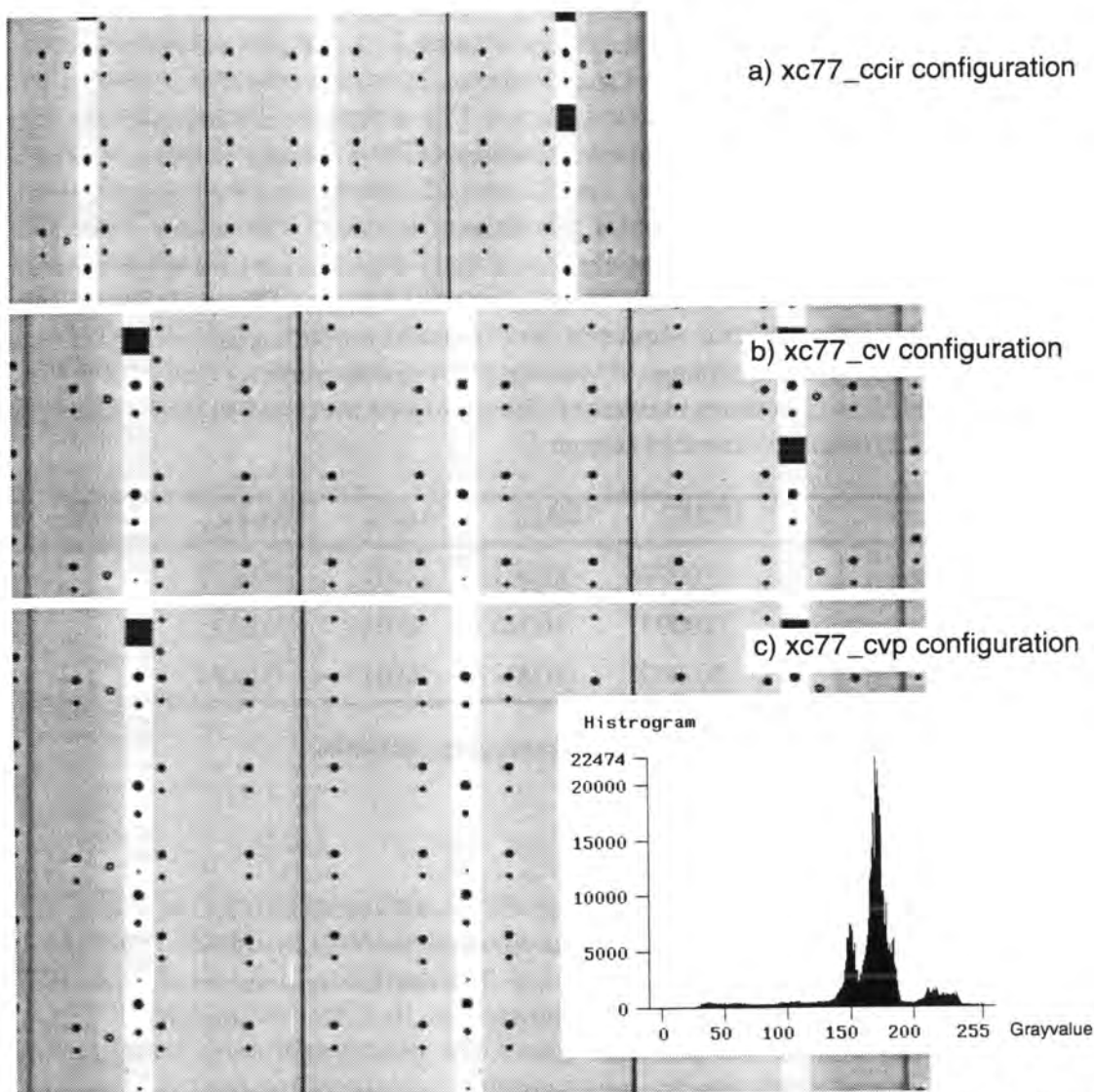


Figure 6.12 Parts of the imagery acquired with the three configurations and histogram of image acquired with the xc77_cvp configuration.

order as given in Table 6.4. Note the difference in the x-scale and the size between figures a and b. The scale difference is typical for many systems where the sampling rate cannot be adjusted. Part of the imagery is lost with the first configuration (xc77_ccir) as

the size is set (and in many systems fixed) to 512 by 512 pixel. The histogram of figure c shows the distribution of the grayvalues for that image, which is representative for the imagery grabbed with all three configurations.

Whenever a series of images which should be identical has been acquired it is worthwhile to check the **average and standard deviation** of the imagery. This does not necessarily indicate anything about the synchronization, but large changes do usually indicate a problem. This can originate from many sources such as lighting, power supply, instability of DC restoration, etc.

The averages for each of the series are within 0.02 DN peak-to-peak. Even the averages between the configurations vary by only 2 DN. The situation for the standard deviation for the grayvalues of the images is similar. The good correspondence within each series must be attributed to the short time span (0.2 sec) within which it was acquired. The differences between the series are typical in comparison to the long-term stability for the xc77_cvp configuration.

Analysis by Image Subtraction

A simple method to check the influence of the synchronization is the **subtraction of images**. Two consecutive images are subtracted and the resulting grayvalues are stretched to extend over the full range from 0 to 255 DN. Parts of the resulting images are shown in Figure 6.13. The figures a and b show the differences occurring at positions with strong grayvalue gradients in x direction. This is visible at the locations of the dark plumblines. The grayvalue differences only show that a shift has occurred, but it is not

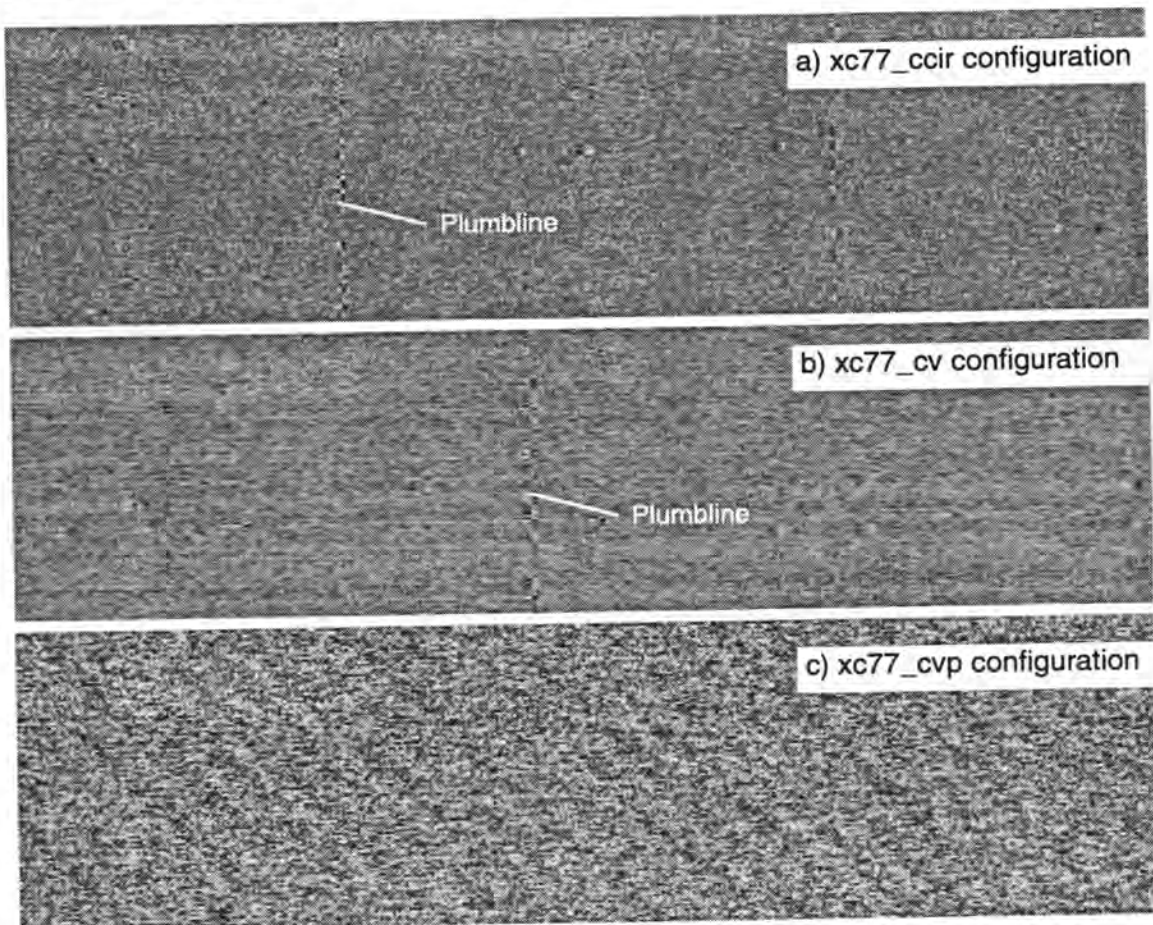


Figure 6.13 Subtraction of consecutive images.

simple to interpret it in terms of the size of the displacement. In Figure 6.13b exhibits horizontal stripes of different brightness. These are attributable to effects between line-jitter and the pixel-clock cross-talk on the video signal. In the `xc77_cv` configuration sampling occurs very close to the pixel-clock frequency. Line-jitter results in a shift of the sampling point with respect to the pixel-clock for the whole line. This in turn leads to shifts in the average grayvalue for lines due to the pixel-clock cross-talk on the video signal. Figure c shows the same portion of imagery as figure b, but for the `xc77_cvp` configuration. The structure of the object (plumblines, targets) is no longer visible, only the phase pattern already discussed in chapter 5 can be seen. Table 6.5 gives the statistics when taking the absolute values of the differences between consecutive images. It shows that the statistics are very similar for both PLL based configurations. The use of the pixel-clock results in a large improvement of the statistics.

Configuration	Average	Standard Deviation	Maximum value	[DN]
<code>xc77_ccir</code>	1.46	1.28	23	
<code>xc77_cv</code>	1.44	1.25	22	
<code>xc77_cvp</code>	1.39	1.13	9	

Table 6.5 Statistics of subtraction using absolute value of grayvalue differences.

Analysis with Temporal Noise from Averaging

A second method analyses the **temporal noise** determined by **averaging the imagery**. The RMS temporal noise is 1.40, 1.34, and 1.25 for the `xc77_ccir`, `xc77_cv`, and `xc7_cvp` configurations respectively. The difference between `xc77_ccir` and `xc77_cv` could be a

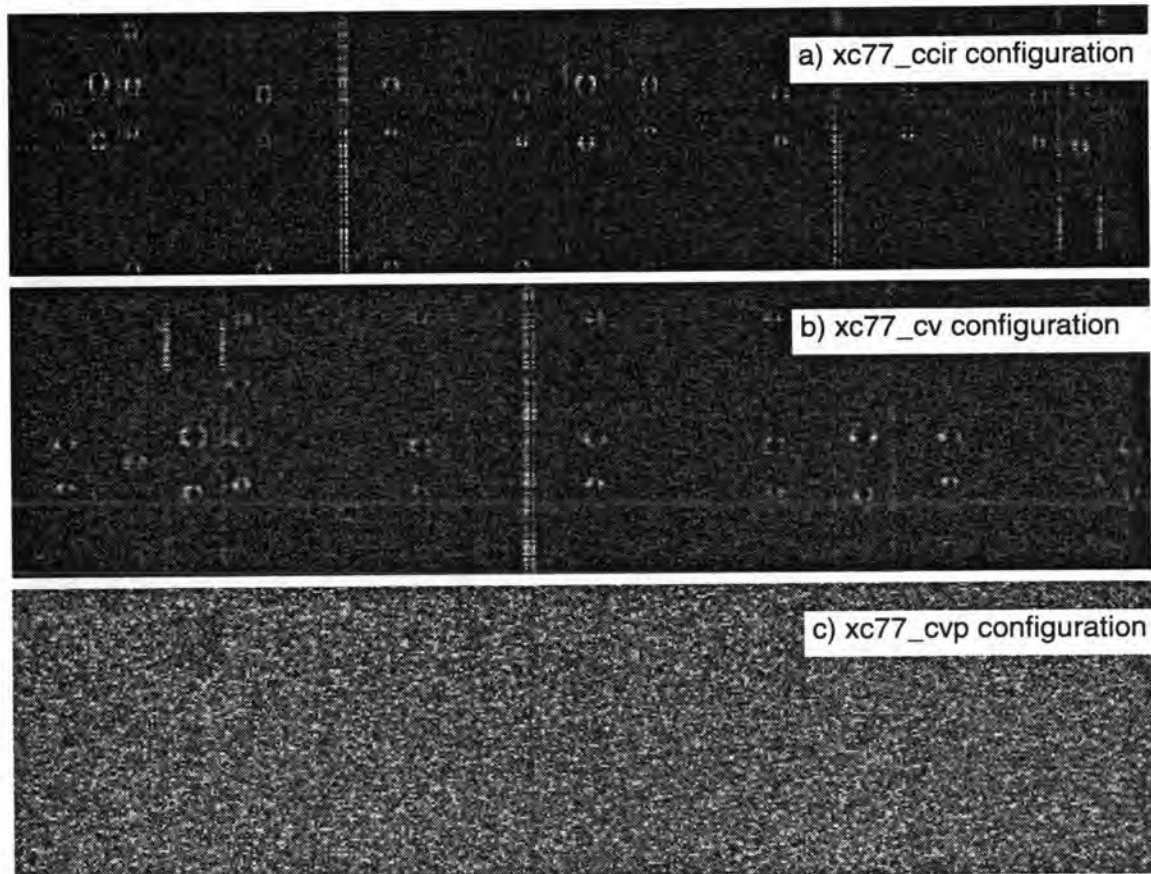


Figure 6.14 Temporal noise for different synchronization methods.

statistical effect. The temporal noise is even further reduced for the `xc77_cvp` configuration as line-jitter is eliminated. Figure 6.14 shows the temporal noise determined from the five images of each series. The images have been stretched to show the differences in temporal noise. Figures a and b show that the largest temporal noise occurs at positions which have the largest grayvalue gradients in x-direction, i.e. at the borders of the targets and the vertical plumblines. Figure c on the other hand exhibits, at first glance, a random noise distribution, but the original imagery is still discernible (on a monitor one can find the rods, the targets and the plumblines). This is according to expectations as temporal noise from shot noise must be higher in brighter areas of the object as it is the square root of the number of electrons collected at the sensor element.

Analysis using the Relation of Temporal Noise to Grayvalues and Gradients

The radiometric method where synchronization errors are best detectable is the **analysis of temporal noise versus grayvalues and gradients**. Theory predicts a linear dependence of temporal noise (within the shot noise domain) on the grayvalues and independence of noise and gradients. The average temporal noise was determined for each grayvalue, and each level of gradient in x and y. The results were plotted with the average temporal noise against grayvalue, gradient in x, and gradient in y. Figure 6.15 shows

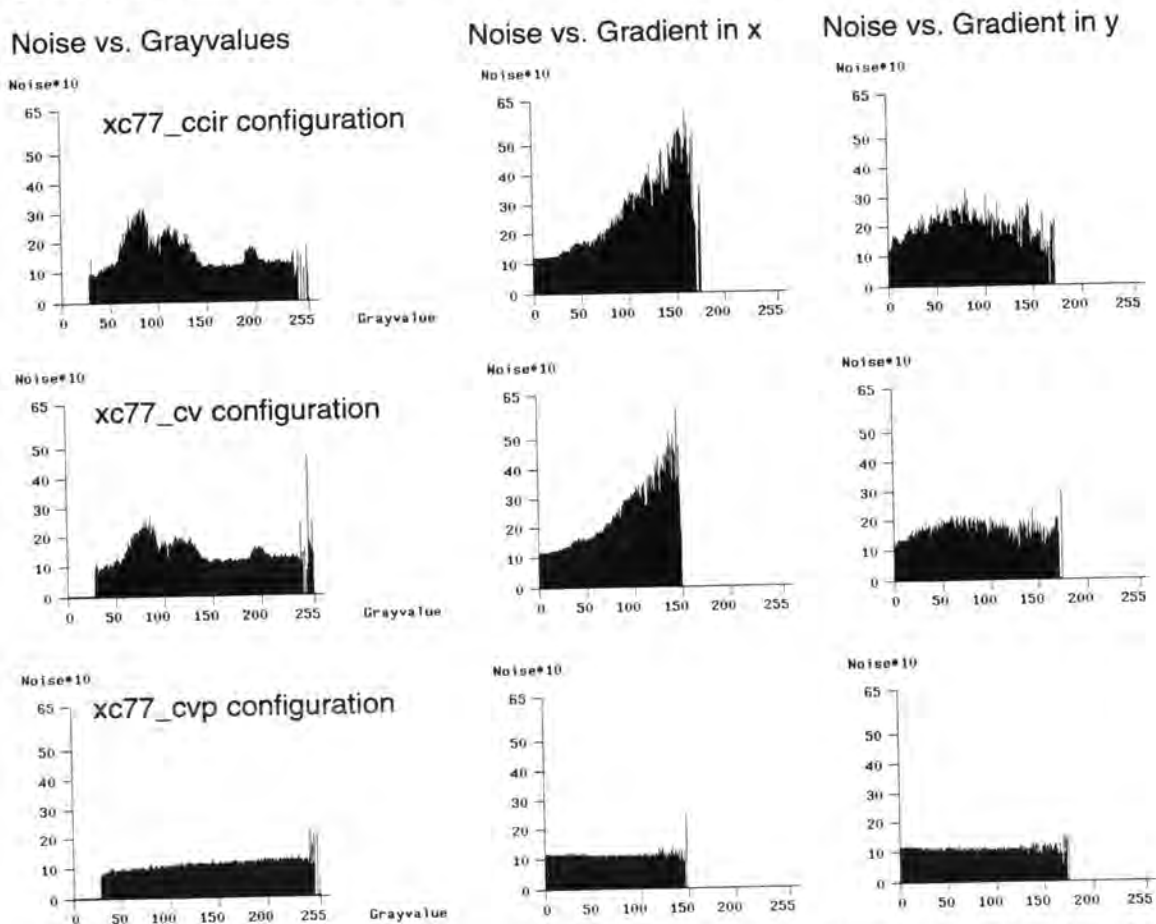


Figure 6.15 Plots of temporal noise versus grayvalue, gradient in x and gradient in y for three configurations. Note that the values for the noise were multiplied with 10. The plots show that the temporal noise shows abnormal characteristics for both configurations using PLL line-synchronization (`xc77_ccir`, `xc77_cv`).

these plots for the three test configurations. For both the xc77_ccir and xc77_cv configurations the plot of noise versus grayvalues exhibits an unexpected increase in the region with grayvalues of 80 to 130. These are the regions of grayvalues which correspond to the positions with the largest gradients. The plots of noise versus gradient in x show the strong increase of temporal noise with increasing gradients in x for both configurations for the PLL line-synchronization. The temporal noise as determined through averaging is influenced by line-jitter due to the variation of the image position from frame to frame. The effect is thus larger for locations with large gradients as the positional changes induce the largest grayvalue variations at these positions. The plot of temporal noise versus gradient in y shows a secondary effect of line-jitter. Horizontal displacements induce changes of grayvalues at positions where gradients in both image directions exist. This results in the observed increase of temporal noise at certain gradients in y.

The plots for the xc77_cvp configurations exhibit the linear characteristic between noise and the grayvalues as well as the independence between noise and graylevel gradient. All three results agree with the theoretical expectations. A linefit between the average noise and the gradient in x results in a slope of 0.22, 0.24 and 0.0 for the xc77_ccir, xc7_cv, and xc77_cvp configurations respectively. The slope for noise versus gradient in y is not significant for all three configurations. Only the form of the curve changes and the level of temporal noise increases at some gradients. Note that the level of temporal noise is, as expected, similar for all configurations for very low gradients.

Positional Repeatability and Geometric Deformations

This method uses the **repeatability of the position of points in image space**. The 18 large targets on the vertical bars of the testfield are used. Their pixel coordinates are determined with LSM using a 13x13 template. Table 6.6 gives the repeatability measures for the three configurations in pixel, micron and for the x-axis also in nsec.

Version	Configuration	RMS _x [Pixel]	RMS _y [Pixel]	RMS _x [μm]	RMS _y [μm]	RMS _x [nsec]
31	xc77_ccir	0.0157	0.0039	0.212	0.043	1.5
32	xc77_cv	0.0267	0.0044	0.294	0.048	1.9
33	xc77_cvp	0.0045	0.0040	0.0495	0.044	0.3
<i>Improvement 32/33</i>		<i>5.9</i>	<i>1.1</i>			
34	cv versus cvp	0.0887	0.0064	0.0976	0.070	6.9

Table 6.6 RMS values from repeatability analysis for different synchronizations.

Version	Configuration	MAX _x [Pixel]	MAX _y [Pixel]	MAX _x [μm]	MAX _y [μm]	MAX _x [nsec]
31	xc77_ccir	0.0354	0.0112	0.478	0.123	3.4
32	xc77_cv	0.0621	0.0141	0.683	0.155	4.4
33	xc77_cvp	0.0107	0.0089	0.118	0.098	0.8
<i>Improvement 32/33</i>		<i>5.8</i>	<i>1.6</i>			
34	cv versus cvp	0.2491	0.0163	2.74	0.179	17.6

Table 6.7 Maximum residuals from repeatability analysis for different synchronizations.

Versions 31 to 33 use their respective average as reference for the repeatability analysis. The results show that line-jitter alone results in an increase of the RMS values in the order of 0.02 to 0.03 pixel. As for a given timing error, the error in pixel depends on the sampling speed. The timing error in nsec is thus a better measure to characterize the performance of the PLL. For this frame-grabber the RMS timing error is between 1.5 to 2 nsec for both the *xc77_ccir* and *xc77_cv* configurations. The short time stability of the PLL averaged over an area of 13 lines is thus a few nanoseconds, which can be considered as very good. The comparison of version 32 and 33 with the *xc77_cv* and *xc77_cvp* configurations shows that pixel-synchronous sampling eliminates line-jitter. The improvement of the RMS errors and the maximum errors is a factor of almost 6 for the *x* coordinates. The improvement in *y* coordinates is very small. Latter improvement must be attributed to a secondary influence of line-jitter on the positional repeatability in *y* direction, i.e. the displacements in *x* direction induce variations of the position in *y*. The fact that pixel-synchronous sampling does eliminate all timing errors is also shown by the similar magnitude of the repeatability in both *x* and *y* direction. The difference in positional repeatability is a factor of 4 to 6 for the PLL based synchronization methods and 1.1 for pixel-synchronous methods in this case, as is shown in Figure 6.16a in the plot of the residuals for the *xc77_cv* configuration. The maximum errors occurring with PLL line-synchronization can exceed 0.1 pixel (see Figure 6.16 and Table 6.7), which shows that such a system is poorly suited for high precision photogrammetry.

A comparison of the geometry obtained between the *xc77_cv* and the *xc77_cvp* configurations shows the following. First a translation of 0.3 and 2.0 pixel can be found in *x* and *y* respectively. The translation in *x* stems from a different definition of the HSYNC signal when it is used in the PLL for the *xc77_cv* configuration versus the edge detection circuit for the *xc77_cvp* configuration. The difference in *y*-direction is simply a result of the different settings for the Look-up-Tables of the frame grabber controlling the active image region. Removing the average shift of each image as compared to the average of version 33 results in the statistics given in version 34 of Table 6.6, Table 6.7, and a plot shown in Figure 6.16b. The RMS values and maximum errors increase significantly, with the maximum reaching 0.25 pixel. The plot of the residuals shown in figure a below shows the shear effect which was already detected during the frame grabber testing.

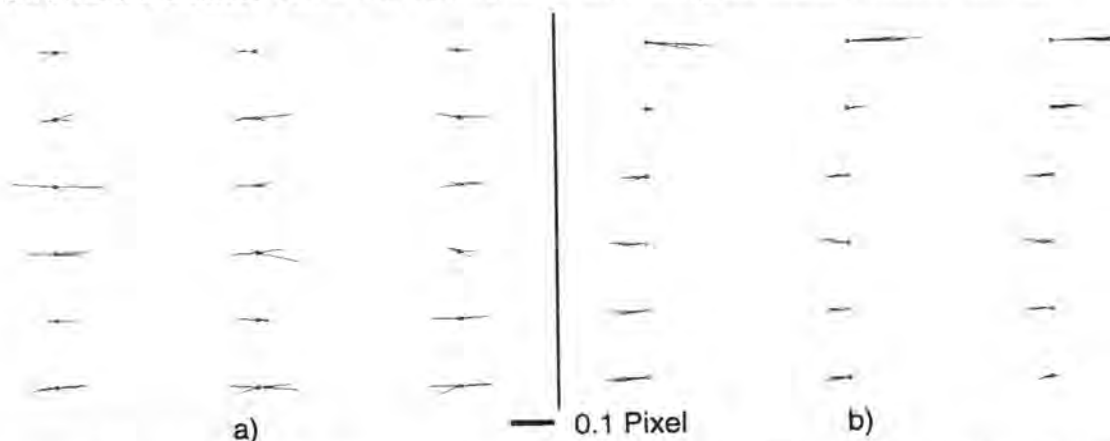


Figure 6.16 Analysis of geometry. a) Plot of residuals for the *xc77_cv* configurations. The large difference in *x* and *y* is evident.
 b) Plot of residuals from a comparison of the results from the *xc77_cv* with the average of the positions from the *xc77_cvp* configuration. The skew resulting from long-periodic effects of line-jitter is evident.

Another method to analyze the performance of the synchronization is via the **position of a vertical line**. The position of the left plumbline shown in Figure 6.1 was measured in each row with LSM in images acquired with the `xc77_cv` and the `xc77_cvp` configurations. Figure 6.18 shows the position of the line for each row of the image. The larger

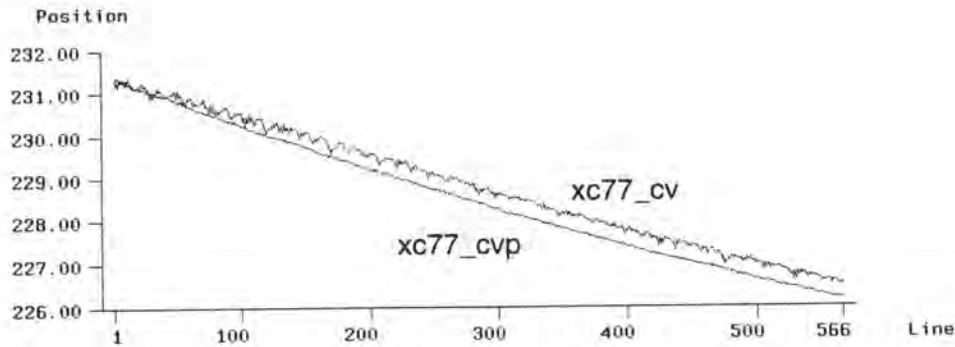


Figure 6.17 Position of plumbline for `xc77_cv` and `xc77_cvp` configurations.

variations of the position for the `xc77_cv` configuration are already visible in this plot. The shear of almost 0.3 pixel (computed from the inclination of respective line fits) is evident. Thus, as already found during the frame grabber testing, synchronization with PLL and composite video results not only in local distortions but also in a massive shear of the imagery. Figure 6.18a shows the residuals of a line fit to the line measured in the image acquired with PLL line-synchronization. The plot for the `xc7_cvp` configuration (b) shows the influence of distortion. The large changes of the line position due to line-jitter in the `xc77_cv` configuration are almost obscuring the otherwise clear trend of the radial distortion. Figure 6.18b shows the differences of the position from row to row. The peak-to-peak variations reach almost 0.6 pixel in the `xc77_cv` configurations, whereas they are only slightly larger than 0.1 pixel for pixel-synchronous sampling.

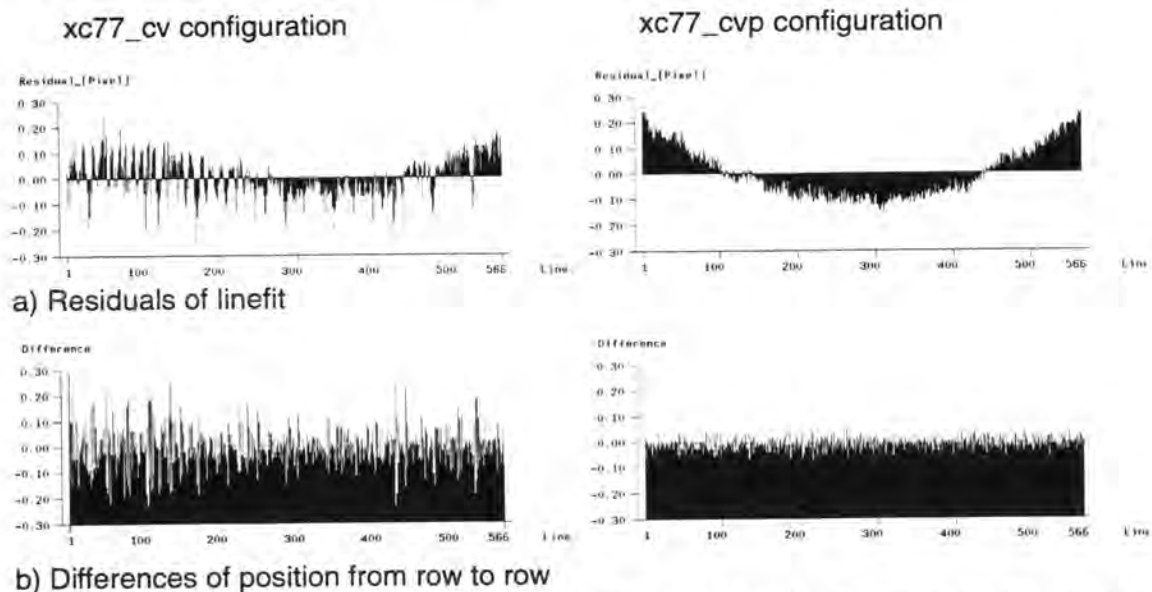


Figure 6.18 Residuals from line fit and differences of position from row to row for a line acquired with PLL line-synchronization and with pixel-synchronous frame grabbing.

Line-Displacement

Line-displacement is one of the potential problems which can still occur with pixel-synchronous sampling. It has only been observed when the horizontal synchronization signal is derived from composite video. Theoretically it can also occur when a horizontal synchronization signal from the camera is used. The image in Figure 6.19 shows the effects of line-displacement. The nice feature of line-displacement is that it is easily visible. Theoretically one could detect the line-displacement and correct the image. This might, however, prove too time consuming, and in many cases impossible.

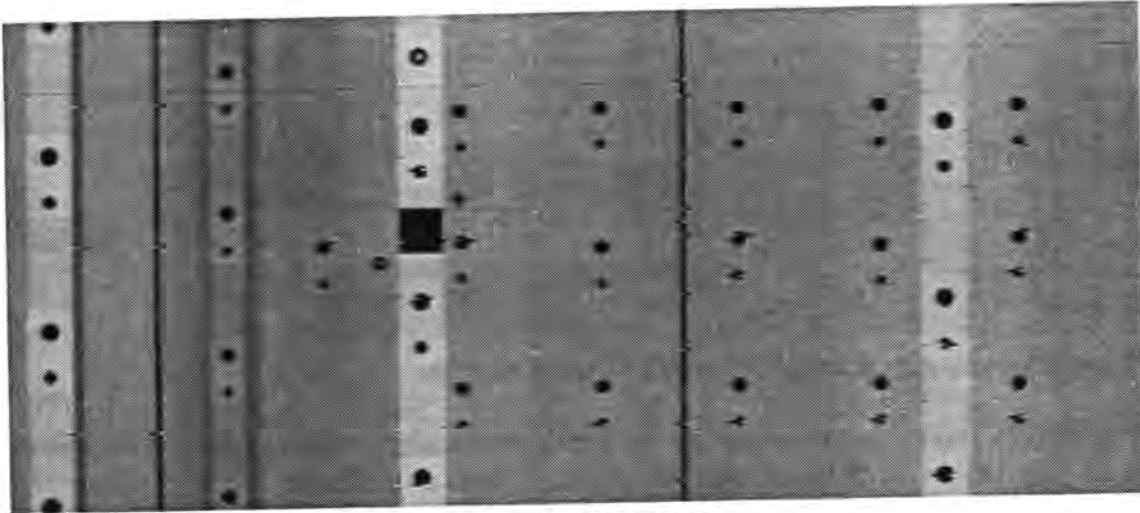


Figure 6.19 Image showing typical line-displacement.

6.3.2 Analog versus Digital Transmission

The comparison of analog and digital transmission is performed analogous to the investigation of PLL versus pixel-synchronous frame grabbing. An identical test configuration is used. The analog and digital data was acquired from a Megaplus camera (provided by Volkswagen AG) with the MAX-SCAN frame grabber. Both provide for analog or digital output and input respectively. The analog signals used are video, vertical sync, horizontal sync, and pixel-clock.

Two series of five images each were acquired with each configuration. Figure 6.20 shows a reduced image and histogram. The camera and the scene brightness are not very well adjusted as there are no grayvalues up to ~ 60 DN for the analog transmission and ~ 40 DN for the digitally transmitted imagery (due to differences in the settings of the camera and the frame grabber).

First the average and standard deviation of the grayvalues of all images were analyzed. The average grayvalue of analog transmitted images differed in some series by up to 3 DN. The other series showed a peak-to-peak difference of 0.49 DN, and the series using digital transmission had peak-to-peak differences of 0.68 and 0.15 DN respectively. These variations were larger than those for the preceding study. The acquisition of the imagery extended over several minutes for each of the series versus only 0.2 sec for the one with the XC77. The average grayvalue of the analog transmitted imagery differed from the digital transmitted by ~ 24 DN or almost 10% of full range (using settings for offset and gain adjusted to standard video signals).

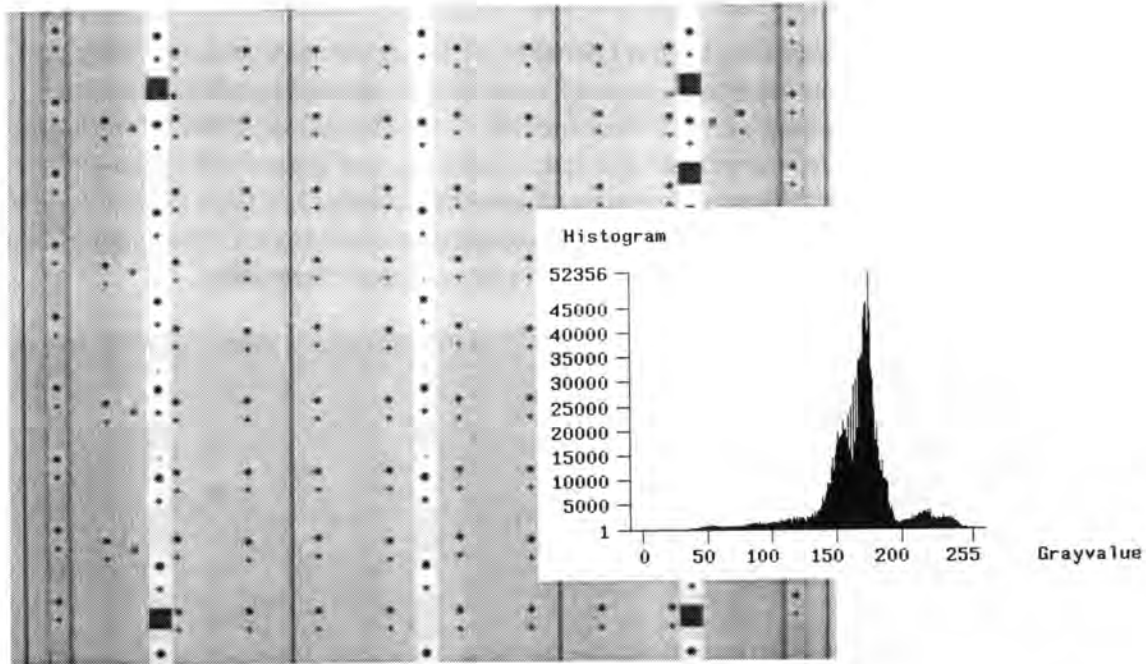


Figure 6.20 Image (size is 1280 x 1024) and histogram.

Figure 6.21 shows the subtraction of two analog transmitted images with differing averages. The structures of the testfield are visible as well as horizontal bands of varying intensity can be detected. Subtraction of images with better corresponding averages resulted in similar results as those for the subtraction of digital images. Both nevertheless exhibit barely visible horizontal bands. The maximum values of the absolute differences are between 10 to 15 DN, depending on the selection of the images, for both analog and digital transmitted images. This corresponds quite well to the results obtained with the XC77 above.

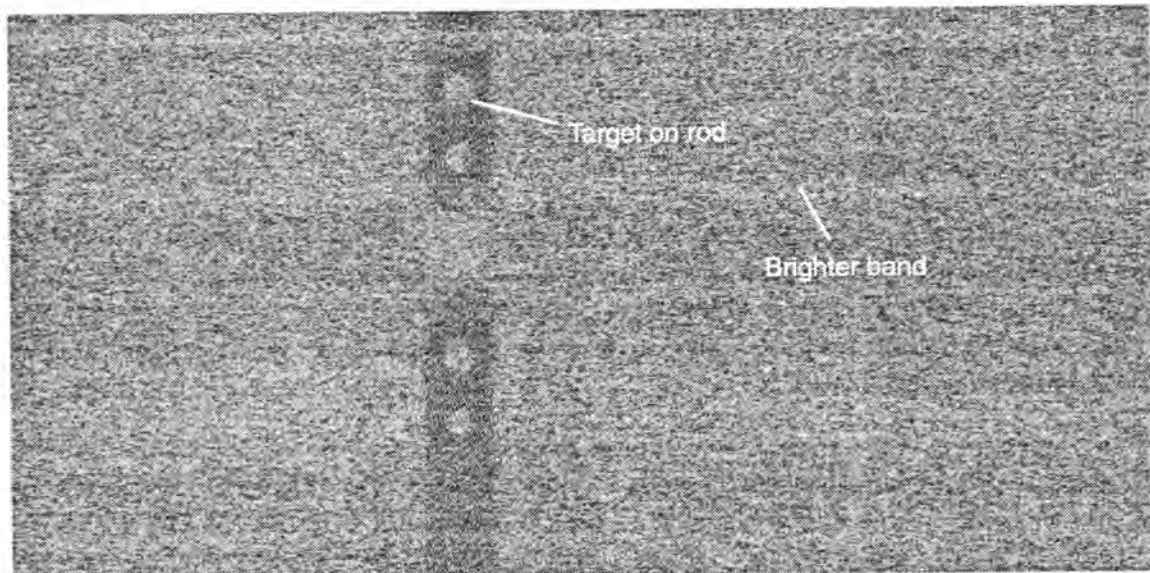


Figure 6.21 Results of subtraction of two analog transmitted images with averages differing by 3 DN (From first series of analog transmitted images).

Figure 6.22 a) shows visualizations of the **temporal noise**. Without compensating for the average and standard deviation the visualization of temporal noise for the first series of

analog transmitted imagery exhibits similar characteristics as the subtraction. After a radiometric adjustment for average and standard deviation a typical temporal noise image such as those for the digitally transmitted imagery is obtained. All dark targets as well as the plumblines are easily visible on a monitor screen.

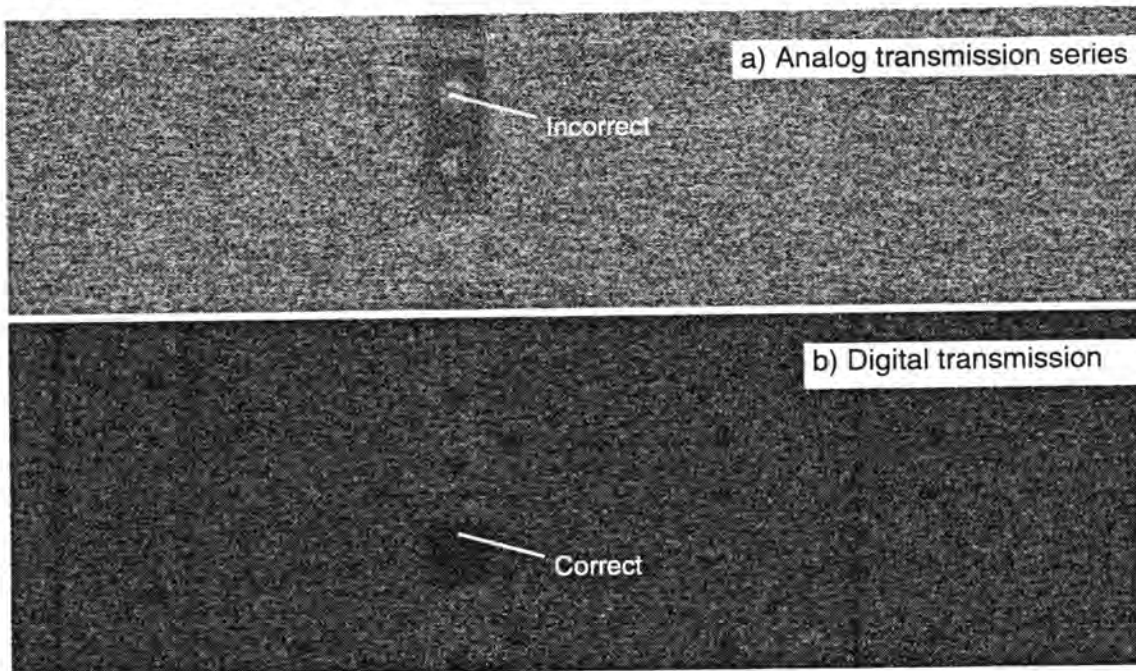


Figure 6.22 Temporal noise with analog and digital transmission. Series 1 of the analog transmitted series contains one image with a clearly different average. This results in the stronger appearance of the image structure as compared to the digital transmitted imagery.

The analysis of temporal noise versus grayvalues and gradients is shown in Figure 6.22. The topmost figure shows that temporal noise would decrease with increasing grayvalues. This contradicts theory and is a result of the changes in average intensity and the standard deviation as discussed above. After the radiometric correction for mean and standard deviation the expected form is obtained as can be seen from Figure 6.22b. Comparing the figures from the analog transmitted imagery to that of the digitally transmitted imagery indicates that the levels are still somewhat higher. The level of temporal noise appears to be higher for analog transmitted imagery in comparison to digital transmitted data. The digital transmitted data showed several other strange effects. The peak for the plot of temporal noise versus grayvalues at the grayvalue 255 is attributable to a blemish and can therefore be excluded (the sensor contains defective pixels and columns). The drop-off of temporal noise starting at 200 DN indicates that the saturation of the camera is starting (sensors show a drop of temporal noise when entering the saturation and eventually reach a noise level of 0 at saturation and when blooming occurs).

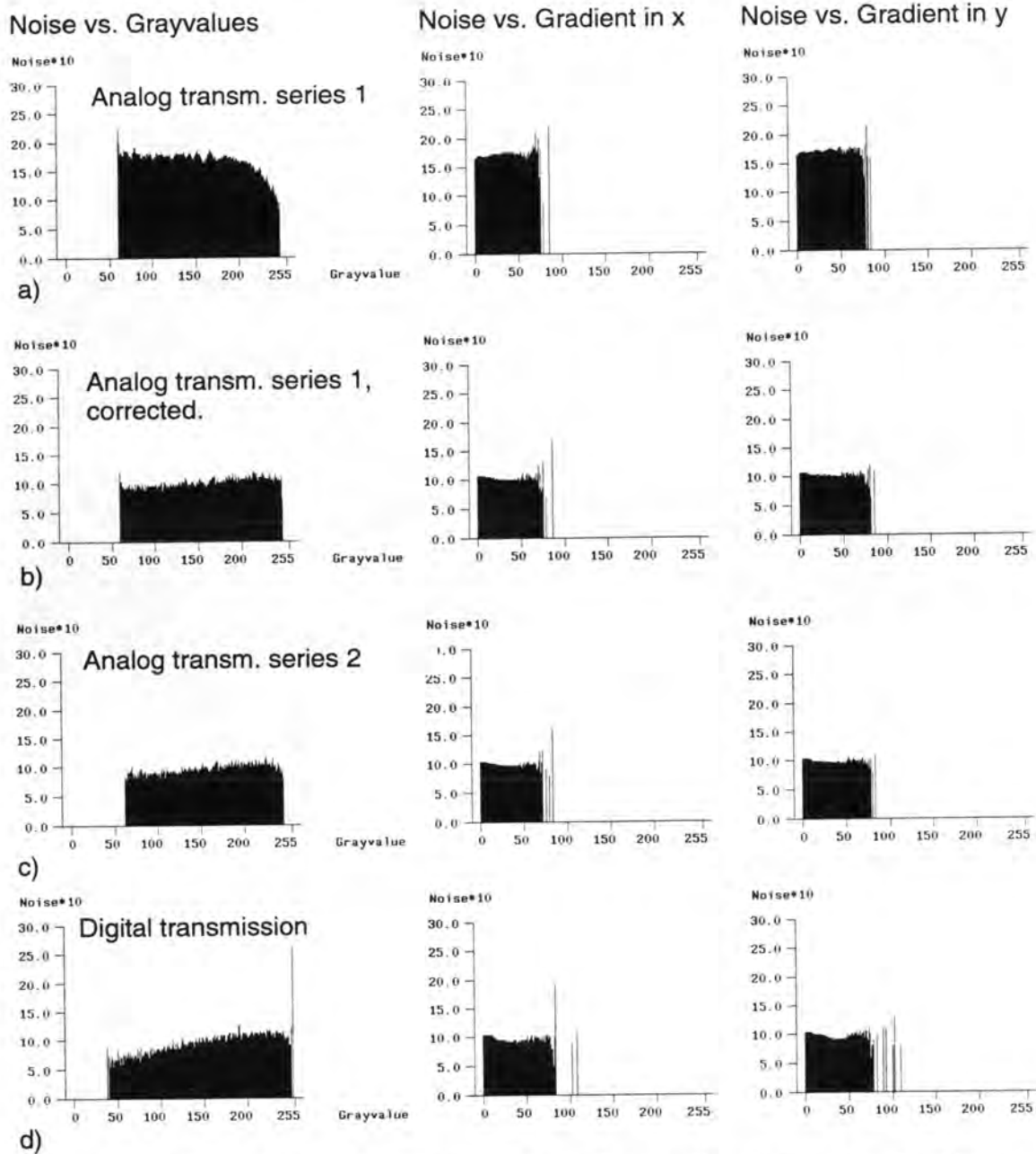


Figure 6.22 Plots of temporal noise versus grayvalue, gradient in x and gradient in y for three configurations. Note that the values for the noise were multiplied by 10.

- a) Temporal noise of analog transmitted imagery before radiometric correction
- b) after radiometric correction.
- c) Temporal noise of a second series of analog images
- d) Temporal noise for a series of digitally transmitted imagery

The **repeatability** of the target positions is determined using a 17 x 17 pixel large template. The results of the repeatability analysis are given in Table 6.8. The results of versions 41 to 44 show that the results are practically identical. The level of performance is quite astonishing considering that with the 6.8 μm pixel spacing of the Megaplus camera a repeatability of 27 to 43 nm can be achieved over several minutes. The maximum residuals reach only 129 and 115 nm in x and y respectively.

Version	Configuration	RMS _x	RMS _y	MAX _x	MAX _y
		[Pixel]	[Pixel]	[Pixel]	[Pixel]
41	Analog series 1	0.0048	0.0059	0.0126	0.0150
42	Analog series 2	0.0050	0.0059	0.0136	0.0169
43	Digital series 1	0.0063	0.0040	0.0189	0.0098
44	Digital series 2	0.0054	0.0055	0.0156	0.0155
45	A1 vs D1	0.0077	0.0089	0.0232	0.0213
46	A2 vs D2	0.0090	0.0085	0.0268	0.0258

Table 6.8 RMS values from repeatability analysis for pixel-synchronous and digital transmission.

Versions 45 and 46 are a comparison of the analog transmitted data with the average of the digitally transmitted imagery of the respective series when neglecting the influence of a translation between the images. The translation is attributable to the different selections of the active image region by the frame grabber for the analog and digitally transmitted imagery. The time span between the analog and digitally transmitted series is several minutes in each case. This might be one reason for the decrease of the performance.

It can be concluded that although the radiometric characteristics of digital transmission are more stable no difference in the geometric fidelity of analog transmission with pixel-synchronous frame grabbing and digital transmission can be found.

6.4 Target Size

A test with seven targets ranging in size from 2 pixels to almost 20 pixels was used to assess the relation between target size and repeatability. Two series of 5 images each were acquired using pixel-synchronous frame grabbing (*xc77_cvp* configuration) one week after another. Figure 6.23 shows part of an image with one group of the targets. Each image contains six groups of targets. Table 6.9 gives the results of the repeatability analysis. The diameter of the targets is given in object space (DO, mm) and in the imagery (DI, pixel). The contrast was computed as the grayvalue difference of each target versus the background divided by the contrast difference of the largest target. The "Ratio" in x and y indicates the RMS value divided by the best RMS value for the respective coordinate direction.

DO	DI	Contrast	RMS _x	RMS _y	Ratio _x	Ratio _y
[mm]	[Pixel]		[Pixel]	[Pixel]		
5	2	0.40	0.0158	0.0170	4.4	4.4
7.1	3	0.65	0.0086	0.0121	2.4	3.1
10	4	0.85	0.0082	0.0061	2.3	1.6
14	6	0.96	0.0049	0.0054	1.4	1.4
20	9	0.97	0.0048	0.0053	1.3	1.4
28	12	1.0	0.0036	0.0039	1.0	1.0
40	17	1.0	0.0036	0.0048	1.0	1.2

Table 6.9 Repeatability as a function of target size.

with:

- DO..... diameter of target in object space
 DI..... diameter of target in image space
 Contrast..... maximum contrast of target with respect to background relative to largest target

Figure 6.23c shows a plot of the RMS-values versus the target size in object space. Both the results of Table 6.9 and the plot indicate a dramatic increase in repeatability as the target diameter increases from 2 to 6 pixel. Thereafter the improvement in precision becomes very small. No difference can be found between the targets with diameters of 12 and 17 pixel. A comparison with the contrast values indicates that the repeatability exhibits an inverse relation to the contrast. The contrast is decreased due to the system MTF. This demonstrates the relationship between MTF and geometric precision, whereby a better MTF provides for a better precision (at least for small targets).

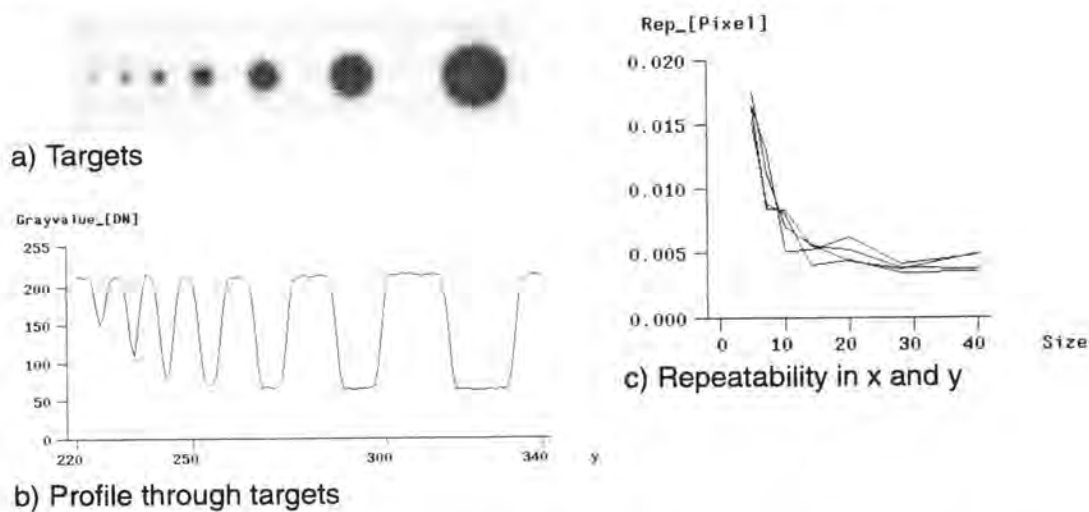


Figure 6.23 Analysis of repeatability as a function of target size and template size.

- Image with targets.
- Grayvalue profile through targets showing the decrease in contrast for smaller targets.
- Repeatability as a function of target size in the image/object showing improving repeatability for increasing target sizes up to approximately 8 pixel diameter.

Based on this empirical study it was concluded that targets should have a diameter of at least 6 pixels to attain utmost internal precision. The rule of thumb which was developed over the last years - stating that targets should span between 5 and 10 pixels - was shown to be valid, although five pixels are on the lower limit. The results are also in accordance with the findings of *Förstner, 1982; Trinder, 1988*.

6.5 Test Configurations for Warm-Up-Effects and Repeatability

The camera was placed approximately 3 m in front of the large testfield with a 9 mm CCTV-lens. Figure 6.24 shows the locations of the camera, testfield and illumination. Images were acquired over a period of 8 days. The complete installation of the camera, illumination and image acquisition system was set up one week prior to the start of the test series with the image acquisition system running, but the camera switched off. The image acquisition system was always reconfigured for the acquisition of each image as

several types of cameras were used in this test (besides the XC77 a Megaplus camera was used with the analog and digital interface). During the first days images were acquired at short intervals. Thereafter only a few images were acquired each day. At the end of the eight days a series of twenty frames were acquired. The data of this last test was used for the evaluation of the performance of LSM above.

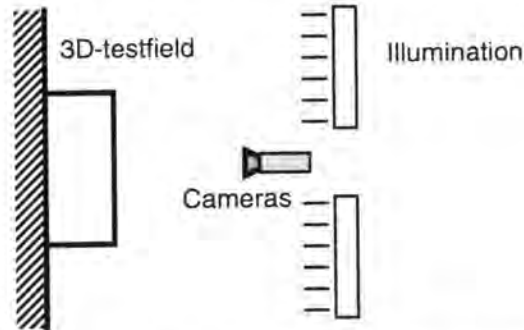


Figure 6.24 Test arrangement for warm-up and repeatability evaluation

6.6 Warm-Up-Effects

Warm-up-effects have been studied by *Gülch, 1984 and 1985; Luhmann, 1988; Heikkilä, 1988; Curry et al., 1986; Dähler, 1987; Wieting, 1990*. Figure 6.25 shows plots for data acquired during the first three hours. Figure 6.25a shows a plot of the times when images were acquired with the XC77. At first images were grabbed each minute. Later on the rate was reduced to one image each 5 minutes and finally to even longer intervals. Figure 6.25b shows the average image intensity and Figure 6.25c the standard deviation of the grayvalues for each of the images. Both exhibit large changes for the first thirty minutes. Figure 6.25d indicates the average displacement of 90 points with respect to the average position of a set of 20 images taken at the end of the repeatability test series (corresponds to version 2 of section 6.1). A significant shift occurred in the position of the targets in the initial state and the reference values. The curve for the average image displacement for the y coordinate shows a displacement of 0.1 pixel within the first 30 to 60 minutes, and a slow drift thereafter (0.02 pixel for the rest of the day). The x-coordinate exhibits a similar drift. Large displacements occur at two instances coinciding with the large changes in average image intensity and the standard deviation of grayvalues (at 10 and 35 minutes). No clear explanation could be found for this phenomenon. In case of strong cross-talk of the pixel-clock on the video signal the shift of the sampling point of the ADC could result in a shift of the grayvalues and of the image position. The change in time computed from the shift would correspond to 21 nsec or 1/3 of the clock frequency. Figure 6.25e shows a plot of the residuals from the repeatability analysis for a point in the middle of the image. It exhibits very similar characteristics as shown by the average image position.

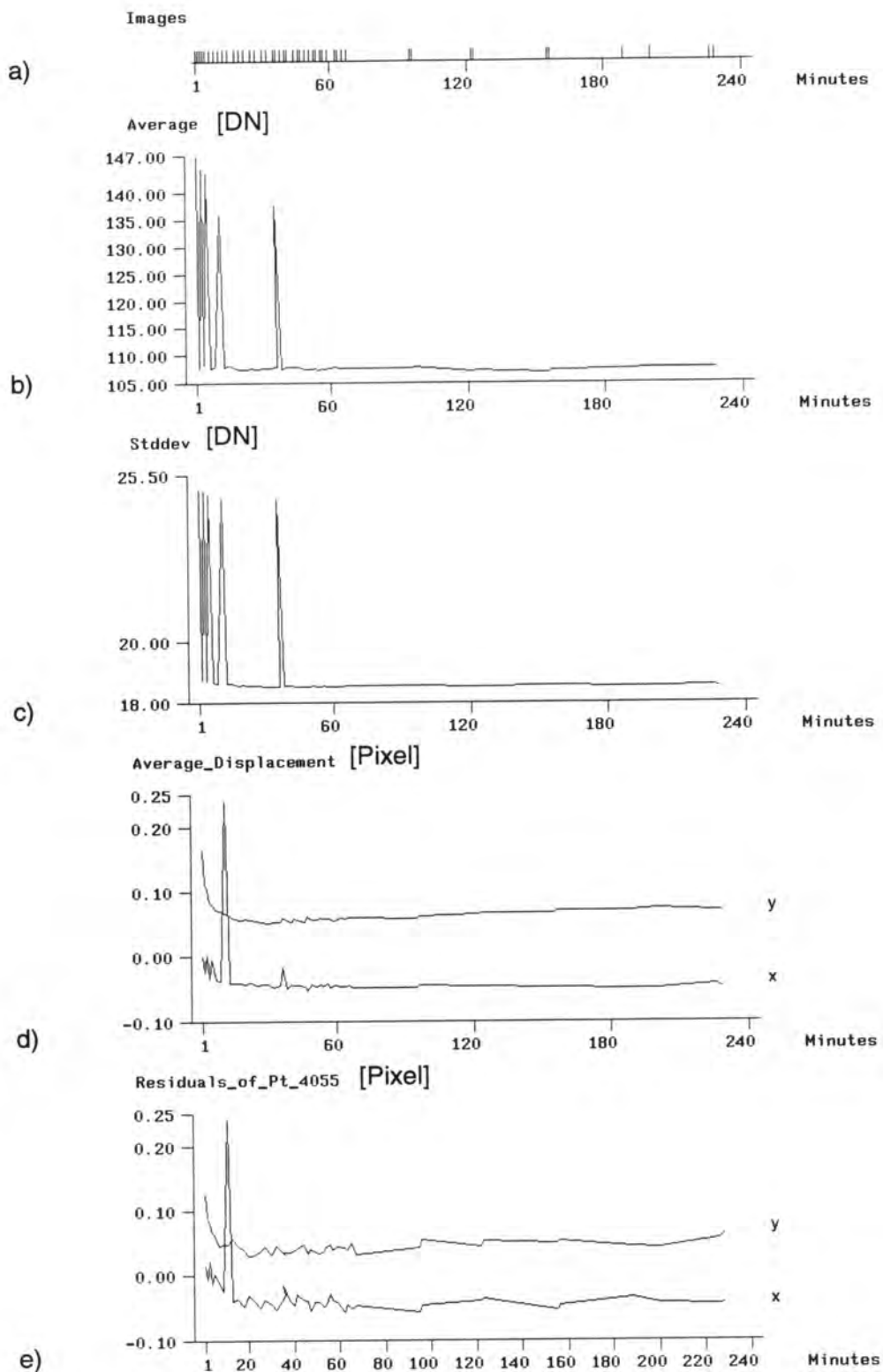


Figure 6.25 Warm-up-effects of XC77 with pixel-synchronous frame grabbing. a) Times where images were acquired. b) Average of grayvalues of images. c) Standard deviation of grayvalues. d) Average displacement of target positions. e) Displacement of one point.

The residuals for the first hour with respect to version 2 (of section 6.1) are shown in Figure 6.26a. The scale for the residuals is a factor 10 smaller than for the typical plots of residuals shown in the sections above and later on. The systematic shift which is shown in Figure 6.25 d is also apparent in this plot as well as the one image with the large shift. Figure 6.26b shows a plot for the repeatability of the imagery from the first day starting one hour after the cameras have been switched on. Table 6.10 gives the results of the repeatability analysis for the data of the first day starting one, two and three hours after the start of the testing (Versions 1, 2, 3 respectively). There is still a small improvement for the y-axis when excluding the results up to three hours. This is attributable to the small drift which is still occurring in the y-direction and shown in Figure 6.25d. The results of version 2 show that a repeatability of 0.01 pixel and better can already be obtained after one hour of warm-up.

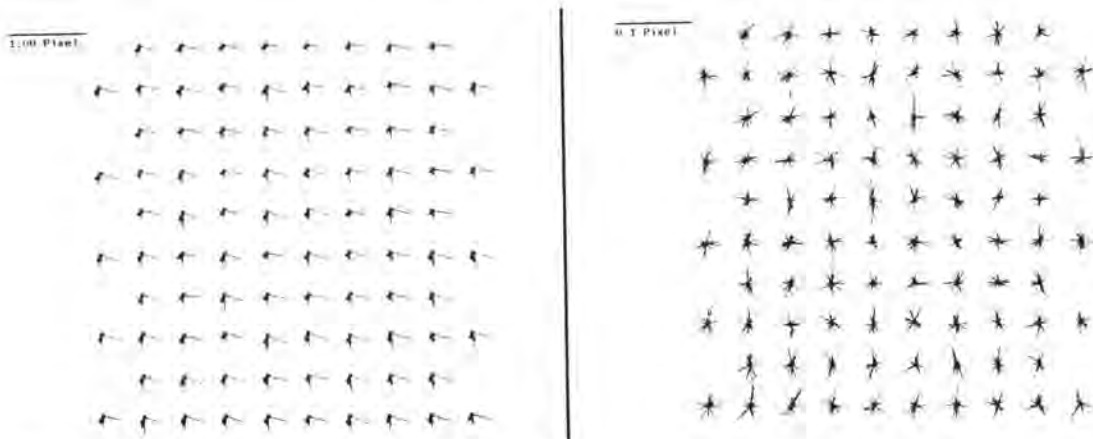


Figure 6.26 Repeatability of first day.
 a) Displacements during first hour compared to the reference from the end of the series.
 b) Repeatability of the first day starting two hours after initialization.

Version	Images	RMS _x [Pixel]	RMS _y [Pixel]	Max _x [Pixel]	Max _y [Pixel]
1	24	0.0077	0.0100	0.0243	0.0364
2	18	0.0075	0.0081	-0.0233	0.0363
3	14	0.0077	0.0074	-0.0230	0.0337

Table 6.10 Influence of warm-up-effects

RMS_x..... Root mean square of residuals in x
 RMS_y..... Root mean square of residuals in y
 MAX_x..... Maximum residual in x
 MAX_y..... Maximum residual in y

It must be noted that the time period required by a certain camera for warm-up is dependent on its construction. The results shown here are typical for small CCTV type CCD-cameras. The deformation for the XC77 are different when PLL line-synchronization is used. In that case the variation of the frequency of the quartz oscillator due to temperature leads to additional displacements in x-direction. The displacements with pixel-synchronous sampling are more pronounced in y direction due to the physical construction of the XC77, where sensor and lens are only connected by the aluminium bottom of the camera.

6.7 Repeatability

The data of 9 days was used for this test. Figure 6.27a shows the times when images were acquired. Figure 6.27b shows the average image intensity, which was within a few grayvalues for most of the time. Larger variations were found only during the beginning (warm-up period), for one image on day 2, and at the end.

Again the average image intensity and the positional analysis for an individual point 90 points are shown. One can detect once more the connection between the average image intensity and the changes in the x position. Furthermore a large difference (~ 0.04 pixel) existed between the positions of the first 5 days and that of days 8 and 9. One image exhibited line-displacement and was removed from the analysis. At the end of the series a large jump in average image intensity and difference in the position was observed, the origin of which could not be determined. The camera was mounted on a heavy aluminium pole which should not show any physical deformation. The conditions of the test were with respect to temperature changes problematic, as the air-conditioning is shut off over night and on the weekend, which was day 6 and 7. During this time the room temperature increased by 5°C , potentially leading to changes.

The results of different evaluations of the data are compiled in Table 6.11. Versions 51 and 52 give the results for all images with the average of the last 20 frames acquired in a series as reference. The average shift of each image in x and y was subtracted for the repeatability analysis of version 52. The RMS values of this version are plotted in Figure 6.28b.

Version	Images	RMS _x [Pixel]	RMS _y [Pixel]	Max _x [Pixel]	Max _y [Pixel]
51	93	0.0473	0.0605	0.2672	0.2291
52 (no trend)	93	0.0100	0.0149	0.0609	0.0689
53 after 1 hour	61	0.0390	0.0540	0.0831	0.1261
54 after 1 hour (no trend)	61	0.0090	0.0135	0.0343	0.0483
55 day 2 to 5	14	0.0087	0.0111	0.0304	0.0382
56 day 8 and 9	23	0.0140	0.0081	0.0551	0.0399

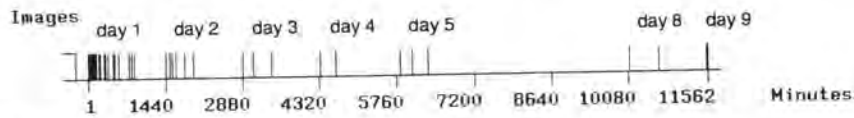
Table 6.11 Repeatability

Versions 53 and 54 use all data after the first hour with the same reference as versions 51 and 52. The average shifts were again removed for version 54. The plots of residuals of these versions are given in Figure 6.29. The systematic differences of the position which occurred during days 5 and 8 are evident. This is most probably attributable to changes in temperature caused by switching off the air conditioning during this period (weekend). When removing the average shifts, a repeatability of 0.01 pixel is achievable for several days.

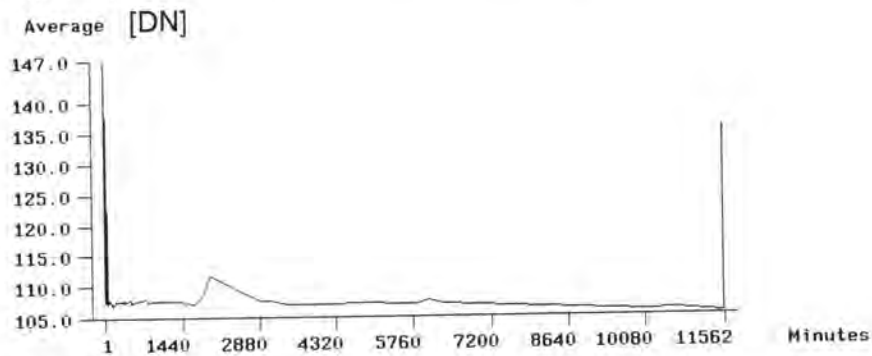
Version 55 is an analysis of the data from days 2 to 5 and version 56 of days 8 to 9. The RMS values are plotted in Figure 6.28 and the residuals are plotted in Figure 6.30. The larger RMS values of the y-direction of version 55 are again most probably effects of temperature changes (the air conditioning is also off over night). The large change occurring at the end of the series is probably the effect of some inadvertent changes to the illumination.

The following conclusions can be drawn:

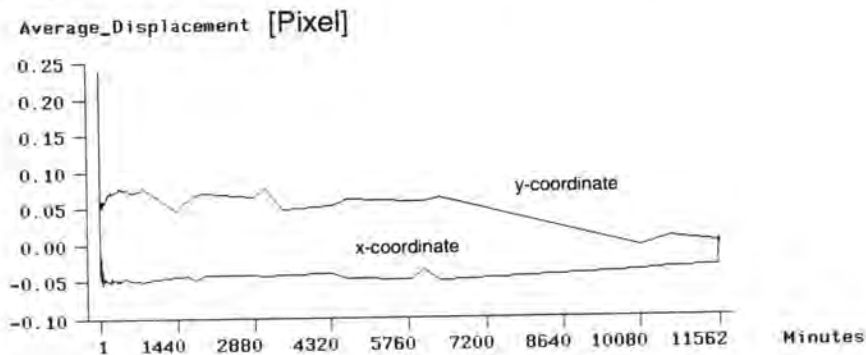
- An inexplicable connection between the average image intensity and the position was found.
- A positional repeatability of 0.01 pixel over several days can be achieved.
- Camera and image acquisition system should be turned on sufficiently long to reach a temperature equilibrium. The time required to warm up depends to a large extent on the camera but is at least 1 hour for typical CCTV-type cameras



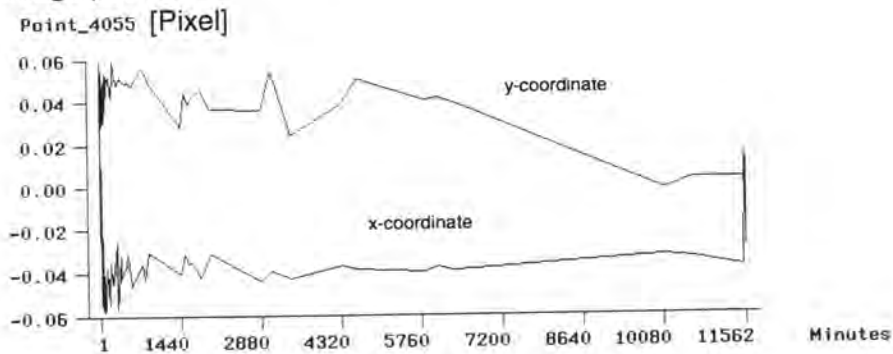
a) Time of image acquisition



b) Average image Intensity

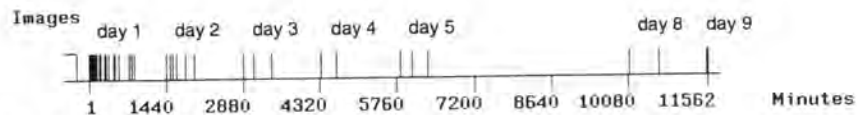


c) Average image position

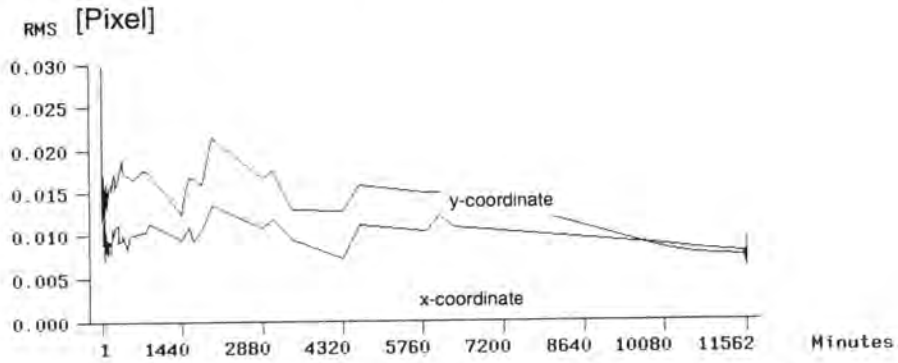


d) Residuals of one point

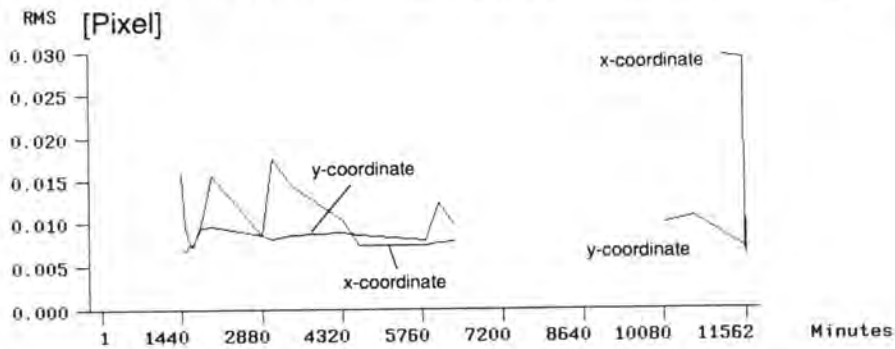
Figure 6.27 Repeatability analysis for a period of 9 days.



a) Time of image acquisition



b) RMS values for repeatability with removal of the translation for each image



c) RMS values for repeatability for images of days 2 to 5 and days 8 and 9

Figure 6.28 Repeatability when correcting for trend (b) and repeatability for the duration of days 2 to 5 and days 8 to 9 (c).

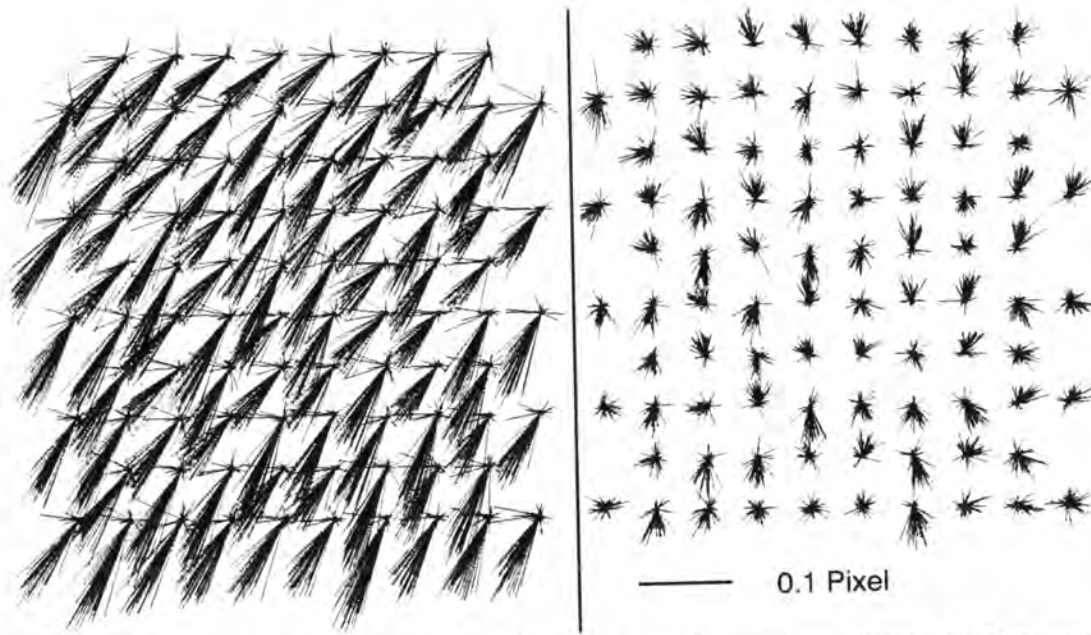


Figure 6.29 Repeatability for all days without removal of average image displacement (left, version 53) and with removal thereof (right, version 54).

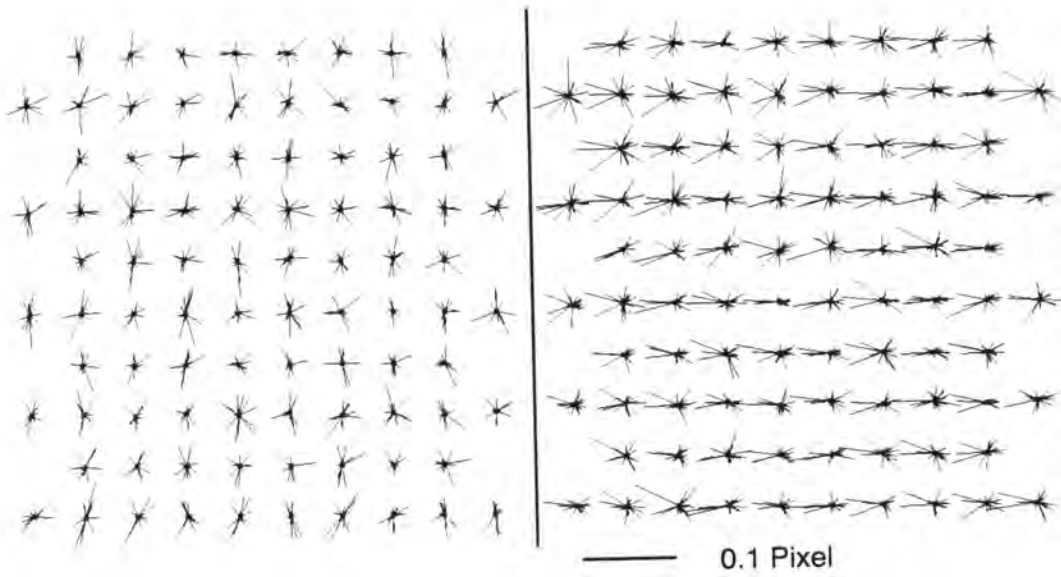


Figure 6.30 Repeatability for days 2 to 5 (left, version 55) and days 8 and 9 (right, version 56)

6.8 Local Illumination Gradients

The illumination of targets as well as any object is critical for the measurement precision. Most illumination systems vary their brightness with the frequency of the power supply. This is a problem when shuttered cameras with short exposure times and a different frame rate as the power supply frequency are used. No degrading effects could be found for Frame Transfer and Interline Transfer sensors with integration times of approximately 20 and 40 msec respectively. The spectral characteristics of the illumination has several influences. To make best use of the light energy emitted by the lamps, they should emit their light in a spectral region where the camera is most sensitive. The effect of the spectral distribution on PRNU can lead to a degradation of the uniformity and thus induce positional changes (compare section 5.3). These changes would result in a geometric non-uniformity which is dependent on the spectral light distribution. The magnitude of these displacements was not studied but was assumed to be very small. The MTF can be degraded at long wavelength due to optical cross-talk (see e.g. *Beyer, 1992*). A decrease in MTF can on one hand reduce aliasing and on the other degrade the contrast and thus the measurement accuracy. The most apparent problem associated with illumination are shadows and local illumination gradients. They were investigated as one possible source of systematic errors found in the analysis of the three-dimensional accuracy test. Great care was taken to create a uniform and diffuse illumination. Nevertheless points close to areas with shadows exhibit systematic displacements parallel to the intensity gradient (see section 7.4.3). The following tests were performed to assess the magnitude of the displacement and the effect of the template size thereupon.

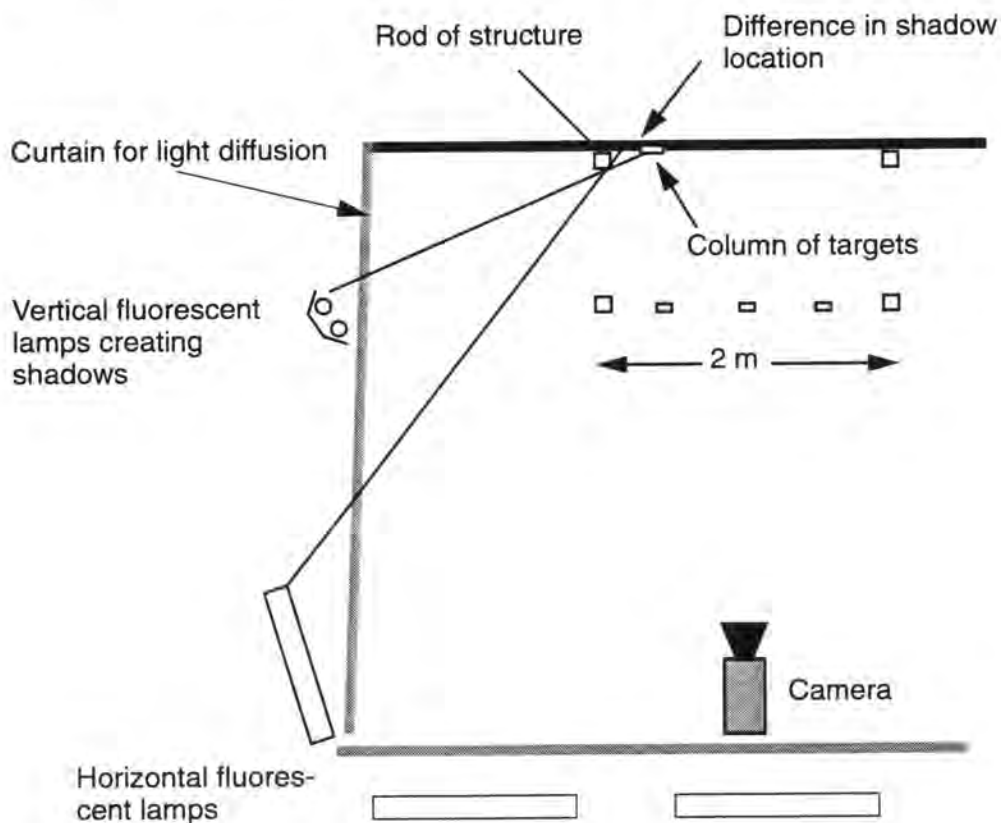


Figure 6.31 Plane view of testfield, curtains, and camera stations.

6.8.1 Empirical Verification

Figure 6.31 shows the configuration of the lighting system, the testfield structure, and the camera. The latter is positioned to cover the testfield area used in the three-dimensional test and to image the columns of points in question. The lamps causing the problem are the fluorescent lamps located very close to the front wall of the testfield and oriented vertically. They considerably improve the brightness of the wall (see Figure 6.32), but the resulting shadow of the vertical rod of the structure reaches the column of targets.

Series of images with these lights on and off were acquired in order to evaluate the influence of these lights on the image position as determined by LSM. First a series of five frames was taken with the frontmost lights on, then two series of five frames each were grabbed with the lights switched off, and finally another series with the lights on was acquired. The first and last series allow to verify whether or not the setup had been stable over the period of the investigation. Figure 6.32a and b show zoomed portions of the im-

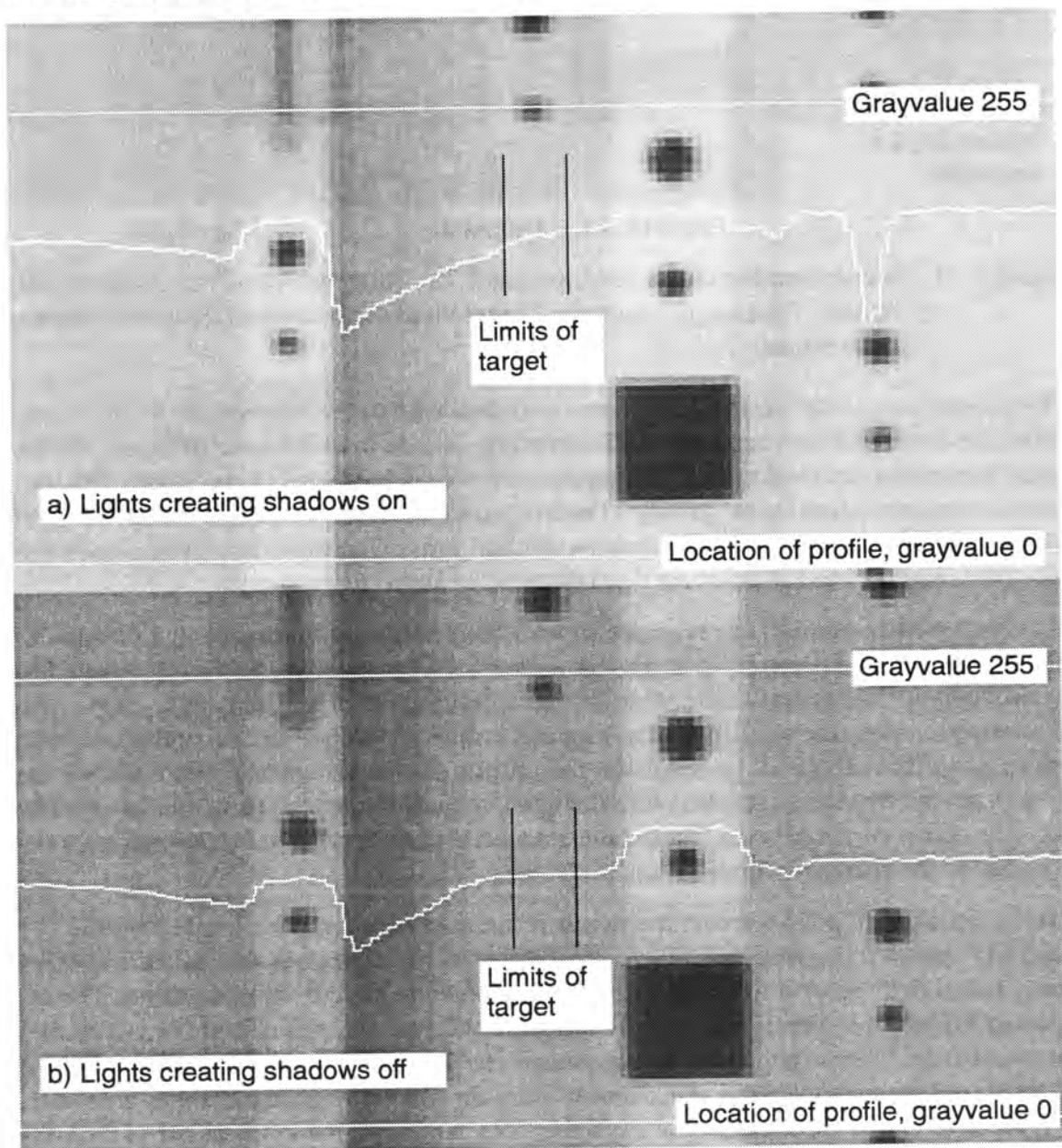


Figure 6.32 Imagery with profiles. a) with lights on the side on. b) with the lights off.

agery, in a) with the frontal lights in question switched on and in b) switched off. The average intensity of the imagery decreases by a factor 1.3 when these lights are off. The difference of the intensity within the area of the target is evident from the profiles. The intensity gradient within the limits of the target as indicated in the figure is 3.8% with the lights to the side on and is reduced to 0.6% with them switched off.

Figure 6.33 shows two patches for a target on a column after convergence of LSM and a template. The difference in the template size results in a smaller or larger area of the target which is used for the LSM.

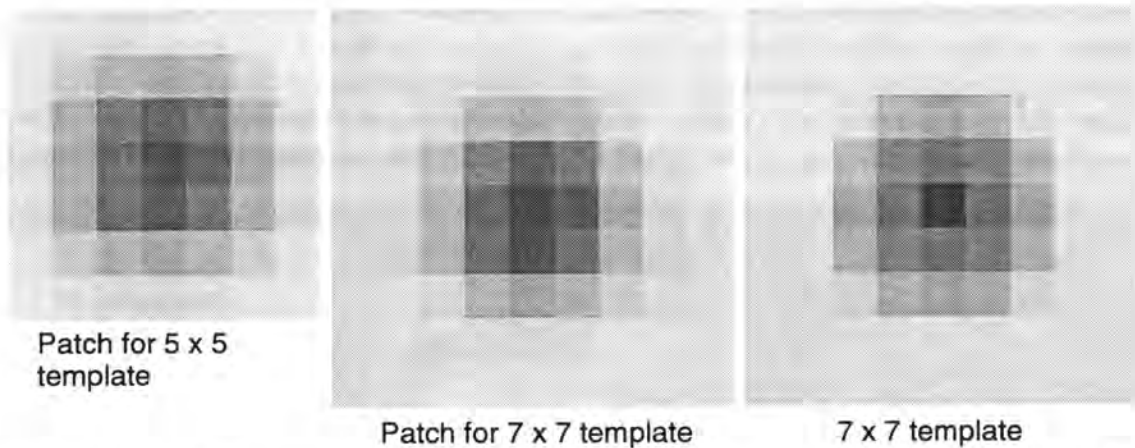


Figure 6.33 Patches and templates for 5 x 5 and 7 x 7 template sizes for a point of left column. The images include a 1 pixel wide seam around the actual patches and template.

The coordinates of all large targets were measured with a 5 x 5 as well as a 7 x 7 template and averaged for each series. The average of the first series of images with the lights generating the shadows on the targets switched off was used as reference. The targets are separated into three groups. The first group includes all targets except those of the two columns affected by the shadows of the lights. The other two groups each use only the targets of the leftmost and the rightmost columns respectively.

For each of these groups the repeatability was determined with the average position of the targets in the first series with the lights creating the shadows off as reference. The comparison of the second series with the same lighting configuration, taken at the end, was used to assess the stability of that group of targets for each of the two templates (versions xx1). The effects of the lights on the position of the groups is computed with the data from the two series grabbed with the lights in question on and using the same reference as above (versions xx2). These indicate whether or not positional displacements occur due to the change in illumination.

The results for all points except the points of the two columns (Version 112 versus 111 and 212 versus 211) given in Table 6.12 indicate that the change in illumination induces only minor, with respect to the measurement accuracy negligible, displacements. The repeatability in the x-direction is slightly degraded whereas the repeatability in y-direction is unaffected. The origin of this is apparent from Figure 6.34 and Figure 6.35. Figure 6.34 shows the vectors of the repeatability analysis when no lighting changes are made. Figure 6.35 shows the influence of the lights. The targets on the leftmost bar of the test-field structure as well as the ones on the wall exhibit systematic displacements of approximately 0.02 pixel in x-direction.

The effect of the displacement due to the lighting and as a function of the template size is shown with the other comparisons. The average displacement for the targets of the left column is 0.027 and 0.015 pixel for the 7 x 7 and 5 x 5 template (versions 122 and 222), and the maximum displacements are 0.043 and 0.029 pixel respectively. The values for the right columns are -0.016 and 0.009 for the average and -0.032 and -0.021 for the maximum values (versions 132 and 232). The difference in the displacements for the two columns could be attributable to the differences in the lighting arrangement, i.e. the position of the lights with respect to the testfield and the background to the sides.

Version / # Pts.	Shift _x [Pixel]	Shift _y [Pixel]	RMS _x [Pixel]	RMS _y [Pixel]	MAX _x [Pixel]	MAX _y [Pixel]
7 x 7 template						
111 / 150	-0.000	0.000	0.006	0.005	-0.017	0.017
112	-0.002	0.000	0.007	0.005	-0.023	0.017
121 / 6 left	0.001	0.004	0.006	0.005	0.010	0.008
122	0.027	0.001	0.028	0.006	0.044	0.013
131 / 6 right	-0.000	0.001	0.007	0.006	-0.011	0.012
132	-0.016	-0.002	0.018	0.006	-0.032	0.011
5 x 5 template						
211 / 150	0.000	0.000	0.005	0.005	-0.016	0.015
212	-0.002	0.000	0.006	0.005	-0.016	0.015
221 / 6 left	0.000	0.007	0.006	0.008	0.009	0.014
222	0.015	0.004	0.016	0.006	0.029	0.013
231 / 6 right	0.002	0.002	0.005	0.005	0.009	0.012
232	-0.009	0.001	0.011	0.007	-0.021	0.018

Table 6.12 Analysis of shadows.

This investigation proves that shadows are a very serious problem and limit the achievable accuracy. The analysis shows furthermore that the influence can be decreased with a 5 x 5 instead of a 7 x 7 template by a factor of almost 2 for the type of targets used. This demonstrates that this type of targets, in contrast to retroreflective targets, is very susceptible to local changes in illumination.

It was shown that:

- The displacements due to shadows reach 0.04 pixel.
- The magnitude of the average displacements are between 0.01 and 0.03 pixel.
- The effects of the shadows is in this case reduced by a factor of almost 2 when a 5 x 5 template instead of a 7 x 7 template is used.

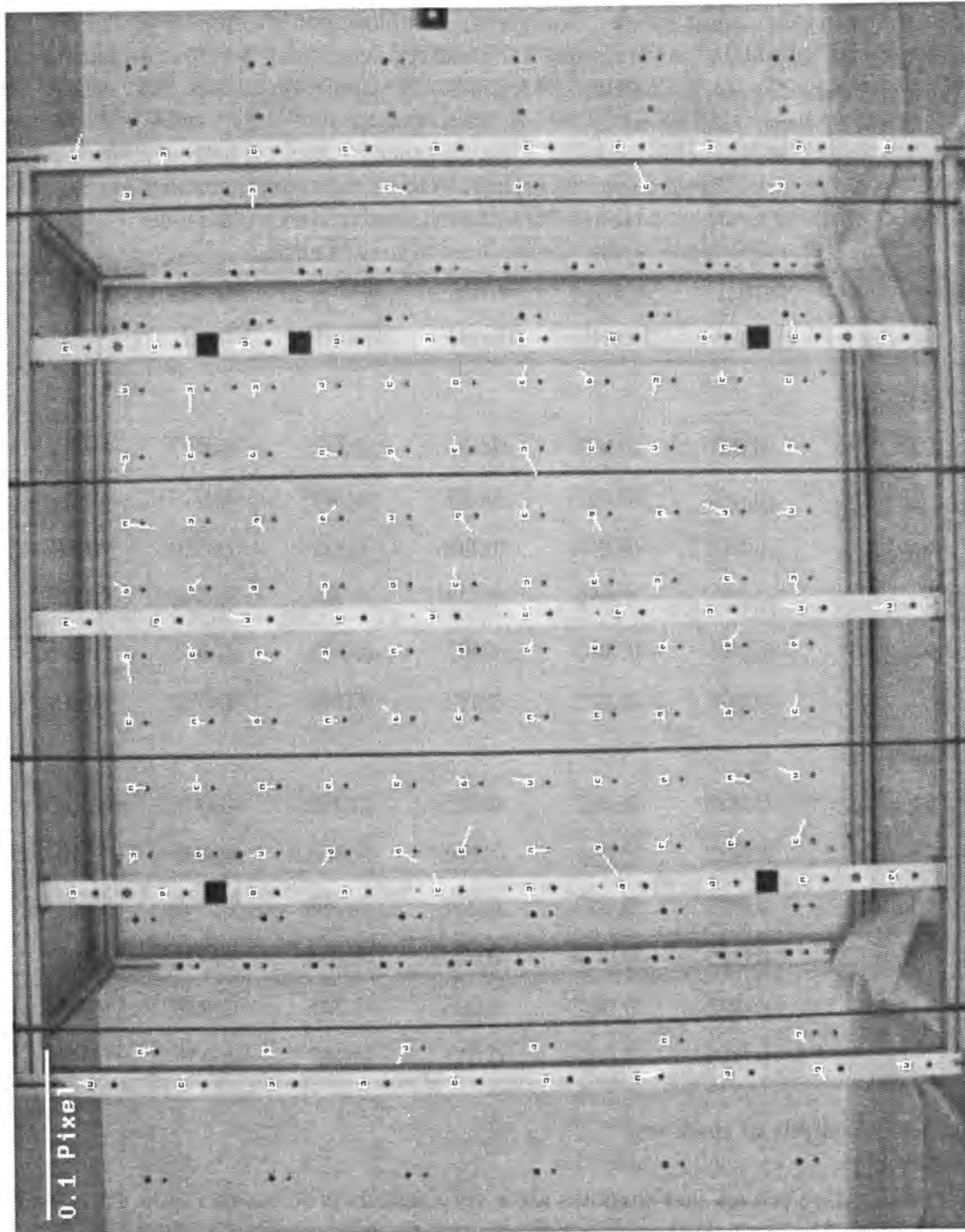


Figure 6.34 Repeatability analysis for the 7 x 7 template of version 111.

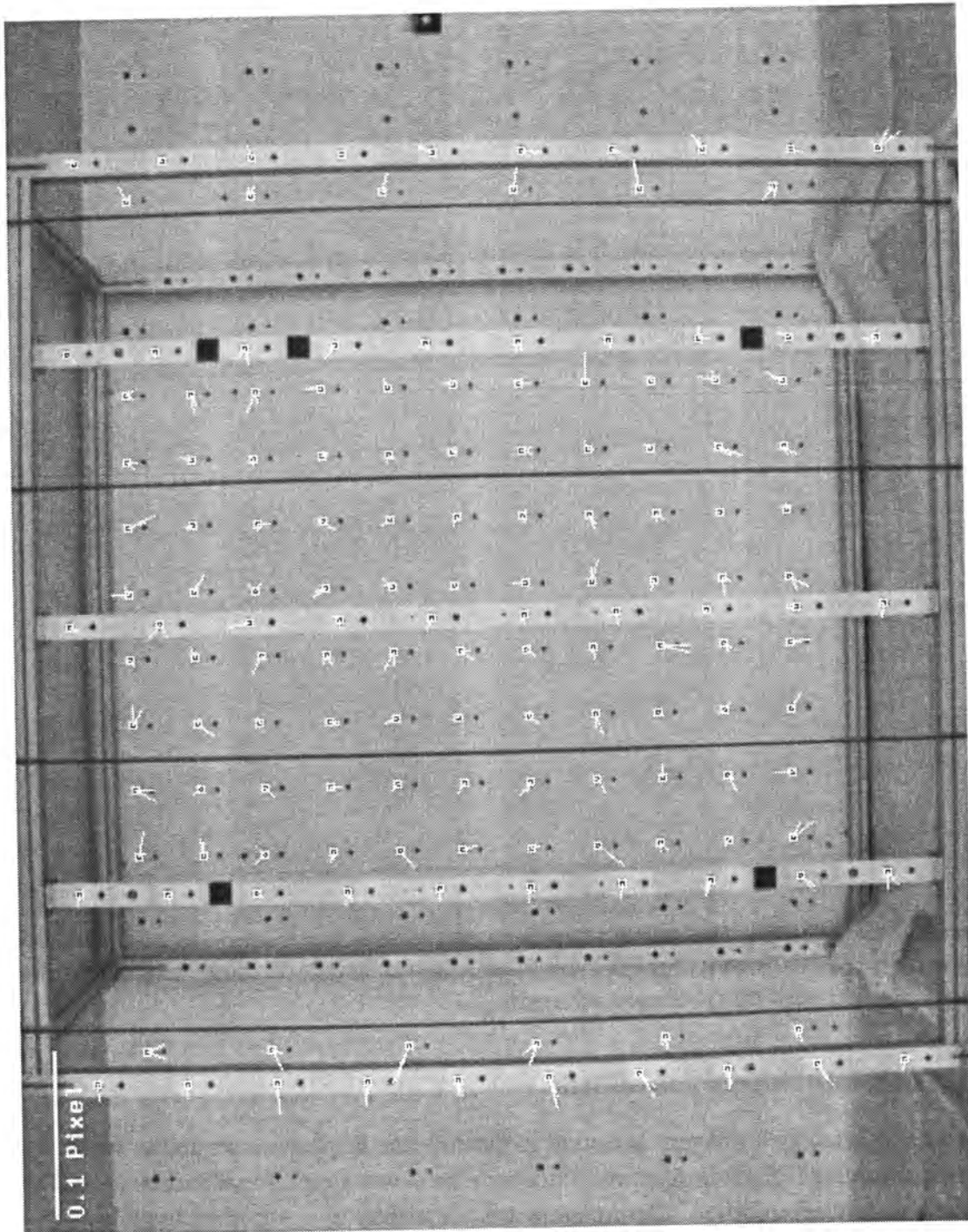


Figure 6.35 Repeatability analysis for the 7 x 7 template of version 112 showing the positional variations induced by the change in illumination.



Figure 6.36 Displacements for 7 x 7 template (a and b) and 5 x 5 template (c and d) for left and right columns of targets.

6.8.2 Assessment with Simulated Data

A test using simulated imagery was used to quantify the displacements and to verify the empirical findings. The template used in above tests was used both as template and as image which was modified. The imagery was disturbed by a simulated shadow. The shadow is assumed to result in a variation of the illumination intensity which in turn is used to modify the grayvalues with a multiplicative factor (only an approximation of reality). Figure 6.37a shows the thus modified image with a profile through the centre of the target. The gradient of the illumination was chosen as 4% over ten pixels in the x-direction. Ten measurements with LSM and templates of 5 x 5, 7 x 7, 9 x 9, and 11 x 11 pixel diameter were used to measure ten modified targets each and the average displacement in x direction was computed. The effective area of the template/image used in LSM for some of the template sizes is shown in Figure 6.37. Table 6.13 gives the error of the position determination with LSM. The error for the 5 x 5 template is approximately half as big as the larger templates.

The explanation for this, at first sight strange, behavior lies in the effect of the local illumination variation and the quantization. The original and modified grayvalues for the central row of the image are depicted in Figure 6.37b. The grayvalues in the top row are the original values and those in the bottom row the modified ones. The gradient does have less effect for smaller grayvalues as it is multiplicative and might not have any effect due to rounding. The central 3 pixel region shows no effect of the gradient as the grayvalues are too low and the gradient is too small. The central 5 pixel region shows a small difference. The slope has more effect the "brighter" the pixels are. Thus the illumination gradient has less effect for the 5 x 5 template than for the 7 x 7 template. The 5 x 5 template is confined to the dark central region where the illumination gradient has less effect, and thus the error in the position is smaller.

Target size	Error [Pixel]
5	0.018
7	0.034
9	0.035
11	0.034

Table 6.13 Error due to shadows determined with simulations.

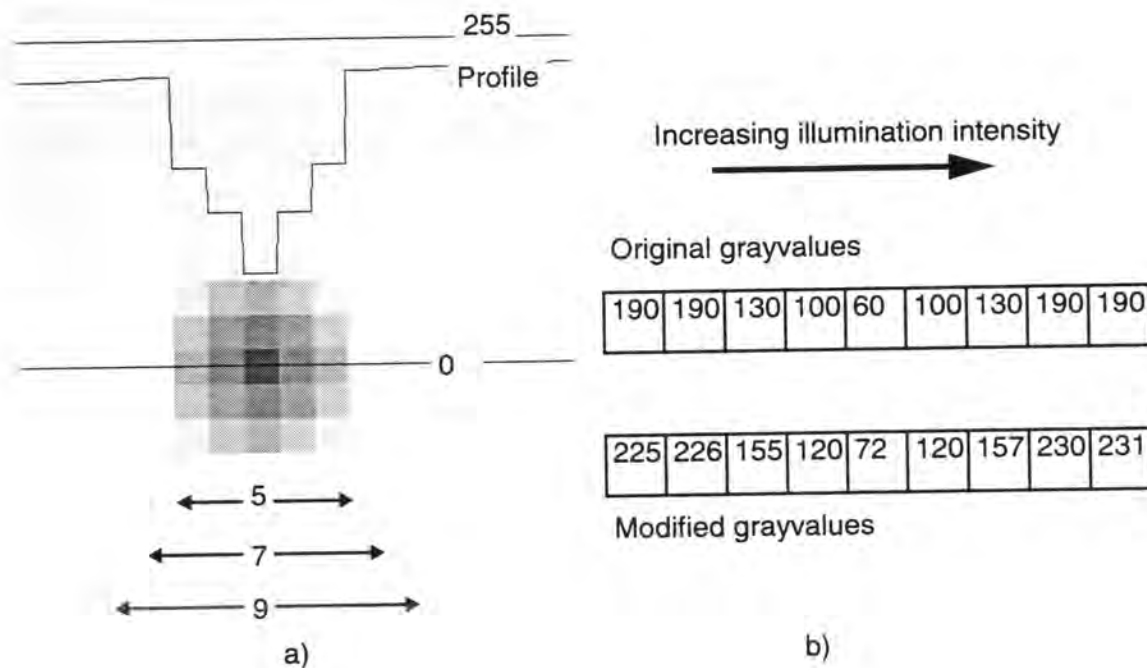


Figure 6.37 Local illumination gradient.

- Modified image with profile and sizes of templates.
- Original and modified data of central row of target.

6.9 Conclusions of Chapter

The investigations showed that extremely high internal precisions of up to 0.004 pixel can be attained. Several factors which can introduce large degradations of the internal precision have been localized and their effects discussed. Oscillations of Least Squares Matching with the targets and templates used were found to lead to errors of several tenths of the pixel spacing. With a detection and elimination of these oscillations the effects of variations in the solution of LSM due to the discrete nature of the procedure were shown to be negligible through empirical tests employing a variation of initial values. Signal transmission and synchronization are another source of errors. Several tests relying on the radiometric degradations induced by line-jitter or other instabilities were developed to rapidly analyze the performance of synchronization. It was shown that pixel-synchronous sampling provides for an identical geometry as digital transmission. The geometric deformation, in first order a shear, and line-jitter found through a comparison of PLL line-synchronization with pixel-synchronous sampling confirmed the findings of the frame grabber performance tests. The empirical analysis of the relation between target size showed that the targets used must have a diameter of at least 6 pixel (distance between inflection points of grayvalue profile) to attain an inner precision of 0.005 pixel. The improvement attainable with even larger diameters appears to be negligible.

Warm-up-effects were shown to reach 0.1 pixel with pixel-synchronous frame grabbing. This is primarily due to thermal deformations of the camera body. The warm-up time of the SONY-XC77CE, typical for CCTV-cameras, was determined to be at least one hour. After three hours a long-term stability of 0.01 pixel was attained for periods extending several hours.

Displacements due to local illumination gradients were found to be several hundreds of a pixel for a gradient of 4%. Furthermore it was shown that the effects thereof could be decreased when a smaller template size was used.

7 THREE-DIMENSIONAL PERFORMANCE ANALYSIS WITH A TESTFIELD

A number of factors influencing the radiometric and/or geometric performance of the imaging process with solid-state sensors were investigated above. The majority of the sources leading to degradations were eliminated by tuning the system as well as other countermeasures. For example, effects of DC-restoration were eliminated by selecting the correct settings, degradations of the uniformity due to the adding of sync signals in the camera were eliminated by reducing the image format, pixel-synchronous sampling was implemented to eliminate line-jitter, and warm-up-effects were circumvented by assuring that sufficient time for the frame grabber(s) and camera(s) to warm-up was given. This chapter addresses the analysis of the (geometric) performance of the system, once known error sources were eliminated. Other important factors, such as synchronization will also be addressed. The testfield was used to compare the results obtained with the CCD-camera(s) to a reference which was determined with an independent measurement technique. Thus not only precision but also accuracy were verified.

7.1 Mathematical Model

For the purpose of reference the mathematical model, additional parameters, and some formulas for the quality analysis are reviewed. The coordinates of targets measured in digital images refer to the pixel coordinate system. As shown in Figure 7.1 this coordi-

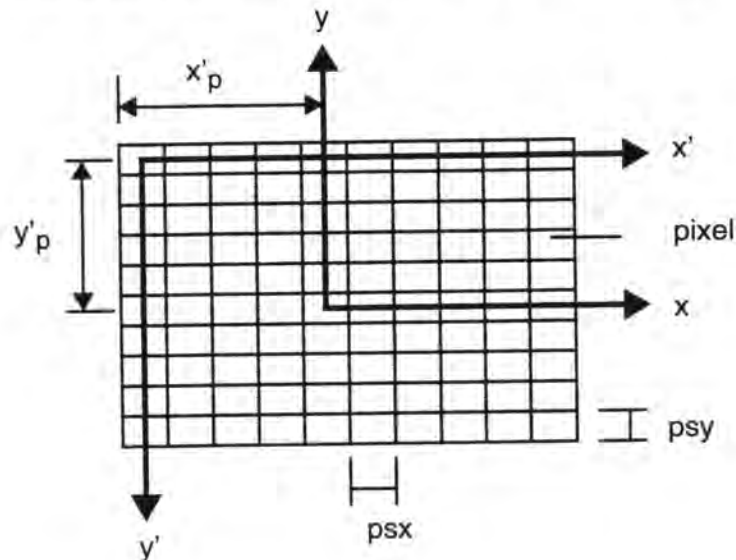


Figure 7.1 The pixel and image coordinate systems

nate system is defined as a left-handed coordinate system with the origin at the centre of the left topmost pixel and with the x -axis parallel to the rows and the y -axis parallel to the columns of the digital image. Image coordinates refer to the right handed image coordinate system. Its origin is usually placed such that it coincides with the location of the principal point in the image plane. The transformation from pixel to image coordinates is defined via the **pixel-to-image coordinate transformation**:

$$x = (x' - x'_p) \times psx \quad (7.1)$$

$$y = (y'_p - y') \times psy \quad (7.2)$$

with:

- x, y image coordinates
- x', y' pixel coordinates
- x'_p, y'_p location of principal point in pixel
- psx, psy pixel spacing in x and y

The mathematical model of the bundle adjustment with self-calibration is based on the **collinearity equations**. They are formulated as:

$$F_x = (x - x_p) = -c \frac{U}{W} + \Delta x \quad (7.3)$$

$$F_y = (y - y_p) = -c \frac{V}{W} + \Delta y$$

using the auxiliaries:

$$\begin{bmatrix} U \\ V \\ W \end{bmatrix} = D \begin{bmatrix} X - X_0 \\ Y - Y_0 \\ Z - Z_0 \end{bmatrix} \quad (7.4)$$

with:

- x, y image coordinates
- x_p, y_p, c elements of interior orientation
- X, Y, Z object coordinates of point
- D 3 by 3 orthogonal rotation matrix
- X_0, Y_0, Z_0 object coordinates of perspective centre
- $\Delta x, \Delta y$ correction term of additional parameter set

The **additional parameters** used in these tests can be grouped into additional parameters modelling the interior orientation, parameters to model inadequacies of solid-state sensors and synchronization, parameters modelling lens distortion, parameters to model other effects such as deviations from a flat surface, and parameters to absorb arbitrary deformations.

Additional parameters modelling the interior orientation ($\Delta x_p, \Delta y_p, \Delta c$), scale factor in x (s_x), shear (a) are formulated as:

$$\Delta x_1 = \Delta x_p - \frac{\bar{x}}{c} \Delta c - \bar{x} s_x + \bar{y} a \quad (7.5)$$

$$\Delta y_1 = \Delta y_p - \frac{\bar{y}}{c} \Delta c + \bar{x} a \quad (7.6)$$

with:

$$\bar{x} = x - x_p$$

$$\bar{y} = y - y_p$$

$$r = \sqrt{\bar{x}^2 + \bar{y}^2}$$

$\Delta x_p, \Delta y_p, \Delta c$. change of interior orientation elements

s_x scale in x

a shear

The location of the principal point is not specified for most CCD-cameras and varies from camera to camera with the precision at which sensors are mounted into cameras (often poorly) and depends furthermore on the configuration of the frame grabber. The scale in x is required to model the imprecise specification of the sensor element spacing and additional imprecisions introduced with PLL line-synchronization. In latter case the pixel spacing in x must be computed from the sensor element spacing, the sensor clock frequency and the sampling frequency via:

$$psx = sxx \frac{f_{\text{sensor}}}{f_{\text{sampling}}} \quad (7.7)$$

with:

psx pixel spacing in x
 sxx sensor element spacing in x
 f_{sensor} sensor clock frequency
 f_{sampling} sampling frequency

The shear (a) must be included when composite video signals and PLL line-synchronization are used. It was shown that this synchronization method can induce among other degradations a shear of up to several tenth of the pixel spacing (*Beyer, 1991c and e*).

Radial symmetric lens distortion (K_1, K_2, K_3) and decentering distortion (P_1, P_2) is modelled by (*Brown, 1971*):

$$\Delta x_2 = \bar{x}r^2K_1 + \bar{x}r^4K_2 + \bar{x}r^6K_3 + (r^2 + 2\bar{x}^2)P_1 + 2\bar{x}\bar{y}P_2 \quad (7.8)$$

$$\Delta y_2 = \bar{y}r^2K_1 + \bar{y}r^4K_2 + \bar{y}r^6K_3 + 2\bar{x}\bar{y}P_1 + (r^2 + 2\bar{y}^2)P_2 \quad (7.9)$$

where:

K_1, K_2, K_3 first three parameters of radial symmetric distortion
 P_1, P_2 first two parameters for decentering distortion

As shown later, radial symmetric lens distortion is the largest systematic error source when using solid-state cameras with low cost CCTV-type lenses and short focal lengths (5 to 20 mm). The strong barrel distortion of the 9 mm lens used in the tests is apparent in the curved outline of the testfield structure and the plumbines of the image shown in Figure 7.4.

A set developed by *Brown, 1976* is used to model irregularities of the sensor element spacing (a_1 to a_{12}) and potential unflatness of the sensor surface (a_{13} to a_{15}):

$$\Delta x_3 = \bar{x}a_1 + \bar{y}a_2 + \bar{x}\bar{y}a_3 + \bar{y}^2a_4 + \bar{x}^2\bar{y}a_5 + \bar{x}\bar{y}^2a_6 + \bar{x}^2\bar{y}^2a_7 + \quad (7.10)$$

$$\frac{\bar{x}}{c} [(\bar{x}^2 - \bar{y}^2) a_{13} + \bar{x}^2\bar{y}^2a_{14} + (\bar{x}^4 - \bar{y}^4) a_{15}]$$

$$\Delta y_3 = \bar{x}\bar{y}a_8 + \bar{x}^2a_9 + \bar{x}^2\bar{y}a_{10} + \bar{x}\bar{y}^2a_{11} + \bar{x}^2\bar{y}^2a_{12} + \quad (7.11)$$

$$\frac{\bar{y}}{c} [(\bar{x}^2 - \bar{y}^2) a_{13} + \bar{x}^2\bar{y}^2a_{14} + (\bar{x}^4 - \bar{y}^4) a_{15}]$$

An additional parameter set with 44 parameters modelling arbitrary deformations on a 5 by 5 grid in image space via orthogonal polynomials may also be used (*Grün, 1978*).

The above additional parameter sets can be combined to model the various sources of systematic errors. The first three sets can for example be used as:

$$\Delta x = \Delta x_1 + \Delta x_2 + \Delta x_3 \quad (7.12)$$

$$\Delta y = \Delta y_1 + \Delta y_2 + \Delta y_3 \quad (7.13)$$

Leading to:

$$\Delta x_1 = \Delta x_p - \frac{\bar{x}}{c} \Delta c - \bar{x} s_x + \bar{y} a + \quad (7.14)$$

$$\begin{aligned} & \bar{x}r^2K_1 + \bar{x}r^4K_2 + \bar{x}r^6K_3 + (r^2 + 2\bar{x}^2)P_1 + 2\bar{x}\bar{y}P_2 + \\ & \bar{x}a_1 + \bar{y}a_2 + \bar{x}\bar{y}a_3 + \bar{y}^2a_4 + \bar{x}^2\bar{y}a_5 + \bar{x}\bar{y}^2a_6 + \bar{x}^2\bar{y}^2a_7 + \\ & \frac{\bar{x}}{c} [(\bar{x}^2 - \bar{y}^2)a_{13} + \bar{x}^2\bar{y}^2a_{14} + (\bar{x}^4 - \bar{y}^4)a_{15}] \end{aligned}$$

$$\Delta y_1 = \Delta y_p - \frac{\bar{y}}{c} \Delta c + \bar{x} a \quad (7.15)$$

$$\begin{aligned} & \bar{y}r^2K_1 + \bar{y}r^4K_2 + \bar{y}r^6K_3 + 2\bar{x}\bar{y}P_1 + (r^2 + 2\bar{y}^2)P_2 + \\ & \bar{x}\bar{y}a_8 + \bar{x}^2a_9 + \bar{x}^2\bar{y}a_{10} + \bar{x}\bar{y}^2a_{11} + \bar{x}^2\bar{y}^2a_{12} + \\ & \frac{\bar{y}}{c} [(\bar{x}^2 - \bar{y}^2)a_{13} + \bar{x}^2\bar{y}^2a_{14} + (\bar{x}^4 - \bar{y}^4)a_{15}] \end{aligned}$$

Linear dependent parameters of equations (7.14) and (7.15) must be eliminated to circumvent correlations. Thus a_1 , a_2 , a_4 , and a_9 were eliminated when the sets are combined by assigning appropriate standard deviations / weights. The bundle adjustment module of DEDIP allows the user to introduce image variant additional parameters as well as the assignment of standard deviations to parameters for the purpose of weighing and/or elimination of parameters.

As discussed later-on, the **parameters of the pixel-to-image coordinate transformation** are initially very rough approximations. They are updated during the bundle adjustment from corresponding additional parameters with the following procedure. First the image coordinates are transformed to pixel coordinates using initial parameters for the pixel-to-image coordinate transformation. Then the parameters are updated using the additional parameter values for the location of the principal point, the camera constant, and the scale in x using equations (7.16) to (7.19). Finally the pixel coordinates are transformed back to image coordinates with the updated parameters of the pixel-to-image coordinate transformation. Now the additional parameters used in the update are reset to zero and the bundle adjustment is continued. The update of the parameters of the pixel-to-image coordinate transformation from the additional parameters for the i^{th} update is performed by:

$$x_p^i = x_p^{i-1} + \Delta x_p \quad (7.16)$$

$$y_p^i = y_p^{i-1} + \Delta y_p \quad (7.17)$$

$$c^i = c^{i-1} + \Delta c \quad (7.18)$$

$$psx^i = psx^{i-1} (1 + s_x) \tag{7.19}$$

with:

xxxⁱ value of parameter after update
 xxxⁱ⁻¹ value of parameter before ith update

The vector of unknown object coordinates, exterior orientation elements, and additional parameters (in the event that they are used) is computed via:

$$\hat{x} = (A^T P A)^{-1} A^T P l \tag{7.20}$$

and the residuals of the observations, i.e. the image coordinates and observed object coordinates of control points, with:

$$v = A \hat{x} - l \tag{7.21}$$

The standard deviation of unit weight *a posteriori* is estimated using:

$$\hat{\sigma}_0 = \sqrt{\frac{v^T P v}{r}} \tag{7.22}$$

with:

r redundancy or degree of freedom

The evaluation of the precision and accuracy is performed by computing precision estimates of object points. The standard deviations of object space coordinates are given by:

$$\hat{\sigma}_{X_i} = \hat{\sigma}_0 \sqrt{q_{X_i X_i}}, \quad \hat{\sigma}_{Y_i} = \hat{\sigma}_0 \sqrt{q_{Y_i Y_i}}, \quad \hat{\sigma}_{Z_i} = \hat{\sigma}_0 \sqrt{q_{Z_i Z_i}} \tag{7.23}$$

with:

q_{X_iX_i} diagonal element of the inverse of the normal equation matrix at the position of the corresponding unknown

From these the **average precision of the object coordinates** of check points is computed by:

$$\hat{\sigma}_X = \sqrt{\frac{\sum \hat{\sigma}_{X_i}^2}{n_X}}, \quad \hat{\sigma}_Y = \sqrt{\frac{\sum \hat{\sigma}_{Y_i}^2}{n_Y}}, \quad \hat{\sigma}_Z = \sqrt{\frac{\sum \hat{\sigma}_{Z_i}^2}{n_Z}} \tag{7.24}$$

with:

n_X, n_Y, n_Z number of check point coordinates

An **RMS error of object coordinates (empirical accuracy in object space)** is computed from the comparison of the check point coordinates with the reference coordinates by:

$$\mu_X = \sqrt{\frac{\sum (X_i^r - X_i)^2}{n_X}}, \quad \mu_Y = \sqrt{\frac{\sum (Y_i^r - Y_i)^2}{n_Y}}, \quad \mu_Z = \sqrt{\frac{\sum (Z_i^r - Z_i)^2}{n_Z}} \tag{7.25}$$

where:

X^r, Y^r, Z^r reference coordinates of check points
 n_X, n_Y, n_Z number of checkpoint coordinates in X, Y and Z

This comparison can also be performed in image space by projecting the estimated object coordinates and the reference coordinates of check points into the image. The **RMS error in image space (empirical accuracy in image space)** is then computed with:

$$\mu_x = \sqrt{\frac{\sum (x_i^r - x_i)^2}{n_x}}, \quad \mu_y = \sqrt{\frac{\sum (y_i^r - y_i)^2}{n_y}} \quad (7.26)$$

where:

x_i, y_i adjusted image coordinates

x_i^r, y_i^r image coordinates computed from checkpoint coordinates

n_x, n_y number of reference coordinates in all images

7.2 Test Arrangement and Network

The testfield and the measurement of the reference coordinates were discussed in section 2.4. The measurement of the reference coordinates was performed with two identical sets before and after the acquisition of the imagery. This assured that potential deformations of the testfield can be detected. The reference coordinates determined with theodolites refer to a small dot in the centre of the larger black target used by the CCD-camera(s). The centricity of the centre with respect to the circumference of the larger black target was assessed by measuring the coordinates of the centre and the edge of the target in both coordinate directions on the films. The RMS error of the centricity was between 5 and 6 μm . The films were then used to produce the paper prints via contact copying. The centricity of the final targets, consisting of photographic paper glued onto an aluminium sheet, was not verified.

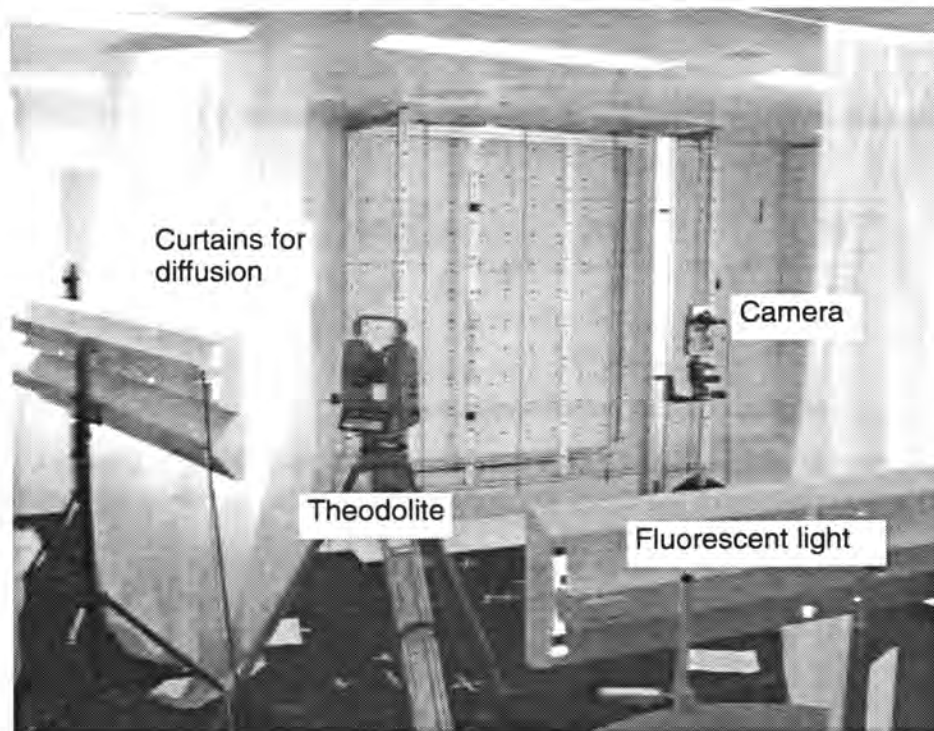


Figure 7.2 Image showing the lights, curtain, camera and testfield.

For a number of reasons, such as space restrictions for the placement of the cameras, only a part of the testfield spanning 2600 by 2000 by 1100 mm in X, Y and Z respectively (see Figure 7.3) was used. This part contains 162 targets with a diameter of 20 mm. The average precision of the reference coordinates for these targets is 0.02, 0.02 and 0.03 mm in X, Y and Z respectively.

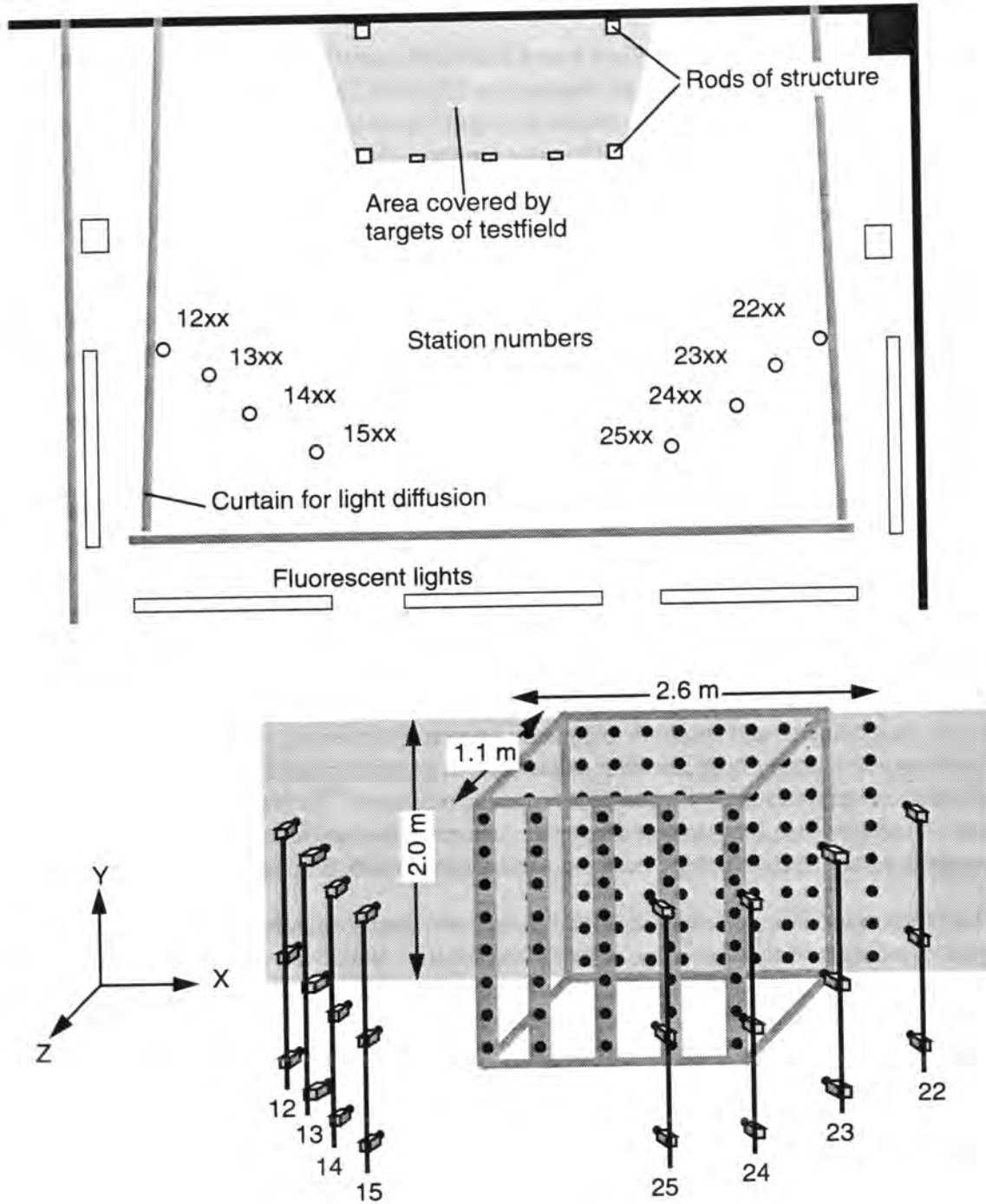


Figure 7.3 Schematic plane and perspective views of the test arrangement. The plane view shows the locations of the fluorescent lights and the arrangement of the curtain. The perspective view indicates the arrangement of the stations with respect to the testfield.

Fluorescent lights which are electronically triggered at 35 kHz and have a spectral distribution similar to daylight are used as illumination. They were placed in a semicircle with curtains as diffusors (see Figure 7.2 and Figure 7.3). The arrangement of illumination and curtains was established after a large number of trials where illumination gradients due to spatial variations of the illumination and/or shadows were eliminated as good as possible.

A SONY-XC77CE camera with a 9 mm FUJINON lens was used. It was mounted in a rolling device on a stable aluminium pole (see Figure 7.2). This pole created light shadows spread over a large area, the effects of which could not be determined. The imagery was acquired with a MAX-SCAN frame grabber. Warm-up-effects were excluded by switching on the complete setup (lights, camera, frame grabber) one week before taking the imagery. The room temperature varied nevertheless by 5 to 10°C as the air-conditioning was switched off over night and on weekends. This leads to thermal deformations of the testfield and the wall. The temperature for the theodolite measurements and the acquisition of the imagery can vary by a few degrees although they were performed during the same time of day. This was due to changes in the air circulation within the room caused by variations in the arrangement of the curtains. They were only closed for the acquisition of the imagery and had to be partially removed for the theodolite measurements.

Space restrictions to the sides, top and bottom, i.e. to the sides by the room and illumination and the top and bottom by the ceiling and floor respectively, constrained the design of a suitable network. The occlusions of targets on the wall by the five vertical bars of the structure and the three plumbines reduced the choice of suitable positions. This was a considerable problem as all stations in the same column had identical occlusions. With 6 frames located on stations in a column the number of rays onto a target would be reduced by 6 and in case of a symmetrical arrangement by 12 rays. The locations of the stations were thus planned and thereafter adjusted according to visibility constraints. The optimum target diameter could not be realized. It was found in section 6.4 that the optimum diameter as determined by repeatability would be 8 pixel. The targets of the front structure would be less than a meter from the camera when imaging the wall at the corresponding image scale in which case too few targets would be imaged.

The imagery of the test was acquired using two synchronization modes. Due to disk space restrictions only one image per synchronization mode was grabbed at each station. The frame grabber was "initialized" after images were taken with one setting at two camera positions. The network consists of camera stations arranged in eight columns. At each of these columns images were acquired at three heights and with rolls of 0 and 90 degrees (see Figure 7.3). This resulted in 48 images per synchronization mode. The image scale varies between 1 : 200 and 1 : 560 resulting in target diameters of 3.3 to 9 pixels when excluding geometric foreshortening. Figure 7.4 shows an image grabbed at station 13 in the middle position without roll. The zooms of the three areas illustrate the problem of the large scale difference and the small target size. The target in region 1 is excluded from the measurements as the dark area to the left will influence the position determination by LSM. The target in region 2 shows a target imaged with a diameter of 3 pixels. This is furthermore reduced by geometric foreshortening, light scattering, and the limited resolution of the camera. Region 3 shows a target image with a diameter of almost 9 pixels in the vertical direction. This would be the optimum target size from point of view repeatability. It is, however, evident that the majority of targets are below the op-

timum size. The average image scale is 1 : 380 resulting in a diameter of less than 5 pixels without considering all other degrading factors.

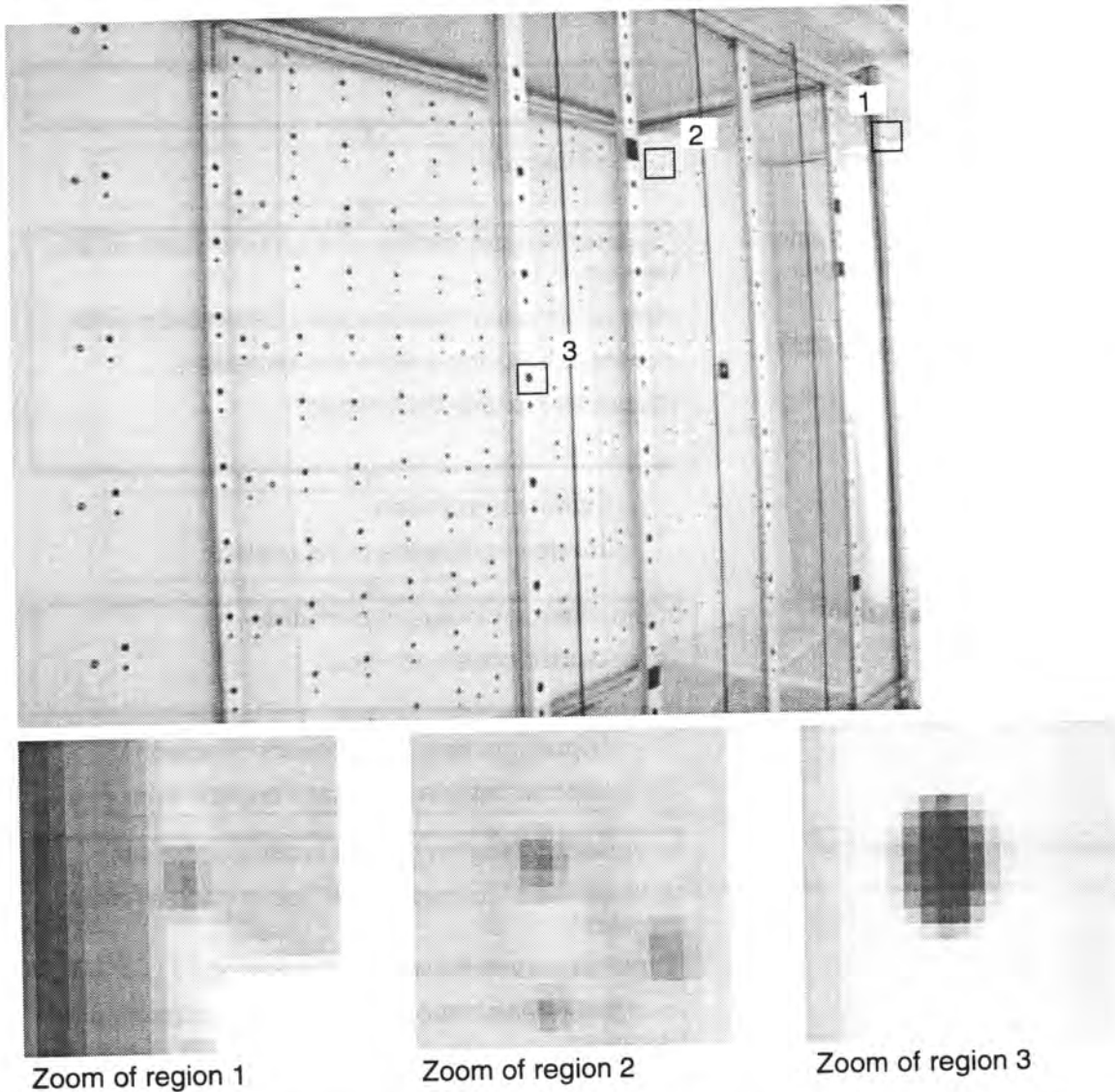


Figure 7.4 An image of the testfield taken at station 12 and zoomed portions thereof showing the large range in size of target images.

7.3 Measurement of Image Coordinates

Figure 7.5 shows the processing steps of the three-dimensional performance analysis. The steps can be classified as:

- image acquisition
- determination of approximations
- automatic measurement of image coordinates
- bundle adjustment
- analysis of results

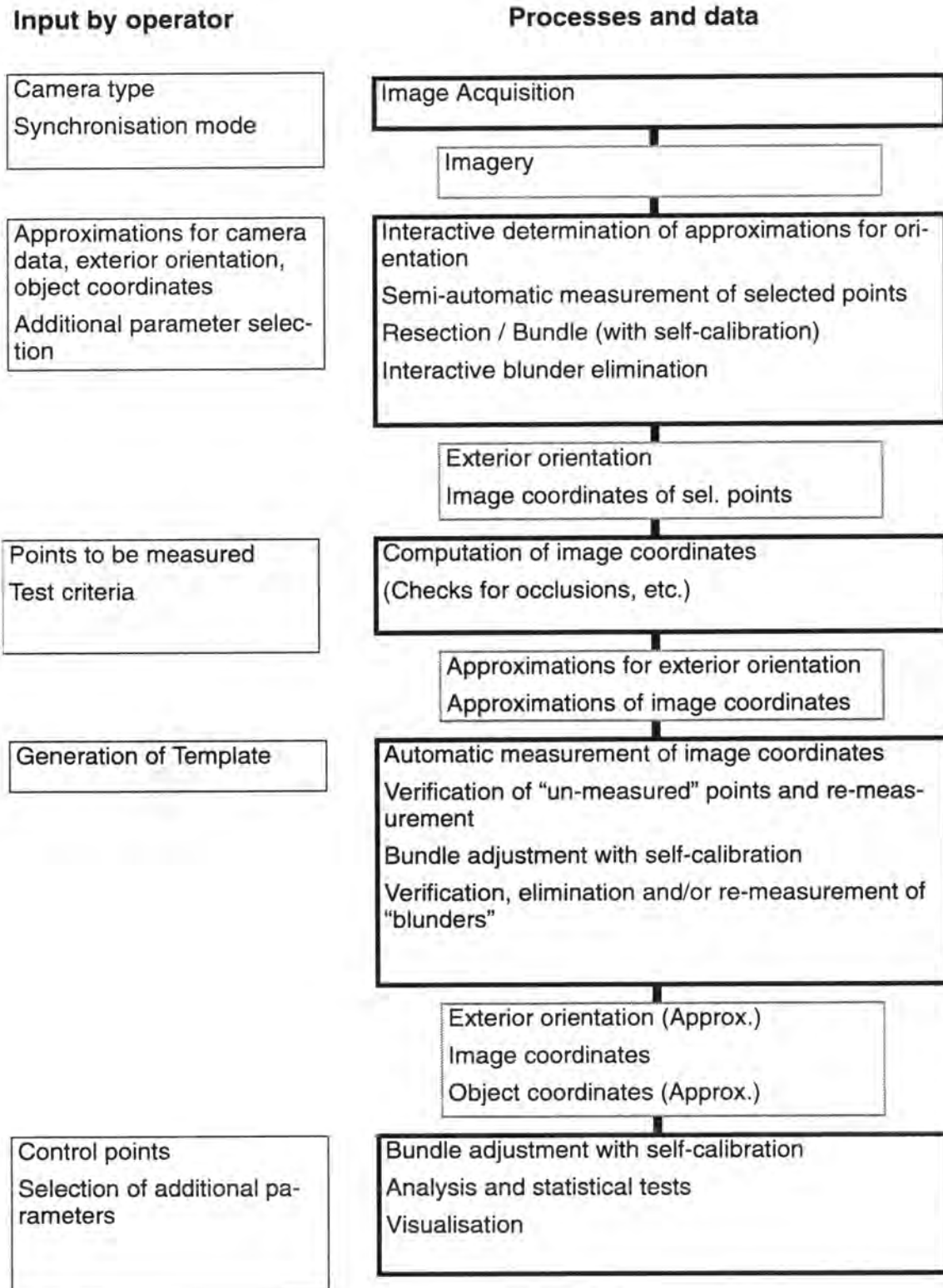


Figure 7.5 Operator input, processes and data of the three-dimensional performance analysis.

7.3.1 Approximations

Initially no precise data is available for the parameters of the pixel-to-image coordinate transformation and the elements of the interior orientation. The initial values for the pixel-to-image coordinate transformation are computed from specifications of lens, camera, and frame grabber. The location of the principal point was assumed to be in the image centre. The pixel spacing in y was set identical to the sensor element spacing as the sensor used was an Interline Transfer CCD and was driven in the standard interlaced mode. The pixel spacing in x was also set equal to the corresponding sensor element spacing because pixel-synchronous sampling was used. The PLL line-synchronization was configured such that the sampling frequency was practically identically (excluding effects of line-jitter) to the sensor clock frequency. Thus the pixel spacing in x was as well set equal to the sensor element spacing in this synchronization mode. The initial pixel spacing thus was $11 \times 11 \mu\text{m}$ in x and y respectively. The camera constant was computed via the lens equation. It was set to the focal length as the lens is focused to infinity.

Starting with these approximations, with the reference coordinates of all targets from the theodolite measurements as control points, and rough approximations of the locations of the cameras (good to approximately 500 mm) an interactive determination of the missing exterior orientation elements and the measurement of some points per image was performed.

Figure 7.6 shows the workstation screen during the derivation of approximations of exterior orientation elements and the semi-automatic measurement of image coordinates. The panel for the derivation of the approximations for exterior orientation is shown to the right of the image and to the bottom the panel for interactive target location with the settings for LSM. The user can define the location of the camera station and compute the rotation elements by giving the coordinates of the point at which the camera is aimed, as well as by indicating the axis to which the y -axis of the image is parallel to. The image coordinates of object points are then computed and plotted onto the image. This can be used to adjust exterior orientation elements via the buttons on the right side of the panel. After each adjustment the image coordinates of the plotted points are re-computed and the plot updated.

A template was created using a representative image of a target. The grayvalues along the x and y axis across the centre of the target were measured and a function of grayvalue versus radius from the centre was created. This was used to generate a centered and radial symmetric template (see template in Figure 7.6). Only 3 shaping parameters (5 parameters of the affine transformation) were used in LSM as the template is radial symmetric and the derivatives were computed from the template only. The following selections were used in LSM. A radiometric correction for mean and standard deviation of the grayvalues of the patch was applied in each iteration and bilinear interpolation of the patch was selected. The iteration criteria in LSM were set to 0.0005 pixel for the average absolute values of the shifts and 0.005 for the average absolute values of the scales (only the ones which are not eliminated are used). The maximum number of iterations was set to 50.

The panel for interactive target location shows that semi-automatic target location is selected. When the measurement mode is entered, one can only change the setting for the point number in that panel. All other selections are locked. The numbering method during interactive measurement can be either an incremental point numbering or the number can be taken from the closest point. The latter is of interest if the poor approximations

available are insufficient for automated measurement, but close enough to guide the user to the correct points. In that mode the user needs only provide better approximations by pointing with the cursor to the point and pressing the left mouse button to initiate the measurement.

It is necessary that a few points in each image need to be measured semi-automatically by the operator in order to identify them. For this purpose the point numbers were given by hand and the incremental numbering scheme was used. Six points on the wall and up to four points on the front were usually measured. Experience showed that it is better to measure up to 10 points per image to obtain good approximations for the automatic measurement. If the approximations are not within the convergence radius of LSM the time spent to sort out the resulting measurement errors is much larger (considering that almost 162 targets are to be measured per image). The LSM algorithm indicates an error status during initial measurement only in cases where points too close to the edge of the image are selected or too poor approximations are given. In rare occasions it can happen that the LSM fails if the scale between template and patch is too different, i.e. larger than a factor of 4 to 5. When the image coordinates of selected points were measured in some or all images, a bundle adjustment with self calibration was performed. The location of the principal point, the camera constant, and the first parameter for radial symmetric distortion were used (the first three with a standard deviation of 0.01 mm). Typically some mis-identifications needed to be corrected before the process of generation of suitable approximations for the automatic measurement was finished. The standard deviation of unit weight of the initial orientation/calibration with a bundle adjustment with the additional parameters of (7.5), (7.6), (7.8), and (7.9) as well as all 48 images acquired pixel-synchronously is 2.4 μm . This corresponds to 0.2 of the pixel spacing and the approximations for the image coordinates computed with the resulting exterior orientation and additional parameters were sufficiently precise for automatic measurement. All tasks including the setup of files, the detection and elimination of some mis-identifications, until the establishment of good approximations required only two hours. This makes an average of 25 seconds per point or 2.5 minutes per image.

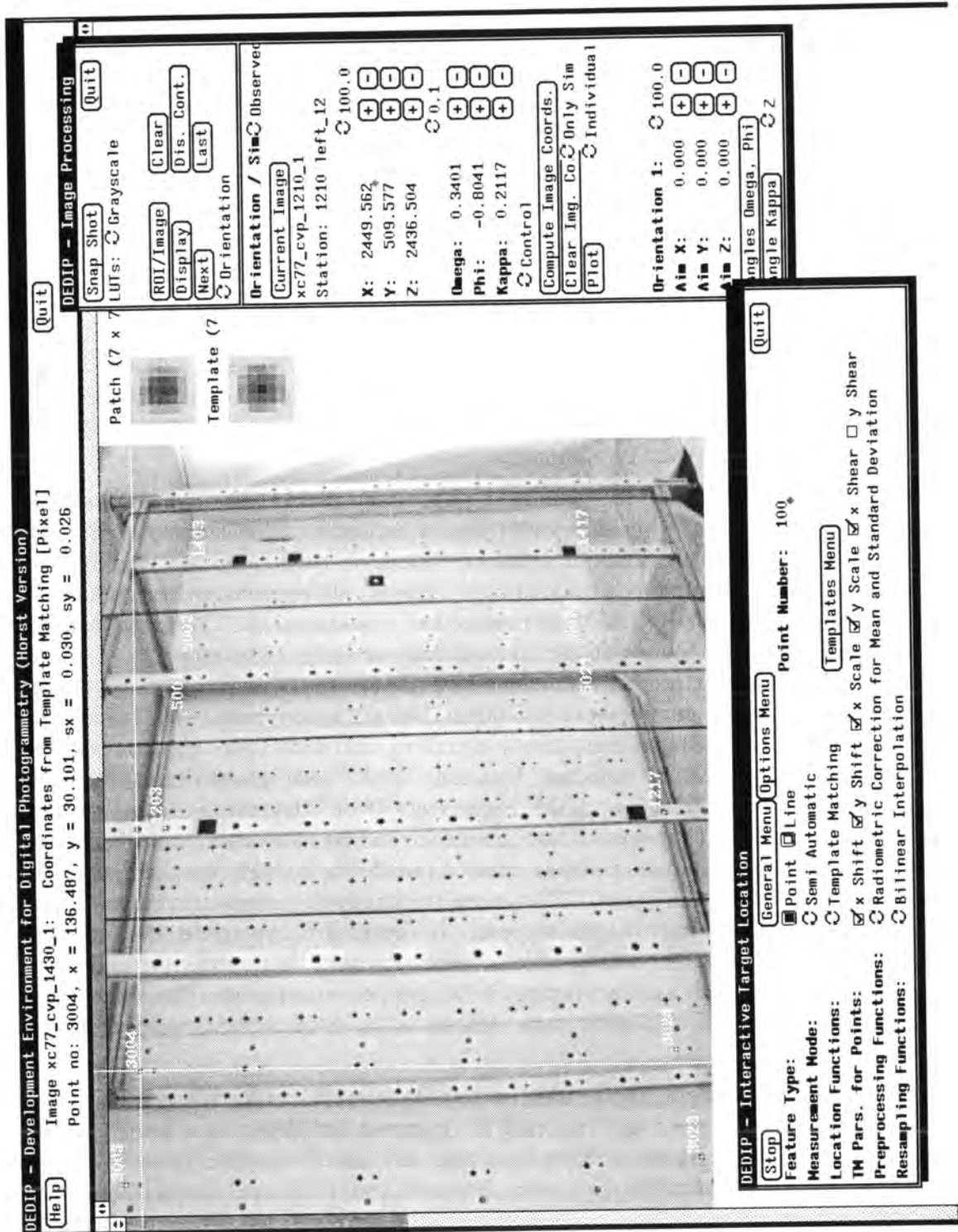


Figure 7.6 Semiautomatic measurement of pixel coordinates for the initial orientation and calibration.

7.3.2 Automatic Measurement

To compute image coordinates the user can select among different sets of points, i.e. besides control and check points a file with points to be measured can be used to define a subset of points. The computation of the image coordinate approximations can be performed without any checks for image format, occlusions, etc. or with a series of checks. Problems can occur when a target of the wall is:

- (1) outside the image format
- (2) falls on areas of the front structure without texture
- (3) falls on or close to plumb lines
- (4) is partially occluded by the front structure
- (5) falls close to targets on the front structure

A target lying on the wall and front structure would also have been outside the convergence radius of LSM if the approximations are too poor. The above problems can be eliminated to a large extent when appropriate checks are performed. The performance without and with checks shall be compared.

When the image coordinates are generated without any check, LSM might either detect the problem, determine the position with reduced accuracy, or measure a wrong target (mis-identification). These situations result in "blunders" which are not a deficiency of LSM but of the approximations provided to it. Targets with approximations outside the image format are rejected by LSM and marked as "un-measurable". When approximations of points fall onto areas outside the convergence range of a target or on an area without appropriate texture, this is detected by LSM in DEDIP. It might also not converge within the maximum number of iterations. Both situations result in an "un-measurable" tag for the point. Some of the points of the third and fourth case can also result in a similar situation and are thus "detected" by LSM. The 5th case results in mis-identifications, which cannot be detected by LSM. In this test 878 of 7164 resulted in an "un-measurable" tag by LSM. They were all attributable to the first four cases described above. After the automatic elimination of these points a bundle adjustment was computed. The verification tool shown in Figure 7.7 was used to iteratively eliminate points of cases three to five. Here the order in which points are detected is inverse to the one given above. Case 5 results in mis-identifications, which are easily detectable due to the large redundancy of at least 20 and an average of 38 rays per object point. The detection of partially occluded points was much more difficult as the displacements were often very small.

Figure 7.7 shows the interactive verification tool. Points with residuals larger than a user definable threshold are searched. This could be improved and placed on a statistical basis with data snooping. If a point is found it is indicated and the number of rays onto it is given. The images in which the point was measured (and if selected also in those where the point was not measured but is potentially visible) are displayed with a user definable zoom factor. The point number and residual vectors are plotted. The image name and the size of the residual is given in the top left corner of each image (see enlargement in centre). If the residual is below the given criteria the graphics of that image are plotted in green, otherwise red is used to highlight an erroneous situation. Twelve images are displayed simultaneously on the screen. The next, or last, set of images can be selected by pressing the appropriate buttons on the panel. If an erroneous point is found, the user can either delete it interactively, re-measure it automatically, or re-measure it semi-automatically. This tool has proven very useful for cleaning up data sets with several thousand

points and if it is required to investigate the origin of each blunder. For this test only points of above cases and points with clearly too poor image quality (target image on too few pixel and/or too oblique), like the one shown in region 1 of Figure 7.4, were eliminated.

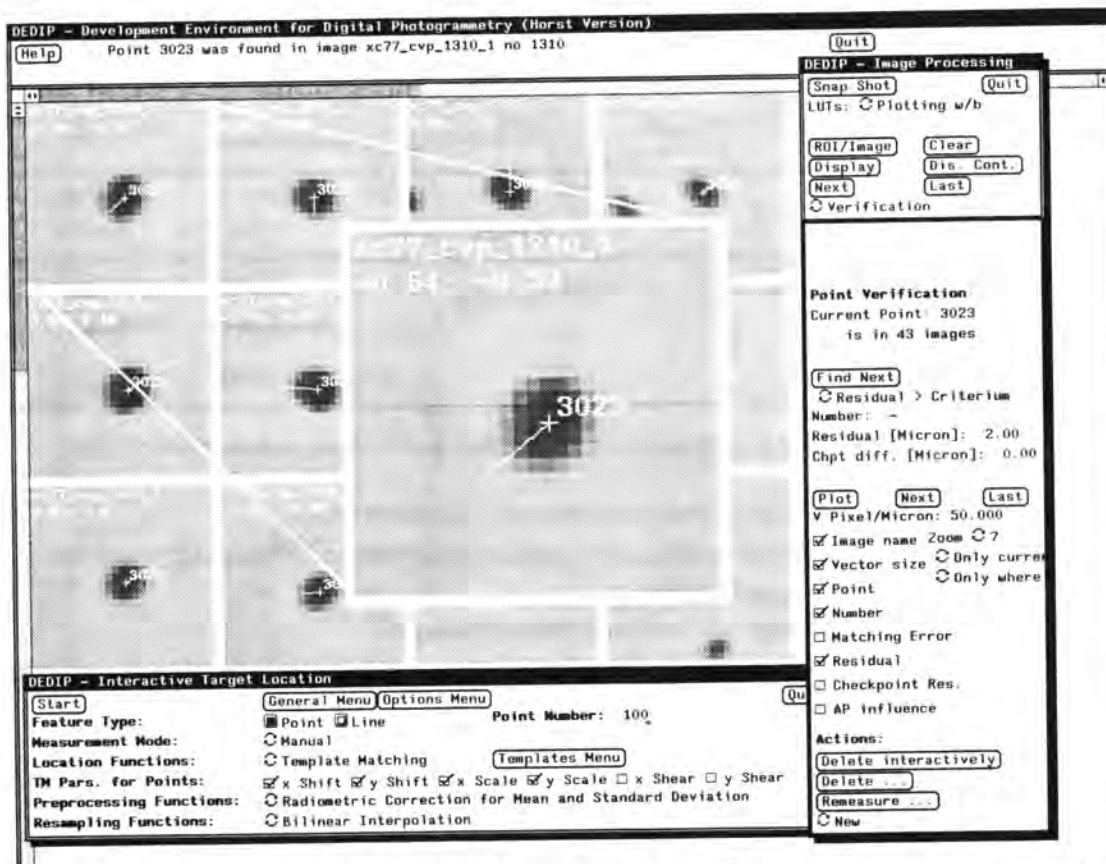


Figure 7.7 Interactive verification of errors from template matching, image coordinate residuals, and comparison to checkpoints.

7.3.3 Measurement Speed

The measurement speed of the automatic measurement with LSM depends on many parameters. Some of them are the implementation of the algorithm, the template size, the number of iterations, the machine on which the computations are performed, the activity of the computer network, and on which disk the protocol file is written. It is always very difficult to discuss performance as factors such as implementation and the system configuration can have a determinant effect. The implementation used here can be characterized as maximum flexibility (for tests) and maximum overhead (for result analysis). A few numbers shall demonstrate the influence of the hardware configuration. All three versions given in Table 7.1 were computed with a 7 by 7 template using 48 images and measuring the pixel coordinates of 7164 points. The output file created in the process is over 18 Mbyte in size. Each patch is zoomed and displayed in each iteration. The test was performed with no other activity on the computer network.

Two types of elapsed time measurements were used. Once the time from start to end of measurements was determined with a stop watch. Additionally the time per iteration was obtained via a system function and the time per point was calculated using the average number of iterations per point, which was 15. The difference in speed is quite large. Approximately 4-5 points/sec were on the SPARCStation 1, over 6 points/sec on the SUN-

4/490 when writing the output file to a laserdisk, and over 8 points/sec if the file was written to a local disk which had a 3 MByte/sec transfer rate (a slow version of an IPI disk). This shows that speed is strongly dependent on the specific system configuration and that performance measures are only useful if the specific configuration is known. A large speed-up can be achieved if the tremendous overhead for visualization and data analysis is eliminated. Measurement rates of 50 to 100 points per second should be attainable with workstations performing at 5 to 10 double precision MFLOPS (Million Floating Point Operations Per Second).

	t_1 [minutes]	t_1/pt [sec]	t_2/it [sec]	t_2/pt [sec]
SPARCStation 1 with laserdisk	35	0.29	0.015	0.23
Sun-4/490 with laserdisk	23	0.19	0.011	0.16
Sun-4/490 on local disk	16	0.13	0.008	0.12

Table 7.1 Computational performance of some hardware configurations for LSM.

- t_1 elapsed time in minutes as measured with a stop watch
 t_1/pt elapsed time per image point computed from the total elapsed time and the number of points measured
 t_2/it elapsed time per iteration as given by program
 t_2/pt elapsed time per image point computed from elapsed time per iteration and the average number of iterations

7.4 Performance with Pixel-synchronous Frame Grabbing

The performance of the system and the effects of some important factors will be discussed now. First the imagery acquired with pixel-synchronous sampling is used to assess the influence of several factors. The effects of using the additional parameters, the change of the parameters of the pixel-to-image coordinate transformation and interior orientation are shown. Influences of shadows are discussed and ways to reduce their degradations are evaluated. Thereafter the modelling of other systematic errors is attempted and possible influences limiting the precision and accuracy are discussed. Finally the effects of synchronization are analyzed by comparing the results obtained with PLL line-synchronization to those of pixel-synchronous frame grabbing.

All precision estimates were computed with a standard deviation of unit weight a priori of 0.44 μm . The empirical accuracy measures were calculated after a spatial similarity transformation onto the checkpoints.

7.4.1 Modelling of Systematic Errors

The large influence of additional parameters is demonstrated with two versions. The first version (cvp253) was computed using the initial values for the pixel-to-image coordinate transformation and without additional parameters. The second version was computed using the location of the principal point ($\Delta x_p, \Delta y_p$), the camera constant (Δc), a scale factor in x (s_x), a shear (a), three parameters for radial symmetric distortion (K_1, K_2, K_3), and two parameters for decentering distortion (P_1, P_2) as additional parameters together with the update procedure of the pixel-to-image coordinate transformation and the interior orientation elements as discussed in section 7.1 (additional parameters of equations (7.5),

(7.6), (7.8), and (7.9)). Both versions use the pixel-synchronous grabbed imagery and 30 control points.

V	AP	Co	Ch	r	$\hat{\sigma}_0$	$\hat{\sigma}_X$ [mm]	$\hat{\sigma}_Y$ [mm]	$\hat{\sigma}_Z$ [mm]	μ_X [mm]	μ_Y [mm]	μ_Z [mm]	μ_x [μm]	μ_y [μm]
cvp253	0	30	56	11554	11.7	0.027	0.023	0.035	4.207	4.063	3.657	12.13	11.98
cvp223	10	30	56	11547	0.36	0.027	0.023	0.035	0.086	0.058	0.114	0.24	0.22
					32.5				48.9	70.1	32.1	50.5	54.5

Table 7.2 Results of bundle adjustment with and without additional parameters.

- V Version
- AP Number of additional parameters
- Co Number of control points (m denotes minimum control)
- Ch Number of check points
- r Redundancy
- $\hat{\sigma}_0$ Variance of unit weight *a posteriori*
- $\hat{\sigma}_X, \hat{\sigma}_Y, \hat{\sigma}_Z$ Theoretical precision of check point coordinates
- μ_X, μ_Y, μ_Z Root Mean Square Error from comparison to check point coordinates in object space
- μ_x, μ_y Root Mean Square Error from comparison to check point coordinates in image space

The standard deviation of unit weight is improved by a factor of 33. The precision of object coordinates, computed with the standard deviation of unit weight *a priori*, is identical. The empirical accuracy is improved by a factor of up to 70 in object space and a factor of up to 50 in image space.

Table 7.3 gives the initial and updated values for those parameters of the pixel-to-image coordinate transformation which are updated from additional parameters and the camera constant. The change of the scale in x as compared to the initial values corresponds to 0.38 μm across the sensor for version cvp223. The ratio of the sensor element spacing in x and y as given in the data sheets is thus very precise. The location of the principal point is displaced by 3 and 11 pixels in x and y respectively. The camera constant was changed by 17.9 μm in relation to its initial value. This is a change of only 0.2% from the initial value.

Parameter	Initial	Adjusted.	Stddev
pixel spacing in x [mm/pixel]	0.011	0.0109995	0.0000036
principal point x [mm]	0.0	0.0323	0.00031
principal point y [mm]	0.0	0.1191	0.00025
camera constant [mm]	9.0	8.9821	0.00018

Table 7.3 Initial and adjusted values of pixel spacing and interior orientation elements with the standard deviation from version cvp223.

The determinability of additional parameters is verified by their influence on the trace of the inverse of the normal equation matrix for the object coordinates. The largest influencing factor (effect on trace by parameter divided by trace of object points) is 4.e-3 for the camera constant. This is also expressed by the identical precision measures of version cvp253 and cvp223. The test of the complete set of additional parameters shows that a

significant systematic error contribution could be determined ($T = 1236053.5$, $F(10, 11547, 95\%) = 1.83$, see *Gruen, 1978* for testing procedure). Testing the highly correlated additional parameters for radial symmetric lens distortion shows them to be significant as a group too. The correlations among additional parameters and object coordinates are 0.03 on average and 0.19 maximum. Those between additional parameters and exterior orientation elements reach 0.92 and are 0.12 on average. The correlations between additional parameters reach 0.98 for K_2 and K_3 but the average correlation is 0.15. Table 7.4 gives the correlation matrix for additional parameters.

	Δx_p	Δy_p	Δc	s_x	a	K_1	K_2	K_3	P_1	P_2
Δx_p	1.000	0.015	-0.001	0.001	0.052	-0.004	0.004	-0.004	0.950	-0.001
Δy_p		1.000	0.035	0.028	0.006	-0.014	0.010	-0.005	0.009	0.896
Δc			1.000	0.058	0.003	-0.528	0.454	-0.395	-0.000	0.019
s_x				1.000	0.001	-0.036	0.058	-0.061	-0.003	0.059
a					1.000	-0.001	-0.000	0.000	0.069	0.008
K_1						1.000	-0.965	0.906	0.000	-0.003
K_2							1.000	-0.982	-0.001	0.007
K_3								1.000	0.002	-0.000
P_1									1.000	-0.001
P_2										1.000

Table 7.4 Correlation among additional parameters for version cvp223.

The additional parameters and the ratio between their absolute value and standard deviation is given in Table 7.5. The ratio shows the precision with which they are determined (the standard deviation is computed with the standard deviation of unit weight *a posteriori*). They are all significant when using the student test value for a probability of 0.97, i.e. 1.96. Considering all criteria, then the determination of the additional parameters with the network can be considered to be very strong.

Parameter	Adjusted value	Test value	Student test criteria
a	-1.66e-5	9.3	1.96
K_1	-2.65e-3	754.8	1.96
K_2	5.17e-5	166.5	1.96
K_3	-2.87e-7	35.2	1.96
P_1	-6.03e-5	48.1	1.96
P_2	-7.84e-5	70.2	1.96

Table 7.5 Additional parameters and test values for version cvp223 (see *Gruen, 1978* for testing procedure).

The influence of additional parameters at a point with coordinates $x = 3.0$ and $y = 2.0$ mm is given in Table 7.6. The influence of the shear parameter is very small. The effects of distortion are predominant with the first parameter of radial symmetric distortion having an influence which is 4 times larger than the second parameter and 50 times larger than the third. Figure 7.8 shows the distortion profile for radial symmetric distortion and Figure 7.9 plots of the effects of additional parameters on a grid spaced at 1 mm extending 6 by 4 mm of the 8 by 6 mm sensor size.

Parameter	Δx [μm]	Δy [μm]	
a	-0.03	-0.05	
K_1	-97.22	-61.62	
K_2	23.39	14.82	
K_3	-1.60	-1.02	
P_1	-2.05	-0.76	
P_2	-0.87	-1.52	
Total	-78.38	-50.15	vector = 93 μm

Table 7.6 Influence of additional parameters at an image point $x = 3$, $y = 2$ mm.

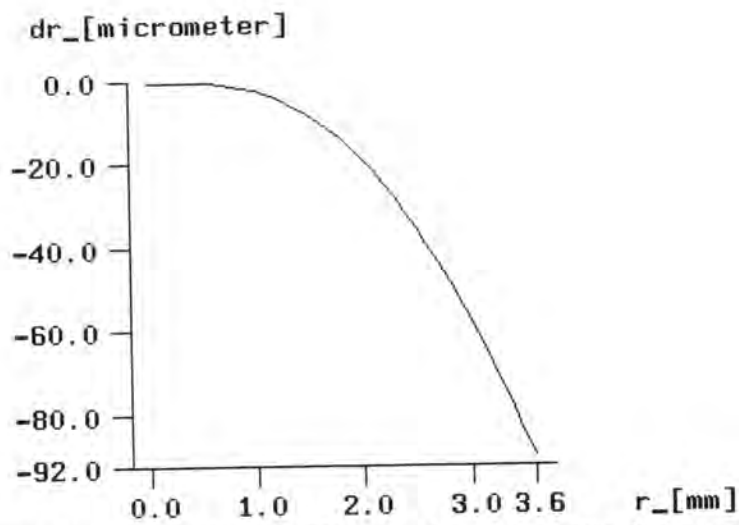


Figure 7.8 Distortion profile for radial symmetric distortion (K_1 , K_2 , K_3).

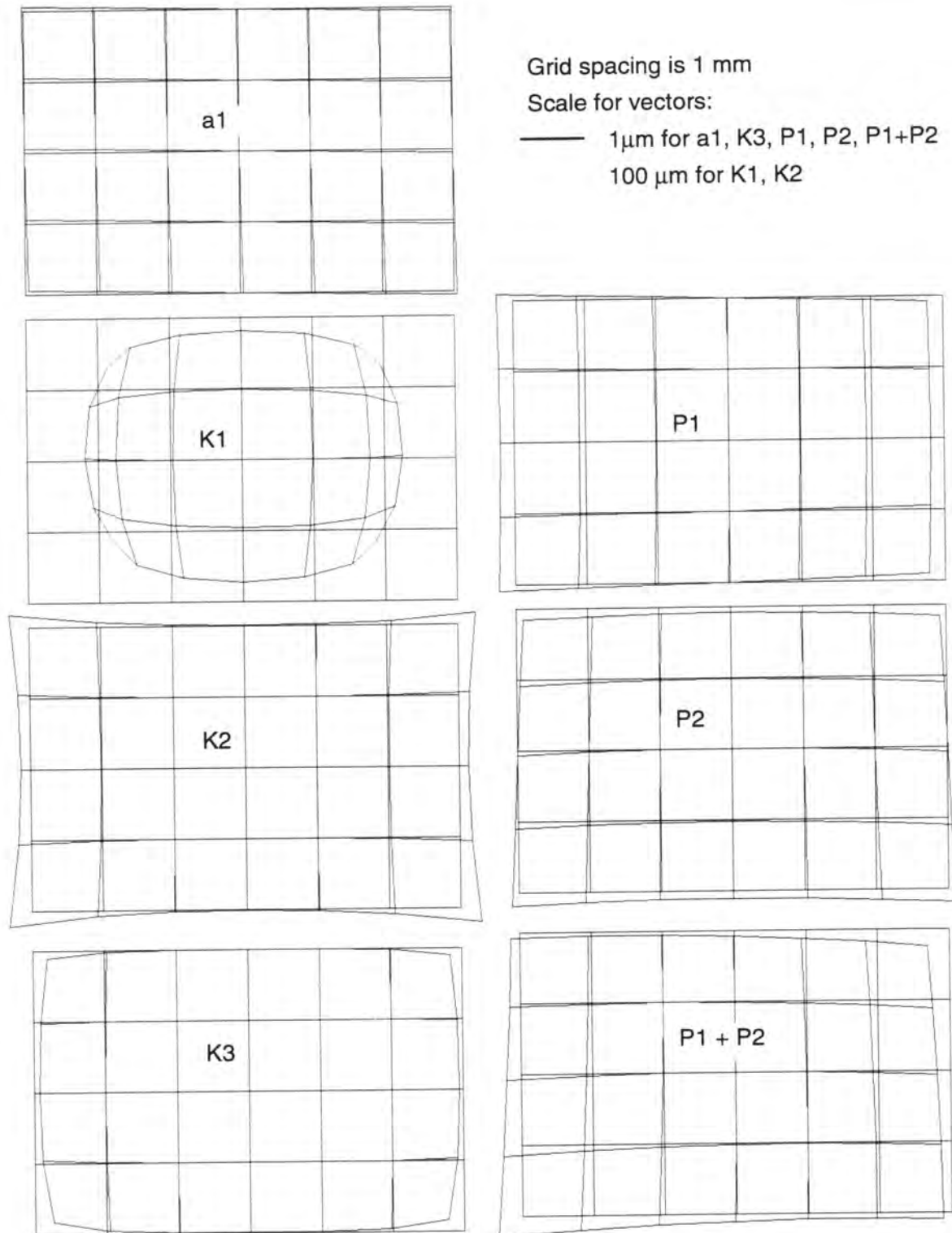


Figure 7.9 Effects of additional parameters of version cvp223 on a 6 by 4 mm grid (image format is 8 by 6 mm).

7.4.2 Potential Limiting Factors

The precision of object coordinates of version cvp223 (see Table 7.2) corresponds to a relative precision of 1 part in 96000, 87000, and 3100 in X, Y and Z respectively. The precision in Z is 0.001% of the average distance to object points, or 1 part in 98000 thereof. The RMS errors computed from check points correspond to an accuracy of 1 part in 30000, 35000, and 9600 in X, Y, and Z respectively. The accuracy in image space is $1/46^{\text{th}}$ and $1/50^{\text{th}}$ of the pixel spacing in x and y. The precision and accuracy is excellent considering the small average target size in image space and the large differences of scale. The large discrepancy between the theoretical and empirical precision measures requires further analysis. Some factors which could be the source of the difference are discussed in the following.

The comparison of theoretical and empirical precision measures assumes that the reference coordinates are at least a factor three more accurate than the ones to be checked. Correcting the precision estimates for the object coordinates by that of the reference coordinates (0.02 mm in X, Y and 0.03 mm in Z) and the standard deviation of the **centricity of the targets** used by theodolites with respect to those of the CCD-camera (0.005 mm in X and Y) results for version cvp223 in a precision of 0.034, 0.031, and 0.046 in X, Y and Z respectively. Although this is a quite large decrease these values are still factors of 2.5, 1.9 and 2.5 better than the empirical values in the respective coordinate directions. This can thus only explain part of the discrepancy.

LSM uses an **affine transformation** to model the effects of perspective. This approximation of a perspective transformation is valid as long as the angle spanned by the rays to the patch is very small, i.e. the rays are practically parallel. This assumption might very well be violated in close-range applications with very large targets or a large imaging scale. The difference between the correct and the measured position of circular targets as determined with LSM is identical as with methods using the centre of the elliptical image of the circle as the location of the centre of the object circle. The difference between the correct and the measured position can be approximately computed using the elements as defined in Figure 7.10 with a formula given in *Lenz, 1988*:

$$dy = \frac{r^2}{Z^2} \sin \alpha \cos \alpha (1 + \tan \alpha \tan \beta) \quad (7.27)$$

where:

- dy difference between correct and measured position
- r radius of target
- Z Z coordinate of target

The size of the error was computed for the targets on the wall and on the structure. The largest effect is observed for the outermost stations (largest α) where the displacement reaches $0.17 \mu\text{m}$, whereas it reaches only $0.05 \mu\text{m}$ for the targets on the wall. As indicated by the formula, the size of the displacement varies for one image with the angle β . When all targets are within one plane the average displacement would induce a shift of the principal point and the difference in the error would result in a scaling of the image. As the targets are located on two object space planes the effects are similar. The average displacement and scale will thus be absorbed by the corresponding two additional parameters. For the network in question the displacement is opposite with respect to the image coordinate system for the images of stations 12 to 15 and 22 to 25 and is rotated by 90 degrees for those using a roll. It thus cannot be absorbed by the additional parameters of version cvp223 as they are introduced as block invariant parameters. To what extent

these effects are perspectively compensated by exterior orientation elements has not been investigated, but it is assumed to be at least partially compensated by them. This error is one potential contributing factor to the discrepancy between theoretical and empirical precision estimates, but it cannot explain the large difference.

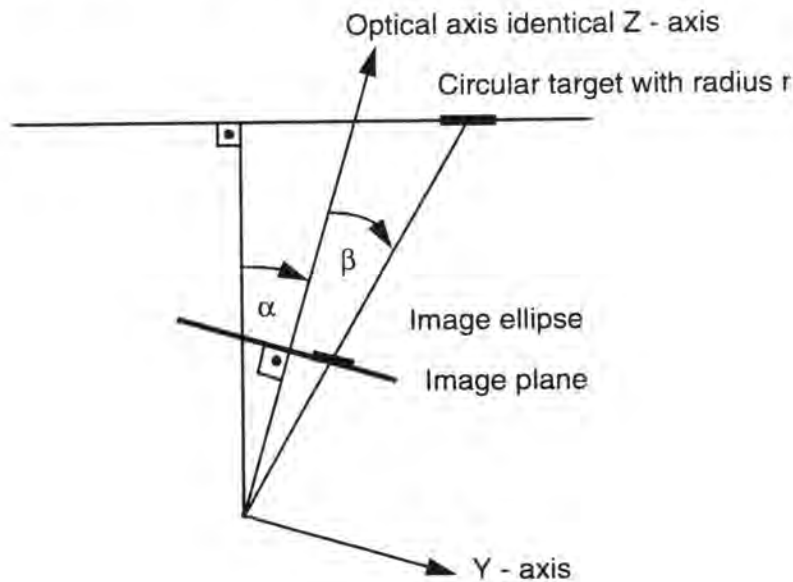


Figure 7.10 Geometry for assessing the difference between the location of the centre of the object circle in the image and the centre of its elliptical image.

For a **further analysis of the results** the residuals in image space, the residuals at control points in object space, and the differences to the reference coordinates in image and object space are analyzed. Figure 7.11, Figure 7.12, and Figure 7.13 show the respective plots for version cvp223. The plot of residuals in Figure 7.11a and the plot of control point residuals in object space Figure 7.11b indicate systematic patterns. The plots for the differences to check points in image space represent the plots for the six images taken at stations 15xx. They reveal large systematic patterns with a magnitude of approximately 0.2 to 0.3 μm . These patterns originate at points in particular columns as shown in Figure 7.12b for an image taken at station 1330. This is supported by the plots showing the differences to check points in object space. The arrows in Figure 7.13a indicate the targets on the five bars of the structure. Interestingly the vectors are very similar for targets within columns. Targets on the wall close to the ceiling do also exhibit a downward trend. This is also apparent in Figure 7.13b where the targets within one column come to lie on each other. Especially points in columns 4, 5, 12 and 17 exhibit large discrepancies (the columns in the figures are numbered for easier reference). It is also evident from Figure 7.13b that the displacement in object space will result in different displacements in image space dependent on the projection direction, up to the point where some discrepancies will not even show up in the images. The displacement of the targets on the top, and to some degree those at the bottom, can be seen in Figure 7.13c. The targets of these columns lie on different regions in the image space and are thus quite probably not a result of a systematic error that can be modelled but a deficiency that has to do with the targets.

To eliminate the influence of the control points onto the geometry of the photogrammetric network a version with a minimum constraint control point distribution was comput-

ed. Two points on the left and right extreme at the bottom of the wall are introduced as control points in X, Y, and Z and the leftmost target in the second row from top on the wall is introduced as a control point in Z. The results of the bundle adjustment and comparison to check points are given in Table 7.7.

V	AP	Co	Ch	r	$\hat{\sigma}_0$	σ_X [mm]	σ_Y [mm]	σ_Z [mm]	μ_X [mm]	μ_Y [mm]	μ_Z [mm]	μ_x [μm]	μ_y [μm]
cvp223	10	30	56	11547	0.36	0.027	0.023	0.035	0.086	0.058	0.114	0.24	0.22
cvp221	10	m	83	11464	0.34	0.047	0.052	0.063	0.124	0.091	0.111	0.33	0.28
<i>cvp223 / cvp221</i>									<i>0.7</i>	<i>0.6</i>	<i>1.0</i>	<i>0.7</i>	<i>0.8</i>

Table 7.7 Results of bundle adjustment with 30 control points and a minimum constraint configuration.

The difference in precision values of the object coordinates is affected by the difference in datum and can therefore not be directly compared. The comparison to check points were in both cases performed after a three-dimensional similarity transformation onto the check points. The difference between the empirical precision estimates of the two versions are significant in X and Y (see Table 7.8).

	X	Y	Z	all in [mm]
Difference	0.038	0.033	0.003	
Standard deviation of diff.	0.0072	0.0073	0.0097	
Ratio	5.3	4.5	0.3	

Table 7.8 Testing of difference of empirical precision estimates with the test criterion $t(0.95, 139) = 1.66$.

The plots of the residuals of version cvp223 and cvp221 differ only slightly (see Figure 7.11 and Figure 7.14). The plots of the checkpoint residuals in image space show the systematic differences clearer. The plot of checkpoint differences in object space confirms the trends observed above. The systematic differences become clearer, especially for the points of the wall close to the ceiling.

Project: xc910620_cvp Version: 223
 Image: xc77_cvp_1510_1 Checkpoint differences
 Scale for Points $\overline{\hspace{1cm}}$ 1.100 mm in x
 $\overline{\hspace{1cm}}$ 1.100 mm in y
 Scale for Vectors $\overline{\hspace{1cm}}$ 0.200 micron (20.000 for APs)

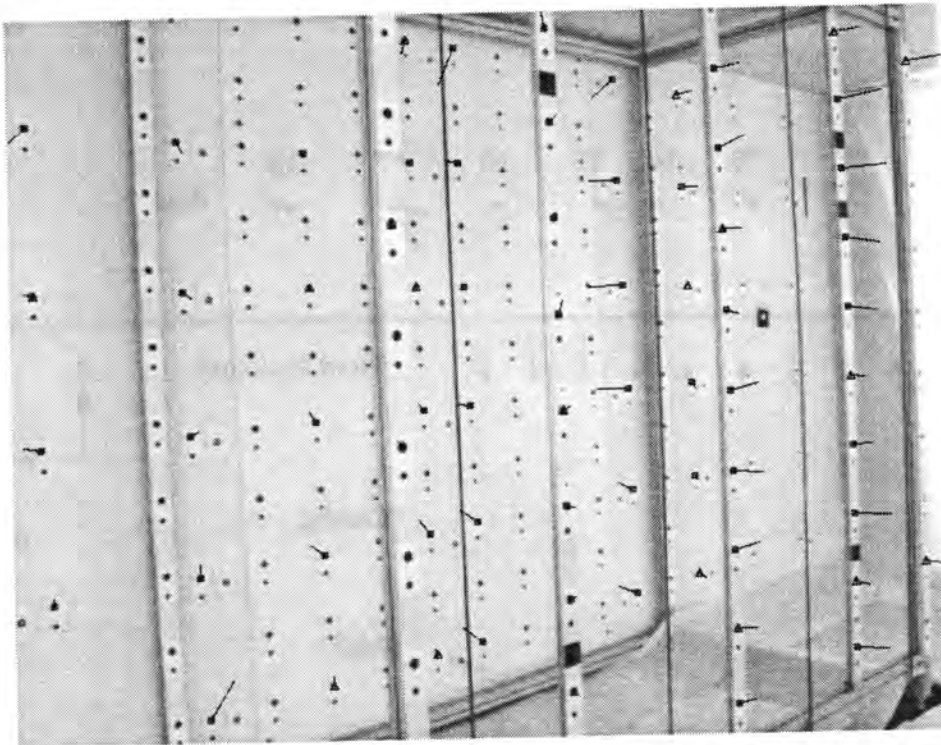
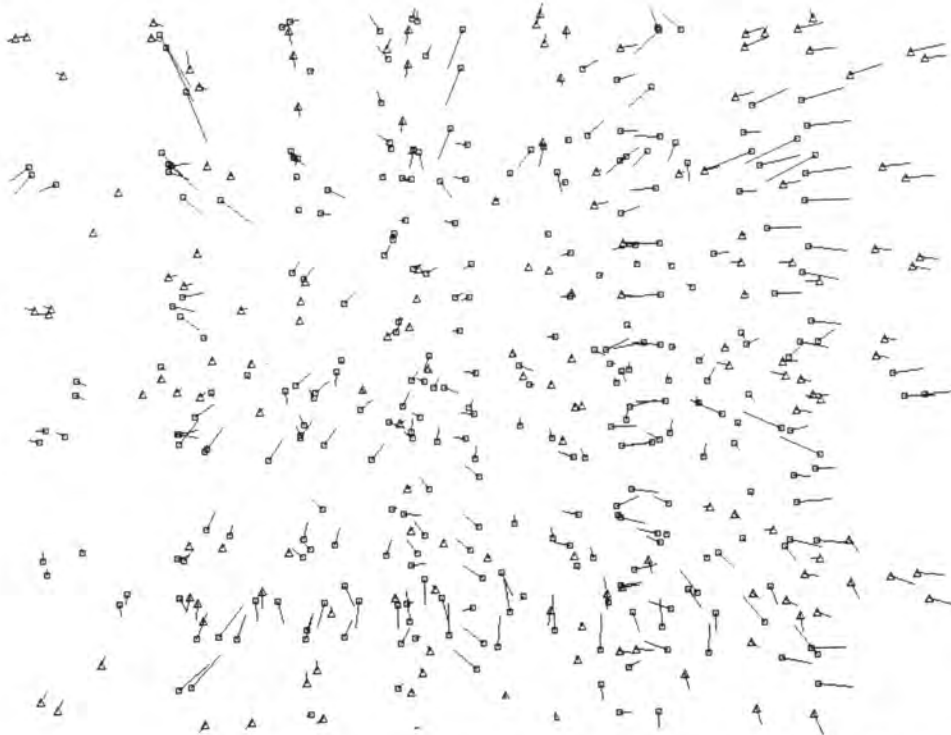


Figure 7.12 Check point differences for version cvp223 for 6 images of stations 15xx (top) and an image at station 1330 (bottom).

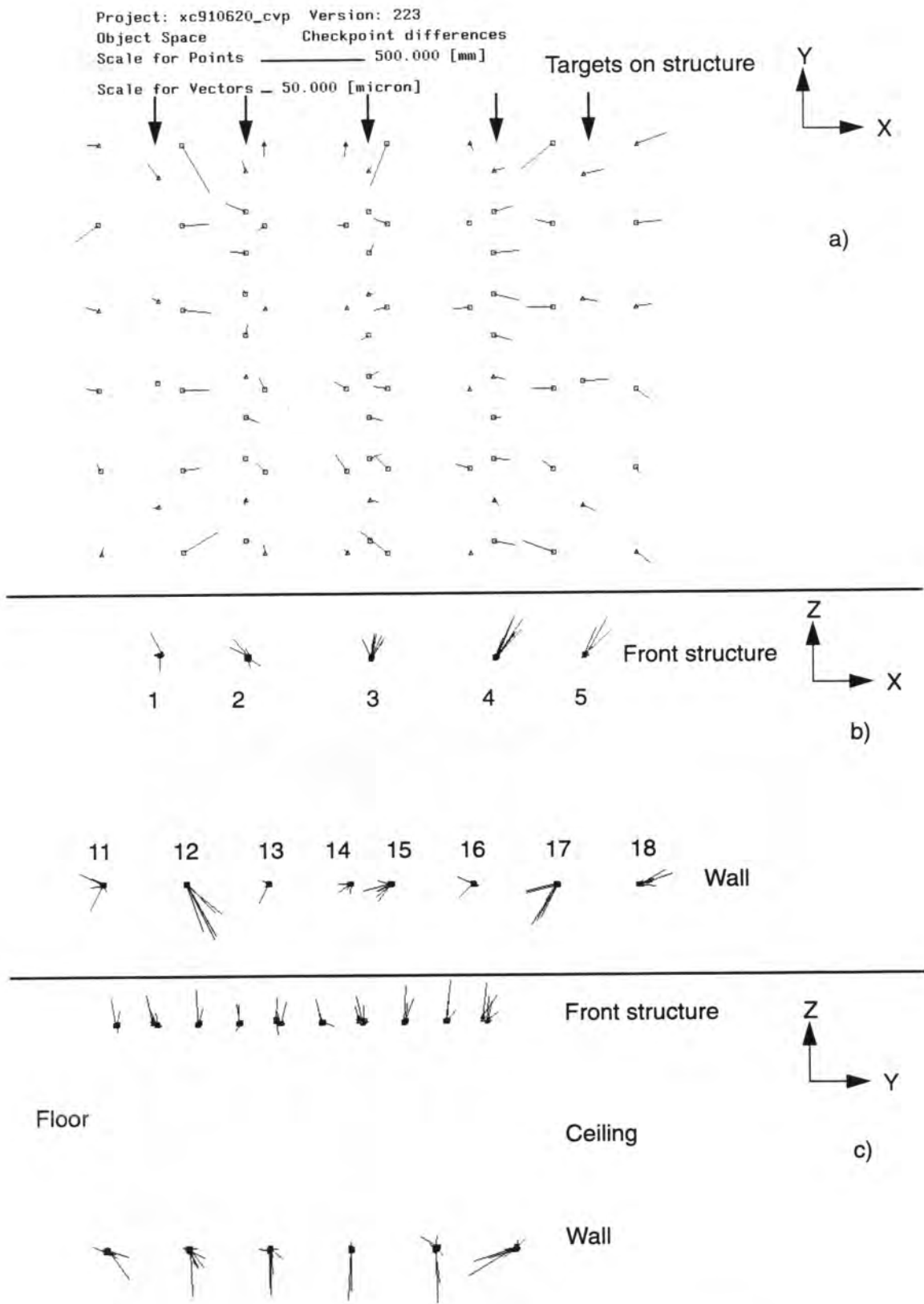
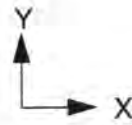
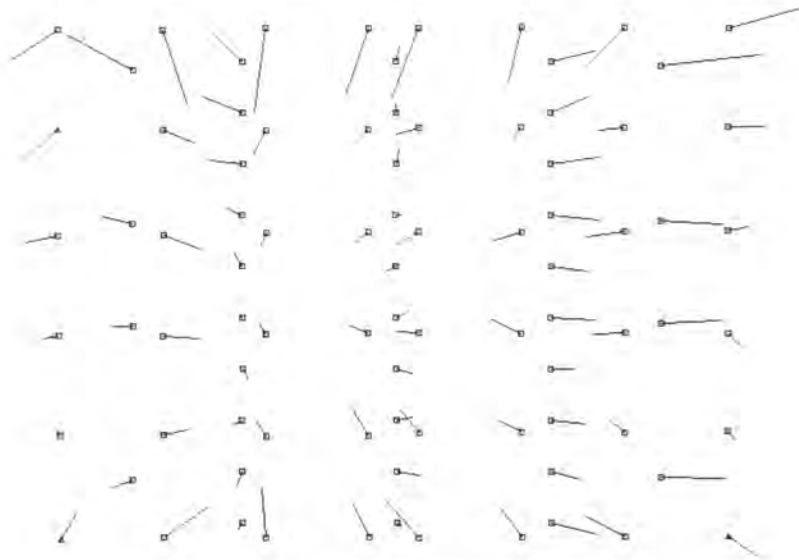


Figure 7.13 Differences to check points in object space for version cvp223.



Figure 7.14 Residuals (top) and checkpoint differences (bottom) for images taken at stations 15xx of version cvp221.

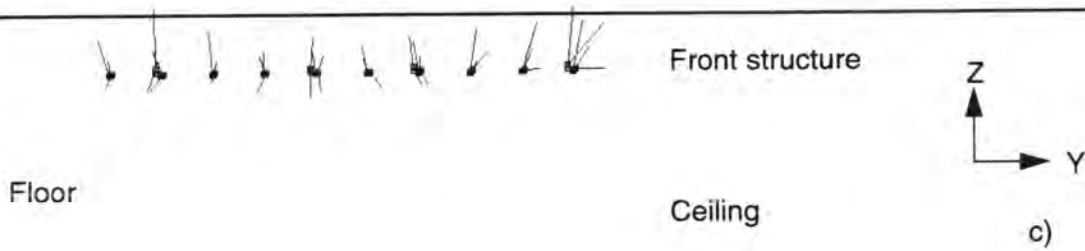
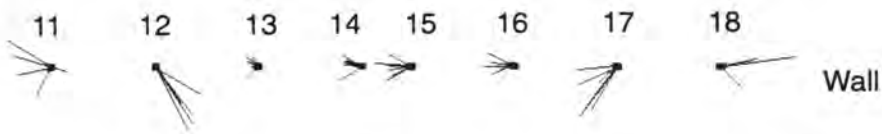
Project: xc910620_cvp Version: 221
 Object Space Checkpoint differences
 Scale for Points _____ 500.000 [mm]
 Scale for Vectors - 50.000 [micron]



a)



b)



c)



Figure 7.15 Differences to check points in object space for version cvp221.

7.4.3 Influence of Local Illumination Gradients

The areas of columns showing the systematic differences and those close to the ceiling and the floor were analyzed to locate the origin of the displacements. Grayvalue profiles in these regions reveal local illumination gradients. Figure 7.16 shows zoomed portions of an image taken at station 1530 with grayvalue profiles. The portions are taken at columns 12 and 17 (see figures of checkpoint residuals above such as Figure 7.15) and for a target on the wall close to the ceiling. The gradients amount to 3 to 5% of the intensity (background left and right of target) in columns 12 and 17 and to slightly less for those close to the ceiling. The gradients in columns 12 and 17 were traced to shadows due to lights which were placed close to the testfield (see section 6.8). The fall-off towards the ceiling of the room is a result of the different reflectivity at the darker ceiling (the fall-off due to the dark floor was already detected before the imagery was acquired and white paper was placed to alleviate it).

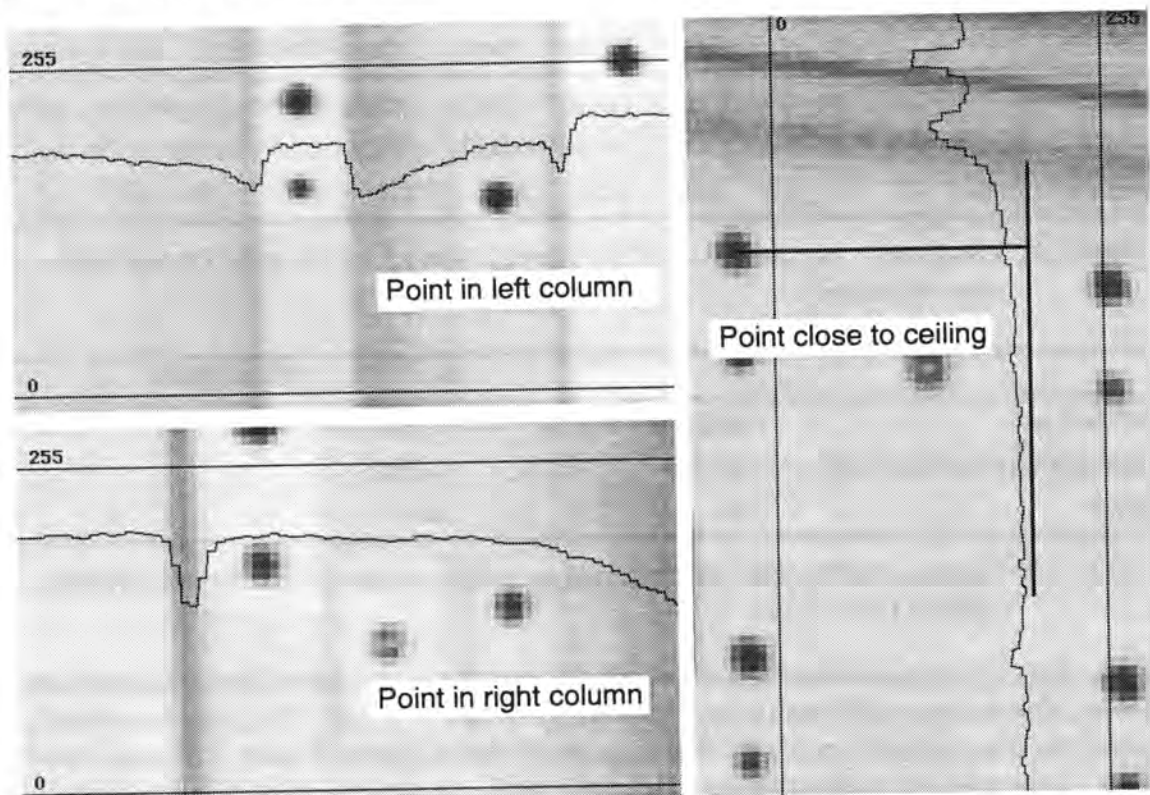


Figure 7.16 Shadows and light intensity variations. The profiles refer to the line with grayvalue 0.

The effect of illumination intensity gradients on the position determined with LSM was investigated in section 6.8. It was shown there that the effects of illumination intensity gradients can be reduced for the targets in columns 12 and 17 when a **5 x 5 template instead of a 7 x 7 template** is used. As the displacement is assumed to differ depending on how the target is imaged (obliqueness and scale) no simple correction can be performed. Based on the results of section 6.8 a reduction of the influence of local illumination gradients should be achievable when using a 5 x 5 instead of a 7 x 7 template in LSM.

Table 7.11 gives the results of version cvp223, measured with a 7 x 7 template, and those of version cvp243, which was measured using a 5 x 5 template. The squared mean of the standard deviations of image coordinates from the LSM are 0.49 and 0.40 versus 0.38

and $0.33 \mu\text{m}$ (0.045, 0.036, 0.035, 0.030 pixel) in x and y for the version *cvp223* and *cvp243* respectively (with 6119 and 6118 image points). The weights of the image coordinates are a factor of 1.6 larger for version *cvp243* (5 x 5 template) than for version *cvp223*. The increase of the standard deviation of unit weight *a posteriori* is thus at least partially attributable to the difference in the average weight. This is also evident from the quadratic mean of the image coordinate residuals which are 0.32, 0.29 and 0.28, 0.26 μm in x and y for versions *cvp223* and *cvp243* respectively. The precision of the object space coordinates, both computed with a standard deviation of unit weight *a priori* of $0.44 \mu\text{m}$, is improved by a factor of 1.2. As the geometry of the two networks is otherwise identical (except for a few rays) this difference is attributable to the different weights for the image coordinates of the two versions. The empirical accuracy measures are improved by a factor of 1.3 on average. This improvement is significant for the X and Z axes only (see Table 7.10).

V	AP	Co	Ch	r	$\hat{\sigma}_0$	σ_X [mm]	σ_Y [mm]	σ_Z [mm]	μ_X [mm]	μ_Y [mm]	μ_Z [mm]	μ_x [μm]	μ_y [μm]
<i>cvp223</i>	10	30	56	11547	0.36	0.027	0.023	0.035	0.086	0.058	0.114	0.24	0.22
<i>cvp243</i>	10	30	56	11547	0.42	0.023	0.019	0.029	0.068	0.050	0.084	0.19	0.17
<i>cvp223 / cvp243</i>					0.9	1.2	1.2	1.2	1.3	1.2	1.4	1.3	1.3

Table 7.9 Results for template size of 7 x 7 (*cvp223*) and 5 x 5 (*cvp243*) in the presence of shadows.

	X	Y	Z	all in [mm]
Difference	0.018	0.008	0.030	
Standard deviation of diff.	0.0063	0.0054	0.0082	
Ratio	2.8	1.5	3.6	

Table 7.10 Testing of difference of empirical precision estimates with the test criterion $t(0.95, 112) = 1.66$.

It can thus be concluded that the use of a 5 x 5 template leads under these circumstances (local illumination gradients) to an improvement of the accuracy. The plots of residuals, checkpoints in images space and check points in object space (Figure 7.17 and Figure 7.18), indicate that the effects of local intensity gradients are nevertheless not completely eliminated. The remaining discrepancies can be a result of these residual displacement as well as other sources.

Scale for Vectors — 0.200 micron (20.000 for APs)



Figure 7.17 Residuals (top) and checkpoint differences (bottom) for images taken at station 15xx of version cvp243.

Project: xc910620_cvp Version: 243
 Object Space Checkpoint differences
 Scale for Points ————— 500.000 [mm]
 Scale for Vectors — 50.000 [micron]

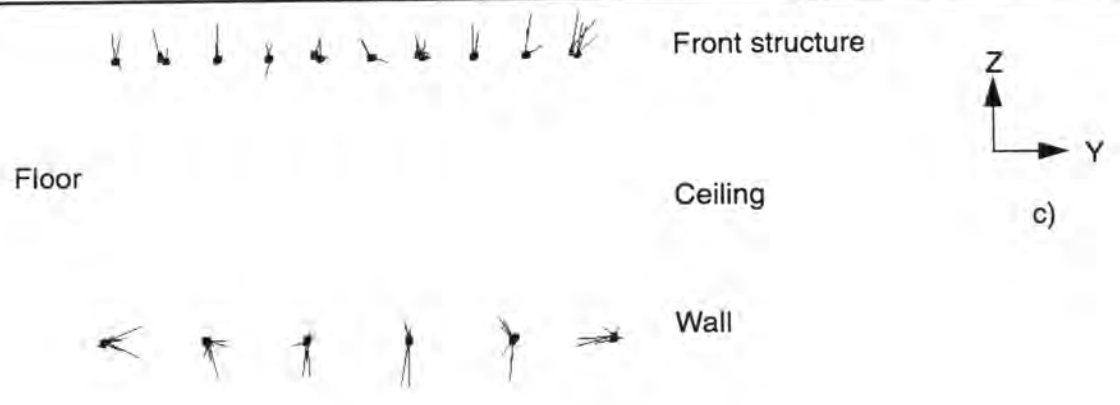
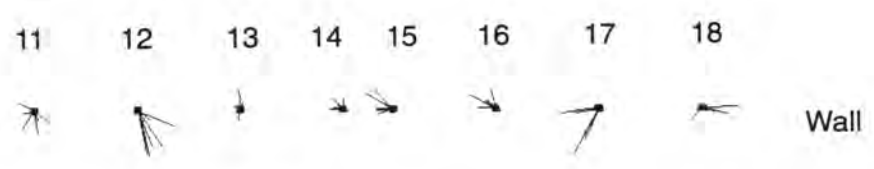
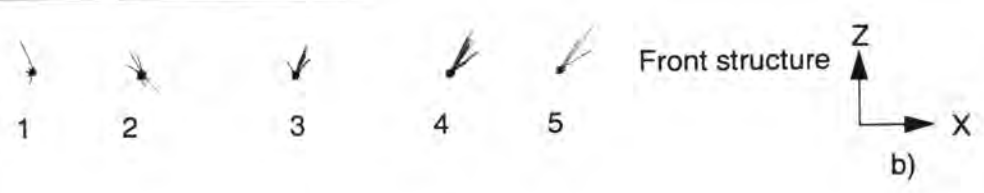
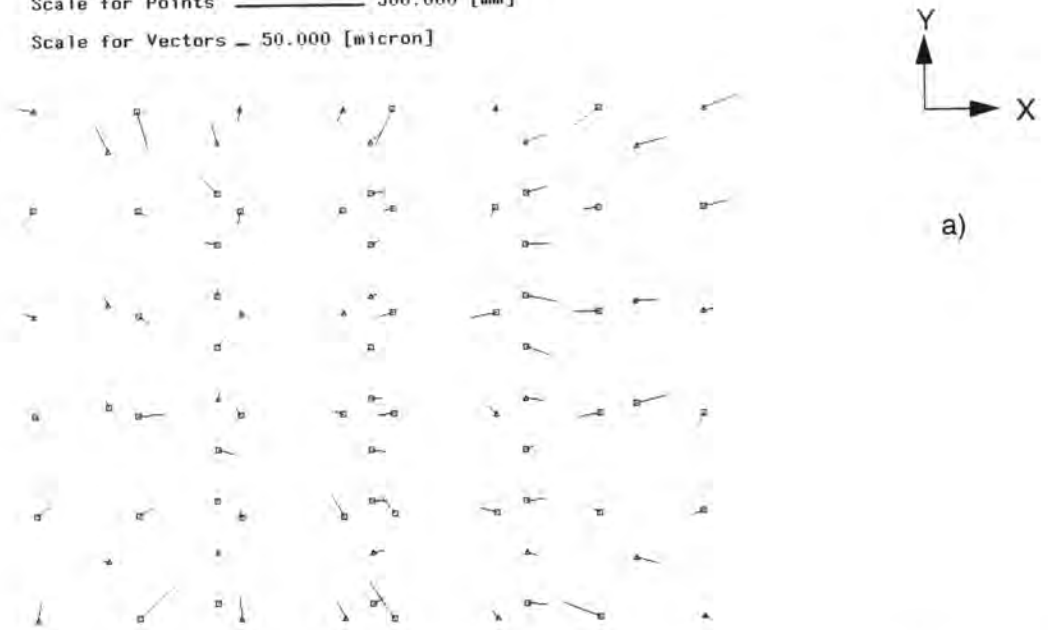


Figure 7.18 Differences to control and check points in object space for version cvp243.

Because of aforementioned illumination problems, it was decided to **eliminate the points in columns 12 and 17** as well as those on the wall which are close to the ceiling. The degrading effects of the local illumination gradients at these targets should thus be eliminated. Again two versions, one using the data measured with the 7 x 7 and the other with the 5 x 5 template, were computed and the results compiled in Table 7.11

V	AP	Co	Ch	r	$\hat{\sigma}_0$	σ_X [mm]	σ_Y [mm]	σ_Z [mm]	μ_X [mm]	μ_Y [mm]	μ_Z [mm]	μ_x [μm]	μ_y [μm]
cvp323	10	30	40	9881	0.35	0.027	0.022	0.033	0.065	0.050	0.064	0.18	0.15
cvp343	10	30	40	9879	0.42	0.023	0.019	0.028	0.062	0.039	0.056	0.16	0.14
<i>cvp323 / cvp343</i>					<i>0.8</i>	<i>1.2</i>	<i>1.2</i>	<i>1.2</i>	<i>1.1</i>	<i>1.4</i>	<i>1.1</i>	<i>1.2</i>	<i>1.1</i>
<i>cvp223 / cvp323</i>					<i>1.0</i>	<i>1.0</i>	<i>1.0</i>	<i>1.1</i>	<i>1.3</i>	<i>1.2</i>	<i>1.8</i>	<i>1.3</i>	<i>1.5</i>
<i>cvp243 / cvp343</i>					<i>1.0</i>	<i>1.0</i>	<i>1.0</i>	<i>1.0</i>	<i>1.1</i>	<i>1.3</i>	<i>1.5</i>	<i>1.2</i>	<i>1.2</i>

Table 7.11 Results for template size of 7 x 7 and 5 x 5 in the presence of shadows after elimination of points in columns 12 and 17 as well as points on the wall close to the ceiling.

The standard deviations of unit weight *a posteriori* and the precision estimates are basically unchanged. The improvement factors of the empirical precision estimates with the corresponding versions before the elimination of the points show that the results are again improved. The improvement is, as expected, larger for the 7 x 7 template as the effect of the local illumination gradient is larger for those. The plots of the checkpoint differences in object space of both versions given in Figure 7.18 and Figure 7.18 indicate a remaining systematic difference though. Especially targets in columns 4 and 5 of the front structure as well as 15 and 16 of the wall exhibit at this point unexplained effects. These effects are investigated in the following section.

Project: xc910620_cvp Version: 323
 Object Space Checkpoint differences
 Scale for Points _____ 500.000 [mm]
 Scale for Vectors _ 50.000 [micron]

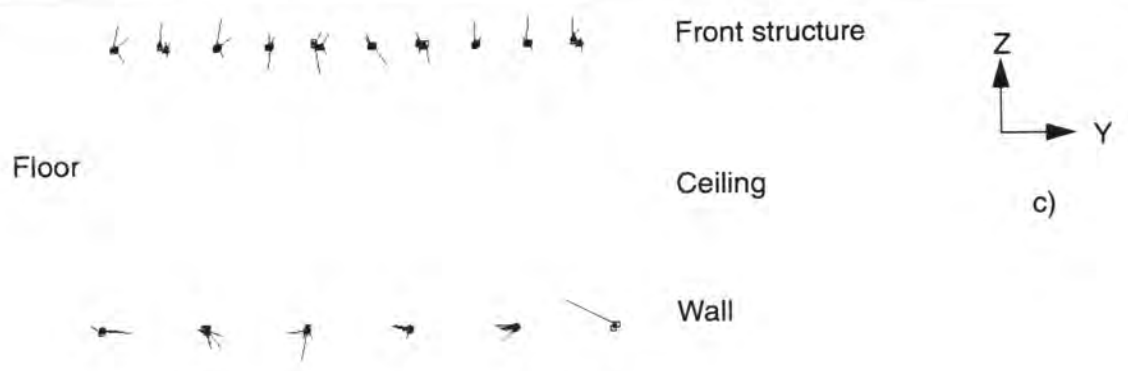
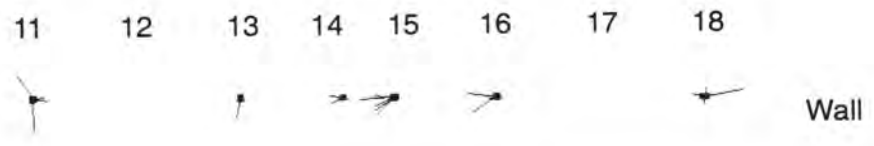
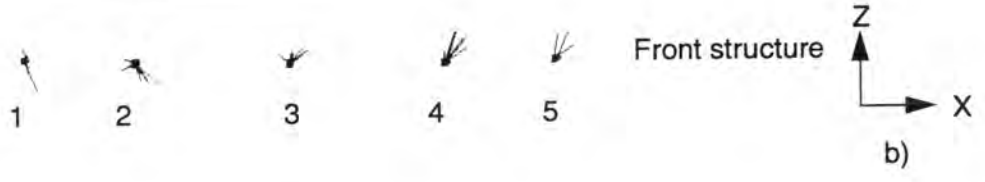
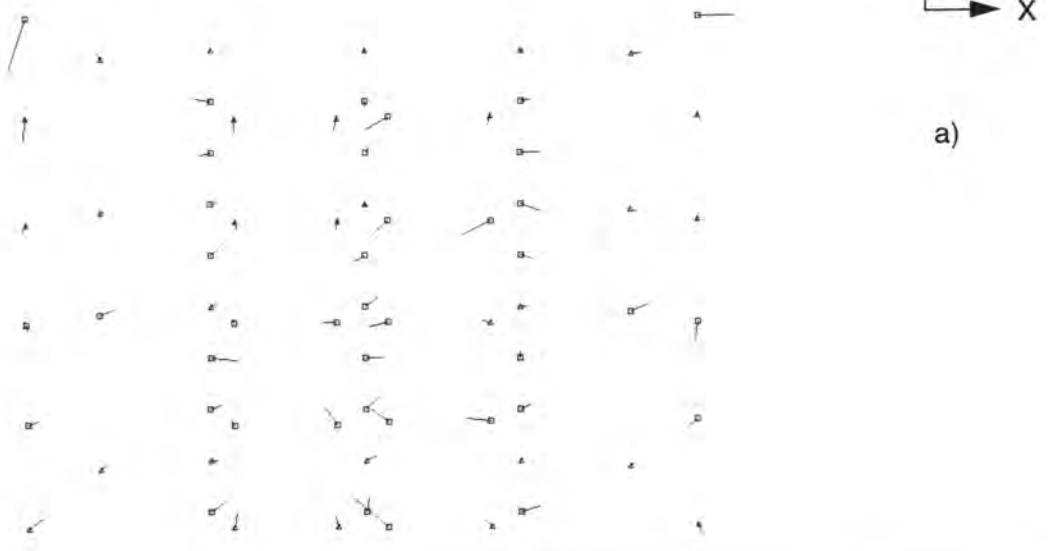


Figure 7.19 Differences to control and check points in object space for version cvp323.

Project: xc910620_cvp Version: 343
 Object Space Checkpoint differences
 Scale for Points $\rule{1cm}{0.4pt}$ 500.000 [mm]
 Scale for Vectors $\rule{1cm}{0.4pt}$ 50.000 [micron]

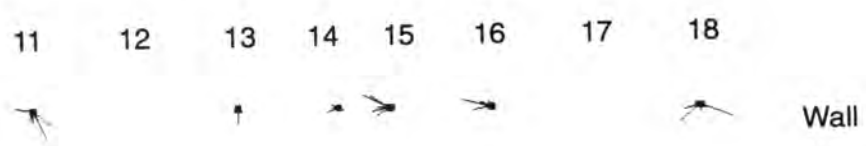
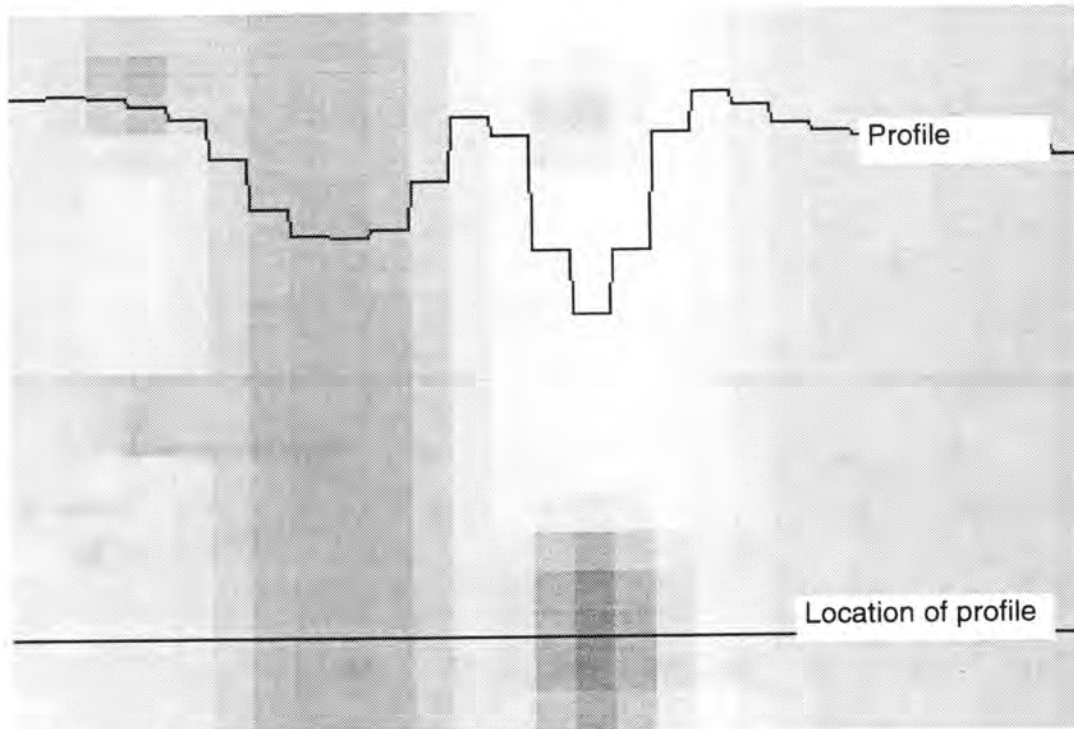


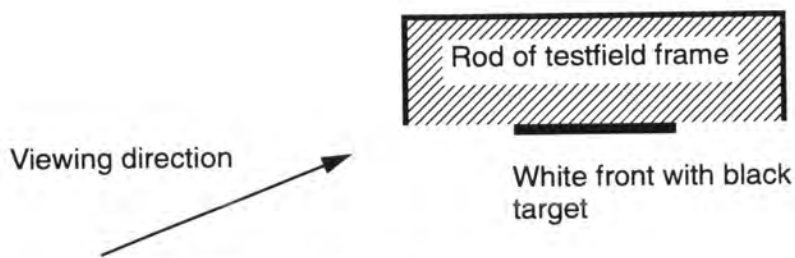
Figure 7.20 Differences to control and check points in object space for version cvp343.

7.4.4 Degradations from Obliqueness and Small Image Scale

Figure 7.21 a) shows a zoomed portion of a target with a profile of the grayvalues and b) the planview of a section of the testfield frame structure. The schematic drawing below indicates the relative position of the rod with respect to the viewing direction. The dark left side of the rod leads to a decrease in the grayvalues of the background to the left of the target, whereas the right side of the target adjoins to the white wall, which is only slightly darker than the white front of the rod. As shown by the profile in Figure 7.21 the combined effect of this difference of the background is similar to the influence of illumination gradients.



a) Zoomed part of image with target on control frame.



b) Planview of control frame structure.

Figure 7.21 Image of target on front structure under oblique view.

The problem is also evident from Figure 7.4. The obliqueness of targets on a number of columns is too large and they should have been removed from the data before the measurement (actually this should already be tested during network design). Table 7.12 indicates the **stations and target columns which were eliminated** due to the excessive obliqueness/poor incidence angle.

Stations	Columns eliminated
12xx	13xx, 14xx, 15xx (3, 4, 5)
13xx	14xx, 15xx (4, 5)
14xx	14xx, 15xx (4, 5)
22xx	11xx, 12xx, 13xx (1, 2, 3)
23xx	11xx, 12xx (1, 2)
24xx	11xx, 12xx (1, 2)

Table 7.12 Eliminations due to effects of sides of structure on images of targets (numbers in brackets refer to the ones in the figures).

The results of the ensuing version *cvp601* are given in Table 7.15 together with the improvement factor with respect to the version before the elimination of the points in the columns. The precision estimates decrease as the number of rays of the targets on the structure is drastically reduced and the use of the format becomes poor for all frames with oblique views, i.e. 12xx, 13xx, 22xx, and 23xx. The empirical precision measures indicate as expected a small improvement. The plot of residuals is unchanged, but one of the checkpoint differences in image space (see Figure 7.17) shows that the systematic effects have decreased. There is nevertheless a small local discrepancy. This is also evident from the plots of the differences to check points in object space shown in Figure 7.18. The empirical precision measures are still a factor of 1.6, 1.4 and 1.1 larger than the theoretical estimates from the bundle adjustment in X, Y, and Z when correcting latter for the precision of the reference coordinates and the centricity of reference and target used.

Again a version using minimum control was computed (*cvp611*). The empirical precision measures of this version are much lower than for the 30 control point version. This indicates that some of the deformations between the photogrammetric and the geodetic model were removed by deforming the photogrammetric data set when using 30 control points. The plots of version *cvp611* show the remaining systematic differences (see Figure 7.17 and Figure 7.18). Although a number of points were eliminated, the average number of rays per point of version *cvp611* was 34.3

V	AP	Co	Ch	r	$\hat{\sigma}_0$	σ_X [mm]	σ_Y [mm]	σ_Z [mm]	μ_X [mm]	μ_Y [mm]	μ_Z [mm]	μ_x [μ m]	μ_y [μ m]
<i>cvp601</i>	10	30	38	8969	0.38	0.026	0.020	0.032	0.052	0.040	0.048	0.13	0.13
<i>cvp343 / cvp601</i>						0.88	0.95	0.88	1.2	1.0	1.2	1.2	1.1
<i>cvp611</i>	10	m	65	8886	0.37	0.044	0.048	0.056	0.085	0.075	0.064	0.23	0.22

Table 7.13 Results of bundle adjustments with different additional parameter sets.

Further Additional Parameters

The elimination of additional targets affected by small illumination gradients and effects of uneven background brightness in combination with insufficient "resolution" (i.e. insufficient image scale) was not deemed justifiable. It was instead decided to model potential systematic error components with an extension of the additional parameters.

Table 7.14 gives the versions, the control point distributions, and the number of additional parameters used for the versions. Table 7.15 gives the results obtained when introducing combinations of the set of 10 additional parameters with that of 15 additional

parameters given in (7.10) and (7.11) (versions cvp602 and cvp612) and the set of 44 additional parameters developed by Grün, 1978 (versions cvp603 and cvp613). Additional parameters leading to perfect correlations with parameters of the set containing 10 additional parameters were eliminated (4 for cvp601/cvp612, 8 for cvp603/cvp613).

	Control points	Additional parameters
cvp601	30	10
cvp602	30	25
cvp603	30	54
cvp611	min. constraint	10
cvp612	min. constraint	25
cvp613	min. constraint	54

Table 7.14 Description of versions

The results show that the parameters are still determinable, i.e. the precision of object coordinates is increased only slightly and the maximum correlation among object coordinates and additional parameters was slightly changed. The complete sets, i.e. the extended part of the set, test as significant (see Table 7.17) as well as 6 and 16 individual parameters of version cvp612 and cvp613 respectively are significant with a one-dimensional student test. The accuracy is not improved though by the introduction of further block invariant parameters. The accuracy therefore seems to be limited by the local illumination gradients and "poor image quality", i.e. the small image scale. The "poor image quality" was a result of the large variation in the image scale, the very small size of targets in the imagery, and influences of the surroundings of the targets onto the target due to the imaging onto a too small number of pixels is understood. This is documented with the collection of all images for two representative targets in Figure 7.26. The object space distance reaches from 1790 to 4903 mm with an average of 3355 mm.

V	AP	Co	Ch	r	$\hat{\sigma}_0$	σ_X [mm]	σ_Y [mm]	σ_Z [mm]	μ_X [mm]	μ_Y [mm]	μ_Z [mm]	μ_x [μm]	μ_y [μm]
cvp601	10	30	38	8969	0.38	0.026	0.020	0.032	0.052	0.040	0.048	0.13	0.13
cvp602	25	30	38	8958	0.38	0.026	0.021	0.032	0.055	0.044	0.053	0.14	0.14
cvp603	54	30	38	8933	0.38	0.026	0.021	0.032	0.056	0.044	0.052	0.14	0.14
cvp611	10	m	65	8886	0.37	0.044	0.048	0.056	0.085	0.075	0.064	0.23	0.22
cvp612	25	m	65	8875	0.36	0.046	0.049	0.0567	0.090	0.078	0.071	0.24	0.23
cvp613	54	m	65	8850	0.36	0.048	0.050	0.057	0.093	0.080	0.069	0.25	0.23

Table 7.15 Results of bundle adjustments with different additional parameter sets.

	$\rho_{ob,max}$	$\rho_{ob,av}$	$\rho_{ext,max}$	$\rho_{ext,av}$	$\rho_{ap,max}$	$\rho_{ap,av}$
cvp611	0.198	0.038	0.848	0.124	0.980	0.154
cvp612	0.245	0.038	0.930	0.102	0.970	0.120
cvp613	0.226	0.026	0.968	0.075	0.978	0.080

Table 7.16 Correlations between object coordinates, exterior orientation elements and additional parameters for three versions with increasing number of additional

parameters.

with:

- $\rho_{ob,max}$ maximum correlation between object coordinates and additional parameters
 $\rho_{ob,av}$ average correlation between object coordinates and additional parameters
 $\rho_{ext,max}$ maximum correlation between exterior orientation elements and additional parameters
 $\rho_{ext,av}$ average correlation between exterior orientation elements and additional parameters
 $\rho_{ap,max}$ maximum correlation among additional parameters
 $\rho_{ap,av}$ average correlation among additional parameters

	Test value	Test criterion
cvp612 (pars. 11 to 25)	11.7	F (0.95, 11, 8875) = 1.84
cvp613 (pars. 11 to 54)	9.2	F (0.95, 36, 8850) = 1.47

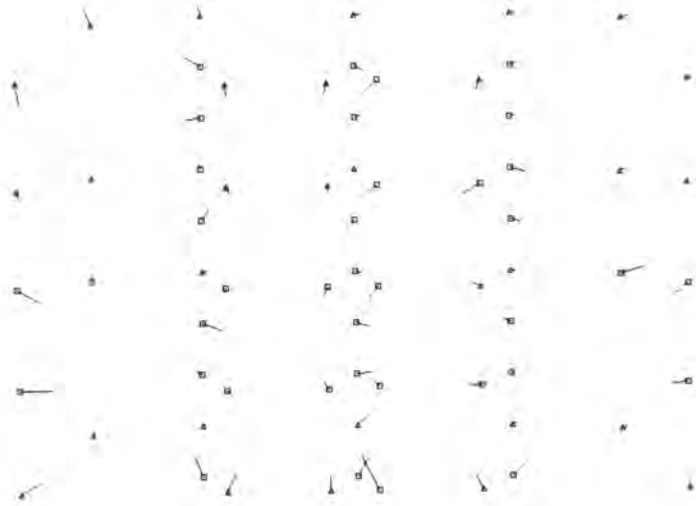
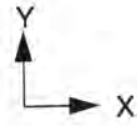
Table 7.17 Testing of additional parameter groups.

Scale for Vectors — 0.200 micron (20.000 for APs)



Figure 7.22 Residuals (top) and checkpoint differences (bottom) for images taken at station 15xx. of version cvp601.

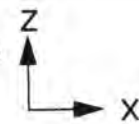
Project: xc910620_cvp Version: 601
 Object Space Checkpoint differences
 Scale for Points _____ 500.000 [mm]
 Scale for Vectors _ 50.000 [micron]



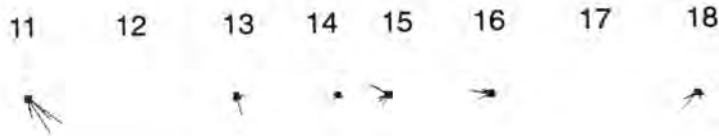
a)



Front structure



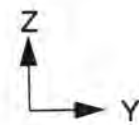
b)



Wall



Front structure



c)

Floor

Ceiling



Wall

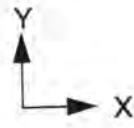
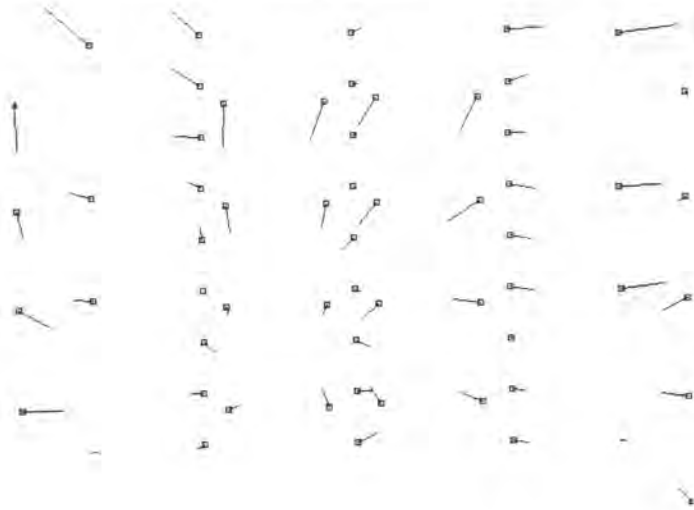
Figure 7.23 Differences to control and check points in object space for version cvp601.

Scale for Vectors — 0.200 micron (20.000 for APs)

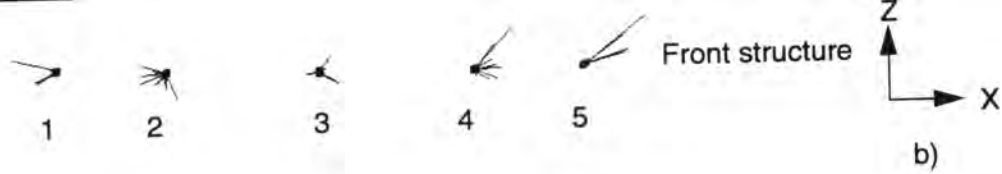


Figure 7.24 Residuals (top) and checkpoint differences (bottom) for images taken at station 15xx of version cvp611.

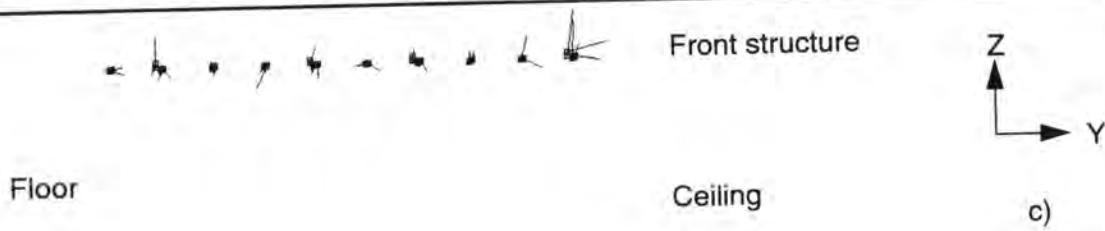
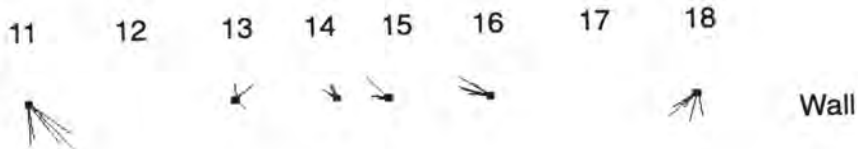
Project: xc910620_cvp Version: 611
 Object Space Checkpoint differences
 Scale for Points --- 500,000 [mm]
 Scale for Vectors --- 50,000 [micron]



a)



b)



Floor

Ceiling

c)



Figure 7.25 Differences to control and check points in object space for version cvp611.

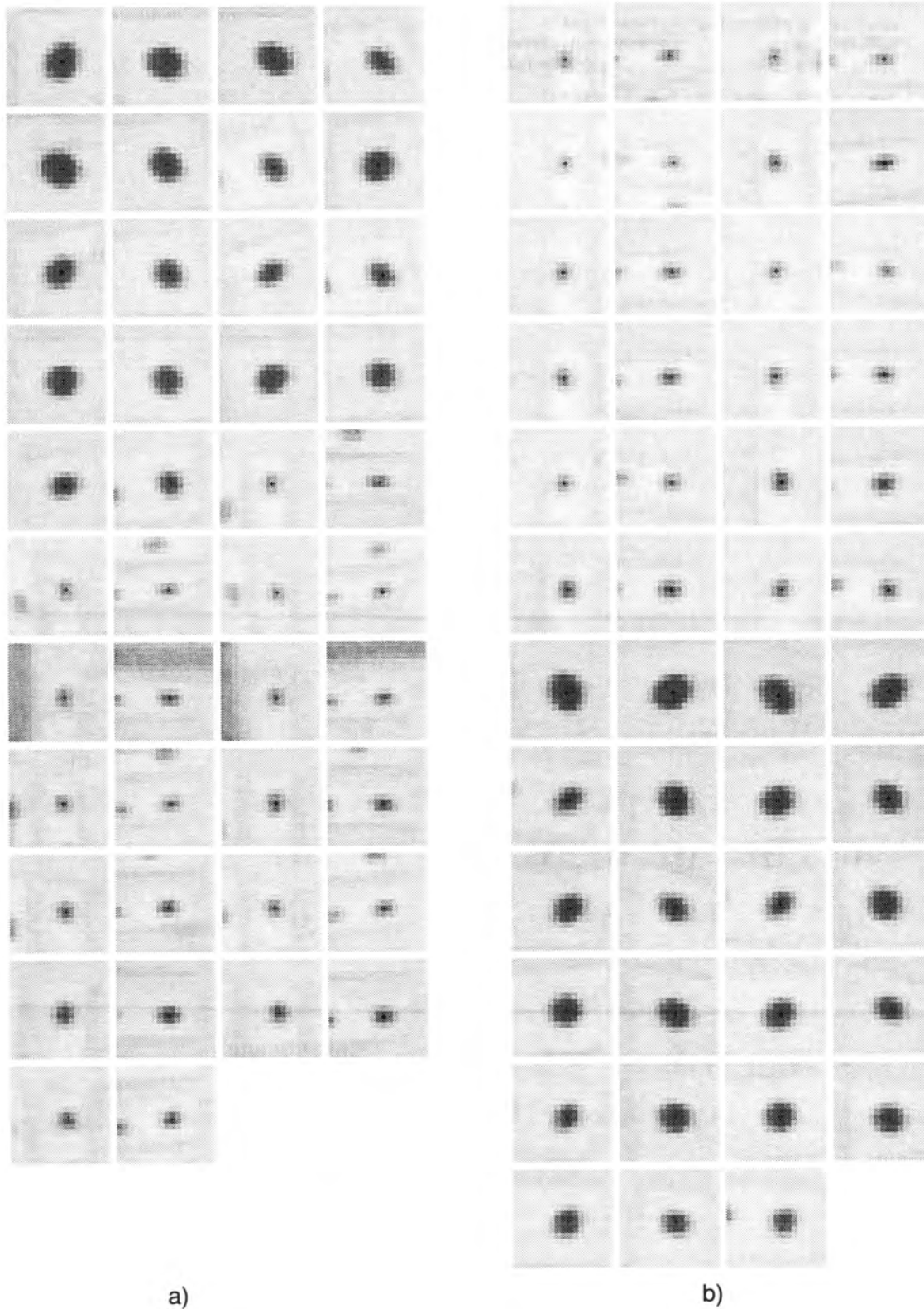


Figure 7.26 a) Areas of the 42 images of target 3023 (target at left bottom of wall).
b) Areas of the 47 images of target 5022 (target at right top of wall).

7.5 Performance with PLL Line-Synchronisation

The analysis of repeatability in section 6.7 has shown that the internal precision of imagery acquired with PLL line-synchronization is significantly worse than that of images acquired pixel-synchronously. Furthermore a shear can be introduced when the horizontal synchronization is derived from composite video. The effects of line-jitter and the geometric deformation on the accuracy of three-dimensional measurements is to be analyzed by comparing it to pixel-synchronous sampled imagery. The imagery was acquired at identical positions, thus eliminating influences from differences in the network geometry. The following parameters are compared:

- geometry in image space
- location of a vertical line
- results of a bundle adjustment

The geometry of the image is compared using identically measured image coordinates, i.e. both data sets were measured with the same template and identical settings for LSM (5 x 5 template). Figure 7.27 shows plots of the differences of images coordinates with the pixel-synchronously acquired imagery as reference and an elimination of the average translation between the images. Figure 7.27a shows the differences for the six images acquired at stations 15xx and Figure 7.27b those at stations 25xx. The large differences, apparent as horizontally-oriented vectors reaching over 0.1 pixel, are due to line-jitter. The plots show furthermore the shear introduced by using composite video with PLL line-synchronization. The amount of shear does not appear to be uniform across the image, i.e. it seems to decrease to the right of the image. The RMS and maximum values of the differences are plotted in Figure 7.28a. The RMS differences between the two data sets are 0.1 and 0.05 pixels in x and y respectively. This is in accordance with the results obtained during the analysis performed in section 6.3.1. The maximum differences are also larger in x, reaching up to 0.22 pixel. The average displacement is shown in Figure 7.28b and c. It varies for only a few hundredth pixel for each coordinate direction and shows an offset of 0.125 and 1.988 pixel in x and y respectively. The difference in x can be a result of the different location of the sampling point during analog-to-digital conversion. The very small difference in y from 2 pixel of 0.012 pixel allows to assess the stability of the camera stand within the few minutes it took to acquire the first frame, store it to disk, reset the board (only every second time), and acquire the frame with the other synchronization. The two pixel difference is a result of different board settings.

The position of a line in the middle of a frame grabbed at station 1330 was measured in images acquired with both synchronizations. The plots of residuals to a line fit are shown in Figure 7.29, on top for the pixel-synchronous acquired image and on bottom for the one with PLL line-synchronization. The effect of distortion is apparent for both. The instability of the line position is much larger for PLL line-synchronization. The difference in slope of the two curves was used to compute the shear between the two images from top to bottom, resulting in 0.08 pixel. This is not in contradiction to the findings of section 6.3.1, although a value of 0.3 pixel was given there. The shear between the images is a function of the location within the image. This can for example be seen in Figure 7.27, where the difference in the vectors at the points on top and bottom decreases to the right of the image. The shear of 0.3 pixel given in section 6.3.1 refers to a line at the left side of the image whereas the line used here is in the middle of the image. The overall shear of the image should thus be in the order of 0.1 pixel.

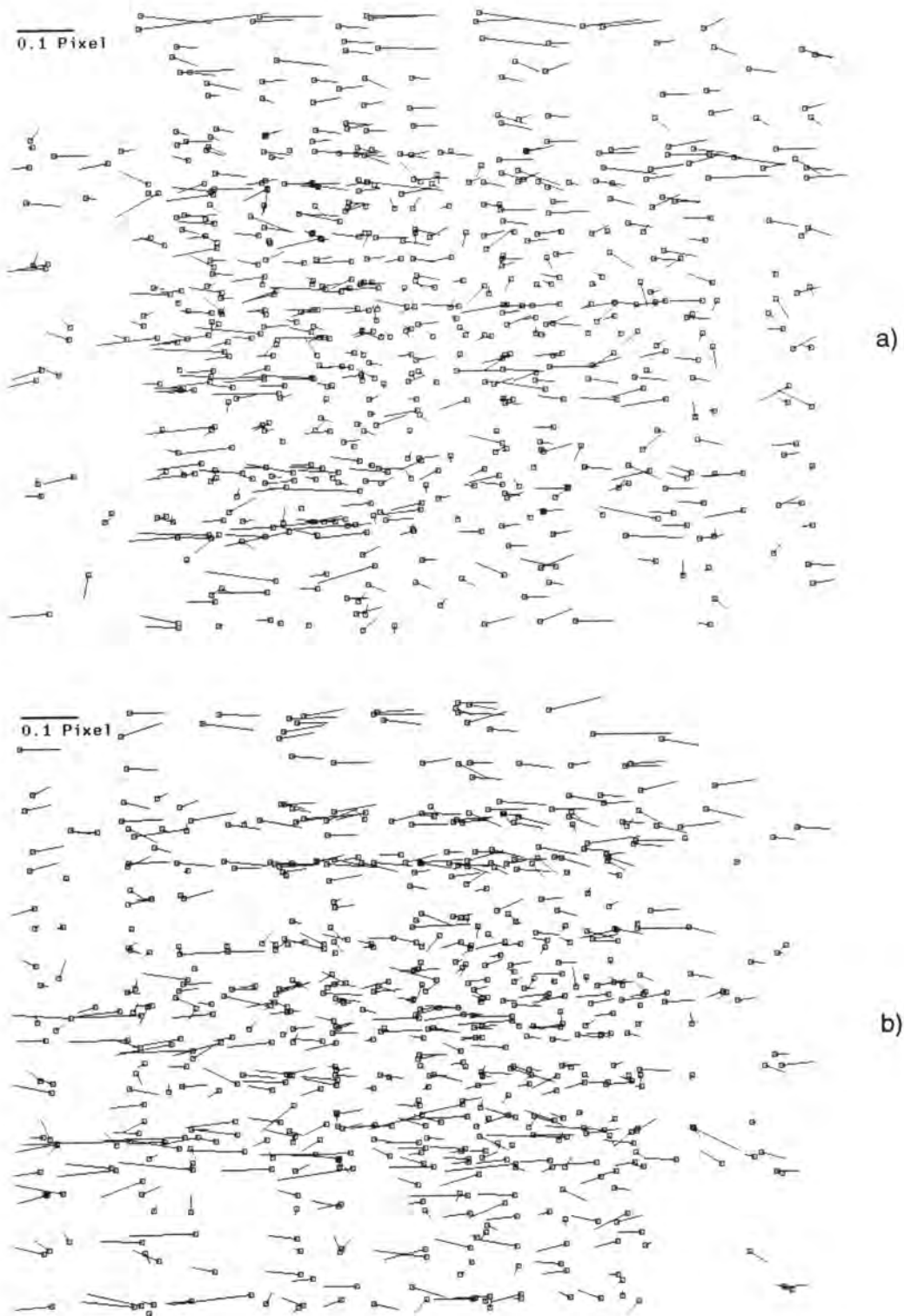
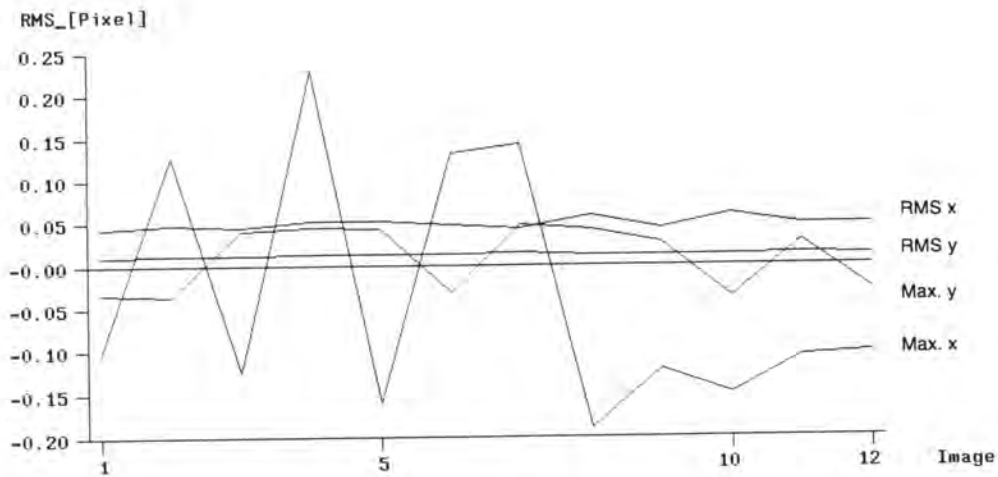
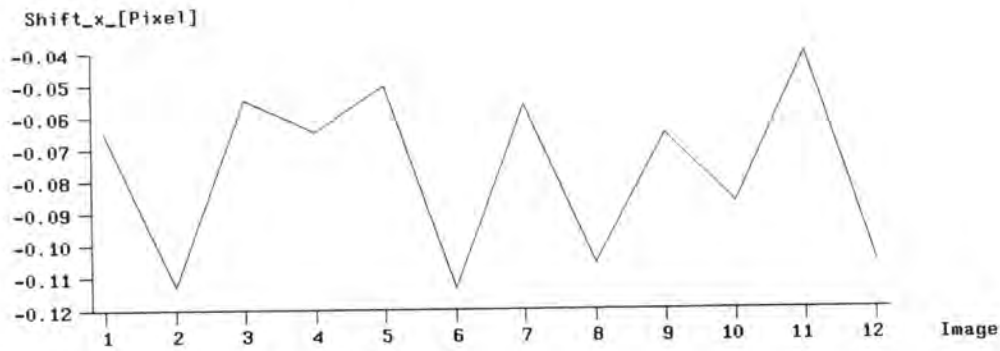


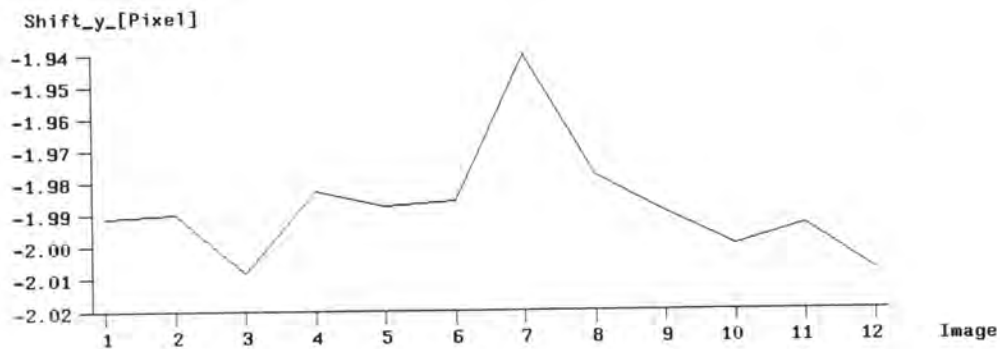
Figure 7.27 Comparison of image coordinates of imagery acquired pixel-synchronously and with PLL line-synchronisation images. They are the plots of stations 15xx (in a) and 25xx (in b). The coordinates were measured with a 5 x 5 template by LSM.



a) RMS and maximum errors of comparison.



b) Average displacement in x.



c) Average displacement in y.

Figure 7.28 Results of comparison of image coordinates between pixel-synchronous and PLL line-synchronisation.

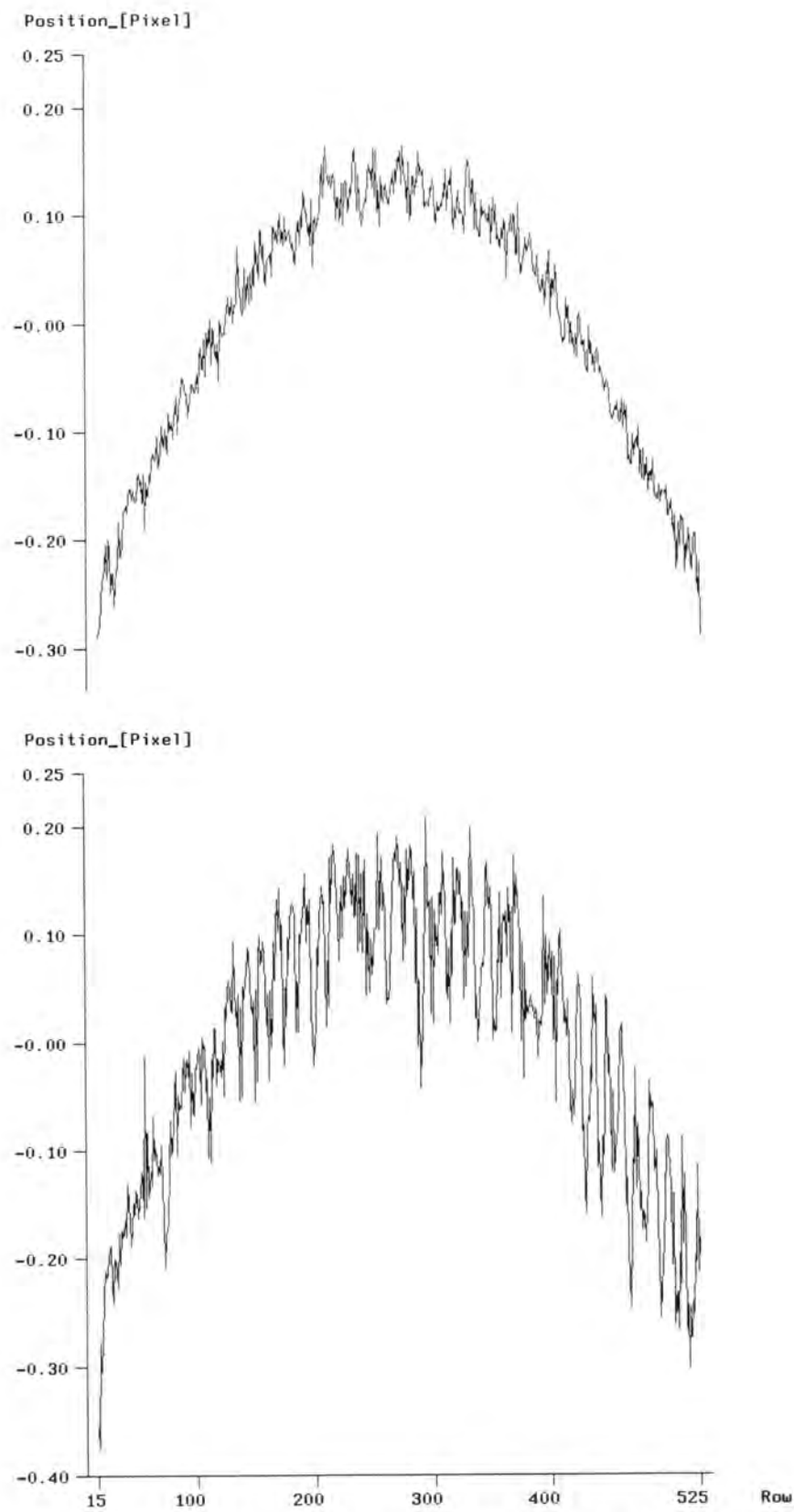


Figure 7.29 Residuals from line fit to plumblines for pixel-synchronous (top) and PLL line-synchronization (bottom).

The squared averages of the standard deviations from LSM for the two data sets are given in Table 7.18. The quite large degradation for both coordinate directions could be attributable to a decrease of the image quality induced by line-jitter. The ratio between the standard deviation in x and y is larger for the imagery acquired with PLL line-synchronization.

	σ_x [μm]	σ_y [μm]	
pixel-synchronous	0.39	0.33	(4797 points)
PLL line-synchronisation	0.49	0.40	(4794 points)
<i>ratio</i>	<i>1.26</i>	<i>1.21</i>	

Table 7.18 Squared mean of standard deviation of image coordinates from LSM for PLL line-synchronization and pixel-synchronous sampling.

Two versions were computed to assess the three-dimensional performance. Both versions use a set of 10 additional parameters, version cv601 uses 30 control points and version cv611 uses a minimum datum. The control, additional parameters, and all other settings of the bundle adjustment were set equal to those of the corresponding versions computed with the pixel-synchronously acquired imagery above (cvp601 and cvp611). The results of latter versions are included in Table 7.19 with those of the PLL line-synchronization for reasons of comparison only.

V	AP	Co	Ch	r	$\hat{\sigma}_0$	σ_X [mm]	σ_Y [mm]	σ_Z [mm]	μ_X [mm]	μ_Y [mm]	μ_Z [mm]	μ_x [μm]	μ_y [μm]
cvp601	10	30	38	8969	0.38	0.026	0.020	0.032	0.052	0.040	0.048	0.13	0.13
cv601	10	30	38	8963	0.46	0.033	0.025	0.039	0.056	0.039	0.061	0.14	0.14
<i>cv601 / cvp601</i>					<i>1.2</i>	<i>1.3</i>	<i>1.3</i>	<i>1.2</i>	<i>1.1</i>	<i>1.0</i>	<i>1.3</i>	<i>1.08</i>	<i>1.08</i>
cvp611	10	m	65	8886	0.37	0.044	0.048	0.056	0.085	0.075	0.064	0.23	0.22
cv611	10	m	65	8880	0.46	0.053	0.054	0.064	0.095	0.069	0.069	0.24	0.24
<i>cv611 / cvp611</i>					<i>1.2</i>	<i>1.2</i>	<i>1.1</i>	<i>1.1</i>	<i>1.1</i>	<i>0.9</i>	<i>1.1</i>	<i>1.04</i>	<i>1.09</i>

Table 7.19 Results for pixel-synchronous (cvp601, cvp611) and PLL line-synchronization (cv601, cv611).

The difference of the theoretical precision estimates must be attributed to differences in the weights of the image coordinates (the network geometry is with the exception of a few rays identical). The empirical precision estimates indicate a small degradation in comparison to the results obtained with the pixel-synchronously acquired imagery. The average coordinate accuracy from the comparison to the check point coordinates are improved by a factor of 1.13 in the 30 control point versions and by 1.05 for the minimum control versions. The differences are not significant though at a 95% confidence level.

The squared mean of residuals for the four versions are given in Table 7.20. The results show an increase by a factor 2.0 for the residuals in x. They are smaller than those in y for pixel-synchronous sampling, but are almost twice as large as those in y for PLL line-synchronization. The latter difference is a result of line-jitter.

	vx [μm]	vy [μm]	
cvp601	0.24	0.27	(4797 points)
cv601	0.48	0.29	(4794 points)
cv601 / cvp601	2.0	1.1	
cvp611	0.23	0.27	
cv611	0.47	0.29	
cv611 / cvp611	2.0	1.1	

Table 7.20 Squared mean of image coordinate residuals.

Table 7.21 gives the adjusted values for the additional parameters and Table 7.22 those for the pixel-to-image coordinate transformation and the camera constant. Interestingly the values for the location of the principal point in y are almost identical although they should differ by 2 pixel or 0.022 mm. It is assumed that the effect is compensated by other parameters. The large difference in the first parameter of decentering distortion could be a result of correlations as well. The effect of such correlations was investigated with film-based cameras by *Fryer and Fraser, 1986*.

The shear as determined through additional parameters is a factor 6 larger for the results of PLL line-synchronization. Its effect for the pixel-synchronously grabbed imagery is 0.15 μm across the horizontal extent of the image. It is 0.8 and 0.6 μm for the horizontal and vertical extent of the image in the case of PLL line-synchronization. This amounts to a deformation similar as the one determined from the position of the plumbline.

Par.	cvp611		cv611		Difference
	Adj.	Stddev.	Adj.	Stddev.	
a	-1.88e-05	1.89e-06	-1.08e-04	2.90e-06	0.00089
K ₁	-2.70e-03	3.83e-06	-2.70e-03	5.93e-06	0.0
K ₂	5.62e-05	3.63e-07	5.71e-05	5.67e-07	0.0000009
K ₃	-4.17e-07	1.01e-08	-4.46e-07	1.60e-08	2.9e-8
P ₁	-6.48e-05	1.67e-06	-7.82e-05	2.58e-06	1.34e-5
P ₂	-7.51e-05	1.38e-06	-7.53e-05	2.10e-06	2.0e-7

Table 7.21 Additional parameters for PLL line-synchronization and pixel-synchronous grabbing.

Parameter	cvp611	cv611	σ_{cvp611}
pixel spacing in x [mm/pixel]	0.0109998	0.0109997	0.0000038
principal point x [mm]	0.0316	0.0328	0.00036
principal point y [mm]	0.1195	0.1188	0.00031
camera constant [mm]	8.9802	8.9803	0.00024

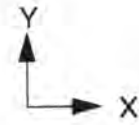
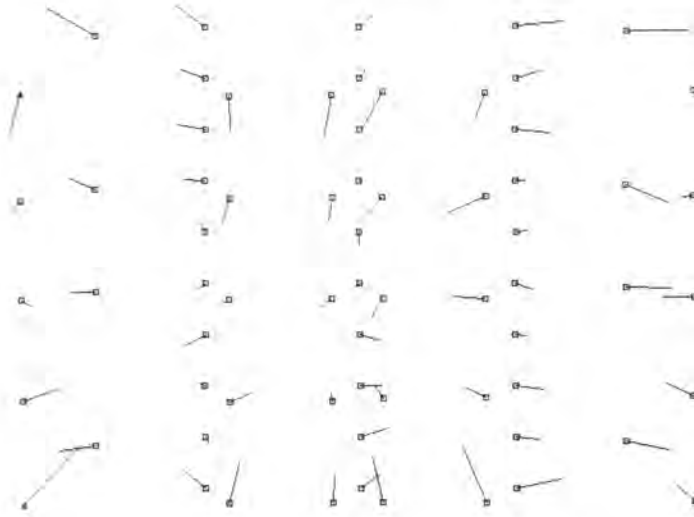
Table 7.22 Initial and adjusted values of pixel spacing and interior orientation elements with the standard deviation from version cvp223.

Scale for Vectors = 0.200 micron (20,000 for APs)

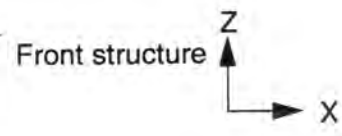


Figure 7.30 Residuals (top) and checkpoint differences for images taken at station 15xx of version cv611.

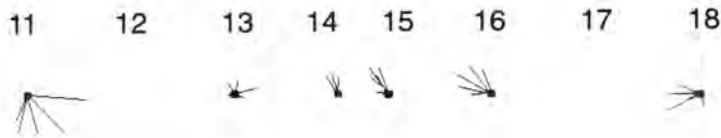
Project: xc910620_cv Version: 611
 Object Space Checkpoint differences
 Scale for Points ——— 500.000 [mm]
 Scale for Vectors — 50.000 [micron]



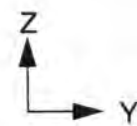
a)



b)



Wall



c)

Figure 7.31 Differences to check points in object space for version cv611.

7.6 Comparison of Results from the Two Synchronization Modes

The results of pixel-synchronous frame grabbing and PLL line-synchronization were compared by using the object space coordinates of former (version cvp611) as reference coordinates for latter (version cv611). The results of the accuracy analysis are given in Table 7.23. The relative accuracy indicated by the RMS values in object space are 1 part in 70 000 and 60 000 in X and Y respectively. The accuracy in image space is 1/100th of the pixel spacing. Figure 7.18 shows the difference vectors in object space of the comparison. Interestingly there are (small) systematic differences at targets of some columns.

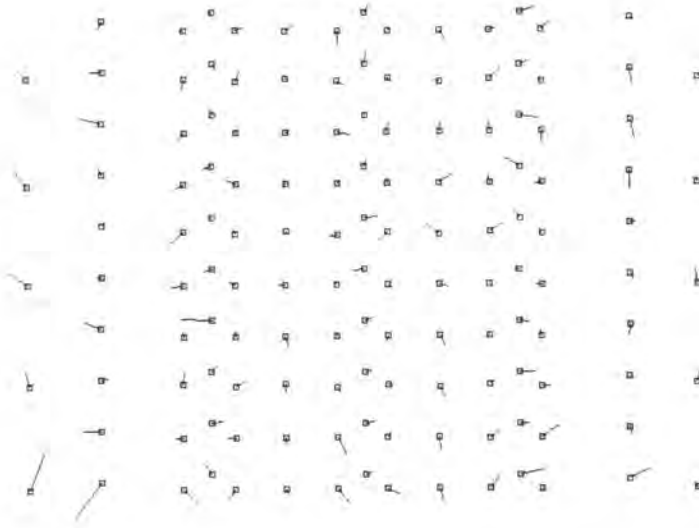
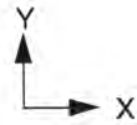
	X [mm]	Y [mm]	Z [mm]	x [μ m]	y [μ m]
Max.	0.127	0.141	0.140		
RMS	0.036	0.033	0.044	0.11	0.10

Table 7.23 Statistics of comparison of object coordinates from cvp611 and cv611 for 140 object points (after a similarity transformation).

The high level of agreement between the results of the two data sets indicates furthermore the level of accuracy which should be attainable once local illumination gradients and effects related to "poor image quality" are eliminated.

This demonstrates that the effects of PLL line-synchronization can be absorbed by high-redundancy and the use of a shear as additional parameter to at least 1/100th of the pixel spacing. This makes it feasible to use considerably less expensive hardware in applications where an extremely high redundancy can be used.

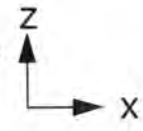
Project: Version: 1
 Object Space Checkpoint differences
 Scale for Points _____ 500.000 [mm]
 Scale for Vectors _ 50.000 [micron]



a)



Front structure



b)



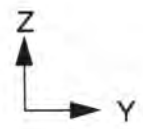
Wall



Front structure

Floor

Ceiling



c)



Wall

Figure 7.32 Differences of object point coordinates of version cvp611 and cv611.

7.7 Conclusions of the Three-Dimensional Performance Analysis

The results of the three-dimensional performance analysis demonstrate on one hand the excellent performance of the system and on the other a number of limiting factors which need to be addressed in the future.

The relative accuracy in object space (mean RMS coordinate error divided by the largest object dimension) attained with the minimum control configuration and pixel-synchronous frame grabbing corresponds to 1 part in 46000. An accuracy of $1/50^{\text{th}}$ of the pixel spacing was attained with the same configuration in image space. The value is in good agreement with the quadratic mean of image coordinate residuals, which are 0.23 and $0.27 \mu\text{m}$ or $1/48^{\text{th}}$ and $1/41^{\text{st}}$ of the pixel spacing in x and y respectively. These results are in agreement with those of other investigations (e.g. Bösemann *et al.*, 1990; Gustafson, 1991; Shortis *et al.*, 1991; El-Hakim and Barakat, 1989). A direct comparison with the tests performed by these researchers is very difficult though. The type and size of targets, the "depth" dimension of the object/testfield, the number of frames, and other parameters are too different in all cases.

Major deficiencies found in this test are the effects of local illumination gradients and of "poor image quality". Both can be reduced with retroreflective targets. Local variations of the illumination intensity would be vastly reduced as the illumination for the targets is close to the lens and the global fall-off is of much smaller magnitude across the extent of the area of the retroreflective target. The influence of the background would also be reduced due to the tremendous reflectivity of these targets. In case of a testfield, the background can be black, which effectively reduces non-uniformities of the illumination even further. Tests have furthermore shown that retroreflective targets of identical size as targets appear, due to scattering, significantly larger in the imagery. This in turn increases the measurement precision. Retro-reflective targets exclude influences of variations in the reflectivity of ceiling, floor, and walls as the light coming from those directions is not returned to the camera. Using a camera with a larger number of sensor elements can be used to decrease the influence of local illumination gradients and of "poor image quality".

The accuracy of the reference coordinates was a major limit for accuracy verification. More accurate reference coordinates can be obtained by using large format film cameras with high precision digital comparators (Gustafson, 1991 and Shortis *et al.*, 1991) and coordinate measurement machines (El-Hakim and Barakat, 1989). Theodolites with CCD-cameras could also be used if they are capable of measuring the identical targets.

8 CONCLUSIONS

A modular RTPS with a significantly higher degree in flexibility and accuracy than existing systems was developed. The flexibility of the system was demonstrated in a number of applications under laboratory or experimental conditions (*Gruen and Baltsavias, 1988; Gruen and Stallmann, 1991; Novak et al., 1990; Baltsavias and Stallmann, 1991*) as well as in a pilot study under industrial conditions (*Beyer, 1991abd*). The high accuracy demonstrated with an off-the-shelf camera of standard "resolution" and under difficult conditions with respect to the volume contained, the size of the targets, and the lighting is superior to that of any other system to date. The hardware architecture chosen in 1986 is still unmatched in terms of flexibility of solid-state cameras which can be connected to it. The modular architecture of the system has also been chosen by industrial developers of photogrammetric inspection systems (*Luhmann, 1991*). The system proved furthermore to be ideally suited for an extensive analysis of the radiometric and geometric characteristics of the many elements involved in image acquisition with solid-state sensors. Both the development of the very flexible and powerful software package DEDIP and a number of new findings should help to advance Real-Time Photogrammetry.

The analysis of the optical and electronic elements of the camera allowed to locate several potential degrading factors. The specifications of the characteristics of the optical elements (IR-filter, diffusor, sensor) must be required from manufacturers. A stable connection of sensor, optical elements, and lens is another problem to be addressed. Several electronic elements leading to degradations were found. Effects of DC-restoration, temporal noise, sources of systematic noise, linearity, impulse response, modulation transfer function, and synchronization were analyzed. The investigation showed on one hand that there are numerous problems which can degrade the radiometric image quality and on the other the excellent performance of the system. The analysis of synchronization led to the detection of a large shear due to the use of the composite video signal and PLL line-synchronization. The high performance of pixel-synchronous frame grabbing and LSM was demonstrated through the positional analysis of a vertical line. The internal precision was, with 0.005 of the pixel spacing, significantly better than the precision aimed at.

A small indication of the numerous problems was given by the analysis of camera and frame grabber. It was shown that after extensive efforts to optimize the radiometric properties, an excellent uniformity of the gain was attained. This uniformity requires a regularity of the sensor element spacing better than 1%. The importance of the investigations performed was to provide simple techniques for pinpointing problems which have significant effects on the three-dimensional accuracy of the system.

The influence of several factors on the internal precision, called repeatability, were investigated. The problem of oscillations in LSM for the measurement of circular targets was addressed. Methods for the investigation of synchronization were developed. The effects of various synchronization techniques on the radiometric and geometric quality of the transmission of imagery from camera to frame grabber showed several new effects. It was proven that the geometric performance of pixel-synchronous frame grabbing is identical to digital transmission and thus - within the limits of the precision attainable with the current techniques - without loss. The shear due to composite video and PLL line-synchronization, already detected during the analysis of the frame grabber, could be verified. The degradations induced by line-jitter can be interpreted both as a geometric or a radiometric instability. Warm-up-effects and repeatability over short and long periods, are basic investigations to assess the limitations of a system and to locate potential prob-

lems. The excellent repeatability of the system demonstrated over several days were an indication of the high quality of the image acquisition system, only attained after the many refinements. The empirical investigation of the relation of target size and repeatability provide effective means to determine an optimum target size. The effects of shadows and illumination intensity variations were significantly underestimated heretofore. The importance of illumination and targets on the accuracy has been shown to be of major importance. Local illumination gradients, stability in time (for very short illumination times) and the spectral characteristics, which affect the PRNU, are some of the factors to be considered.

The performance of the system and the influence of a number of factors on the accuracy of positioning reveal the capabilities of the system. The speed and robustness of target location with an appropriate use of a priori information were demonstrated. The influence of synchronization, and the relation of template size and effects of shadows were analyzed. The results showed that accuracies comparable and exceeding those of semi-metric medium format film cameras can be attained with inexpensive off-the-shelf CCD-cameras. Accuracies exceeding the 50th of the pixel spacing should be attainable when the major limitations addressed are eliminated.

A wealth of problems remain to be solved. The excellent results obtained with PLL line-synchronization require the verification of the accuracy potential of image acquisition systems which exhibit comparatively worse characteristics. Of particular interest are video cameras, which include - for prices comparable to CCTV-cameras - a video recorder. They are particularly easy to handle and the incorporated video recorder can be used as intermediate storage. As these systems do typically include color-sensors, the effects thereof, the influence of color encoding schemes, and the degradations due to the analog recording on the video tapes are to be analyzed. Similarly the effects of various data reduction schemes such as JPEG should be investigated. On the other end the performance of cooled cameras, cameras providing for more than eight bit per pixel, and the use of large area sensors are avenues to attain even higher accuracies. Better algorithms for target location, e.g. methods to detect occlusions, illumination variations, and to assess the quality of the target image, and calibration need to be developed. New approaches for calibration should aim at a higher-degree of robustness, automation and/or accuracy as well as efficient techniques for the verification of accuracy. The techniques and experiences shown in this work form a sound basis for further investigations.

9 REFERENCES

Abbreviations:

ASPRS	American Society of Photogrammetry and Remote Sensing
AVN	Allgemeine Vermessungsnachrichten
BuL	Bildmessung und Luftbildwesen
BMFT.....	Bundesministerium für Forschung und Technologie
DGK.....	Deutsche Geodätische Kommission
IAPRS	International Archives for Photogrammetry and Remote Sensing
IEDM	International Electron Devices Meeting, Technical Digest
IJCPR	International Joint Conference on Pattern Recognition
ISPRS.....	International Society for Photogrammetry and Remote Sensing
ISSCC	IEEE International Solid-State Circuits Conference, Digest of Technical Papers
JIT	Journal of Imaging Technology
MITI.....	Ministry of Trade and Industry (Japan)
OE	Optical Engineering
SPIE	Society of Optical Engineering
PAMI.....	IEEE Transactions on Pattern Analysis and Machine Intelligence
PE.....	Photogrammetric Engineering
PE&RS.....	Photogrammetric Engineering and Remote Sensing

- Abi-Ayad, Arslane, 1989. Calibrages Statique et Dynamique de Cameras. Dissertation, Institut National Polytechnique de Toulouse, France.
- Akazawa, Y., Iwata, A., Wakimoto, T., Kmato, T., Nakamura, H., Ikawa, H., 1987. A 400MSPS 8b Flash AD Conversion LSI.. 1987 IEEE International Solid-State Circuits Conference (ISSCC 87), pp. 98-99.
- Allan, R., 1984. Largest CCD imager carries 1024 by 1024 pixels. *Electronic Design*, January 12, 1984, pp. 41-42.
- Amorese, P., 1988. Test Point Probing Through MaxScan. Application Note, Datacube Inc., 5/1988, 12 pages.
- B+K Elektronik, 1990. WIPIX data sheet. B & K Elektronik GmbH, Kolberger Strasse 3, 8440 Straubing.
- Babey, S.K., Anger, C.D., Green, B.D., 1985. Digital charge coupled device (CCD) camera system architecture. *SPIE*, Vol. 579, Solid State Imaging Arrays, pp. 39-45.
- Baltsavias, E.P., 1991. Multiphoto Geometrically Constrained Matching. Dissertation, ETH-Zurich.
- Baltsavias, E.P., Beyer, H.A., Fritsch, D., Lenz, R.K., 1990. Fundamentals of Real-Time Photogrammetry. Tutorial notes ISPRS Commission V Symposium, Zurich, Switzerland, September 3 1990.
- Baltsavias, E.P., Stallmann, D., 1991. Trinocular Vision for Automatic and Robust Three-Dimensional Determination of the Trajectories of Moving Objects. *Photogrammetric Engineering and Remote Sensing*, Vol. 57, No. 8, August 1991, pp. 1079-1086.
- Bani-Hashemi, A., 1991. Finding the Aspect-Ratio of an Imaging System. Proceedings 1991 IEEE Computer Society Conference on Computer Vision and Pattern Recognition. pp. 122-126.
- Beyer, H.A., 1987a. Some Aspects of the Geometric Calibration of CCD-Cameras. Proceedings of the Intercommission Conference on Fast Processing of Photogrammetric Data, Interlaken, Switzerland, pp. 68 - 81.
- Beyer, H.A., 1987b. Einige grundlegende Designfragen für die Entwicklungsumgebung für Digitale Photogrammetrie auf den Sun Workstations. (DEDIP Development Environment for Digital Photogrammetry). Internal Report.

- Beyer, H.A., 1988. Line-jitter and Geometric Calibration of CCD-Cameras. *International Archives of Photogrammetry and Remote Sensing*, Vol. 27, Part B10, pp. 315-324. and in: *ISPRS Journal of Photogrammetry and Remote Sensing*, 45, 1990, pp. 17-32.
- Beyer, H.A., Faessler, H.P., and Wen J., 1989. Real-Time Photogrammetry in High-Speed Robotics. In: *Optical 3-D Measurement Techniques*, Gruen and Kahmen (Editors), Herbert Wichmann Verlag, Karlsruhe, pp. 271 - 280.
- Beyer, H.A., 1991a. Automated Dimensional Inspection of Cars in Crash Tests with Digital Photogrammetry. *SPIE Vol. 1526*, pp. 134-141.
- Beyer, H.A., 1991b. Optoelektronische Vermessung von Crashfahrzeugen - Erste Resultate eines Pilotversuches -. *Mustererkennung 1991*, Springer Verlag, Informatik Fachberichte 290, pp. 328-336.
- Beyer, H.A., 1991c. Untersuchungen zur geometrischen Qualität der Datenübertragung bei der Bildaufnahme mit CCD-Kameras. 13. *Mustererkennung 1991*, Springer Verlag, Informatik Fachberichte 290, pp. 386-394.
- Beyer, H.A., 1991d. Photogrammetric On-Line Inspection for Car Crash Analysis - Results of a Pilot Project, *First Australian Photogrammetric Conference*, 7 - 9 November 1991, Sydney, Australia.
- Beyer, H.A., 1991e. Evaluating the Geometric Performance of Signal Transmission, *First Australian Photogrammetric Conference*, 7 - 9 November 1991, Sydney, Australia.
- Beyer, H.A., 1991f. Fundamentals of Digital Imaging Hardware, Tutorial Notes for a Tutorial given at the School of Surveying, University of New South Wales, 80 pages.
- Beyer, H.A., 1992. An Introduction to Solid-State Sensors. In preparation.
- Blouke, M.M., Janesick, J.R., Elliott, T., Hall, J.E., Cowens, M.W., May, P.J., 1987. Current Status of the 800 x 800 Charge-Coupled-Device Image Sensor. *OE*, September 1987, Vol. 26 No. 9, pp. 864-874.
- Bösemann, W., Godding, R., Riechmann, W., 1990. Photogrammetric Investigation of CCD Cameras. *SPIE Vol. 1395*, pp. 119-126.
- Boyle, W.S., Smith, G.E., 1970. Charge Coupled Semiconductor Devices. *The Bell System Technical Journal*, April 1970, pp. 587-593.
- Brown, D.C., 1976. The Bundle Adjustment - Progress and Prospects. *International Archives of Photogrammetry*, Vol. XXI, Part 3, Invited Paper, Commission III, ISP Kongress Helsinki.
- Brown, D.C., 1971. Close-Range Camera Calibration. *Photogrammetric Engineering*, 37 (8), pp. 855-866.
- Büchli, R., Heeb, E., Knop, K., 1985. Low cost smart camera. *SPIE*, Vol. 595, *Computer Vision for Robots*, pp. 278-283.
- Burner, A.W., Snow, W.L., and Goad, W.K., 1985. Close Range Photogrammetry With Video Cameras. *Technical Papers - 51st Annual Meeting ASP*, Vol. 1, ASPRS, 62-77.
- Burner, A.W., Snow, W.L., Shortis, M.R., Goad, W.K., 1990. Laboratory Calibration and Characterization of Video Cameras. *SPIE Vol. 1395*, pp. 664-671.
- Burr-Brown, 1989. ADS807, ADS808, 12-Bit Resolution Sampling A/D Converter with Microprocessor Interface. Burr-Brown Corporation Buschner, R., Viehmann, D., 1988. Application of the Thomson-CSF TH 7884 CCD Matrix Sensor for the Imaging Spectrometer ROSIS. *SPIE*, Vol. 1027, *Image Processing II*, pp. 52-58.
- Curry, S. Baumrind, S., Anderson, J.M., 1986. Calibration of an Array Camera. *PE&RS*, Vol. 52, No. 5, pp. 627-636.
- Dähler, J., 1986. Charge Coupled Devices (CCD) (in German). Institut of Geodesy and Photogrammetry, Report No. 107. March 1986.
- Dähler, J., 1987. Problems in Digital Image Acquisition with CCD-Cameras. in: *Proceedings of the ISPRS Intercommission Conference*, Interlaken, pp.48-59.
- Datacube, 1988. MAX-SCAN User Manual. Datacube, Inc., Peabody, MA. 01960.

- Dunbar, P., 1986. Machine Vision. An examination of what's new in vision hardware, BYTE, January 1986, pp. 161-173.
- El-Hakim, S.F., 1986. A real-Time System for Object Measurement with CCD cameras. IAPRS, Vol. 26, Part 5, pp. 363-373.
- El-Hakim, S.F., and Barakat, M. A., 1989. A Vision-Based Coordinate Measuring Machine (VCMM). In: Optical 3-D Measurement Techniques, Gruen and Kahmen (Editors), Herbert Wichmann Verlag, Karlsruhe, pp. 216 - 228.
- Faugeras, O.D., Toscani, G., 1987. Camera Calibration for 3D Computer Vision. Proceedings International Workshop on Machine Vision and Machine Intelligence, Tokyo, Japan, February 2-5, 1987.
- Förstner, W., 1982. On the Geometric Precision of Digital Correlation. International Archives of Photogrammetry and Remote Sensing, Volume 24 - III, Proceedings of the Symposium: Mathematical Models, Accuracy Aspects and Quality Control, June 7-11, 1982, Helsinki University of Technology, Otaniemi, Finland, pp. 176-189.
- Fraser, C.S., 1992. Photogrammetric Measurement to one part in a Million. Photogrammetric Engineering and Remote Sensing, Vol. 58, No. 3, March 1992, pp. 305-310.
- Frey, P.W., 1990. Charakterisierung eines CCD-Bildsensors. Diplomarbeit ETH-Zürich.
- Fryer, J.G., Fraser, C.S., 1986. On the Calibration of Underwater Cameras. Photogrammetric Record, 12(67): 73-85 (April 1986), pp. 73-85.
- Grift, van de R.E.J., Venn, van de M., 1987. An 8b 50 MHz Video ADC with Folding and Interpolation Techniques. 1987 IEEE International Solid-State Circuits Conference (ISSCC 87), pp. 94-95.
- Gruen, A.W., 1978. Accuracy, Reliability and Statistics in Close-Range Photogrammetry. Presented paper, Inter-Congress Symposium, ISPRS Commission V, Stockholm, August 1978.
- Gruen, A., 1985. Adaptive Least Squares Correlation - A Powerful Image Matching Technique. South African Journal of Photogrammetry, Remote Sensing and Cartography, 14 (3), pp. 175-187.
- Gruen, A., 1986. The Digital Photogrammetric Station at the ETH Zurich. Paper presented at the ISPRS Commission II Symposium, Baltimore, Maryland, May 26-30.
- Grün, A.W., 1988. Towards Real-Time Photogrammetry. Photogrammetria, 42 (1988), pp. 209-244.
- Grün, A.W., Baltsavias, E.P., 1987. Geometrically Constrained Multiphoto Matching. Proceedings of the Intercommission Conference on Fast Processing of Photogrammetric Data, Interlaken, Switzerland, pp. 204-230.
- Gruen, A., Baltsavias, E., 1988. Automatic 3-D measurement of human faces with CCD-cameras. SPIE Vol. 1030, pp. 106-116.
- Gruen, A.W., Beyer, H.A., 1986. Real-Time Photogrammetry at the Digital Photogrammetric Station (DIPS) of ETH Zurich. Paper presented at the ISPRS Commission V Symposium, "Real-Time Photogrammetry - A New Challenge", June 16-19, 1986, Ottawa, and in: The Canadian Surveyor, Vol. 41., No. 2, Summer 1987, pp. 181-199.
- Grün, A., Beyer, H., 1990. DIPS II - Turning a Standard Computer Workstation into a Digital Photogrammetric Station. International Archives of Photogrammetry and Remote Sensing, Vol. 28, Part. 2, pp. 247-255. and: ZPF - Zeitschrift für Photogrammetrie und Fernerkundung, 1/1991, pp. 2-10.
- Grün, A., Beyer, H., Dähler, J., 1987. Photogrammetrische Punktbestimmung im Real-Time Modus. Schlussbericht ETHZ-Forschungsprojekt. Bericht Nr. 144 des Instituts für Geodäsie und Photogrammetrie, ETH-Zürich.
- Grün, A., Stallmann, D., 1991. High accuracy edge matching with an extension of the MPGC-matching algorithm. SPIE Vol. 1526, pp. 42-55.
- Gülch, E., 1984. Geometric Calibration fo two CCD-Cameras used for Ditial Image Correlation on the Planicomp C100. IAPRS, Vol. XXV, Part A3a, pp. 159-168.

- Gülch, E., 1985. Instrumental Realisation and Calibration of Digital Correlation with the Planicomp Proceedings of the 40th Photogrammetric Week at Stuttgart University, 30.9 - 5.10.85 Institut für Photogrammetrie der Universität Stuttgart.
- Gustafson, P.C., 1991. An Accuracy/Repeatability Test for a Video Photogrammetric Measurement. SPIE Vol. 1526, Industrial Vision Metrology, pp. 36 - 41.
- Haggrén, H., 1984. New vistas for Industrial Photogrammetry. IAPRS, Vol. 25, Part A5, commission V, ISPRS Congress Rio de Janeiro, pp. 382-391.
- Haggrén, H., 1986. Real-time Photogrammetry as used for Machine Vision Applications. Proceedings Symposium "Real-Time Photogrammetry - A New Challenge", June 16-19, 1986, Ottawa, Canada, IAPRS, Vol. 26, Part 5, pp. 374-382.
- Haggrén, H., 1991. Real-Time Photogrammetry and Robot Vision. 43. Photogrammetrisch Woche, Universität Stuttgart, 9 - 14 September 1991, pp. 245 - 251.
- Haggrén, H., Heikkilä, J., 1989. A Simulation Study of Close-Range Photogrammetric Measuring of the Windshield Frames in Automobile Manufacturing. To be published.
- Hantke, D., Philipp, H. Sparrer, G. Tschirnich, J., 1985, CCD-Zeilen sind Präzisionsmasstäbe. Feingerätetechnik, 1985, pp. 290-292.
- HCS, 1990. Technical Description MX5 CCD Camera. HCS Vision Technology B.V., Eindhoven, The Netherlands.
- Heikkilä, J., 1988. Some Tests on the Stability of the Digitization of analog Video Signal. Photogrammetric Journal of Finland, Vol. 11, No. 1, 1988, pp. 12-19.
- Heinrich, M.L., Feaster, B.B., Wu, Z.L., Mitra, S., Krile, T.F., 1986. A Versatile Video Image Digitizer for PC-Based Image Processing Systems. SPIE Vol. 697, Applications of Digital Image Processing IX, pp. 86-91.
- Hopkins, R., 1988. Advanced Television Systems. IEEE Transactions on Consumer Electronics, Vol. 34, No. 1, February 1988, pp. 1-15.
- Horowitz, P., Hill, W., 1982. The Art of Electronics. Cambridge University Press, Cambridge London, New York, New Rochelle, Melbourne, Sydney.
- Jurgen, R.K., 1988. High-definition television update. IEEE Spectrum, April 1988, pp. 56-62.
- Kamgar-Parsi, B., Eastman, R.D., 1991. Calibration of a Stereo System with Small Relative Angles. Proceedings 1991 IEEE Computer Society Conference on Computer Vision and Pattern Recognition. pp. 44-51.
- Kratky, V., 1979. Real-Time Photogrammetric Support of Dynamic Three-Dimensional Control. PE&RS, 45, pp. 1231-1242.
- Kunt, M., 1988. La Télévision: Passé, Présent, Avenir. Polyrama, Ecole Polytechnique Federale Lausanne, June 1988, pp. 31-36.
- Lake, D. 1990b. Solid State Cameras: The Next Five Years. Advanced Imaging, August 1990, pp. 30-36.
- Lenz, R., 1987. Lens Distortion Corrected CCD-Camera Calibration with Co-Planar Calibration Points for Real-Time 3D Measurements. Proceedings of the Intercommission Conference on Fast Processing of Photogrammetric Data, Interlaken, Switzerland, 60-67.
- Lenz, R. 1988. Videometrie mit CCD-Sensoren und ihre Anwendung in der Robotik. Habilitationsschrift, Technische Universität München, München.
- Lenz, R., 1990. Messung der Übertragungseigenschaften einer hochauflösenden Farbkamera mit CCD-Flächensensor. Mustererkennung 1990, 12. DAGM-Symposium, Springer Verlag, pp. 29-35.
- Lenz, R.K., Fritsch, D., 1988. On the Accuracy of Videometry. International Archives of Photogrammetry and Remote Sensing, Vol. 27, Part B5, Commission V, pp. 335-345.

- Lenz, R.K., Tsai, R., 1988. Techniques for Calibration of the Scale Factor and Image Center for High Accuracy 3D Machine Vision Metrology. 1987 IEEE International Conference on Robotics and Automation. pp. 57-61.
- Lü, Y., 1988a. Interest Operator and Fast Implementation. Institut für Geodäsie und Photogrammetrie, Bericht No. 145.
- Lü, Y., 1988b. A simple algorithm for edge detection. Institut für Geodäsie und Photogrammetrie, Bericht No. 145.
- Lü, Y., Zhang, Z., 1988. Fast Implementation for Generating Epipolar Line Images with one-dimensional resampling. Institut für Geodäsie und Photogrammetrie, Bericht No. 145.
- Luhmann, T., 1988. Ein hochauflösendes automatisches Bildmeßsystem. Wissenschaftliche Arbeiten der Fachrichtung Vermessungswesen der Universität Hannover, Nr. 154, Hannover.
- Luhmann, T., 1991. An integrated system for real-time and on-line applications in industrial photogrammetry. SPIE Vol. 1395, pp. 488-495.
- Luhmann, T., Wester-Ebbinghaus, W., 1987. On Geometric Calibration of Digitized Video Images of CCD Arrays. Proceedings of the ISPRS Intercommission Conference, Interlaken, pp. 35-47.
- MacLean, S.G., Rioux, M., Blais, F., Grodski, J., Milgram, P., Pinkney, H.F.L., Aikenhead, B.A., 1990. Vision System Development in a Space Simulation Laboratory. SPIE Vol. 1395, pp. 8-15.
- Murai, S., Otomo, F. and Otani, H., 1986. Automated three-dimensional Measurements using stereo CCD camera in the Application to Close-Range Photogrammetry. IAPRS, Vol. 26, Part 5, pp. 409-413.
- Ninomiya, Y., Ohtsuka, Y., Izumi, Y., Gohshi, S., Iwadate, Y., 1988. IEEE Transactions on Broadcasting, Vol. BC-33, No. 4, December 1987, pp. 130-160.
- Novak, K., Baltasvias, E., Grün, A., 1990. Automatische Objektverfolgung in Stereovisionssystemen. Institut für Geodäsie und Photogrammetrie, Bericht No. 170, pp. 1-43.
- Pinkney, H.F.L., 1978. Theory and Development of an On-Line 30 Hz Video Photogrammetric System for Real-Time 3-Dimensional Control. Proceedings of ISP Symposium on Photogrammetry for Industry, August, 1978, Stockholm.
- Pol, V., Bennewitz, J.H., Jewell, T.E., Peters, D.W., 1987. Excimer lase based lithography, a deep-ultraviolet wafer stepper for VLSI processing. OE, Vol. 26, No. 4, April 1987, pp. 311-318.
- Pool, P.J., Suske, W.A.F., Ashton, J.E.U., Bowring, S.R., 1990. Design Aspects and Characterisation of EEF Large Area CCDs for Scientific and Medical Applications. SPIE Vol. 1242, Charge-Coupled Devices and Solid State Optical Sensors (1990), pp. 17-25.
- Putskorius, G.V., Feldkamp, L.A., 1988. Camera Calibration Methodology based on a Linear Perspective Transformation Error Model. ICRA 1988, pp. 1858-1860.
- Raynor, J., 1989. Private Communication.
- Raynor, J., Seitz, P., 1990. The Technology and Practical Problems of Pixel_Synchronous CCD Data Acquisition for Optical Metrology Applications. SPIE, Vol. 1395, pp. 96-103.
- Raynor, J., Seitz, P., Wanner, D., 1990. A Universal Pixel-Synchronous Data Acquisition System for High-Resolution CCD Image Sensors. SPIE, Vol. 1265.
- Rosenberg, P., 1955. Information Theory and Electronic Photogrammetry. Photogrammetric Engineering, 21 (1), pp. 543-555.
- Sangster, F.L.J., 1970. The Bucked Brigade Delay Line, A Shift Register for Analogue Signals, Philips Technical Review 31, pp. 97-110.
- Selcom, 1982. Selective Electronic CoAB, Box 250, S-433, Partille 1, Sweden.

- Shortis, M.R., Burner A.W., Snow, W.L., Goad, W.K., 1991. Calibration Tests of Industrial and Scientific CCD Cameras. First Australian Photogrammetric Conference, 7 - 9 November 1991, Sydney, Australia.
- Siegel, S., 1988. High Performance Multistandard Digitization and Display of Color Television Signals. *Datacube World Review*, pp. 4-7.
- Simmons, D., 1987. Digitizing Standard and High Resolution High Frame Rate Video Camera Signals. *SPIE*, Vol. 849, Automated Inspection and High Speed Vision Architectures, pp. 158-167.
- Stanton, R.H., Alexander, J.W., Dennison, E.W., Glavich, T.A., Hovland, L.F., 1987. Optical tracking using charge-coupled devices. *OE*, Vol. 26, No. 9, September 1987, pp. 930-938.
- Trinder, J.C., 1988. Experiments on Target Location and Image Matching. *International Archives of Photogrammetry and Remote Sensing*, Vol. 27, Part B5, pp. 764-792.
- TRW, 1984. TDC1048 Product Description.
- Tsai, R.Y., 1987. A Versatile Camera Calibration Technique for High-Accuracy 3D Machine Vision Metrology Using Off-the-Shelf TV Cameras and Lenses. *IEEE Journal of Robotics and Automation*, Vol. RA-3, No. 4, August 1987, pp. 323-344.
- Videk, 1987. Several manuals for the Megaplus camera. Videk, USA.
- Wang, L-L., Tsai, W-H., 1991. Camera Calibration by Vanishing Lines for 3-D Computer Vision. *IEEE Transactions on Pattern Analysis and Machine Intelligence*, Vol. 13, No. 4, April 1991, pp. 370-376.
- Wei, G-Q., Ma, S.D., 1991. Two Plane Camera Calibration: A Unified Model. *Proceedings 1991 IEEE Computer Society Conference on Computer Vision and Pattern Recognition*. pp. 44-51.
- Wieting, A., 1990. Untersuchung von CCD-Kameras für die Anwendung in der Industriephotoogrammetrie. Diplomarbeit am Institut für Photogrammetrie und Ingenieurvermessungen, Universität Hannover.
- Wiley, A.G., Wong, K.W., 1990. Metric aspects of zoom vision. *SPIE Vol. 1395*, pp. 112-118.
- Wilkins, D., 1990. Digital Photogrammetric Applications with the Prime-Wild S9 Analytical Plotter. *IAPRS*, Vol. 28, Part 2, pp. 35-42.
- Woltring, J., 1975. Calibration and Measurement in 3D-Monitoring of Human Motion by Optoelectronic Means. I. Preliminaries and Theoretical Aspects. *Biotelemetry*, 2, pp. 169-196.
- Wong, K.W. 1969. Geometric Distortions in Television Imageries. *PE Vol. 35*, No. 5, pp. 493-500.
- Wong, K.W., Ho, W-H., 1986. Close - Range Mapping with a Solid State Camera. *Photogrammetric Engineering and Remote Sensing*, Vol. 52, no. 1, January 1986, pp. 67-74.
- Yoshii, Y., Nakamura, M., Hirasawa, K., Kayanuma, A., Asanao, K., 1987. An 8b 350 MHz Flash ADC. 1987 *IEEE International Solid-State Circuits Conference (ISSCC 87)*, pp. 96-97.

10 ABBREVIATIONS AND GLOSSARY

10.1 Abbreviations

AGC.....	automatic gain control
APL.....	average picture level
CCIR.....	Comité Consultatif International des Radiocommunications
CDS	correlated double sensing
CMM	coordinate measuring machine
CSYNC.....	composite synchronization signal
DIPS.....	Digital Photogrammetric Station
DN	digital number
EIA.....	Electronics Industries Association
ENG	electronic news gathering
FCC.....	Federal Communications Commission
FIFO.....	first in first out
FPN.....	fixed pattern noise
FT.....	frame transfer sensor
HSYNC.....	horizontal synchronization signal
HR480.....	Aqua TV HR480 camera
IT	interline transfer sensor
LPF	low-pass filter
MAX-SCAN.....	frame grabber from Datacube
MTF	modulation transfer function
NTSC.....	National Television Systems Committee
ROI-STORE	frame store from Datacube
RTPS.....	Real-Time Photogrammetric System
sel.....	sensor element
TVHD	télévision à haute définition (HDTV)
VSYNC.....	vertical synchronization signal
XC77.....	SONY-XC77CE camera

10.2 Synchronization Modes for SONY-XC77CE Camera

xc77_ccir	configuration of MAX-SCAN frame grabber for acquisition of imagery from a camera with PLL line-synchronization with a sampling rate of approximately 10.4 MHz
xc77_cv.....	configuration of MAX-SCAN frame grabber for acquisition of imagery from a camera with PLL line-synchronization with a sampling rate of approximately 14.1875 MHz which is as close as possible to the sensor clock frequency of a SONY XC77CE camera
xc77_cvp.....	configuration of MAX-SCAN frame grabber for pixel-synchronous frame grabbing from a SONY XC77CE camera

10.3 Abbreviations used in Tables of Chapter 7

V Version
 AP Number of additional parameters
 Co..... Number of control points (m denotes minimum control)
 Ch..... Number of check points
 r..... Redundancy
 $\hat{\sigma}_0$ Variance of unit weight *a posteriori*
 $\hat{\sigma}_X, \hat{\sigma}_Y, \hat{\sigma}_Z$ Theoretical precision of check point coordinates
 μ_X, μ_Y, μ_Z Root Mean Square Error from comparison to check point coordinates in object space
 μ_x, μ_y Root Mean Square Error from comparison to check point coordinates in image space

10.4 Bundle Versions of Chapter 7

cvpxxx grabbed pixel-synchronously
 cvxxx acquired with PLL line-synchronization

Version	APs	Co	Templ. size	Points eliminated
cvp253	0	30	7 x 7	none
cvp223	10	30	7 x 7	none
cvp221	10	m	7 x 7	none
cvp243	10	30	5 x 5	none
cvp323	10	30	7 x 7	points in columns 12 and 17
cvp343	10	30	5 x 5	points in columns 12 and 17
cvp601	10	30	5 x 5	+ points imaged too obliquely
cvp611	10	m	5 x 5	+ points imaged too obliquely
cvp602	25	30	5 x 5	+ points imaged too obliquely
cvp612	25	m	5 x 5	+ points imaged too obliquely
cvp603	54	30	5 x 5	+ points imaged too obliquely
cvp613	54	m	5 x 5	+ points imaged too obliquely
cv601	10	30	5 x 5	as in cvp601
cv611	10	m	5 x 5	as in cvp601

APs..... number of additional parameters
 Co..... number of control points
 Templ. size size of template in pixels
 Points eliminated ... points that were eliminated for that version (+ ... additional to points already eliminated)

11 ACKNOWLEDGMENTS

I would like to express my gratitude to my advisor, Prof. Dr. A. Grün, who has guided me through my studies as a Masters student at Ohio State University and provided me with advice and support during the duration of my dissertation at ETH-Zurich. He introduced me to the world of Digital Close-Range Photogrammetry and provided the initial idea to set up a Real-Time Photogrammetric System. His suggestions and the many enriching discussions in the initial phase of the development were instrumental to the success of this work. I would also like to thank him for leaving me considerable space for independent work and for the excellent financial support of the project.

I am indebted to my co-advisor, Prof. Dr. H. Tiziani, for reading my dissertation within tight time restrictions. His comments and suggestions were very helpful in improving this work and in furthering my knowledge.

I would also like to thank Dr. Mark Shortis for reading and correcting my "Austrian English", his critical remarks and for the many fruitful discussions. Prof. John Fryer was also kind enough to read parts of the dissertation. His remarks have been very helpful.

Pete Gustafson is thanked for performing one of the reference measurements of the test-field as well as the extensive discussions on calibration problems.

P. Seitz and J. Raynor were kind enough to provide testing equipment and were a tremendous source of information. The many inspiring discussions with them have been very rewarding. Mr. W. Wittwer and Volkswagen AG are thanked for kindly providing a Megaplus camera for tests.

An experimental project such as this requires the support of a large number of persons. The help of colleagues and the personnel of ETH-Zurich has been of invaluable throughout my work. Emmanuel Baltsavias, my companion from the masters studies at Ohio State University, provided software for initial tests and was always readily available for help. Joel Dähler was kind enough to fill me in on the basics of electronics such that I could perform a number of tests with the initial system. Beat Rüedin made sure that I did not have to worry about the time consuming work of keeping our computer system running and his help in solving the many small problems with it. His experience was extremely helpful to solve a number of tricky problems during the installation of hardware and software. Acknowledgements are extended to Scott Mason for reviewing the script. I would also like to thank all those colleagues who were willing to spend long days adjusting lights and test arrangements for investigations and for helping in the painful work of measuring the reference coordinates. Over the years I have learned to appreciate the help of the support staff of the Institute of Geodesy and Photogrammetry for designing and fabricating a large number of specialised mechanical equipment. The friendliness and help of our secretaries has been greatly appreciated.

My acknowledgements extend to my parents who have given me the opportunity to study and who have supported me throughout the many years of my studies. My wife Françoise has provided me with incessable support during this long period and has put up with me working for evenings and weekends.

